

Final Submission

**ONE-STEP GREEN HYDROTHERMAL
SYNTHESIS OF BIOCOMPATIBLE
GRAPHENE/TITANIUM DIOXIDE
NANOCOMPOSITES: TOWARDS THE
DEVELOPMENT OF HIGHLY SENSITIVE AND
SELECTIVE ELECTROCHEMICAL
IMMUNOSENSOR FOR DENGUE DIAGNOSIS**

SIEW QI YAN

**Thesis submitted to the University of Nottingham
for the degree of Doctor of Philosophy**

FEBRUARY 2020

Abstract

Biosensor platforms are powerful analytical devices capable of revolutionising medical diagnostics by providing highly accessible and effective diagnosis at the point-of-care stage. In this work, a high-performance electrochemical-based biosensing platform was developed using graphene/titanium dioxide (G/TiO₂) nanocomposite. The graphene employed in the G/TiO₂ electrode material was synthesised via a sonochemical liquid phase exfoliation method, eradicating the use of harsh chemicals and high temperature conditions. The simple and low temperature hydrothermal synthesis of the G/TiO₂ nanocomposite also ensured the affordability and scalability of the process. Modifying electrodes with the as-synthesised nanocomposite resulted in enhanced electrochemical performances compared to bare electrodes and graphene-modified electrodes. As hydrogen peroxide (H₂O₂) is one of the most common by-products of biological metabolic reactions, a non-enzymatic hydrogen peroxide (H₂O₂) sensor platform was developed to investigate the potential of G/TiO₂ nanocomposite in biosensing applications. The resulting H₂O₂ sensor exhibited high sensitivity with a limit of detection (LOD) of 56.89 nM. Subsequently, a versatile biosensor platform was constructed using 1-pyrenebutyric acid N-hydroxysuccinimide ester (PSE) as the biolinker. The performances of both graphene and G/TiO₂ based immunosensing platforms were evaluated for the detection of Dengue virus antibodies (DENV IgG). For the first time, a consensus envelope glycoprotein domain III (cEDIII) of dengue virus was employed as the biorecognition element for improved selectivity towards DENV IgG, even when challenged against the structurally similar Zika virus antibodies (ZIKV IgG). Moreover, the cEDIII protein was obtained via a novel

plant-based molecular pharming approach which offers remarkable scalability and safety. Both graphene and G/TiO₂ platforms showed promising results in dengue sensing with good sensitivity and selectivity. In addition, the feasibility of the immunosensing platforms in real sample was investigated through the detection of dengue antibodies in mouse serum samples, where both platforms successfully discriminated positive samples from the negative control, suggesting the potential of the immunosensor platforms in replacing conventional diagnostic methods. The G/TiO₂-based immunosensor displayed superior sensing performance compared to the graphene-based platform, with wider linear working range (62.5 pg/mL to 2 ng/mL) and lower limit of detection (LOD) of 2.81 pg/mL. Finally, the biocompatibility enhancement effect provided by the incorporation of TiO₂ nanoparticles onto graphene was studied via cytotoxicity assessments and comparison study on both graphene and G/TiO₂ nanocomposites. Results showed that the cytotoxicity of the nanomaterials is exposure time and dose-dependent, in which higher concentrations and prolonged incubation periods lead to higher magnitude of losses in cell viability. In general, G/TiO₂ nanocomposites exhibited lesser cytotoxic effects on both cell lines compared to graphene with a half maximal inhibitory concentration (IC₅₀) of greater than 500 µg/ml and around 25 µg/ml for MRC5 cells and HaCaT cells, respectively, at 24-hour time-point. The satisfactory biocompatibility of G/TiO₂ nanocomposites indicated its potential in various delicate biomedical applications such as *in-vivo* biosensing where the attribute is highly required.

List of Publications

Refereed Journals

- **Siew, Qi Yan**, Shiau Ying Tham, Hwei-San Loh, Poi Sim Khiew, Wee Siong Chiu, and Michelle TT Tan. "One-step green hydrothermal synthesis of biocompatible graphene/TiO₂ nanocomposites for non-enzymatic H₂O₂ detection and their cytotoxicity effects on human keratinocyte and lung fibroblast cells." *Journal of Materials Chemistry B* 6, no. 8 (2018): 1195-1206. (I.F.: 5.047)
- **Siew, Qi Yan**, Shi Hui Tan, Ee Leen Pang, Hwei-San Loh, and Michelle TT Tan. "Simple One Step Exfoliated Graphene flakes as Potential Electrochemical Immunosensing Platform for Dengue Diagnosis" (Pending submission to Journal).
- **Siew, Qi Yan**, Ee Leen Pang, Hwei-San Loh, and Michelle TT Tan. "Highly Sensitive and Selective Graphene/TiO₂ Impedimetric Immunosensor based on Plant-derived Tetravalent Envelope Glycoprotein Domain III (EDIII) Probe Antigen for Dengue Diagnosis" (Pending submission to Journal).

Conference Presentation

- "One-step green hydrothermal synthesis of graphene/TiO₂ nanocomposites for electrochemical sensing". International Conference on Advanced Materials and Nanotechnology (ICAMN 2016), Kuala Lumpur, 23rd-24th November 2016.

Acknowledgements

I would like to express my utmost gratitude towards my supervisors, Dr. Michelle Tan Tien Tien, Prof. Khiew Poi Sim, and Prof. Sandy Loh Hwei San, whose guidance and technical expertise provided the foundation of this thesis. The invaluable advices and constructive inputs you offer are critical to the success of this multidisciplinary project. Thank you for always being available for consultations despite your hectic schedules. I am genuinely grateful for your support throughout these years.

I would like to thank the Ministry of Higher Education for the Mybrain15 scholarship and Fundamental Research Grant Scheme which provided the funding for my PhD studies and experiments. I am also grateful to the Public Service Department (JPA) for sponsoring my undergraduate studies which provided me the opportunity to embark on this research journey.

I am thankful for my fellow collaborators, Dr Pang Ee Leen, Ms. Tham Shiau Ying, and Ms. Tan Shi Hui. The project could never be completed without your contribution. I thank my seniors in this research group, Dr. Joanna Chia, Dr. Low Sze Shin, and Dr. Ejikeme Raphael Ezeigwe for their guidance. Special thanks to Ms. Lin Lih Poh for her generosity and being a great participant in discussions. Best wishes to all your research works.

Special thanks to the delightful technicians and staffs at our campus, Mr. Andrew, Mr. Fareez, Mr. "Bob", Mr. Asyraff, Mr. Irshad, Mr. Faizal, Ms. Filzah, Ms. Khairani, Ms. Fatihah, Ms. Siti, Ms. Shankari and others for their assistance in laboratory matters; and the postgraduate administrative staffs, Ms. Shikin, Ms Muna, and Ms. Yoges for their continued patience. Special mention to Ms. Shikin for her understanding and

warmth, Khairani for the snacks, and Fareez for treating us dinner. It has been a pleasure working with you all and I wish the best of luck in all your future endeavours. A special mention of thanks as well, to Prof. Dino Isa for his generous access to the equipment in Shaz Lab.

I am forever grateful for my parents for nurturing me and my other family members for their support. I thank all the special people in my life, the different generations of BSS housemates and my friends, especially, who have been there for me throughout this journey, for the wonderful meals and memories. Special thanks to the LOL group (Chung Hong, Billie, Jia Wei, and Chang Nong) for the company and joy they brought in those stress relieving activities. Also, the help offered by Isabelle in the classes is also very much appreciated. I would like to express my deepest gratitude to Chung Hong for his company, help, and rides all these years. A special mention to the magical stray animals that have come and gone too, for the stress relief. To my fellow office mates, thanks for the chit-chats and good luck in your pursuits.

To all the other individuals whom I forgot to mention, please accept my sincere apologies and gratitude.

Table of Contents

Abstract	2
List of Publications	4
Acknowledgements.....	5
List of Figures	12
List of Tables	20
List of Abbreviations	21
Chapter 1: Introduction	29
1.1 Background and Overview	29
1.2 Rationale of Current Study	35
1.3 Outline of Thesis/ Thesis Organisation	39
Chapter 2: Literature Review.....	41
2.1 Background and Overview.....	41
2.2 Biosensor Fundamentals	44
2.2.1 Key Parameters in Development of Biosensor	48
2.2.2 Classifications of Biosensors	51
2.3 Graphene Synthesis and Biosensor Applications	77
2.3.1 Graphene.....	77
2.3.2 Graphene Synthesis	80
2.3.3 Graphene Biosensors.....	100
2.4 Graphene/Metal Oxide Synthesis and Biosensor Applications	106
2.4.1 Graphene/Copper Oxide Biosensor	107
2.4.2 Graphene/Zinc Oxide Biosensor	112
2.4.3 Graphene/Nickel Oxide Biosensor.....	117

2.4.4	Graphene/Titanium Oxide Biosensor	121
2.5	Dengue Diagnostics.....	128
2.5.1	Virus Isolation	132
2.5.2	Nucleic Acid Detection	132
2.5.3	Antigen Detection	134
2.5.4	Serological Tests.....	134
2.5.5	Future Prospects of Dengue Diagnostics.....	137
2.6	Chapter Summary.....	145
Chapter 3 : One-step Green Hydrothermal Synthesis of Graphene/TiO ₂ Nanocomposites for Non-enzymatic H ₂ O ₂ Detection		
		147
3.1	Overview	147
3.2	Experimental Details	150
3.2.1	Materials.....	150
3.2.2	Synthesis of Graphene.....	151
3.2.3	Hydrothermal Synthesis of G/TiO ₂	151
3.2.4	Characterisation of the Materials.....	154
3.3	Results and Discussion	155
3.3.1	Characterisation of the Materials.....	155
3.3.2	Electrochemical Response of Modified Electrodes towards Potassium Ferricyanide.....	162
3.3.3	Electrochemical Response of Modified Electrodes towards H ₂ O ₂	165
3.3.4	Amperometric Detection of H ₂ O ₂	169
3.4	Chapter Summary.....	173

Chapter 4: Simple One Step Exfoliated Graphene Flakes as Potential Electrochemical Immunosensing Platform for Dengue Diagnosis.....	174
4.1 Overview	174
4.2 Experimental Details	179
4.2.1 Materials.....	179
4.2.2 Fabrication of Graphene-modified Electrodes	180
4.2.3 Fabrication of Immunosensing Platform	180
4.2.4 Enzyme-linked Immunosorbent Assay (ELISA)	181
4.2.5 Electrochemical Characterisation of Immunosensor Platform	183
4.3 Results and Discussion	184
4.3.1 Optimisation of Graphene Mass Loading on Sensor Platform	184
4.3.2 Electrochemical Characterisation of Biosensor Platform	187
4.3.3 Optimisation of Biosensor Platform.....	190
4.3.4 Analytical Performance of the Biosensor Platform	194
4.3.5 Specificity Study of the Biosensor Platform.....	196
4.3.6 Preliminary Testing on Mouse Sera Samples.....	198
4.4 Chapter Summary.....	201
Chapter 5 : Highly Sensitive and Selective Graphene/TiO ₂ Impedimetric Immunosensor based on Plant-derived Tetravalent Envelope Glycoprotein Domain III (EDIII) Probe Antigen for Dengue Diagnosis.....	203
5.1 Overview	203
5.2 Experimental Details	205
5.2.1 Materials.....	205
5.2.2 Fabrication of G/TiO ₂ -modified Electrodes	205

5.2.3	Fabrication of Immunosensing Platform	205
5.2.4	Enzyme-Linked Immunosorbent Assay (ELISA).....	207
5.2.5	Electrochemical Characterisation of Immunosensor Platform	207
5.3	Results and Discussion	207
5.3.1	Optimisation of G/TiO ₂ Mass Loading on Biosensor Platform	207
5.3.2	Electrochemical Characterisation of Biosensor Platform	210
5.3.3	Optimisation of Biosensor Platform	213
5.3.4	Analytical Performance of the Biosensor Platform	216
5.3.5	Analytical Performance of the Biosensor Platform on Mouse Sera Samples	221
5.4	Chapter Summary.....	225
Chapter 6	: Cytotoxicity Study of Graphene and G/TiO ₂ Nanomaterials.....	227
6.1	Overview	227
6.2	Experimental Details	229
6.2.1	Materials.....	229
6.2.2	Synthesis of Graphene and G/TiO ₂	229
6.2.3	Cell Culture	229
6.2.4	Cell Proliferation Study	230
6.3	Results and Discussions	231
6.3.1	Microscopic Visualisation of Nanomaterials Interactions with MRC5 and HaCaT Cells	231
6.3.2	Cell Viability Assessment of Nanomaterials.....	235
6.3.3	Discussions	240
6.4	Chapter Summary.....	243

Chapter 7: Conclusions and Future Direction	244
7.1 Conclusions	244
7.2 Future Directions	251

List of Figures

<i>Figure 2.1. Schematic diagram showing the components of a biosensor.</i>	<i>45</i>
<i>Figure 2.2. Graph illustrating the publication trend related to the keyword “biosensor” from year 1994 to 2018 using the Web of Knowledge. The uprising interest towards the biosensing field results in the exponential rise in publications.</i>	<i>46</i>
<i>Figure 2.3. Schematic diagram representing the diverse potential applications of biosensors in areas of medical, food, environment, research, and military.....</i>	<i>47</i>
<i>Figure 2.4. Schematic diagram illustrating the working principle of a typical SPR-based optical biosensor</i>	<i>53</i>
<i>Figure 2.5. A typical set-up for piezoelectric biosensor.</i>	<i>54</i>
<i>Figure 2.6. Schematic representation of a thermometric biosensor.</i>	<i>55</i>
<i>Figure 2.7. Illustration depicts the typical set-up of (a) conventional electrochemical cell, (b) microfluidic electrochemical cell, and (c) disposable screen-printed electrode.....</i>	<i>56</i>
<i>Figure 2.8. Schematic representation of electrochemical biosensor with different transducing techniques</i>	<i>58</i>
<i>Figure 2.9. A typical staircase-like chronoamperometry graph showing the responses from successive additions of analyte. Inset shows the corresponding calibration curve</i>	<i>59</i>
<i>Figure 2.10. Schematic diagram of Clark's enzyme electrode showing the reactions involved.....</i>	<i>61</i>
<i>Figure 2.11. Coupled enzymatic reaction for creatinine and creatine detection</i>	<i>62</i>
<i>Figure 2.12. Schematic diagram depicting two different configurations for amperometric immunosensing: (A) antigen detection via a competitive immunoassay format with a redox-enzyme-labelled antigen; (B) antibody detection via indirect immunoassay format, also known as sandwich-type immunoassay. Ez represents the enzyme that catalyses the oxidation/reduction of the electroactive species.....</i>	<i>63</i>
<i>Figure 2.13. Simultaneous voltammetric detection of vanillin (VAN) and caffeine (CAF) at equal concentration of 1.0–100.0 $\mu\text{g mL}^{-1}$(1-8). Inset shows their respective analytical curves</i>	<i>65</i>

Figure 2.14. Schematic diagram illustrating the CV potential waveform. In CV measurements, the voltage is cycled between two pre-determined potentials, E_1 and E_2 , at a fixed scan rate which is represented by the gradient	66
Figure 2.15. Typical cyclic voltammogram of a fully reversible redox couple ($[Fe(CN)_6]^{4-/3-}$) showcasing the key parameters of peak potentials, peak currents, and peak potential separation	68
Figure 2.16. A) ISE experimental setup consisting a two-electrode electrochemical cell, B) Calibration curve of potential difference against logarithmic sample ion activity. Red trace represents the linear fashion as described by the Nernst equation while blue trace indicates the behaviour of the real electrode with deviations near the detection limit.....	70
Figure 2.17. A typical Nyquist plot depicting the electron-transfer-limited semi-circular region and a diffusion-limited linear region, with key impedance parameters such as charge transfer resistance (R_{ct}), solution resistance (R_s), and frequency (ω)	73
Figure 2.18. Graphical representation of layer-by-layer characterisation of a graphene-based biosensor via EIS	74
Figure 2.19. Schematic diagram illustrating graphene as the 2D building block for the 0D Buckyball, 1D CNT, and 3D graphite	78
Figure 2.20. Scheme illustrating the synthesis methods of graphene	81
Figure 2.21. Schematic diagram illustrating the epitaxial growth of graphene	83
Figure 2.22. A) Schematic diagram illustrating the CVD process, and B) Illustration depicting graphene segregation on substrate surface and the effects of cooling rate	86
Figure 2.23. Scheme illustrating graphene synthesis from ethanol and sodium	88
Figure 2.24. Schematic diagram illustrating "dry ice method"	89
Figure 2.25. Evolution of graphite oxidation schemes	91
Figure 2.26. Illustration depicting A) gradual unzipping of CNT to form graphene nanoribbons, and B) proposed chemical mechanism for nanotube unzipping	94
Figure 2.27. Schematic diagram illustrating the proposed mechanism of electrochemical exfoliation of graphite using 0.1 M H_2SO_4 as the electrolyte	96
Figure 2.28. Schematic representation of the sonochemical liquid phase exfoliation process for graphene synthesis	99

Figure 2.29. Visual representation of PSE functionalisation of graphene for glucose detection and the amperometric response of the graphene-based biosensor on successive additions of glucose with increasing concentrations. Inset shows calibration plot indicating the linear working range	102
Figure 2.30. Schematic representation of the step-by-step assembly of the graphene-enhanced genosensor for H5N1 detection and the analytical results: (A) Amperometric response of bare and G/PSE-modified SPCE with different dilutions of PCR amplicon; (B) Calibration plot of current signals against different dilution factors of H5 PCR amplicon in logarithmic scale	103
Figure 2.31. (a) Chronoamperometric response of the genosensor towards various DNA-t concentrations. (b) Redox current at the oxidation potential of 1.1 V vs logarithmic molar concentrations of DNA-t.....	104
Figure 2.32. Calibration curve of the immunosensor showing linear response of cTn1 concentration towards change in R_{ct} . Inset: normalised impedimetric response towards non-specific IgG and CRP with respect to cTn1	105
Figure 2.33. (a) Amperometric responses of GC electrodes modified with graphene-, CuO nanoparticle-, and CuO/graphene after successive additions of 0.5 mmol L^{-1} glucose in a 0.1 mol L^{-1} NaOH solution. (b) Amperometric response of CuO/graphene-modified GC electrode after subsequent glucose addition in 0.1 mol L^{-1} NaOH solution. Inset shows the corresponding calibration curve at $1 \mu\text{mol L}^{-1}$ glucose. (c) The summary of the pH-dependent diameters of CuO nanoparticles and their respective sensitivities in CuO/graphene-modified GC electrodes.....	108
Figure 2.34. Electrochemical characterisations of the TB@Cu ₂ O@GO immunosensor for AFP detection. (A) Nyquist plots of EIS : GCE showing the stepwise fabrication of the immunosensor: (a) GCE, (b) TB@Cu ₂ O@GO/GCE, (c) anti-AFP/TB@Cu ₂ O@GO/GCE, (d) BSA/anti-AFP/TB@Cu ₂ O@GO /GCE, (e) AFP/BSA/anti-AFP/ TB@Cu ₂ O@GO/GCE; (B) Current signal responses of the immunosensor for the detection of different concentrations of AFP: (a) 0.001 pg/mL, (b) 0.01 pg/mL, (c) 0.1 pg/mL, (d) 1 pg/mL, (e) 0.01 ng/mL, (f) 0.1 ng/mL, (g) 1 ng/mL, (h) 10 ng/mL and (i) 100 ng/mL; (C) Calibration curve of the immunosensor for the detection of different concentrations of AFP; (D) Interference study on the immunosensor for AFP detection..	111

Figure 2.35. CVs of (a) graphene/ GO_x and (b) ZnO/graphene/ GO_x electrodes (i) before and (ii) after the addition of 10 mM glucose in 0.1 M PBS buffer (pH=6). The redox peaks are indicated on the graphs with arrows	114
Figure 2.36. Scheme illustrating the development of G/ZnO genosensor for ssRNA detection and its corresponding Nyquist diagram	116
Figure 2.37. (a) Chronoamperometric response of NiO-GR/GCE in 0.2 mol L^{-1} NaOH solution towards increasing glucose concentrations at 0.35 V. Inset shows the current-time response at low concentrations; (b) Calibration curve of glucose obtained from the modified electrode	118
Figure 2.38. Amperometric glucose sensing performance of GNS/NiO/DNA-GC electrode towards successive additions of glucose in 0.1 M NaOH: (a) Effects of different potentials on the current responses; (b) Effects of different NiO wt% in the hybrid material on the current responses; (c) Detailed chronoamperometric response of the GNS/NiO/DNA-GC electrode (20 wt%) towards successive additions of glucose at 0.6 V	120
Figure 2.39. DPVs of increasing concentrations (0, 0.5, 1.0, 1.5, 2.0, 2.5, 3.5, 4.5, 5.5, 10, 20, 30, 40, 60, 80, 100, 120, 140, 170 and 200 μM) of adenine and guanine (a-t) in 0.1 M HAc-NaAc (pH 4.5) buffer solution. Inset shows (a) peak current against adenine concentration, and (b) peak current against guanine concentration	123
Figure 2.40. Schematic diagram illustrating the fabrication of the sandwich immunosensor for CEA detection and its electrochemical performance. (A) DPVs of the immunosensor towards different concentrations of CEA: 0.005, 0.01, 0.1, 1, 10, 100, and 200 ng mL^{-1} (from a to j); (B) the corresponding calibration curve of peak current vs. CEA concentrations in logarithmic scale showing linearity.....	125
Figure 2.41. (A) Nyquist plots from the EIS technique: (a) GCE, (b) $\text{TiO}_2\text{-NGO/Au@Pd HSs/GCE}$, (c) anti-HE4/ $\text{TiO}_2\text{-NGO/Au@Pd HSs/GCE}$, (d) BSA/anti-HE4/ $\text{TiO}_2\text{-NGO/Au@Pd HSs/GCE}$, (e) HE4 Ag/BSA/anti-HE4/ $\text{TiO}_2\text{-NGO/Au@Pd HSs/GCE}$; (B) Amperometric responses of the immunosensor towards different concentrations of HE4 Ag: (a) 60 nM, (b) 5 nM, (c) 1 nM, (d) 100 pM, (e) 10 pM, (f) 5 pM, (g) 60 fM, (h) 40 fM; (C) Calibration curve of the immunosensor for HE4 Ag detection. Error bar = RSD (n = 5)	127
Figure 2.42. Global presence of dengue	128
Figure 2.43. Dengue diagnostic tests and their comparative merits	131

Figure 2.44. Major diagnostic markers for dengue diagnosis, and their respective detectable periods.	
IgG and IgM level differ depending on whether the infection is primary or secondary	136
Figure 2.45. Schematic diagram of an NS1 rapid diagnostic kit illustrating its procedures and result interpretation	139
Figure 2.46. a) ΔR_{CT} of $SiO_2@APTES-GO$ composite-modified electrode versus (1) 10 pM non-complementary West Nile virus DNA, (2) 10 pM complementary DENV-2 DNA, and (3) 1 fM complementary DENV-2 DNA; b) Nyquist diagram before and after 1 fM complementary DENV-2 RNA hybridisation on $SiO_2@APTES-GO$ composite-modified electrode.....	141
Figure 2.47. A) Calibration curve for NS1 detection and B) Nyquist plots of different concentrations of NS1 (a-h represent 1.0, 6.25, 12.5, 25.0, 75.0, 100.0, 150.0 and 200.0 ng/mL, respectively) in PBS containing 1 mM $[Fe(CN)_6]^{4-/3-}$	142
Figure 2.48. Graphical representation of the NS1-based impedimetric immunosensor setup and the biosensor's performance	143
Figure 3.1. Screen-printed carbon electrode (SPCE) consisting working, counter, and reference electrodes.	150
Figure 3.2. Schematic diagram illustrating the preparation of G/TiO ₂ nanocomposites via a facile green hydrothermal synthesis.	152
Figure 3.3. XRD patterns of graphite, TiO ₂ , and G/TiO ₂ nanocomposites. Peaks indexed to both graphene and TiO ₂ show a successful formation of G/TiO ₂ nanocomposite.	156
Figure 3.4. FESEM images of (a) Graphene, (b) GTi1, (c) GTi2, (d) GTi3, (e) GTi4, (f) GTi5, and (g) EDX spectrum of GTi4. No foreign elements indicated in the EDX spectrum except Si background, indicating the pristine quality of G/TiO ₂ nanocomposites produced.....	158
Figure 3.5. TEM images of (a) graphene, (b) TiO ₂ nanoparticles, (c) G/TiO ₂ -nanocomposites (GTi4), and HRTEM image of (d) G/TiO ₂ nanocomposite (GTi4).	160
Figure 3.6. Raman spectra of graphene and G/TiO ₂ nanocomposite. Raman spectrum of G/TiO ₂ nanocomposite (GTi4) shows additional TiO ₂ peaks along with the original graphene peaks.....	161
Figure 3.7. CVs of 0.5 mM potassium ferricyanide on bare SPCE (Bare), graphene-modified SPCE (G), TiO ₂ -modified SPCE (T), and G/TiO ₂ -modified SPCE (GTi1, GTi2, GTi3, GTi4, GTi5) in 0.1 M PBS (pH 7.4). Scan rate, 50 mV/s. GTi4 exhibits the best electrochemical response.	163

Figure 3.8. Nyquist plots for bare SPCE, graphene-modified SPCE, TiO ₂ -modified SPCE, and G/TiO ₂ -modified SPCE. G/TiO ₂ -modified SPCE shows the least resistance among all 4.	165
Figure 3.9. CVs of 0.5 mM H ₂ O ₂ on bare SPCE, graphene-modified SPCE, TiO ₂ -modified SPCE, and G/TiO ₂ -modified SPCE in 0.1 M PBS (pH 7.4). Scan rate, 50 mV/s. G/TiO ₂ -modified electrode displays the best performance. GTi4 was used in this analysis.	166
Figure 3.10. (i) CVs of 0.5 mM H ₂ O ₂ on G/TiO ₂ -modified SPCE in 0.1 M PBS (pH 7.4) at different scan rates. The scan rate from inner to outer are 25, 50, 75, 100, 125, 150, 175, 200 mV/s, respectively; (ii) peak currents versus scan rates (inset). Linear proportionality can be observed for both anodic and cathodic peak currents.	168
Figure 3.11. Real time amperometric response of G/TiO ₂ -modified electrode for successive additions of H ₂ O ₂ ranging from 1 to 15 mM in 0.1 M PBS at a fixed potential of -0.4 V. The sensitivity of the modified electrode was found to be 0.557 μA/mM and the limit of detection (LOD) was calculated as 56.89 nM.	170
Figure 3.12. Real time amperometric response of G/TiO ₂ -modified electrode for successive additions of 1 mM H ₂ O ₂ , 1 mM AA, 1 mM UA, 1 mM glucose, 1 mM H ₂ O ₂ into 0.1 M PBS at fixed potential of -0.4 V.	172
Figure 4.1. Schematic diagram for the development of graphene/PSE-modified electrochemical immunosensor for dengue detection.....	183
Figure 4.2. CVs (a) and Nyquist plots (b) obtained from electrodes with increasing mass loading of graphene. G04 exhibits the best electrochemical response.	186
Figure 4.3. a) CV measurements of G, G/PSE, G/PSE/cEDIII, G/PSE/cEDIII/milk, G/PSE/cEDIII/milk/IgG. Conductivity reduces as elements on SPCE increases. b) Nyquist plot of G-modified SPCE, G/PSE, G/PSE/cEDIII, G/PSE/cEDIII/milk, G/PSE/cEDIII/milk/IgG. Impedance value increases as elements on SPCE increases.	189
Figure 4.4. Effects of a) cEDIII probe concentration, b) cEDIII probe immobilisation time, and c) target antibody hybridisation time on relative R _{ct} , ΔR(%). The optimum cEDIII probe concentration and immobilisation time were found to be 5 μg/mL and 30 minutes, respectively. The optimised target hybridisation time was 60 minutes.	193

Figure 4.5. Analytical measurement curve obtained for DENV IgG detection of the proposed sensor, using relative R_{ct} , $\Delta R(\%)$ as function of DENV IgG concentration. Inset shows the corresponding calibration plot of the immunosensor. 195

Figure 4.6. Response of immunosensor to antibodies raised against DENV and other viral diseases including ZIKV, H5N1, IBDV, and CAV. Results show that the immunosensor is specific in detecting DENV. 197

Figure 4.7. Response of immunosensor against mouse serum samples. G1 represents blank mouse serum while G2 represents serum extracted from immunised mice. Results show that immunosensor can detect the presence of DENV IgG in serum samples. 199

Figure 5.1. Schematic diagram for the development of G/TiO₂/PSE-modified electrochemical immunosensor for dengue detection..... 206

Figure 5.2. CVs (a) and Nyquist plots (b) obtained from electrodes with increasing mass loading of G/TiO₂ nanocomposites. GT05 exhibits the best electrochemical response..... 209

Figure 5.3. a) CV measurements of G/TiO₂, G/TiO₂/PSE, G/TiO₂/PSE/cEDIII, G/TiO₂/PSE/cEDIII/milk, G/TiO₂/PSE/cEDIII/milk/IgG. Conductivity reduces as elements on SPCE increases. b) Nyquist plot of G/TiO₂-modified SPCE, G/TiO₂/PSE, G/TiO₂/PSE/cEDIII, G/TiO₂/PSE/cEDIII/milk, G/TiO₂/PSE/cEDIII/milk/IgG. Impedance value increases as elements on SPCE increases. 212

Figure 5.4. Effects of a) cEDIII probe concentration, b) cEDIII probe immobilisation time, and c) target antibody hybridisation time on relative R_{ct} , $\Delta R(\%)$. The optimum cEDIII probe concentration and immobilisation time was found to be 1 $\mu\text{g/mL}$ and 60 mins, respectively. The optimised target hybridisation time was 60 mins..... 215

Figure 5.5. Analytical measurement curve obtained for DENV IgG detection of the proposed sensor, using relative R_{ct} , $\Delta R(\%)$ as function of DENV IgG concentration. Inset shows the corresponding calibration plot of the immunosensor. 218

Figure 5.6. Response of immunosensor to antibodies raised against DENV and other viral diseases including H5N1, IBD, VP3 and ZIKV. Results show that the immunosensor is specific in detecting DENV. 219

Figure 5.7. Signal response of the immunosensor towards DENV IgG over a period of 15 days. Signal response decreased slowly over time, indicating an acceptable shelf-life of at least 15 days. 220

<i>Figure 5.8. Effects of different concentrations of blocking buffer on the signal response of immunosensor. Immunosensor blocked by 1% of skim milk solution provided the highest difference between positive and negative samples.....</i>	<i>222</i>
<i>Figure 5.9. Signal response of immunosensor on positive (G1) and negative (G2) serum samples across different dilutions.</i>	<i>223</i>
<i>Figure 6.1. Optical microscopic morphological characterisation of untreated MRC5 cells at (a) 24 h, (b) 48 h, (c) 72 h; and MRC5 cells treated with 50 µg/ml of graphene nanoparticles at (d) 24 h, (e) 48 h, (f) 72 h.; 50 µg/ml of G/TiO₂ nanocomposites at (g) 24 h, (h) 48 h, (i) 72 h.</i>	<i>233</i>
<i>Figure 6.2. Optical microscopic morphological characterisation of untreated HaCaT cells at (a) 24 h, (b) 48 h, (c) 72 h; and HaCaT cells treated with 50 µg/ml of graphene nanoparticles at (d) 24 h, (e) 48 h, (f) 72 h.; 50 µg/ml of G/TiO₂ nanocomposites at (g) 24 h, (h) 48 h, (i) 72 h.</i>	<i>234</i>
<i>Figure 6.3. Cell viability profile of MRC5 cell line treated with graphene and G/TiO₂ nanocomposite of different concentrations at (a) 24 h, (b) 48 h, (c) 72 h. G/TiO₂ nanocomposite was found to be less cytotoxic compared to graphene.....</i>	<i>237</i>
<i>Figure 6.4. Cell viability profile of HaCaT cell line treated with graphene and G/TiO₂ nanocomposite of different concentrations at (a) 24 h, (b) 48 h, (c) 72 h. G/TiO₂ nanocomposite was found to be less cytotoxic compared to graphene.....</i>	<i>239</i>

List of Tables

<i>Table 2.1. Strengths and weaknesses of current dengue diagnostic methods.....</i>	<i>137</i>
<i>Table 3.1. Different mass ratios of graphene to titanium dioxide precursor used to form G/TiO₂ nanocomposites.</i>	<i>153</i>
<i>Table 3.2. Charge transfer resistance R_{ct} and solution resistance R_{sol} of the electrodes.</i>	<i>164</i>
<i>Table 3.3. Comparison between the performance of the proposed G/TiO₂-modified electrode on H₂O₂ detection against H₂O₂ biosensors fabricated from other materials.....</i>	<i>171</i>
<i>Table 4.1. OD values resulted from ELISA and relative R_{ct}, $\Delta R(\%)$ from immunosensor on mouse serum samples.....</i>	<i>199</i>
<i>Table 5.1. SPCEs modified with different volumes of G/TiO₂ suspension and their equivalent mass loadings.</i>	<i>207</i>
<i>Table 5.2. Analytical performances of the proposed immunosensor compared against other dengue biosensor works.....</i>	<i>217</i>
<i>Table 5.3. Signal response from immunosensor and O.D. value resulted from ELISA on mouse serum samples.....</i>	<i>224</i>
<i>Table 6.1. Comparison of IC_{50} for nanomaterials commonly used in biosensors fabrication.</i>	<i>242</i>

List of Abbreviations

AA	Ascorbic acid
Ab	Antibody
AC	Alternating current
ADE	Antibody-dependent enhancement
AFP	Alpha fetoprotein
Ag	Silver
Ag/Cl	Silver chloride
Al ₂ S ₃	Aluminium sulphide
APTES	3-aminopropyl triethoxysilane
Ar	Argon
Au	Gold
BRCA1	Breast cancer type 1
BSA	Bovine serum albumin
C	Carbon
C ₂ H ₄	Acetylene
C ₆ H ₁₄	Hexane
CAF	Caffeine
CAV	Chicken anaemia virus
CCCVd	Coconut Cadang-Cadang Viroid disease
CCD	Charge coupled device
CE	Counter/auxiliary electrode
CEA	Carcinoembryonic antigen

cEDIII	Consensus envelope domain III protein
CeO ₂	Cerium (IV) oxide
CFU	Colony-forming unit
CH ₄	Methane
CNT	Carbon nanotubes
CO	Carbon monoxide
CO ₂	Carbon dioxide
CRG	Chemically reduced graphene
CRP	Human C-reactive protein
CTB	Cholera toxin B subunit
cTn1	Human cardiac troponin 1
Cu	Copper
Cu ₂ O	Copper (I) oxide
CuO	Copper (II) oxide
CV	Cyclic voltammetry
CVD	Chemical vapour deposition
DA	Dopamine
DENV	Dengue virus
DF	Dengue fever
DHF	Dengue haemorrhagic fever
DMA	N,N-dimethylacetamide
DMEM	Dulbecco`s Modified Eagle Media
DMEU	1,3-dimethyl-2-imidazolidinone

DMF	N,N'-dimethylformamide
DNA-c	Capture probe DNA
DNA-r	Receptor probe DNA
DNA-t	Target BRCA1 DNA
DPV	Differential pulse voltammetry
dsDNA	Double strand DNA
DSS	Dengue shock syndrome
E_0	Formal potential
E_1	Initial potential
E_2	Switch potential
EDIII	Envelope domain III protein
EDX	Dispersive x-ray spectroscopy
EIS	Electrochemical impedance spectroscopy
ELISA	Enzyme-linked immunosorbent assay
E_p or E_{pa}	Anodic potential
E_p' or E_{pc}	Cathodic potential
FBS	Fetal bovine serum
$FeCl_3$	Iron (III) chloride
FFTCCV	Fast Fourier transformation continuous cyclic voltammetry
FTO	Fluorine doped tin oxide
GBL	Γ -butyrolactone
GCE	Glassy carbon electrode
GNS	Graphene nanosheet

GO	Graphene oxide
GO _x	Glucose oxidase
H	Hydrogen
H ₂ O ₂	Hydrogen Peroxide
H5N1	Avian influenza
HaCaT	Human adult low calcium temperature keratinocytes
HCl	Hydrochloric acid
HE4 Ag	Human epididymis specific protein 4 antigen
HER2	Human epidermal growth factor receptor 2
HFL1	Human fetal lung fibroblasts 1
hGC	Human chorionic gonadotrophine
HNO ₃	Nitric acid
HOPG	Highly oriented pyrolytic graphite
HPLC	High-performance liquid chromatography
HQ	Hydroquinone
HRP	Horse radish peroxidase
HRP-Ab ₂	Horse radish peroxidase labelled secondary antibody
HRTEM	High resolution TEM
HSP	Hansen Solubility Parameters
<i>I</i> or <i>I_{pa}</i>	Anodic peak current
<i>I'</i> or <i>I_{pc}</i>	Cathodic peak current
IBDV	Infectious bursal disease virus
IC ₅₀	Half maximal inhibitory concentration

IFCC	International Federation of Clinical Chemistry and Laboratory Medicine
IGA	Inorganic graphene analogues
IgA	Immunoglobulin A
IgG	Immunoglobulin G
IgM	Immunoglobulin M
IMAC	Immobilised metal affinity chromatography
ISE	Ion-selective electrodes
ITO	Indium tin oxide
IUPAC	International Union of Pure and Applied Chemistry
IVD	<i>In vitro</i> diagnostics
JE	Japanese encephalitis
LFIA	Lateral flow immunoassay
LOC	Lab-on-a-chip
LOD	Limit of detection
MAC-ELISA	IgM antibody-capture enzyme-linked immunosorbent assay
MB	Methylene blue
Mg	Magnesium
MnO ₂	Manganese (IV) oxide
MRC5	Medical Research Council cell strain 5 (lung fibroblasts)
MTGP	Human mammary tumour associated glycoprotein
MTT assay	3-(4,5-dimethylthiazol-2-yl)-2,5-diphenyltetrazolium bromide) tetrazolium reduction assay
MWCNT	Multi-walled carbon nanotubes

NaOH	Sodium hydroxide
Ni	Nickel
NMP	1-methyl-2-pyrrolidone
NPs	Nanoparticles
NS1	Non-structural protein 1
NTU assay	Neutral red uptake assay
OCP	Open circuit potential
OD	Optical density
PANI	Polyaniline
PBS	Phosphate-buffered saline
PCR	Polymerase chain reaction
Pd	Palladium
pI or IEP	Isoelectric point
POC	Point-of-care
PSA	Prostate specific antigen
PSE	1-pyrenebutyric acid N-hydroxysuccinimide ester
PVDF	Polyvinylidene fluoride
R _a	Lowest Hansen Solubility Parameters distance
R _{ct}	Charge transfer resistance
RE	Reference electrode
RGO or rGO	Reduced graphene oxide
RIA	Radioimmunoassay
RPMI-1640	Roswell Park Memorial Institute growth media 1640

R_s	Solution resistance
RSD	Relative standard deviation
RT-PCR	Reverse transcriptase polymerase chain reaction
scFv	Specific single-chain variable fragment
SEM	Scanning electron microscope
SiC	Silicon carbide
SiO ₂	Silicon dioxide
SPCE	Screen-printed carbon electrodes
SPR	Surface plasmon resonance
ssDNA	Single-stranded DNA
ssPDNA	Single strand probe DNA
ssRNA	Single-stranded RNA
ssTDNA	Single strand target DNA
SWV	Square wave voltammetry
TB	Toluidine blue
TEM	Transmission electron microscopy
TiO ₂	Titanium dioxide
TMB	3,3',5,5'-Tetramethylbenzidine
TTIP or Ti(OiPr) ₄	Titanium (IV) isopropoxide
UA	Uric acid
UF	Undifferentiated febrile illness
UHV	Ultra-high vacuum
VAN	Vanillin

VEGF	Vascular endothelial growth factor
WE	Working electrode
WHO	World Health Organisation
XPS	X-ray photoelectron spectroscopy
XRD	X-ray diffraction
YF	Yellow fever
Z	Impedance
ZIKV	Zika virus
$Z_{im}(\omega)$	Imaginary component of impedance
ZnO	Zinc oxide
$Z_{re}(\omega)$	Real component of impedance
ZrO ₂	Zirconium dioxide
ΔR_{ct}	Change in R_{ct}
ΔE or ΔE_p	Interpeak distance or peak separation
$\Delta R(\%)$.	Relative R_{ct} %
2D	Two dimensional
3D	Three dimensional

Chapter 1: Introduction

1.1 Background and Overview

Humans have been plagued by diseases since its dawn of creation. In fact, diseases are so inevitable that deaths caused by diseases are called death by natural causes. To survive, these diseases can be fought by having proper treatment or taking preventive actions. Sadly, there are still limits to the brilliance of human medicine. In most cases, deadly diseases may only be cured or successfully managed with early diagnosis when they are still at their easily treatable pre-symptomatic stage. With effective early-stage interventions, the survival rate of patients can be improved immensely while also reducing late-stage healthcare expenditure for the healthcare providers at the same time.

Medical diagnostic tests are vital procedures performed to detect and diagnose diseases, which will then determine the treatment decisions for patients. As disease symptoms could be clinical or subclinical, or sometimes indiffereniable, these tests can provide definitive confirmation on the suspicions of a physician post physical examination. The ability to correctly recognise and identify medical conditions is critically important as this would affect whether patients may receive or forgo medical care. This is especially crucial when it comes to life-threatening infectious diseases or cancer where a single misdiagnosis would lead to dire consequences due to lack of proper treatment at early manageable state.

The diagnostic tools that clinicians currently employ to diagnose diseases are *in vitro* diagnostics (IVDs), in which samples of tissues or bodily fluids are analysed to

determine the presence of biomarkers from genetic mutations or immune responses. Not only minimally invasive, IVDs are invaluable in providing key information on a person's health for appropriate patient management to help cure, treat, and even prevent diseases. Therefore, established laboratory assays such as radioimmunoassays (RIA) and enzyme-linked immunoassay (ELISA) are well-adopted worldwide. However, there are still room for improvements for these classical IVDs. Common issues of conventional IVDs include long turnaround time, equipment intensive, tedious protocols, and the requirement of trained laboratory personnel due to their complexity, therefore, not suitable for point-of-care applications ¹. Hence, refined diagnostic techniques with rapid turnaround time, ease of use, high sensitivity and selectivity, and capable of providing differential diagnosis on potentially lethal diseases at early stages are gravely in demand.

The term "biosensor" refers to a powerful and innovative self-contained integrated device capable of detecting/quantifying target analytes by utilising biological/biochemical reactions. The device intimately connects a biological recognition element (biocatalyst) that interacts with the target analyte to a physicochemical detector (transducer) that converts the biological recognition event into a useable output signal, effectively combining the specificity and sensitivity of biological systems with the computing power of microprocessor ²⁻⁴. Ever since the invention of the first glucose biosensor by Clark and Lyons in 1962 ⁵, the biosensor concept has crossed leaps and bounces, flourishing in various fields including biotechnology, food and agriculture processing, health care, medicine, and pollution monitoring ⁶. In the recent years, a huge variety of biosensors have been constructed and developed for numerous medical applications, symbolising the evolving trend in

diagnostic technology ⁷. These biosensor instruments offer several indisputable advantages such as low cost, high specificity and selectivity, rapid response, and simple to operate, making them ideally suited for point-of-care health analysis. Biosensors can be classified into calorimetric, optical, piezoelectric, and electrochemical biosensors based on the technology used for the transducing element. Among these biosensors, electrochemical biosensors are the most widely adapted biosensing devices due to their high sensitivities, ability to produce accurate real time signals and perform regardless of media turbidity, and higher amenability for miniaturisation ⁸. Owing to these advantages, electrochemical biosensors are believed to be promising alternatives for medical diagnosis compared to conventional molecular detection approaches.

Sensitivity and selectivity are among the most important criteria when it comes to the evaluation of the performance of a biosensor. A successful biosensor with high sensitivity and selectivity must possess the ability to detect a specific target at ultra-low levels while maintaining this specificity in the presence of other species. With the phenomenal advancements in nanotechnology, nanomaterials hold prodigious potential in enhancing the performance of electrochemical biosensors. The deployment of highly conductive nanomaterials as the electrode material in biosensor ensures accelerated signal transduction, unequivocally improving its sensitivity. By employing specifically designed sensing solutions, functionalised nanomaterials can also amplify biorecognition events, thus providing biosensors with enhanced selectivity ⁹. In addition, hybridisation between nanomaterials often yields synergistic effect among desirable properties such as catalytic activity, conductivity and biocompatibility, giving rise to a plethora of nanomaterials to be explored.

The ingenious strategy of incorporating nanomaterials into biosensors has led to major improvements in sensors' performances ¹⁰⁻¹². Notably, among the amazing nanomaterials explored, graphene has arisen to be the most promising nanomaterial suitable for a wide array of applications due to its exceptional properties¹³⁻¹⁷. Graphene, a single-atom-thick layer of sp²-bonded carbon atoms arranged into a honeycomb lattice structure, has become the material under spotlight since its discovery in 2004 due to its novel electronic and structural properties ^{18, 19}. The unique two dimensional (2D) environment that graphene offers allows accelerated electron transport which augments the electrochemical catalytic activity of biosensors, leading to enhanced sensitivity and signal amplification ¹⁹⁻²¹. Graphene also holds a very high prospective in the application of sensitive bioanalytical protocols because of its high specific surface area and ease of surface functionalisation that enable easy and reliable immobilisation of biomolecules, which is an extremely favourable quality in developing novel bio-interfaces for biosensing ^{22, 23}.

The unique ability of graphene-based materials to combine desirable properties of different building blocks enables hybrid graphene composites to acquire new desirable properties from the hybridising material while eliminating certain disadvantages of pristine graphene ^{24, 25}. Accordingly, the performance of graphene can be enhanced further by integrating other inorganic nanoparticles such as metal oxide nanoparticles onto the graphene sheets. Metal-oxide nanomaterials such as zinc oxide (ZnO) and titanium dioxide (TiO₂) have been reported to provide a novel mechanism to enhance the electron-transfer between the receptor and the sensing matrix, while offering other desirable properties such as excellent biocompatibility ²⁶. Due to the catalytic and synergistic effect between graphene and metal oxide

nanoparticles and their enhanced electrical and electronic properties, graphene/metal oxide nanocomposites offer tremendous potential for a variety of applications including energy storage, energy conversion and electrochemical sensing devices ^{27, 28}. Apart from the synergistic effect, the metal oxide nanoparticles act as a stabiliser against the aggregation of individual graphene sheets, which is caused by strong van der Waals interactions between graphene layers. Not only that, decorating the edges and surfaces of the graphene sheets with metal oxide nanoparticles also potentially reduces the toxicity of the graphene against cells. The cytotoxicity of graphene was proposed to be dependent on its shape, namely the sharp edges of graphene piercing the membrane of cells and killing them ^{29, 30}. A “coating” on the graphene sheets would protect the cells from the potentially harmful graphene edges. The integration of metal oxide nanoparticles also increases the particle size of graphene, which potentially reduces its size-dependent cytotoxicity. Other factors determining the safety of graphene include its hydrophobicity and aggregation, which can be improved by incorporating metal oxides.

To date, various metal oxide nanoparticles have been incorporated on graphene in efforts to further broaden its applications and enhance its performance in biosensing. Among these metal oxide nanomaterials, titanium dioxide (TiO₂) nanoparticles have attracted remarkable interests due to their superior properties such as large specific surface area, high uniformity, excellent biocompatibility and environmentally-friendly ^{31, 32}. The enlarged specific surface area has been reported to provide a better environment for the immobilisation of biomolecules such as enzymes for biosensing purposes ³³. Due to the amazing properties of both graphene and TiO₂ nanoparticles, the hybridisation of both nanomaterials is expected to induce synergistic effect in the

nanocomposite, producing a tailor-made innovative and versatile material with performance superior to those of the individual materials.

In recent years, the intriguing properties of graphene-based nanocomposites have encouraged researchers to develop various synthesis routes to explore the hybridisation of graphene and TiO₂ nanoparticles. Synthesis methods such as sol-gel, hydrothermal, and microwave-assisted reduction have been employed to incorporate TiO₂ onto graphene-based materials, successfully producing nanocomposites with improved electronic or photocatalytic performance³⁴. Most of these synthesis approaches however comprised of elaborated procedures of producing graphene oxide (GO) via the renowned Hummer's method, followed by chemical reduction processes to obtain reduced graphene oxide (rGO) prior to the hybridisation process with TiO₂. While this approach is well-established, it is still plagued by several apparent disadvantages. Firstly, the harsh acid mixtures involved in the Hummer's method coupled with the high temperatures and long processing time poses heightened risk in synthesis operations³⁵. The as-produced GO would contain numerous functional groups such as hydroxyls and epoxides that may be persistent to removal or reduction processes. Another drawback that comes with these approaches is the usage of strong reducing agents such as hydrazine hydrate in the formation of rGO³⁵. Not only hazardous, hydrazine hydrate also creates dangerous by-products such as hydrogen fluoride³⁶. The resultant rGO was often found to be of inferior quality and less conductive compared to pristine graphene, largely attributed to the residual functional groups and defects destroying the 2D structure and reducing the electronic properties of the carbon material^{37,38}.

1.2 Rationale of Current Study

In order to address the previously mentioned issues, this research attempts to develop a highly sensitive and selective in-vitro disease diagnostic platform that is easily accessible without the requirement of expensive laboratory facilities and complex protocols handled by well-trained professionals, while being able to provide results within short durations, all via the electrochemical biosensor approach. For improved sensitivity, the research first focus on the facile synthesis and characterisation of G/TiO₂. To overcome the safety issues commonly faced by the conventional synthesis methods of graphene-related materials, graphene flakes were synthesised via a safe and environmentally friendly sonochemical liquid exfoliation method, and then subjected to a low temperature hydrothermal process to obtain G/TiO₂ nanocomposites. In an effort to examine the potential of G/TiO₂ nanocomposites as the electrode platform for electrochemical sensing applications, H₂O₂ was used as the model analyte in a series of electrochemical analyses. The potential of the proposed sensor platform was then investigated for detection of infectious diseases. Dengue, one of the most prevalent infectious diseases in Malaysia and other tropical/sub-tropical countries, was chosen as the model disease. Finally, the cytotoxicity effects of both graphene and G/TiO₂ nanocomposite will be evaluated against two mammalian skin lines, MRC5 (lung fibroblasts) and HaCaT (skin keratinocytes), as inhalation and skin contact are the two key exposure routes for nanomaterials.

The specified objectives of the project are as follows:

1. To establish an efficient, facile, and green approach for the synthesis of G/TiO₂ nanocomposite

Currently available G/TiO₂ synthesis methods could be improved on several areas. These include the safety and environmental friendliness of the procedure, and of utmost importance, the final product quality. The synthesis method of G/TiO₂ nanocomposite was investigated with different ratios of TiO₂ precursors to develop high quality G/TiO₂ suitable for biosensing applications. The selection of the optimal precursor ratio is crucial as the different configurations may affect the morphology and structure of the synthesised product, potentially affecting its electrochemical properties and performance.

2. To evaluate the electrochemical properties of G/TiO₂ nanocomposite for its potential in biosensing applications

The electrochemical properties of the as-synthesised G/TiO₂ nanocomposite were studied in detail to provide an insight on its potential in biosensing applications. A comparative study between graphene, TiO₂ and G/TiO₂ nanocomposite was carried out to verify the improvements in terms of electrochemical performance provided by the incorporation of TiO₂ on graphene. As hydrogen peroxide (H₂O₂) is one of the most common by-products of manual biological metabolic reactions, it is the perfect choice as the analyte for elementary biosensing works. A non-enzymatic H₂O₂ sensor was developed using the as-prepared G/TiO₂ and subjected to a series of electrochemical measurements to characterise its electrochemical performance.

3. To develop high performance impedimetric biosensor platform for point-of-care disease detection

The ultimate aim of the research is to develop a high-performance biosensing platform suitable for point-of-care detection of various diseases. Using a versatile biolinker (1-pyrenebutyric acid N-hydroxysuccinimide ester) strategy, any biorecognition molecule with amine on its surface can be anchored to the developed graphene-based nanomaterials as the probe, thus enabling countless customised solutions for the specific detection of various diseases to be developed using this biosensing platform. With immunosensor in mind, dengue was chosen as the focus of this research. Both graphene and G/TiO₂ nanocomposite were evaluated for their performances as electrode platform for immunosensing. The basic electrochemical sensing performances of these nanomaterials were explored in the previous objective using H₂O₂ detection via amperometric technique. In this subsequent objective, the feasibility of these nanomaterials on surface functionalisation with biological recognition element for the detection of target of interest was explored via impedimetric technique. Key parameters such as probe concentrations and incubation times were optimised. The performances of the developed dengue biosensors were characterised in elaborated electrochemical analyses. The sensitivity, specificity, and detection limits of the biosensors were also determined as an indicator of their performances. Subsequently, the biosensors were challenged against mouse serum samples to evaluate its viability in real sample diagnostics.

4. To evaluate the biocompatibility of as-synthesised graphene and G/TiO₂ nanocomposites

While metal oxide nanoparticles are proposed to improve the biocompatibility of graphene, there is a lack of proper cytotoxicity evaluation and comparison between graphene and other popular graphene/metal oxide nanocomposites. The hypothesis of biocompatibility improvement via TiO₂ incorporation will be verified by subjecting the nanomaterials to cytotoxicity assessments. The biocompatibility assessment on graphene and G/TiO₂ nanocomposites will contribute to the material selection for biosensor fabrication, and potentially unlocks future biosensing applications.

1.3 Outline of Thesis/ Thesis Organisation

The general outline of the thesis is presented as follows:

Chapter 1, *Introduction* discusses the problems with current disease diagnostic methods and how nanotechnology innovations, specifically nanomaterials based electrochemical biosensors, can overcome the limitations of these conventional techniques. The objectives of this research are also presented, along with the approaches used to achieve them.

Chapter 2, *Literature Review* covers the biosensor fundamentals, graphene synthesis routes, graphene/metal oxide composite synthesis methods, previous works on graphene and graphene/metal oxide composites-based biosensors, and current dengue diagnostic techniques.

Chapter 3, *One-step Green Hydrothermal Synthesis of Graphene/TiO₂ Nanocomposites for Non-enzymatic H₂O₂ Detection* details the hydrothermal pathway selected for the synthesis of G/TiO₂ nanocomposite and the evaluation of the nanocomposite as a nanomaterial suitable for biosensing purposes. The effects of varying ratios of graphene and TiO₂ precursor on the electrochemical properties of the nanocomposite are also discussed. Biosensor constructed based on the as-produced nanocomposite were subjected to electrochemical measurement for its ability to detect H₂O₂.

Chapter 4, *Dengue Diagnosis of Graphene Impedimetric Biosensor Based on Plant-derived Viral Envelope Glycoprotein Domain III* outlines the development of a dengue immunosensing platform by immobilising dengue envelope domain III (EDIII) protein obtained from plant-based molecular pharming on graphene-enhanced screen-

printed carbon electrodes. Key parameters were optimised and studied. A simple test on mouse serum samples was conducted to verify the sensor's potential in realistic applications.

Chapter 5, *Dengue Diagnosis of Graphene/TiO₂ Impedimetric Biosensor Based on Plant-derived Viral Envelope Glycoprotein Domain III* reports the fabrication of dengue immunosensor based on G/TiO₂ nanocomposite-enhanced electrodes using plant-based EDIII as the probe. Various parameters were optimised for the detection of dengue antibodies using the constructed immunosensor. The as-developed immunosensor was tested against mouse serum sample to evaluate its performance in realistic applications, and compared with responses obtained from conventional in-house indirect ELISA tests.

Chapter 6, *In-vitro Biocompatibility Evaluation of Graphene and Graphene/TiO₂ Nanocomposites on Human Keratinocytes and Lung Fibroblasts Cells* studies the cytotoxic effects of graphene and G/TiO₂ nanocomposites on human skin and lung cells. The nanomaterials were subjected to cell viability assessment assays and their effects on cell morphology were also observed to provide an insight on the biocompatibility of the nanomaterials.

Chapter 7, *Conclusion and Future Directions* summarises the findings and work done in this research. This final chapter also discusses the potentials and future directions that this project can explore.

Chapter 2: Literature Review

2.1 Background and Overview

The earliest record on diagnosis of infectious disease via in-vitro diagnostics (IVDs) could perhaps be dated back to 1917, where pneumococcal polysaccharide was found to be detectable by conducting immunoassay on serum and urine samples from patients with lobar pneumonia ³⁹. In their report, the authors' prescient remarks suggested the possibility of rapid diagnosis of infections through antigen detection. Since then, immunoassays for antigen or antibody detection for disease diagnosis have been explored extensively with keen interest. The pivotal development of radioimmunoassay (RIA) in 1960 ⁴⁰ and enzyme-linked immunoassay (ELISA) in 1971 ^{41, 42} has expedited the disease diagnostics research further, due to the high sensitivities that they offer. Despite their remarkable performances, the ELISA and RIA immunoassay platforms are time consuming, equipment intensive, and complex, hence not suited for point-of-care use.

The immense potential of immunoassays in disease diagnostics has encouraged researchers to search for ways to perform rapid tests at the point-of-care stage. An example of the successful modern immunoassay technology is the lateral flow immunoassay (LFIA) platform where a simple cellulose-based device is used to detect the presence of a target analyte in a liquid sample ^{43, 44}. A well-known application for this technique is the commercial home pregnancy test. As the LFIA format does not require specialised or costly equipment, it is suitable for medical diagnostics in both home testing and point-of-care testing, besides traditional laboratory usage. Today, most rapid diagnostic tests utilise the LFIA technology. Some popular applications for

the diagnosis of infectious disease include streptococcal pharyngitis (strep throat), influenza type A and B, and hepatitis C virus ¹.

Naturally, there is a constant need to improve the performance of current diagnostic assays and to develop innovative strategies to counter new diagnostic challenges. While point-of-care diagnostics have now gained widespread recognition with the maturity of LFIA platform, there are several innovative technologies on the horizon which hold great promises in improving the accessibility, performance, and adoption rate of the diagnostic tests ¹. One of the most promising alternative approach is the biosensor platform. The history of modern biosensors originated from the invention of oxygen electrode by Leland C. Clark, Jr in 1956 ⁴⁵. The invention of Clark oxygen electrode laid the basis for the momentous development of the first glucose biosensor presented by Clark and Lyons in 1962 ⁴⁶. Termed “enzyme electrode” in the published paper, the enzyme glucose oxidase was entrapped in a dialysis membrane over an oxygen probe. The ground-breaking discovery had started a new era of researches in the medical science and technology area. In the past few decades, scientists have been on a mission to improve the quality of human life, as shown by the exceptional growth in the study of biosensors. This intensively competitive area involving multidisciplinary researches including physics, chemistry, biotechnology, material science, life science, and engineering has led to the emergence of various reliable sophisticated and accurate biosensors, be it *in-vivo* or *in-vitro*.

Recently, nanomaterials have been heavily employed in biosensor fabrication following the rapid advancements in the field of nanotechnology. These nanomaterials offer many desirable properties such as large surface area to volume

ratio, high electrical and heat conductivity, and improved surface catalytic activity⁴⁷⁻
⁴⁹. The minute size (1-100 nm) of the nanoparticles are also within the typical size
range of biomolecules, which would enable almost one-to-one interaction between
the nanoparticle and the biomolecule of interest^{50, 51}. Due to these wonderful
attributes, the integration of nanomaterials into biosensing systems promise
enhanced sensitivity, speed, and cost-effectiveness⁵¹. Among the reported
nanomaterials, graphene-based nanomaterials have emerged as a family of
nanomaterials with unprecedented advantages due their superior electronic, optical,
and mechanical properties^{13, 52, 53}. These remarkable qualities have led to the
development of countless innovative strategies to synthesise and manipulate
graphene for biosensing purposes, which include the incorporation of metal oxide
nanoparticles onto graphene sheets with the aim to further improve its performance.
Driven by their promising potentials capable of revolutionising the fields of chemical
and biological analysis, graphene/metal oxide biosensors have spawned huge interest
within the scientific community and given rise to the conception of various novel
biosensing solutions.

Hence, this chapter presents a brief review covering the fundamental knowledge on
biosensors with emphasis given to electrochemical biosensors, graphene and its
synthesis pathways, and graphene/metal oxide-based biosensors (and their
applications). As the model disease selected in the study, a short review on dengue
and its existing diagnostic assays were also presented.

2.2 Biosensor Fundamentals

The International Union of Pure and Applied Chemistry (IUPAC) defines biosensor as “a device that uses specific biochemical reactions mediated by isolated enzymes, immunosystems, tissues, organelles or whole cells to detect chemical compounds usually by electrical, thermal or optical signals”⁵⁴. In other words, a biosensor is an independent analytical device used to detect an analyte and consists of a biological recognition element linked to a physicochemical detector (transducer) to convert the biological response into a signal that’s both quantifiable and processable ^{2, 55, 56}. The schematic diagram in Figure 2.1 illustrates the elements found in a typical biosensor, and the components are detailed as follows ⁵⁷:

- *Analyte*: The substance of interest in need of detection.
- *Bioreceptor*: A molecule capable of biologically recognise the specific analyte and generate signal in forms of light, heat, charge, mass change or pH.
- *Transducer*: Converts the signal generated from the analyte-bioreceptor interaction into a measurable signal.
- *Electronics*: The circuitry element that processes and amplifies the transduced signal.
- *Display*: Display output that generates numbers or figures comprehensible by users based on the quantified signal, making analysis on the results of the biosensor possible.

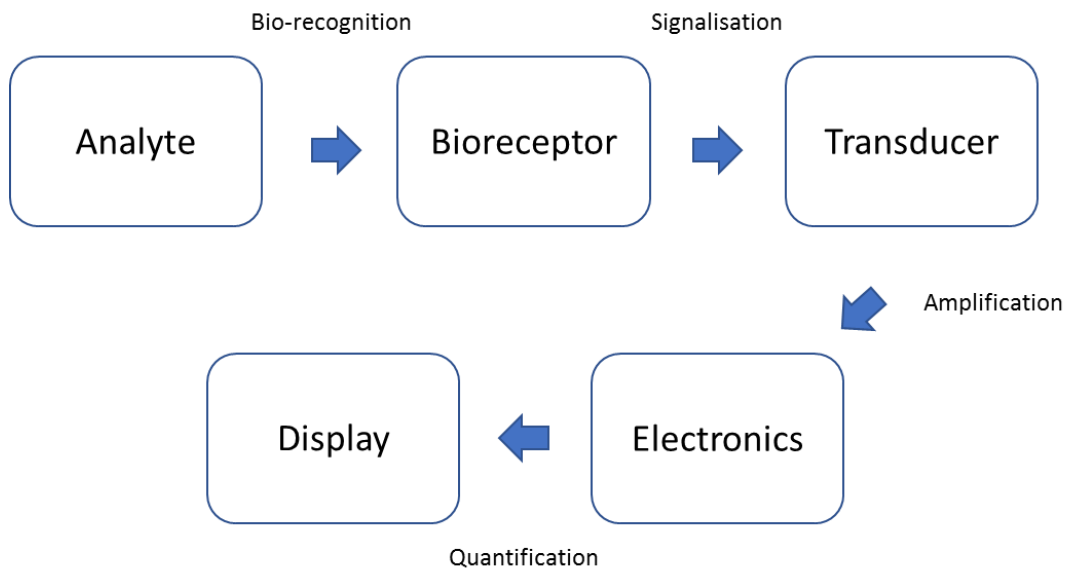


Figure 2.1. Schematic diagram showing the components of a biosensor.

The field of biosensor has experienced an explosive growth over the past decades. Searching the keyword “biosensor” in the Web of Knowledge shows the exponential rise in the number of publications from 1994 to 2018 (Figure 2.2). The publications in last year alone accounts for almost 10% of the total amount of publications on this topic (5248 out of 57,585). The phenomenal growth reflects the interest of the scientific community towards the biosensing field.

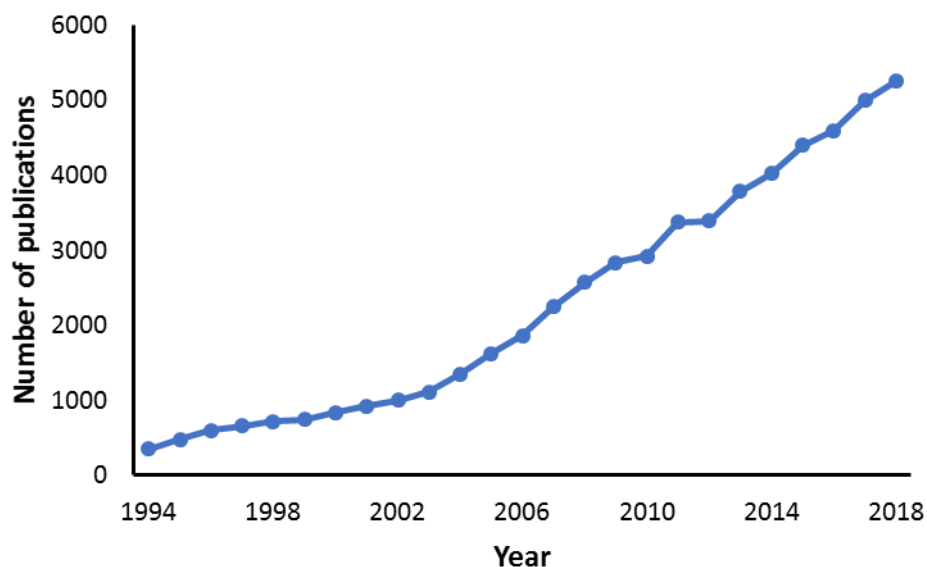


Figure 2.2. Graph illustrating the publication trend related to the keyword “biosensor” from year 1994 to 2018 using the Web of Knowledge. The uprising interest towards the biosensing field results in the exponential rise in publications.

The ever-growing interest of the scientific community towards biosensors could be attributed to the many exquisite advantages offered by biosensors in general. The main advantages of biosensors include high sensitivity that enables analyte detection up to picomolar concentrations, high selectivity due to specific bioreceptor-analyte interaction, real time and continuous detection of target analyte, rapid response time, and ease of miniaturisation that allows on-site testing ⁵⁸.

Due to their pronounced advantages, biosensors have a diverse range of potential applications capable of improving quality of life, namely medical, food, environment, military and research (Figure 2.3) ^{8, 56, 59, 60}. The sensitivity and selectivity of biological compounds allows biosensors to be designed to suit different applications with the appropriate biorecognition element. For medical purposes, biosensors can be applied for disease detection ⁶¹, drug discovery ⁶², and in artificial implantable devices such as

pacemakers and other prosthetics ⁶³. Their specialised functions enable them to be used in food industry to monitor food traceability, quality, safety and nutritional value ⁶⁴. Biosensors can also be used for environmental monitoring, in applications of pollution monitoring and water/soil quality monitoring ⁶⁵. Biosensors are also applicable in research field, in addition to military purposes such as in the area of bioterrorism detection and prevention ⁶⁶.

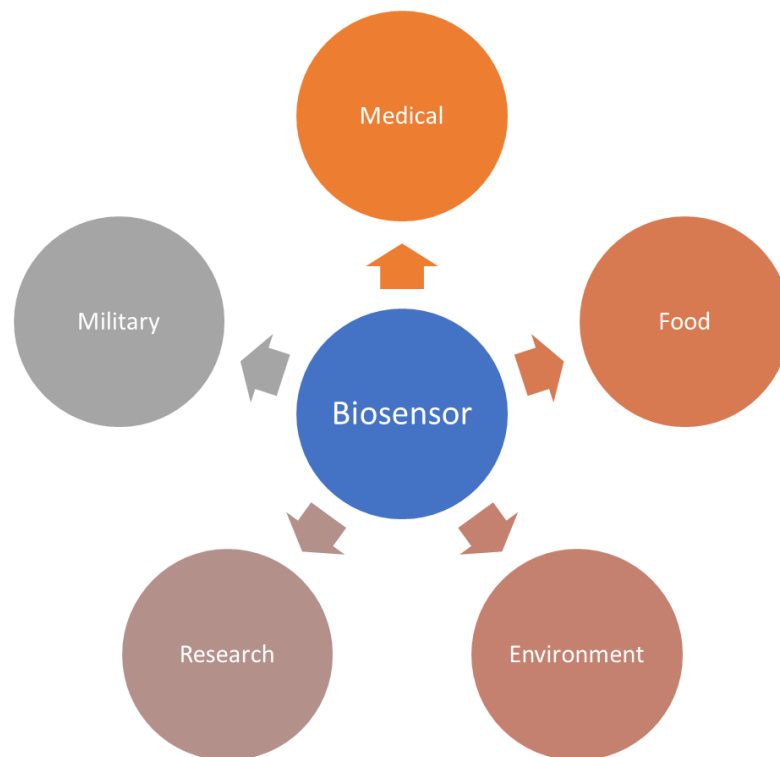


Figure 2.3. Schematic diagram representing the diverse potential applications of biosensors in areas of medical, food, environment, research, and military.

2.2.1 Key Parameters in Development of Biosensor

There are certain qualities to be considered in the assessment of the performance of a biosensor:

2.2.1.1 Selectivity

The selectivity or specificity of the biosensor represents its ability to detect a specific analyte in a sample containing other interfering molecules and contaminants. Biosensors generally offer good selectivity when the appropriate probe or bioreceptor is selected in designing the biosensing interface due to the specific nature of the binding interactions between biomolecule pairs. Some examples of selective binding interactions would be the formation of enzyme-substrate complexes and antigen-antibody immunocomplexes. Therefore, selectivity is always the most important concern in deciding the bioreceptor for the fabrication of a biosensor.

2.2.1.2 Sensitivity

Biosensor applications in biomedical and environmental field often demand analyte detection at very low concentrations up to nanoscale and picoscale. For example, upon detection of prostate-specific antigen (PSA) up to 4 ng/ml, which is a known biomarker for prostate cancer, biopsy tests would be immediately ordered for the patient to confirm the diagnosis. Hence, sensitivity is a vital aspect in constructing a high-performance biosensor.

While early recommendations from IUPAC defined sensitivity as the slope of the calibration curve⁶⁷, modern scientists in the field of analytical and clinical science have adopted the use of detection limits in assessing a biosensor's sensitivity as per suggestions from the International Federation of Clinical Chemistry and Laboratory

Medicine (IFCC) ⁶⁸. The limit of detection (LOD) denotes the detection limit or the minimum analyte concentration that can be detected by a biosensor and distinguished from the background (signal produced by a sample in absence of analyte) for reliable analyte detection ^{69,70}. From a linear calibration curve, the LOD can be expressed using the following equation:

$$LOD = \frac{3\sigma}{Slope} \quad (2.1)$$

Where σ is the standard deviation of signal generated by the blank.

2.2.1.3 Linearity and Linear Dynamic Range

Linearity describes a biosensors' linear relationship between the measured response and the concentration of analyte, which can be graphically represented as a straight line in the calibration curve where an R^2 value of close to 1 indicates a good linearity. A biosensor with good linearity is often needed in most applications as they normally require sensitive analyte detection and concentration measurement over a wide working range. The linear dynamic range of the biosensor specifies the range in analyte concentration where the response can be predicted according to the calibration curve, thus determining the effectiveness and practicality of the biosensor in the desired application.

2.2.1.4 Stability

Stability is the ability of a biosensor to withstand the interference or disturbances from its surroundings, which may cause deviations in the output signals of the biosensor thus affecting its precision and accuracy. One of the factors that influence the stability of a biosensor is the bioreceptor affinity, which is the binding strength between the

bioreceptor and the analyte. High affinity bioreceptors usually involve bonding interactions with strong electrostatic forces or covalent linkage for better stability. As response of electronics and biomolecular interactions can be temperature-sensitive, ambient temperature in and around the biosensing system may affect the stability as well. Another key factor that influences the stability of a biosensor is time. The shelf-life of a biosensor is always limited because bioreceptor molecules generally degrade over time, which potentially causes drifts and errors in analytical measurements.

2.2.1.5 Precision

Repeatability describes the degree of agreement between the results obtained from successive measurements of the same variable conducted under the same conditions⁷¹. In other words, the measurements on the same item are taken by the same operator using the same instrument, under the same conditions, and in a short period of time. Repeatability describes the consistency of the biosensor against itself, providing the same results under the same circumstance, repeatedly. Also known as test-retest reliability, repeatability is exceptionally important in time-lapse study such as monitoring applications.

Reproducibility refers to the degree of agreement between results of successive measurements of the same variable carried out under different measurement conditions, in other words, the ability of the biosensor in generating identical responses for duplicated experimental setups using the same methodology⁷¹. Reproducible signals indicate the reliability and robustness of the biosensor in presence of inferences or ambient noises.

Defined as the degree of proximity between the results of successive measurements of the same variable ⁷², the precision of a biosensor is characterised by its repeatability and reproducibility. The amount of imprecision is described using the term variability and expressed statistically in standard deviations.

2.2.1.6 Accuracy

Accuracy denotes the extent to which the measurement of a biosensor approaches the true value of the measured variable, basically, the difference between the true and measured values ⁷⁴. To determine the accuracy, the measurements are compared to a reference or a standard that provides the “true” value. The biosensor is accurate if their average reading from repeated measurements is close to the true value of the measured variable. For diagnostic biosensors, the results can also be compared to established diagnostic assays to interpret the biosensor’s accuracy.

2.2.2 Classifications of Biosensors

Biosensors can be broadly classified according to either the nature of the biorecognition event or the type of physiochemical signal transduction element employed. Based on the biorecognition elements, biosensors can be classified into enzymatic biosensors (enzyme), immunosensors (antibody/antigen), genosensor (DNA probe), aptasensor (aptamer), and microbial biosensor (microorganisms). The transducer in a biosensor converts the biorecognition event into detectable signal by utilising the physical change that accompanies the given reaction. The detectable signal can be in the form of optical, thermometric, mass change (piezoelectric), and electrochemical, forming four main classes of biosensors.

2.2.2.1 Optical Biosensor

Optical biosensors are optoelectronics-based biosensors that induce changes in the phase, amplitude, polarisation or frequency in the input light in response to biorecognition process. The key components of an optical biosensor include a light source, an optical transmission medium (fibre or waveguide), immobilised bioreceptor (enzymes, antibodies or microbes), and an optical detection system. Based on the detection protocols, optical biosensing can be classified into two: fluorescence-based and label-free. In fluorescence-based optical biosensor, either the analyte or the bioreceptor molecules are labelled with fluorescent tags such as dyes. The intensity of the fluorescence provides an indication on the presence of the target molecules and the strength of interaction between the target and bioreceptor molecules. On the other hand, label-free detection systems do not label or alter the target molecules and the optical signal is generated directly via the interaction between the biorecognition event and the transducer. The most popular optical biosensors are surface plasmon resonance (SPR)-based biosensors, while other optical biosensing systems include interferometric, ellipsometric, and reflectometric interference spectroscopy, surface-enhanced Raman scattering biosensors, evanescent wave fluorescence, and bioluminescent optical fibre biosensors ⁷³. The typical set-up for an SPR-based biosensor is shown in Figure 2.4, along with the elements involved.

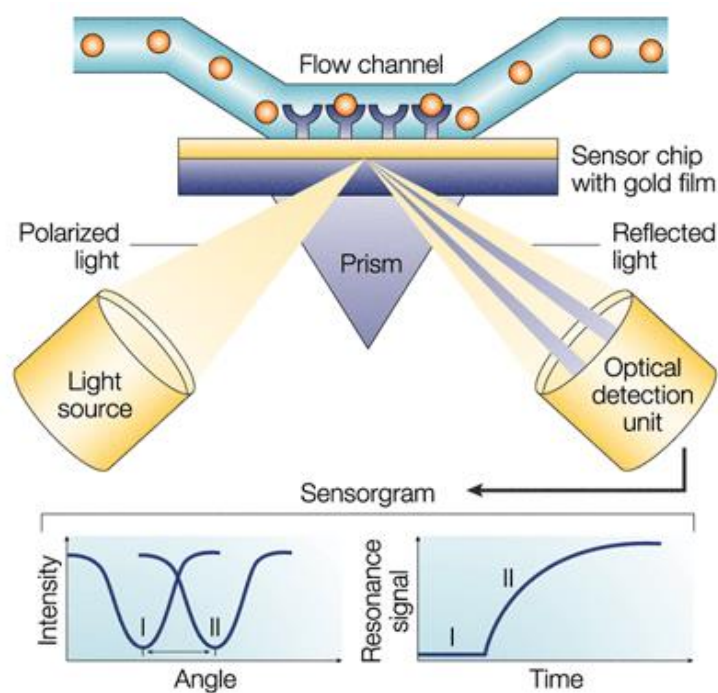


Figure 2.4. Schematic diagram illustrating the working principle of a typical SPR-based optical biosensor ⁷⁴.

2.2.2.2 Piezoelectric Biosensor

Piezoelectricity is defined as the potential difference created across certain materials due to an applied mechanical stress, which is also the basis for piezoelectric-based biosensors. Piezoelectric biosensor functions by measuring the changes in oscillating crystal resonance frequency from the bioreceptor-analyte interactions. The transducer in piezoelectric biosensor is made from a piezoelectric material such as quartz, and the bioreceptor molecule is then coated on the piezoelectric material, vibrating at natural frequency. As piezoelectric materials are anisotropic (no centre of symmetry), an electric signal is produced when they are stressed mechanically (pressure applied). The resonant frequency is heavily dependent on the mass of the crystal and the coating of the biomaterials, which is why it can be measured with immense accuracy. The mass of the analyte adsorbed on the surface of the crystal can

then be calculated based on the change in frequency. The components involved in the experimental set-up of a typical piezoelectric biosensor are displayed in Figure 2.5. Biosensors based on piezoelectric transduction mode offers high sensitivity, high accuracy, portability, robustness, and compatibility with integrated circuit technology^{75, 76}.

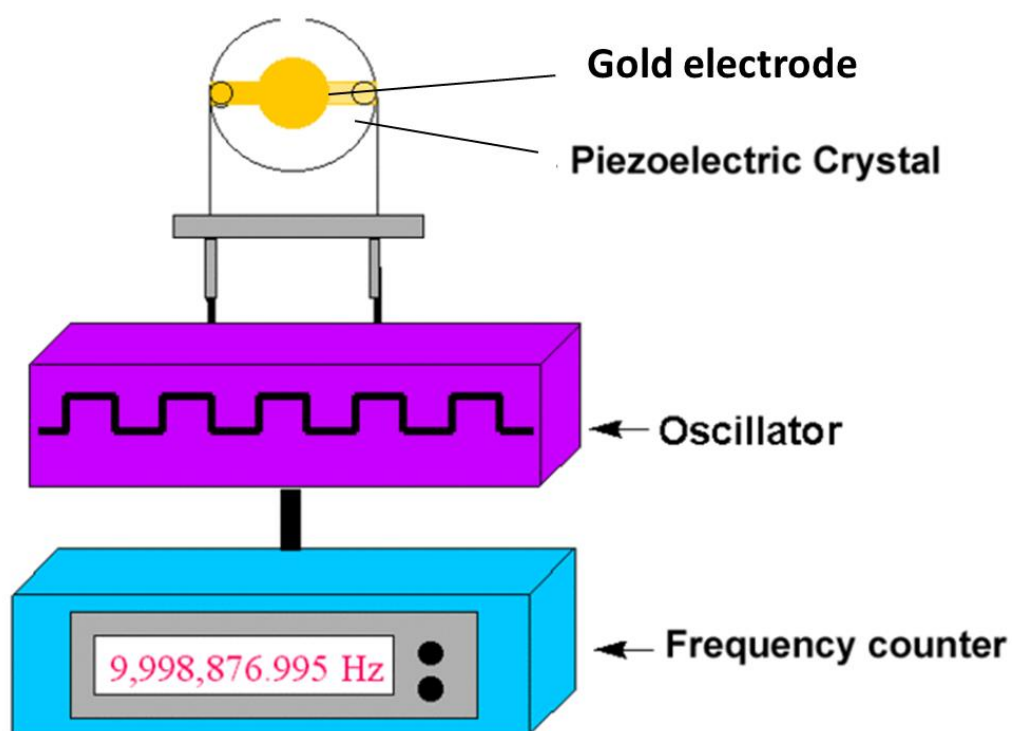


Figure 2.5. A typical set-up for piezoelectric biosensor⁷⁷.

2.2.2.3 Thermometric Biosensor

Thermometric or calorimetric biosensors function based on the principle of reactions where all chemical and biological reactions involve the exchange of heat⁷⁸. The temperature changes within the reaction medium is measured using the transducer in the form of either thermistor or thermophile, and correlates to the molar enthalpy and the amount of the reactants formed or consumed in the biochemical reaction. An

example of a thermometric biosensor is shown in Figure 2.6, with a heat exchanger (aluminium cylinder) fitted in a heat-insulated box. The heat generated by the bioreaction occurring at the immobilised enzyme bed is measured by the thermistors and recorded. The major advantages of this calorimetric technique include stability, possibility of miniaturisation, and enhanced sensitivity. Thermometric transduction method can be used in enzymatic biosensors, DNA/cell biosensors, and immunosensors. Today, the method has found their niche in applications regarding the food industry and environmental monitoring^{79, 80}.

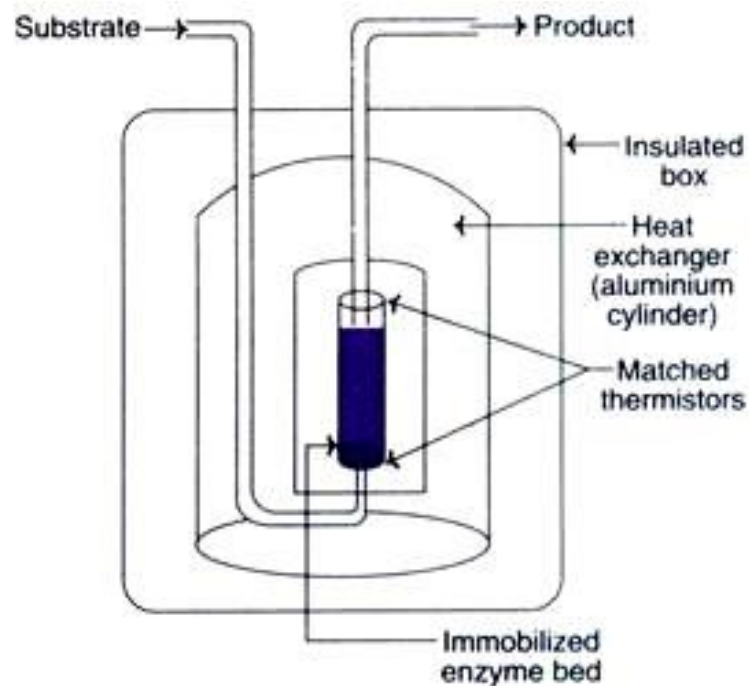


Figure 2.6. Schematic representation of a thermometric biosensor.

2.2.2.4 Electrochemical Biosensor

Electrochemical biosensors are biosensors that employ electrochemical transducer in their biosensing configuration. As recommended by IUPAC in 1999, an electrochemical biosensor is a self-contained integrated device, which is capable of providing specific

quantitative or semi-quantitative analytical information using a biological recognition element (biochemical receptor) which is retained in direct spatial contact with an electrochemical transduction element⁴. This type of biosensor operates by measuring the current produced from redox reactions, directly converting the biorecognition event into electrical signal proportional to the concentration of the analyte present in a sample. A typical electrochemical biosensor set-up consists of the three-electrode system: a working electrode (WE) where the reaction of interest takes place; a reference electrode (RE) that produces a constant potential; and a counter or auxiliary electrode (CE) to close the current circuit. While conventional electrochemical biosensors employ the electrochemical cell system, technology advancements have made miniaturisation possible, evolving electrochemical biosensors set-ups into more portable systems such as microfluidic electrochemical cells and screen-printed electrodes. Figure 2.7 illustrates a conventional electrochemical cell set-up⁸¹, a microfluidic electrochemical cell⁷⁶, and a disposable screen-printed electrode⁸².

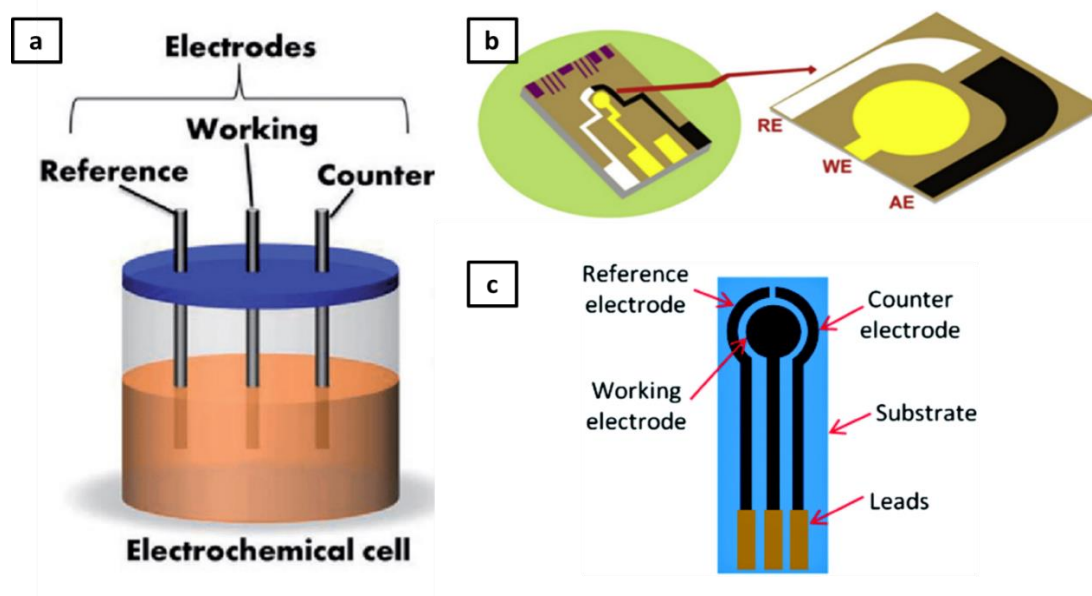


Figure 2.7. Illustration depicts the typical set-up of (a) conventional electrochemical cell⁸¹, (b) microfluidic electrochemical cell⁷⁶, and (c) disposable screen-printed electrode⁸².

Electrochemical biosensors have been the centre of attention in the development of biosensors, especially for clinical applications such as disease detection, drug screening, and health monitoring ⁸³. Offering incredible practicality, sensitivity, and fast response, electrochemical biosensor can be integrated onto a lab-on-a-chip (LOC) system to acquire excellent analytical platforms for point-of-care (POC) applications. Depending on the operating principle, electrochemical biosensors can be further classified into four types: amperometric, potentiometric, voltammetric, and impedimetric. A scheme of electrochemical biosensor is shown in Figure 2.8, highlighting the diverse types of electrochemical biosensors and the different modes of measurements ^{84, 85}.

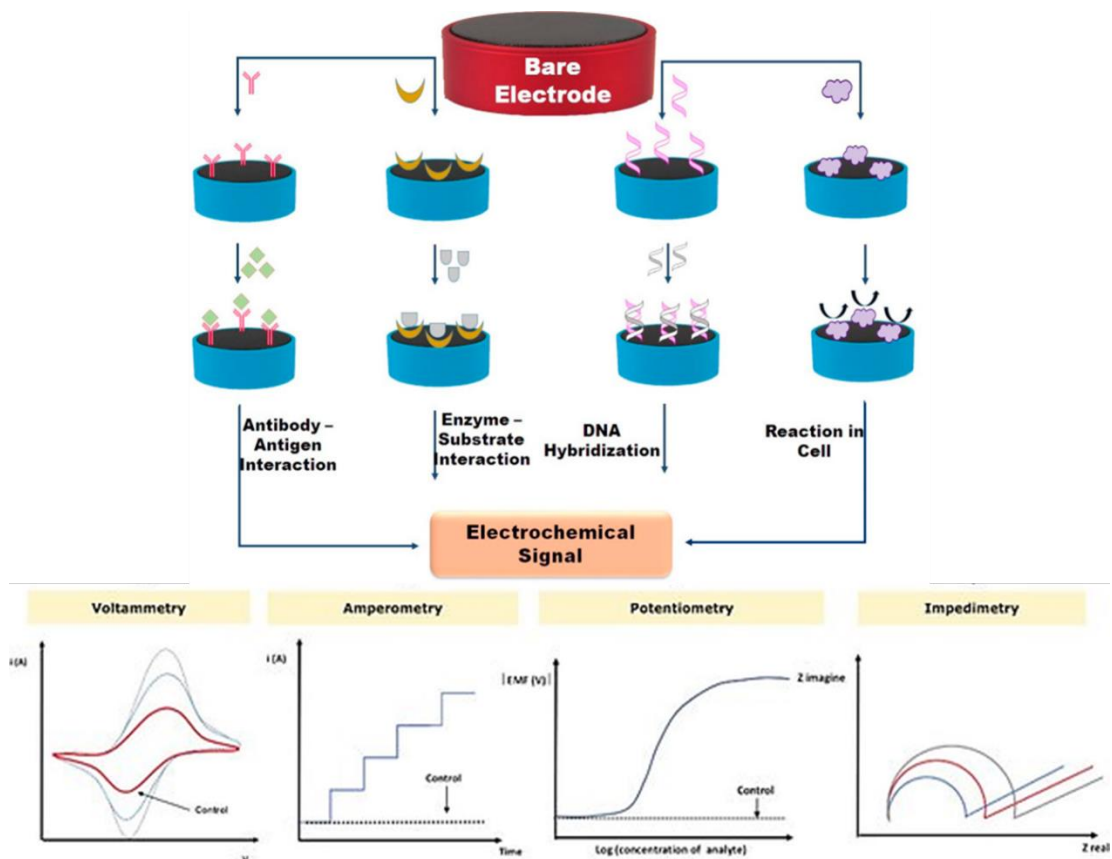


Figure 2.8. Schematic representation of electrochemical biosensor with different transducing techniques^{84, 85}.

2.2.2.4.1 Amperometric Biosensor

Amperometric biosensors function by measuring the currents resulting from the redox reaction of an electroactive species with the bio-recognition probe molecule under a fixed potential applied to the working electrode⁸⁶. The applied potential serves as the driving force for the electron transfer of the electroactive species by forcing it to either gain or lose electrons. The current generated is proportional to the analyte concentration as it represents the rate of electron transfer in the bio-recognition process. The ability to determine the concentration of the analyte molecule makes this type of biosensor extremely useful in a diverse range of applications, rendering it one of the most widespread class of biosensors. Also, by selecting an appropriate

applied potential, amperometric biosensors can achieve good selectivity as the oxidation or reduction potential of each analyte species varies⁸⁷.

A standard electrochemical measurement procedure performed using amperometric biosensors is chronoamperometry, a time-dependent technique in which the current of the electrode is monitored as a function of time. An example of a current-time response curve obtained from a chronoamperometry experiment by an amperometric biosensor is depicted in Figure 2.9. As the current is measured continuously, a staircase-like response was obtained by successive additions of fixed concentrations of analyte at fixed intervals, which cumulatively increases the concentration of analyte in the system thus generating increasing current responses.

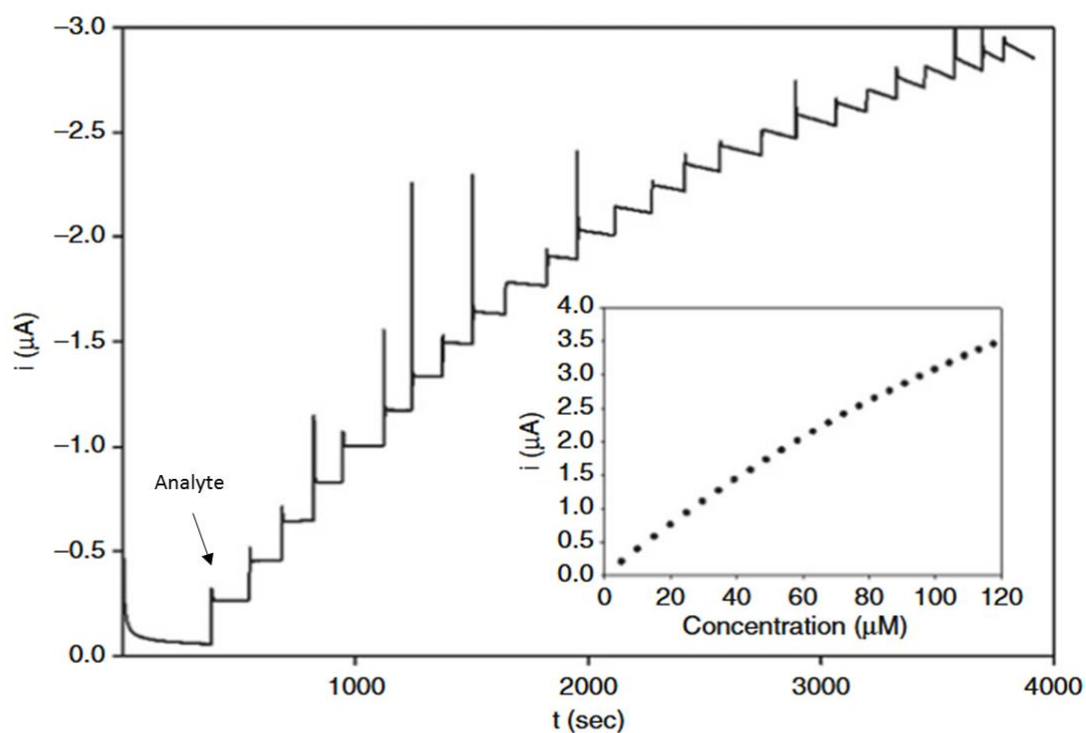


Figure 2.9. A typical staircase-like chronoamperometry graph showing the responses from successive additions of analyte. Inset shows the corresponding calibration curve⁸⁶.

Early generation biosensors function by directly measuring the concentration of substrates or products involved in an enzymatic reaction. These biosensors usually utilise oxidases and hydrogenases enzymes to quantify oxygen reduction or hydrogen peroxide (H_2O_2) generation. One of the most common and established usage of amperometric biosensor is in glucose sensing. Pioneered by Clark and Lyons in the sixties ⁵, the original design had glucose oxidase entrapped onto the surface of a platinum electrode (Figure 2.10). As the analyte, glucose, reaches the trapped glucose oxidase, the enzyme-catalysed oxidation process occurs, producing gluconic acid and H_2O_2 . A negative potential applied onto the cathode electrode will then induce the reduction of oxygen. Therefore, the concentration of the glucose present in the sample can be determined by measuring the amount of oxygen consumed in the oxidation process. Modifications on the design were introduced later to avoid the dependence on oxygen concentration by detecting the amount of H_2O_2 directly ⁸⁸. Nowadays, with decades of refinements, Clark's brilliant design is widely used as blood-glucose biosensors for the screening and treatment of diabetes.

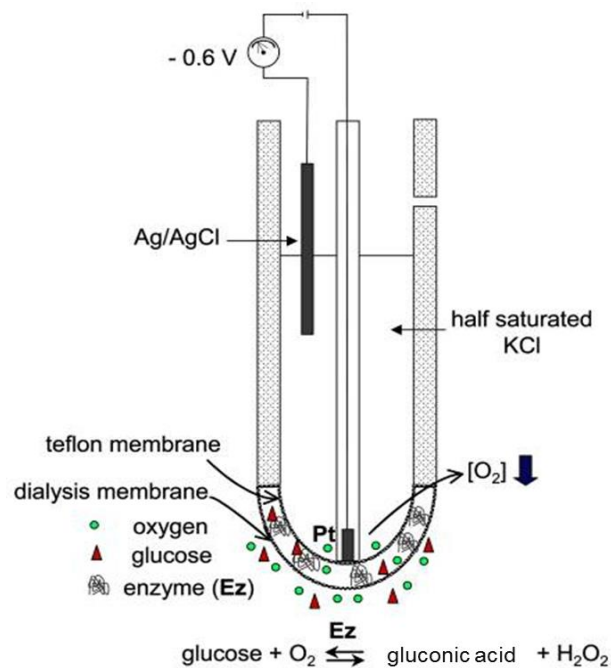


Figure 2.10. Schematic diagram of Clark's enzyme electrode showing the reactions involved ⁸⁹.

Based on the same principles, the change in concentration of a substrate/product in question can be reliably measured with amperometry provided they are electroactive. Unfortunately, in most cases, the analyte of interest is not a natural substrate of a redox enzyme. To overcome this limitation, various strategies have been developed depending on the chemical properties of the analyte. Among them is the use of coupled enzymatic reactions where the analyte participates in another reaction to produce an electroactive species (usually H_2O_2) which can be detected via amperometry. An example of this design would be the work done by Tsuchida *et al.* in the detection of creatine and creatinine ⁹⁰. The determination of these two analytes in biological fluid aids the diagnosis of renal, muscular, and thyroid functions as creatine is an important product of protein catabolism while creatinine is an indicator for kidney function. The coupled enzymatic reactions are shown in Figure 2.11. The

H₂O₂ generated in the process will then produce an amperometric signal when electrochemically transformed at the electrode. Using this similar concept, various amperometric biosensors have been developed for the detection of urea⁹¹, lactate⁹², pyruvate⁹³, and many more.

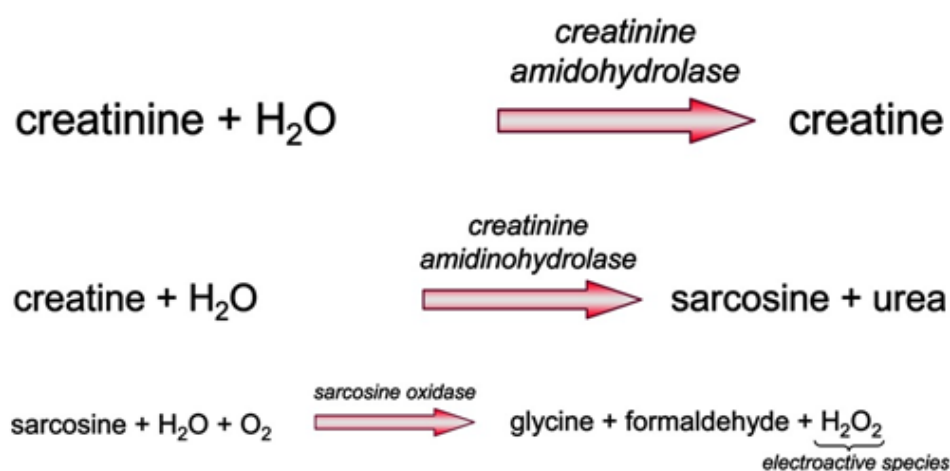


Figure 2.11. Coupled enzymatic reaction for creatinine and creatine detection⁹⁰.

Immunosensors are biosensors that exploit the specific antigen-antibody interaction for the detection of the analyte of interest. One of the popular immunosensor scheme is similar to the design of the competitive enzyme-linked immunosorbent assay (ELISA), in which a competitive immunosensing assay is performed by adding enzyme-labelled antigen to a sample containing the analyte. As shown in Figure 2.12A, in the competitive immunosensor format, the target analyte competes with the enzyme-labelled antigen for the biorecognition active site of the antibody anchored on the electrode. With the applied potential, the substrate of the redox enzyme label produces the electroactive product, generating a detectable current. The current

signal of this competitive immunosensor design diminishes with increasing analyte concentration.

In the diagnosis of infections, the analyte is usually an antibody. In these cases, a slightly different strategy can be used for the immunosensing assay (Figure 2.12B). Instead of antibodies, antigenic particles are immobilised on the electrode to capture specific antibodies in the sample. A redox-enzyme-labelled secondary antibody that binds to a particular region of the antibody analyte will be added next. As the secondary antibody are captured onto the electrode, the substrate of the enzyme label generates a detectable current which indicates the presence of the analyte.

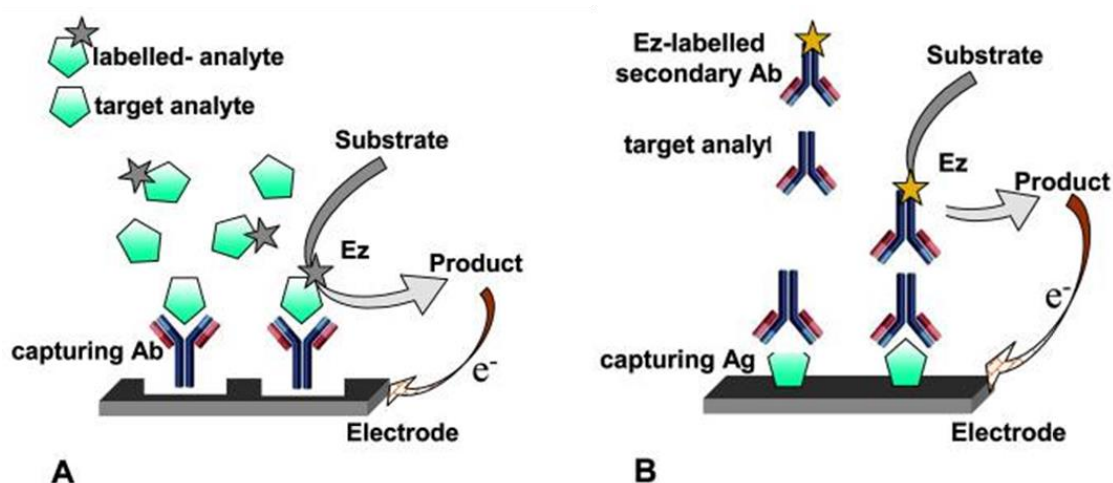


Figure 2.12. Schematic diagram depicting two different configurations for amperometric immunosensing: (A) antigen detection via a competitive immunoassay format with a redox-enzyme-labelled antigen; (B) antibody detection via indirect immunoassay format, also known as sandwich-type immunoassay. Ez represents the enzyme that catalyses the oxidation/reduction of the electroactive species⁸⁹.

Amperometric immunosensors have been proposed for the detection of cancer biomarkers such as prostate specific antigen (PSA)^{94, 95} and carcinoembryonic antigen (CEA)^{96, 97}; hormones such as human chorionic gonadotrophine (hGC)⁹⁸ and

progesterone ⁹⁹; and antibodies from infections such as those from Chagas' disease ^{100, 101} and schistosoma japonicum ¹⁰². Recent works on amperometric immunosensor has also reported on the detection of cardiovascular disease markers like human cardiac troponin 1 (cTn1) and human C-reactive protein (CRP) ¹⁰³. The article reported on the usage of ascorbic monophosphate as an enzymatic substrate of alkaline phosphatase labelling antibodies. The disposable amperometric graphite immunosensors was found suitable for detecting cTn1 in concentration ranging from 0 to 35 $\mu\text{g/L}$ with the sensitivity of 0.67 $\mu\text{A}/(\mu\text{g/L})$.

Amperometric immunosensor was also used to detect epididymis specific protein 4 antigen (HE4 Ag), a novel tumour marker for early ovarian cancer recently ¹⁰⁴. The researchers employed amine-modified graphene-supported gold nanorods (Au NRs/ NH_2 -GS) as the sensor platform to increase the electrode surface area and effective immobilisation of the primary antibodies. Core-shell Au@Pd urchin-shaped nanostructures (Au@Pd USs) was used to label the secondary antibodies and provide a larger active site for H_2O_2 catalysis. The as-constructed sandwich-type amperometric immunosensor showed excellent HE4 Ag detection performance from 1 pmol L^{-1} to 50 nmol L^{-1} with an LOD of 0.33 pmol L^{-1} .

2.2.2.4.2 Voltammetric Biosensor

Voltammetry is considered the electrochemical analysis technique with the best versatility ¹⁰⁵. In voltammetry, current is measured as a function of electrode potential to provide data on the chemical reaction for analysis. In this technique, both the current and the potential play important roles in the analysis. The peak potential represents a specific analyte species while the intensity of the peak current is directly

proportional to the concentration of the corresponding analyte. An interesting characteristic of voltammetry is its ability to detect multiple compounds with different peak potentials in a single electrochemical experiment, in other words, the simultaneous detection of multiple analytes ¹⁰⁶. As shown in the example of Figure 2.13, vanillin and caffeine was simultaneously detected using voltammetric technique ¹⁰⁷.

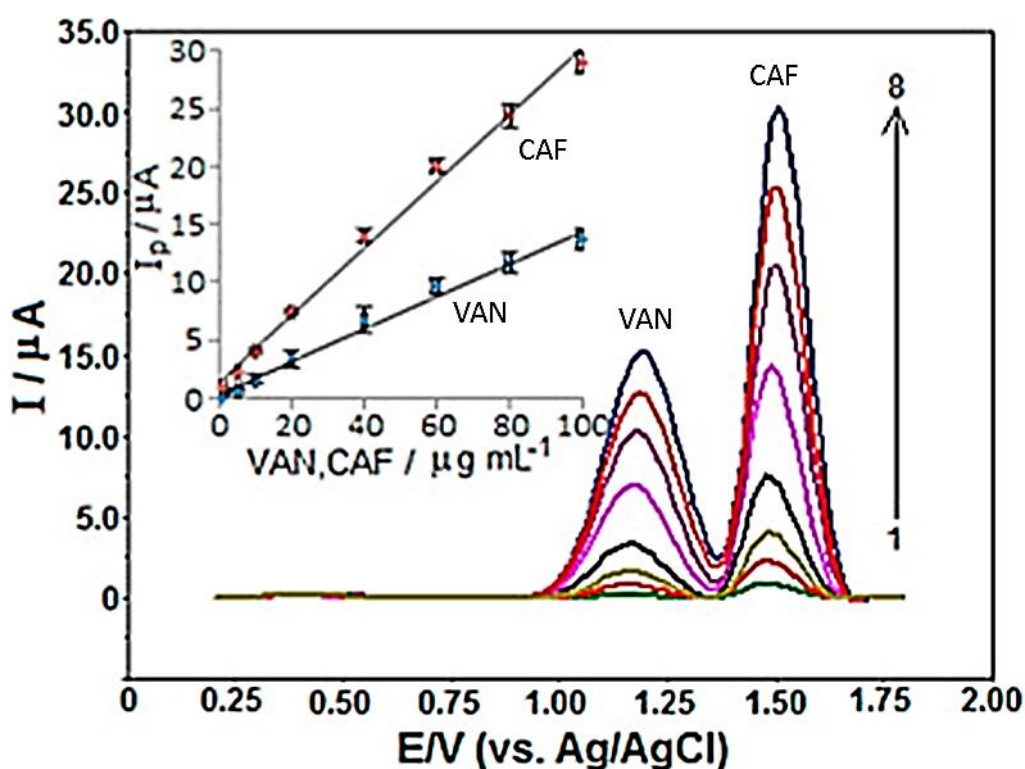


Figure 2.13. Simultaneous voltammetric detection of vanillin (VAN) and caffeine (CAF) at equal concentration of 1.0–100.0 $\mu\text{g mL}^{-1}$ (1–8). Inset shows their respective analytical curves ¹⁰⁷.

There are many different voltammetric techniques that are defined by the waveform describing how the potential is varied as a function of time. The different modes of voltammetry employed in this type of biosensor include linear sweep voltammetry, staircase voltammetry, differential pulse voltammetry, square wave voltammetry, and cyclic voltammetry (CV). Among these techniques, CV is the most widely exploited

technique in the instrumentation of electrochemical biosensor. It is also considered the most versatile electroanalytical tool for the characterisation of redox events as it conveys important information regarding the redox reaction such as its reversibility, the interfacial phenomena at the electrode surface, and the bulk properties of materials on the electrode platform¹⁰⁸. CV is performed by cycling the potential of the working electrode and measuring the resulting current. In a cycle, the forward scan begins at the initial potential (E_1) and proceeds towards the switch potential (E_2). Upon reaching E_2 , the reverse scan brings the voltage back to E_1 . The CV potential waveform input is illustrated in Figure 2.14, detailing the triangular or cyclic pattern.

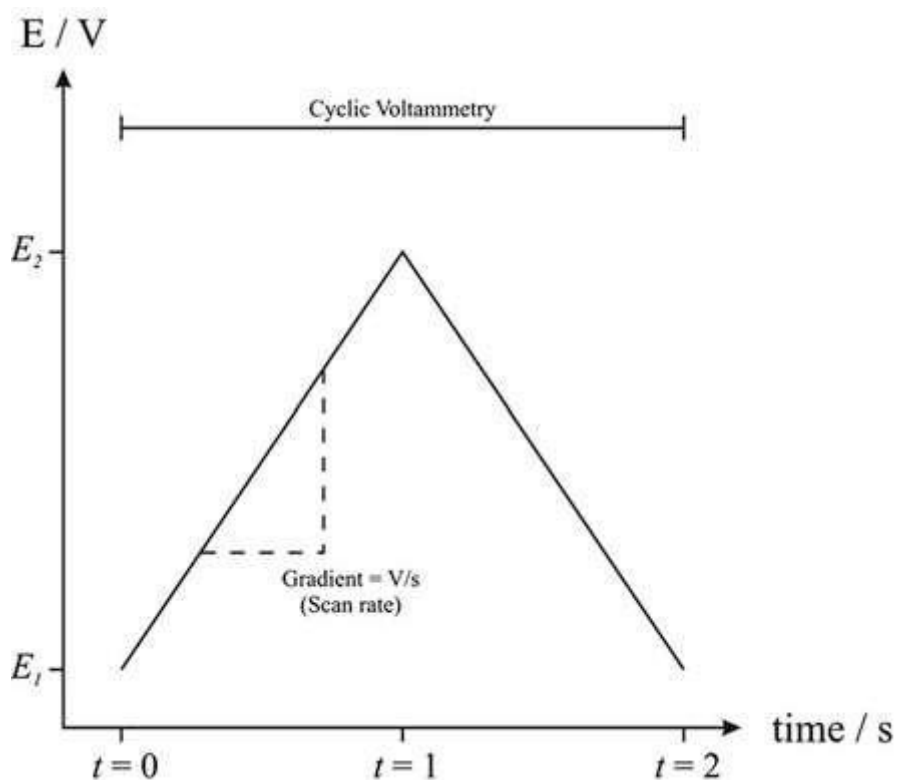


Figure 2.14. Schematic diagram illustrating the CV potential waveform. In CV measurements, the voltage is cycled between two pre-determined potentials, E_1 and E_2 , at a fixed scan rate which is represented by the gradient.¹⁰⁹

Results from CV measurements are displayed in cyclic voltammograms where the measured currents are plotted against the applied potential. There are several important parameters that can be obtained from a CV plot: anodic (E_p or E_{pa}) and cathodic (E_p' or E_{pc}) peak potentials, the corresponding anodic (i or I_{pa}) and cathodic (i' or I_{pc}) peak currents, and the interpeak distance or peak separation (ΔE or ΔE_p). Figure 2.15 shows a classic cyclic voltammogram of a reversible $[\text{Fe}(\text{CN})_6]^{4-/3-}$ redox couple with the key parameters. The two distinct current peaks (i and i') correspond to the oxidation and reduction potentials of $[\text{Fe}(\text{CN})_6]^{4-/3-}$ redox couple while E_p and E_p' are the potentials associated to the respective peak currents. The potential separation between the peaks (ΔE) provides information on the reversibility of the redox reaction. In fully electrokinetically reversible systems, ΔE is equal to $59.2/n$ at room temperature where n is the number of electrons transferred in the reaction ¹¹⁰.

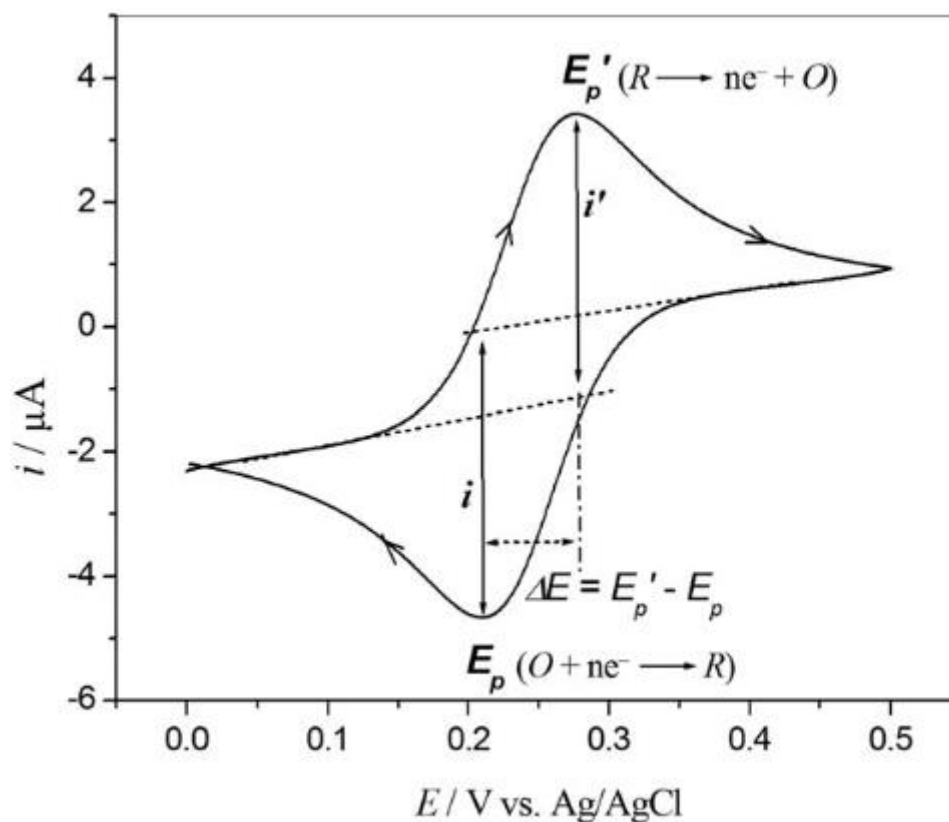


Figure 2.15. Typical cyclic voltammogram of a fully reversible redox couple ($[\text{Fe}(\text{CN})_6]^{4-/3-}$) showcasing the key parameters of peak potentials, peak currents, and peak potential separation ¹¹⁰.

Over the years, voltammetric biosensors have been used in various applications, such as the determination of acrylamide in food samples ¹¹¹, hormone detection of catecholamines ¹¹², disease detection of cystic fibrosis ¹¹³, and drug screening of paracetamol ¹¹⁴. Additionally, voltammetric immunosensor was also used for the diagnosis of celiac disease by quantifying antigliadin antibodies ¹¹⁵. Gliadin, the antigenic marker of celiac disease, was immobilised on SPCEs modified with a carbon nanotube/gold nanoparticle hybrid system. The antigen-antibody interactions are quantified with the aid of alkaline phosphatase labeled anti-human antibodies using cyclic voltammetry. Another voltammetric immunosensing approach was reported by

Singh *et al.* for the diagnosis of Type 1 and Type 2 diabetes ¹¹⁶. In this report, anti-insulin antibody was covalently anchored to the carbon nanotube-pyrenebutyric acid framework on pyrolytic graphite electrodes to capture the serum insulin. By monitoring the decrease in voltammetric current signals, the serum insulin amount can be determined down to picomolar levels with a detection limit of 15 pM. Recently, Thunkhamrak *et al.* have reported on the detection of PSA via voltammetric immunosensor ¹¹⁷. Using graphene oxide modified SPCE hybridised with silver nanoparticles, the voltammetric reduction current was recorded and correlated to the PSA concentration. After optimisation, the immunosensor was able to detect PSA in high sensitivity with an LOD of 0.27 ng mL⁻¹ and a dynamic range from 0.75 to 100.0 ng mL⁻¹.

2.2.2.4.3 Potentiometric Biosensor

Potentiometric biosensors measure the transmembrane potential or potential difference between two electrodes across an ion-selective membrane, which is produced by the biorecognition reaction, at near-zero current ^{76, 118}. The basis of potentiometric biosensors is the Nernst equation, in which the electrode potential (E) relates to the concentration of oxidised/reduced species. Using a general redox reaction equation of $aA + ne^- \rightleftharpoons bB$ as an example, the Nernst equation is as follows:

$$E = E_0 + \frac{RT}{nF} \ln\left(\frac{[C_A]^a}{[C_B]^b}\right) \quad (2.2)$$

where E_0 is the standard redox potential, R is the gas constant, T is the absolute temperature, F is the Faraday constant, n is the number of exchanged electrons in the bioreaction, and C_A and C_B are the concentration of oxidised and reduced species, respectively. As the electrode potential generated at the membrane electrode surface

in equilibrium is proportional to the logarithmic concentration of the analyte, this technique enables the detection of minute concentration changes.

The typical experimental setup for potentiometric sensors such as ion-selective electrodes (ISE) usually involves an electrochemical cell and two reference electrodes for potential measurements. An example of ISE experimental setup and its typical calibration curve are shown in Figure 2.16 ¹¹⁹.

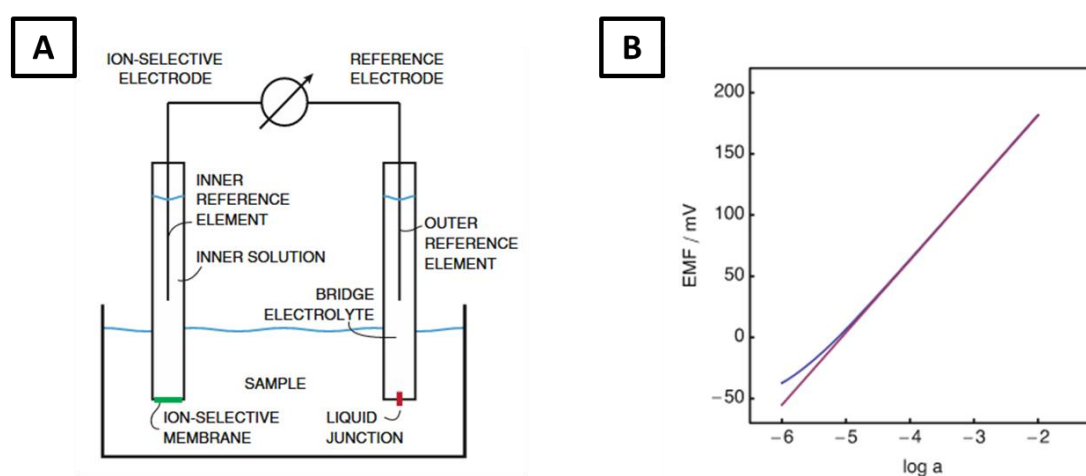


Figure 2.16. A) ISE experimental setup consisting a two-electrode electrochemical cell, B) Calibration curve of potential difference against logarithmic sample ion activity. Red trace represents the linear fashion as described by the Nernst equation while blue trace indicates the behaviour of the real electrode with deviations near the detection limit ¹¹⁹.

In ISE devices, the selective diffusion of analyte ions across the ion-selective membrane generates a potential difference which is then measured by the potentiometer ¹²⁰. Some common applications of ISE sensors include the glass pH electrodes and sensors of dissolved gases and metal ions. These potentiometric sensors can be modified into biosensors by employing biosensing elements on the electrodes, such as the potentiometric biosensor developed for the detection of vascular endothelial growth factor (VEGF) cancer biomarker ¹²¹. As VEGF induces

hyperpermeability in endothelial cells, whole human umbilical vein endothelial cells were attached to the cellulose triacetate membrane of an ISE, leading to sensitive response of the biosensor towards the presence of VEGF. An immunosensor for immunoglobulin G (IgG) detection was developed by immobilising anti-IgG on a silver electrode ¹²². The potential change before and after antigen-antibody reaction was measured, successfully demonstrating IgG detection with a linear response range of 0.2–1.2 ng/ml. Potentiometric biosensors have also found success in the detection of CEA cancer biomarkers by utilising gold-coated silicon chips with a molecularly imprinted alkane thiol surface ¹²³. Recently, a disposable paper-based ISE immunosensor was also developed for real-time detection of *Salmonella typhimurium*, a foodborne pathogenic Gram-negative bacterium ¹²⁴. Integrated with a filter paper pad acting as inner solution reservoir, the paper strip electrode was immobilised with *Salmonella* monoclonal antibody to achieve sensitive detection with an LOD of 5 cells mL⁻¹.

2.2.2.4.4 Impedimetric Biosensor

The term “impedance” is similar to resistance in which they both represent the opposition force to the electrical current in a circuit, albeit with some differences. Unlike resistance, impedance does not obey Ohm’s law, is frequency dependent and is observed in alternating current (AC) with phase shift ¹²⁵. The concept of impedance was first introduced in the 1880s by Oliver Heaviside ¹²⁶, a respected mathematician who laid the foundation for the development of electrochemical impedance spectroscopy (EIS), a technique developed based upon complex mathematical transforms to yield real values of impedance in temporal space ¹²⁷. Heaviside defined

the “operational impedance” as “the complex ratio of the voltage and current in an AC circuit”¹²⁸, denoted today as the Equation 2.3 below:

$$Z(j\omega) = \frac{V(j\omega)}{I(j\omega)} \quad (2.3)$$

Where Z is the impedance, V is the voltage, I is the current, j is the imaginary component and ω is the frequency. The impedance can also be expressed in terms of real $Z_{re}(\omega)$ and imaginary $Z_{im}(\omega)$ components as shown in Equation 2.4

$$Z(j\omega) = Z_{re}(\omega) + jZ_{im}(\omega) \quad (2.4)$$

Where $\omega=2\pi f$ and $j=\sqrt{-1}$ while ω and f (excitation frequency) have units of $\text{rad}\cdot\text{s}^{-1}$ and Hz, respectively. The complex impedance is presented as the sum of both the real, $Z_{re}(\omega)$, and imaginary, $Z_{im}(\omega)$, components that originate from the resistance and capacitance of the electrochemical system, respectively¹²⁹.

EIS is a powerful analytical tool that has long been employed to study electrochemical systems such as corrosion of metals¹³⁰, fuel cells¹³¹, batteries¹³², and electrodeposition¹³³. When conducting an EIS measurement, a small sinusoidal AC voltage (typically 2-10 mV) is applied at a set frequency and the resulting current flowing through the electrochemical cell will be recorded by a potentiostat, which is then converted into impedance values with real and imaginary components as described in Equation 2.3 with the aid of software. By repeating the process across a frequency range, the real (resistive) and imaginary (capacitive) components which are determined by the in-phase and out-of-phase current response, respectively, can be deduced¹³⁴. The impedance results are generally presented by plotting the imaginary component against the real component in a Nyquist plot, which provides visual insight

into the system dynamics. Figure 2.17 shows a typical Nyquist plot with the key impedance parameters including R_{ct} , the charge-transfer resistance which is inversely proportional to the rate of electron transfer, R_s , the solution-phase resistance, and ω , the frequency. As illustrated in the Nyquist plot, the semi-circular portion represent the impedance observed at high frequencies which is limited by the interfacial electron transfer process, while the linear portion at low frequencies corresponds the impedance controlled by the diffusion of the redox probe. Note that in the case of rapid electron transfer process, the impedance spectrum could include only the linear portion whereas very slow electron transfer would result in impedance spectrum consisting a large semi-circle region without the linear part. The R_{ct} , denoted by the diameter of the semi-circular portion, is particularly important in analytical purposes as it measures the impedance increment caused by the analyte that perturbs the sensing interface.

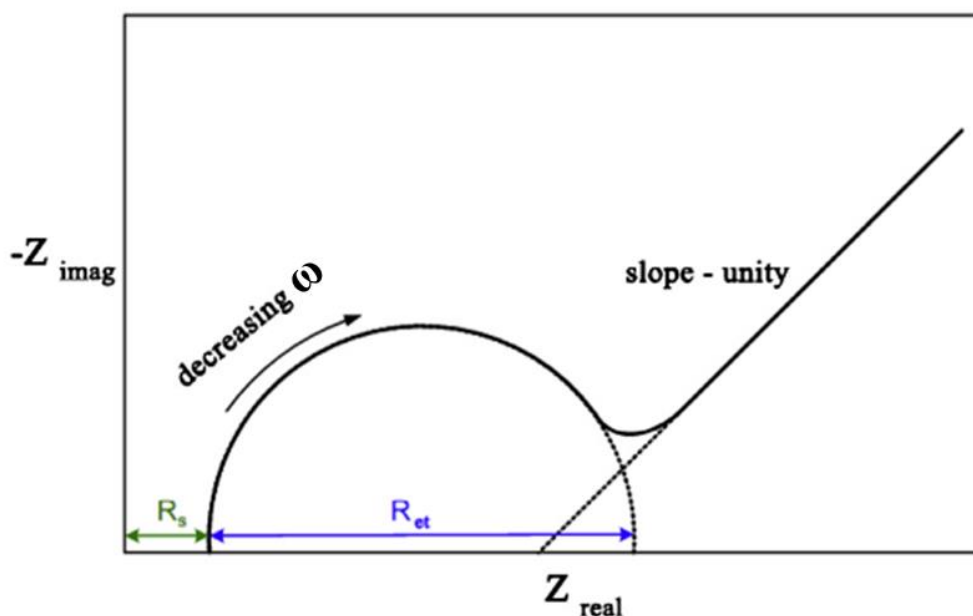


Figure 2.17. A typical Nyquist plot depicting the electron-transfer-limited semi-circular region and a diffusion-limited linear region, with key impedance parameters such as charge transfer resistance (R_{ct}), solution resistance (R_s), and frequency (ω)⁷⁶.

Impedimetric biosensors utilise the EIS technique for rapid characterisation of the structure and functional operation of biomaterial-functionalised electrodes ¹³⁵. When nanomaterials or biomaterials are immobilised on the surface of the electrodes, the capacitance and interfacial electron transfer resistance of the electrodes are modified, thus changing the impedance of the electrodes. As the bio-recognition event occurs, the formation of bioreceptor-analyte complex on the electrode surface results in additional insulative layer on the electrode surface which impedes the current flow. Therefore, the bio-recognition events at the electrode interface can be detected by using this method. In addition, the EIS technique allows verification for the stepwise assembly of the biosensor via layer-by-layer electrochemical characterisation. A simple graphical representation of the layer-by-layer characterisation of impedimetric biosensors using Nyquist plots is shown in Figure 2.18 ¹⁴.

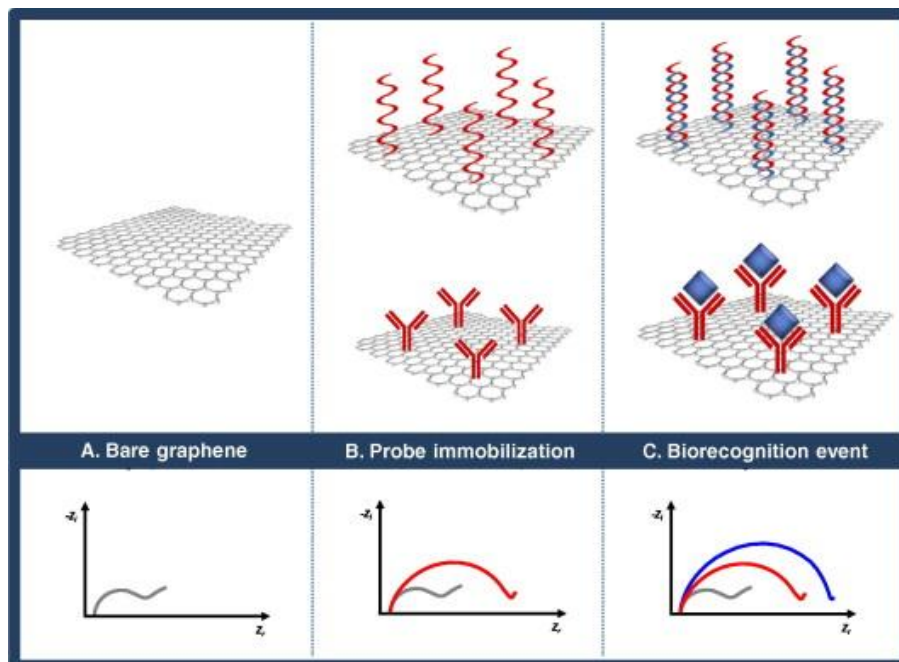


Figure 2.18. Graphical representation of layer-by-layer characterisation of a graphene-based biosensor via EIS ¹⁴.

EIS is invaluable in probing bioaffinity interactions at the electrode surfaces and providing label-free detection of analytes, leading to the diverse applications of impedimetric biosensors¹²⁵. Impedimetric biosensors have been developed for cancer detection, such as the detection of human mammary tumour associated glycoprotein (MTGP)¹³⁶. The monoclonal antibody (GP1D8) of MTGP was first immobilised on gold electrode as the biorecognition probe. Upon specific binding of the MTGP antigen on the electrode, the EIS measurement showed Nyquist plot with increased R_{ct} due to the formation of the antigen-antibody immunocomplex on the electrode surface, causing retardation to the electron transfer process.

Sharma *et al.* have reported on the fabrication of an impedimetric immunosensor for the detection of human epidermal growth factor receptor 2 (HER2), a vital biomarker associated with breast cancer¹³⁷. Specific single-chain variable fragment (scFv) antibody fragments of HER2 were immobilised on gold nanoparticle-modified electrodes for improved antigen binding efficiency. The scFv-based impedimetric immunosensor presented a low detection limit of 0.01 ng mL^{-1} with a wide dynamic range of $0.01\text{--}100 \text{ ng mL}^{-1}$.

Impedimetric mode of sensing has also found success in bacterial detection suitable for food industry applications¹³⁸. *Escherichia coli* O157:H7 is a food and water borne pathogenic strain of *E. coli* that is highly infectious and potentially fatal. The impedimetric biosensor was constructed by immobilising its antibody on a conducting polyaniline (PANI) substrate deposited on gold electrodes with the aid of glutaraldehyde cross-linker, successfully detecting *E. coli* O157:H7 with lower and upper detection limit of 10^2 CFU mL^{-1} and 10^7 CFU mL^{-1} , respectively.

Impedimetric biosensor was also developed as glucose biosensor by immobilising glucose oxidase enzyme via chitosan onto nanostructured copper oxide sputtered thin film on conductive fluorinated-tin-oxide layer ¹³⁹. The biosensor displayed high performance glucose detection with a sensitivity of 0.261 k Ω per mM within 0.2–15 mM and an LOD of 27 μ M.

An impedimetric DNA-based genosensor developed for the detection Zika virus (ZIKV) was recently reported ¹⁴⁰. Oxidised glassy carbon electrode was modified with silsesquioxane-functionalised gold nanoparticles to construct the electrode platform. ZIKV ssDNA probe was then immobilised onto the electrode platform to capture ZIKV target. The change in charge transfer resistance (ΔR_{ct}) was used to quantify the recognition of ZIKV target, yielding an LOD of 0.82 pmol L⁻¹ within a linear range of 1.0 x10⁻¹² to 1.0 x10⁻⁶ mol L⁻¹.

2.3 Graphene Synthesis and Biosensor Applications

2.3.1 Graphene

The rise of nanotechnology has paved a path for innovative applications of nanomaterials in electrochemical sensors and biosensors ⁶⁰. In 2004, a historic moment happened when the 2D allotrope of carbon: graphene, was successfully isolated for the first time ever ¹⁸. The breakthrough discovery earned the scientists, Geim and Novoselov, the 2010 Nobel Prize in Physics as they had unlocked a million possibilities in various research fields. Prior to its discovery, graphene, a two-dimensional monolayer of carbon atoms arranged in a honeycomb lattice structure, is only known as the theoretical basic building block for other carbon allotropes. A good example of these popular carbon allotropes would be graphite, which is widely used since the invention of pencil centuries ago. Graphite is composed by planar sheets of graphene stacking together, held by weak Van der Waals forces, giving graphite its 3D structure. Thus, if these bonds can be broken, it is possible to obtain graphene from a high purity graphite sheet. Other than graphite, graphene is also known to be the building blocks for carbon nanotubes (CNT) and buckyballs or fullerenes (Figure 2.19) ^{141, 142}. Despite the fact that all these carbon allotropes are made of the same basal unit, each of them demonstrates extremely different mechanical, chemical, and electronic properties due to the different crystal structures and orientation of the carbon bonds.

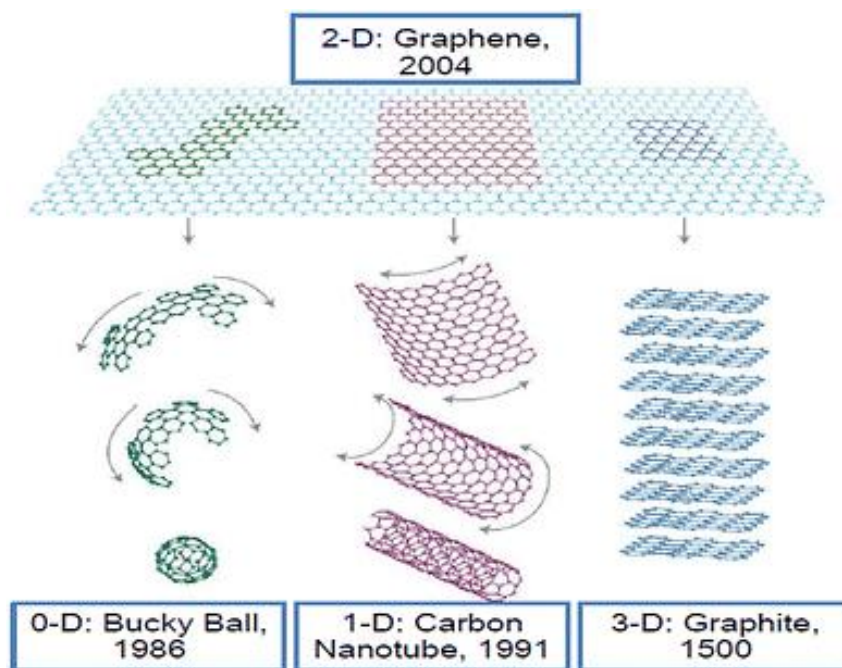


Figure 2.19. Schematic diagram illustrating graphene as the 2D building block for the 0D Buckyball, 1D CNT, and 3D graphite ¹⁴².

Being a 2D planar sheet of sp^2 hybridised carbon atoms, graphene has garnered much attention and scientific interests due to its versatile and remarkable properties. The in-plane 0.142 nm carbon-carbon sigma bond of the sp^2 hybridised carbon bond is one of the strongest bonds found in materials, contributing to its outstanding mechanical strength up to 200 times stronger than steel ¹⁴³. On the other hand, the out-of-plane π bond imparts a delocalised electron network, which results in improved electron conduction from the weak interaction among graphene layers or between graphene and the attached substrates ¹⁴². This “wonder material” ¹⁴⁴ also possesses an exceptionally large theoretical specific surface area ($\sim 2630 \text{ m}^2\text{g}^{-1}$), high intrinsic mobility ($\sim 200,000 \text{ cm}^2 \text{ v}^{-1}\text{s}^{-1}$) ^{145, 146}, Young’s modulus ($\sim 1.0 \text{ TPa}$) ¹⁴⁷, thermal conductivity ($\sim 5000 \text{ Wm}^{-1}\text{K}^{-1}$)¹⁴⁸, and optical transmittance ($\sim 97.7 \%$) ¹⁴⁹. Most importantly, graphene has excellent electrical conductivity while being able to

withstand current density up to 108 A cm^{-2} , making it a suitable choice for the construction high performance electrodes ¹⁵⁰. Due to these amazing attributes, graphene has been employed in a wide range of diverse applications including photonics, electronics, energy storage, adsorbents, biosensors, and other biomedical applications ¹⁵¹⁻¹⁵³.

2.3.2 Graphene Synthesis

The fundamental requirement of producing a good graphene-based biosensor is to have a trustworthy method to fabricate top-notch quality graphene that's reproducible and preferably in larger scale. Since the discovery of graphene, the means to obtain graphene have evolved through the years.

Graphene was first obtained by manual exfoliation of high-quality graphite (HOPG)¹⁸. Using scotch tape, the scientists peeled the sheets off the HOPG repeatedly in this reported approach, yielding excellent quality pristine single layer graphene. This mechanically exfoliated graphene, however, is not viable in terms of mass production, as the laborious peeling is tedious, and could be extremely time consuming. In general, there are two approaches to synthesise graphene; the bottom-up approach and the top-down approach (Figure 2.20), which will be discussed in the following sections.

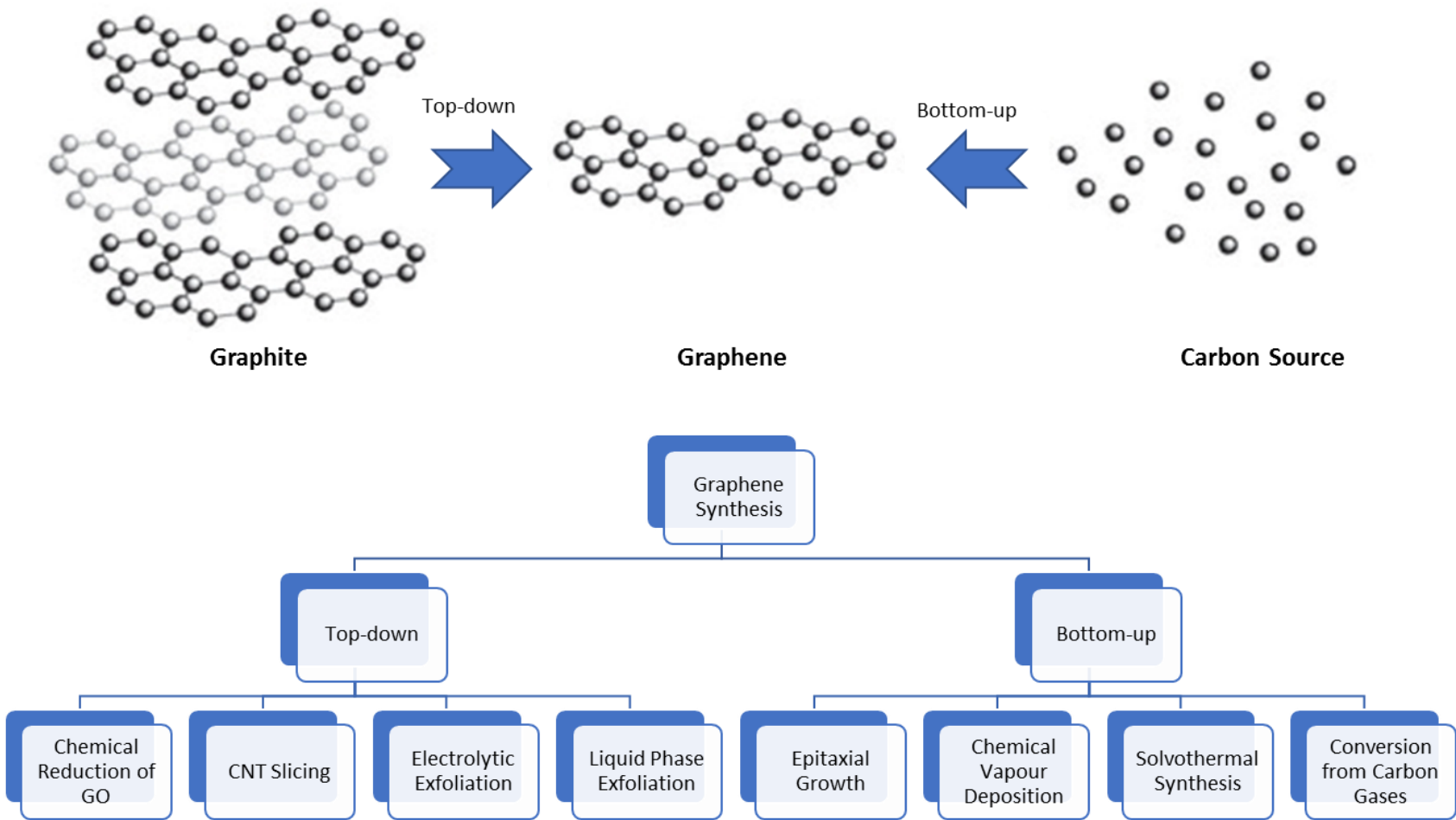


Figure 2.20. Scheme illustrating the synthesis methods of graphene ¹⁴⁹.

2.3.2.1 Bottom-up Approach

Bottom-up approach involves techniques where graphene films are “grown” from substrates, hence the name “bottom-up”. The synthesis techniques in this category are a) thermal decomposition of SiC; b) chemical vapour deposition (CVD), c) solvothermal synthesis, and d) conversion from carbon gases.

2.3.2.1.1 Thermal decomposition of SiC

In 1975, scientists from Philips Research Laboratories found out that ultra-thin graphitic layers can be grown on the surface of silicon carbides (SiC) when heated at high temperatures (1200–1600°C) under ultra-high vacuum (UHV) conditions ¹⁵⁴. As shown in Figure 2.21, the substrate, SiC, undergoes a thermal decomposition or sublimation process (melting point = 1100°C) where the Si atoms are desorbed, leaving excessive C atoms to aggregate and form graphene layers on the substrate surface with increasing temperature. However, the desorption of Si is not self-limiting, leading to the formation of multi-layered epitaxial graphene sheets (~5-100 layers) that lacks homogeneity across the substrate. Having uneven thicknesses across the graphene film is something undesirable as it would adversely affect the electronic properties of the synthesised film ^{155, 156}.

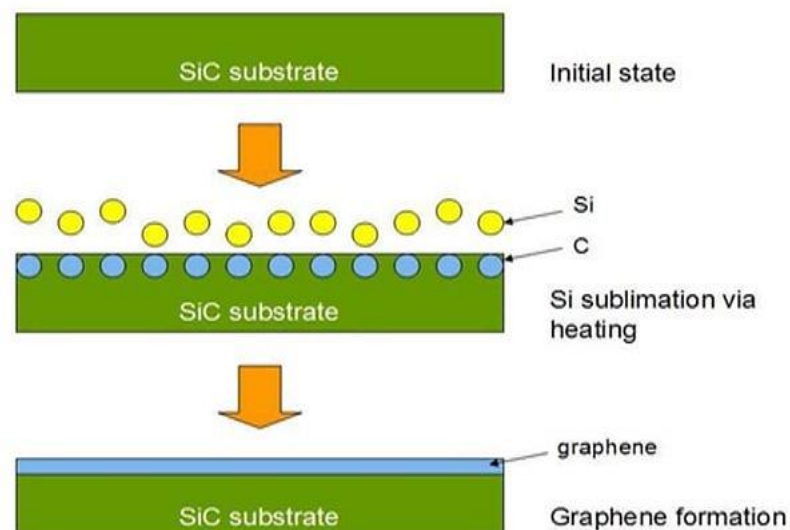


Figure 2.21. Schematic diagram illustrating the epitaxial growth of graphene ¹⁵⁷.

To overcome this issue, experiments were carried out where the annealing process was conducted in an Argon atmosphere instead of UHV ¹⁵⁸. The resulting epitaxial graphene was found to contain larger regions of homogeneous films with even thickness distribution. This improvement was largely attributed to the surface restructuring of the substrate prior to the formation of graphene. In UHV, Si atoms of the SiC substrate began decomposing at temperatures as low as 1150°C. As the Si atoms sublime, graphene layers start to form, growing into more and more layers as the temperature was raised to the optimum growth temperature of graphene, ultimately leading to the inhomogeneous films of multi-layered graphene. In contrast, no Si desorption was found at temperatures up to 1500°C when under Argon atmosphere of 900 mbar. Therefore, homogeneous graphene films could be grown in an Argon atmosphere while limiting Si desorption at the same time, albeit at a much higher operating temperature ¹⁵⁸.

Looking at the currently available synthesis methods for epitaxial growth of graphene, this process would be difficult and expensive to commercialise as it is extremely energy intensive and limited by the SiC substrate size¹⁵⁹. In addition, it is possible that the epitaxial growth produces different polar faces (Si-face or C-face) which might negatively affect the graphene product quality^{160, 161}.

2.3.2.1.2 Chemical Vapour Deposition (CVD)

Chemical vapour deposition (CVD) is a common chemical process employed to produce solid materials of high quality and performance, especially in the semiconductor industry. Implementing this concept in graphene synthesis enables the large-scale pattern growth of graphene sheets with substantially high area with low defect density on the surface of suitable substrates.

To initiate the CVD process, a reactive substrate is first exposed to hydrocarbon gases such as methane (CH₄), acetylene (C₂H₂), ethylene (C₂H₄), and hexane (C₆H₁₄) to allow the absorption of carbon into the metal substrate (i.e.: Cu and Ni films) at very high temperatures (650–1000°C)^{162, 163}. The carbon precursors dissociate into free carbon and hydrogen atoms as they are in contact with the hot surface of the metallic substrates. The carbon atoms then diffuse across the surface and the bulk/body of the metallic catalyst, forming sheets of graphene on the catalyst surface as they reach the carbon solubility limit¹⁶⁴.

In decades of research regarding CVD of hydrocarbons, the thickness of the products was known to be difficult to control due to the large amounts of carbon absorbed onto the surface, often forming graphite crystals rather than graphene films¹⁶⁵. A solution to this problem was proposed by Kim *et al.* where a thin layer (300 nm) of nickel (Ni)

was first deposited on the surface of a Si/SiO₂ wafer which was then heated up to 1000 °C in a quartz tube in an argon atmosphere. The sample was then heated and purged with the reaction mixture (CH₄: H₂: Ar = 50: 65: 200) before it was rapidly cooled down at a cooling rate of 10 °C/s to ~ 25 °C (Figure 2.22B). With the improved method, graphene films with few layers at maximum were successfully produced. In comparison, graphene produced on thick Ni foils (1 mm) yielded graphene with the thickness of more than 10 layers. Therefore, it was concluded that the thickness of the graphene films produced was determined by the thickness of the substrate¹⁶⁵.

Apart from substrate thickness, the cooling rate also greatly affects the graphene production. Yu *et al.* found that different cooling rates led to different segregation behaviours, which has a significant effect on the thickness and quality of the produced graphene¹⁶⁶. A moderate cooling rate is important to suppress the formation of excess graphene layers by limiting the migration of C atoms from the bulk material into the segregated layer. If the cooling rate is too fast, the mobility of C atoms would be obliterated before they have the chance to diffuse into the segregated layer; if the rate is too slow, too many atoms migrate into the bulk material, leaving very little left to segregate as films on the substrate surface. The effects of different cooling rates on the segregation behaviours of graphene are depicted in Figure 2.22B.

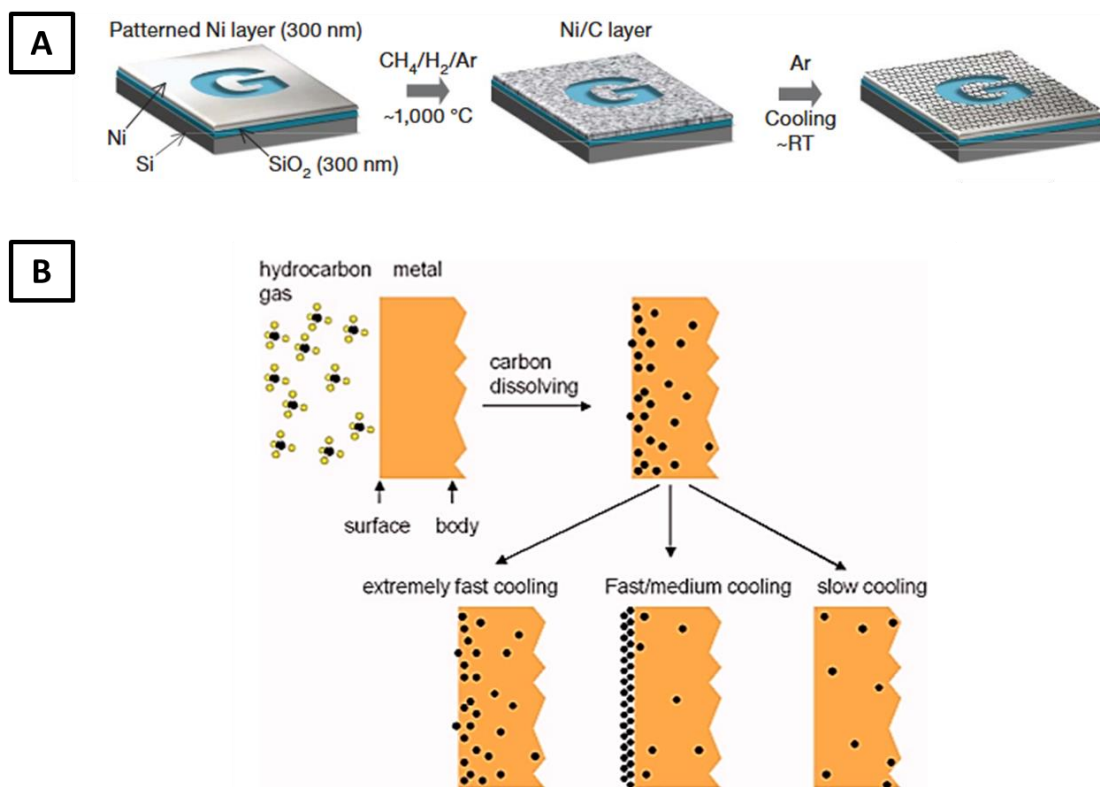


Figure 2.22. A) Schematic diagram illustrating the CVD process¹⁶⁵, and B) Illustration depicting graphene segregation on substrate surface and the effects of cooling rate¹⁶⁶.

Unlike epitaxial graphene growth, CVD graphene is grown on a conductive substrate which requires an extra step to transfer the produced films onto other insulating substrates¹⁵⁸. Yu *et al.* suggested using nitric acid (HNO₃) to dissolve the nickel layer but its detrimental effect on the graphene prompted Kim *et al.* to propose aqueous iron (III) chloride (FeCl₃) to remove the nickel layer. Another alternative dry-transfer route was also developed by Kim *et al.* whereby another substrate, PDMS was deposited onto the graphene and the nickel was etched away via FeCl₃.

Despite the pristine nature of the synthesised product, the CVD route of graphene synthesis is still considered immature for commercialisation due to the high production costs and low yield¹⁴⁹.

2.3.2.1.3 Solvothermal Synthesis

A novel method reported in the past decade was a bottom-up chemical synthesis of gram-scale carbon nanosheets from ethanol and sodium¹⁶⁷. In a typical solvothermal synthesis, sodium and ethanol of 1:1 molar ratio is heated in a sealed Teflon-lined reactor vessel at 220 °C for 72 hours to produce a graphene-precursor. While oxidation of sodium and reduction of ethanol normally yields crystalline sodium ethoxide, the metal alkoxide was not the dominant product in the precursor. Due to the conditions of the closed, heated reactor and the auto-generated pressure, the free alcohol is encapsulated into sodium ethoxide in a clathrate-like structure. The solid solvothermal product comprises of sodium ethoxide-ethanol clathrate along with some metal hydroxide that might have been formed in the presence of water. The intermediate material would then undergo low-temperature flash pyrolysis and the final product washed with deionized water. As ethanol is vaporised in the pyrolysis process, the clathrate-like structure bursts, resulting in powdered sample of graphene. The suspended solid is then vacuum filtered and dried at 100 °C for 24 hours to yield 100 mg for each ml of ethanol used. Surface area measurements indicated the Langmuir surface area of the graphene structure to be 612 m² g⁻¹ and 1692 m² g⁻¹ in solid state and in dispersed ethanol solutions, respectively. The disparity in surface area is largely attributed to the dissipation of free sheets in dilute solutions. Following Choucair *et al.*'s work, researches regarding the optimisations on this method have been reported. A simplified schematic diagram is presented in Figure 2.23 for better illustration¹⁶⁸.

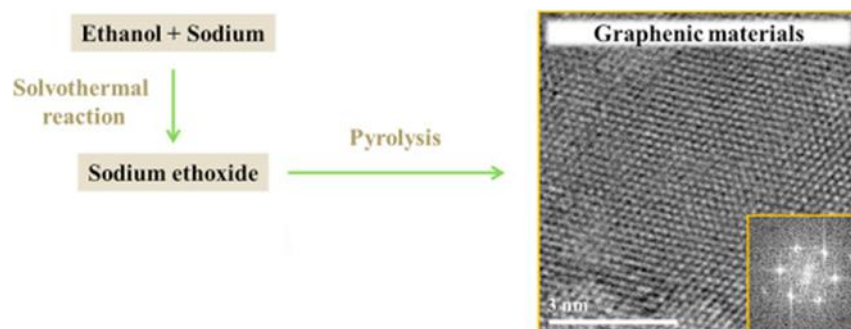


Figure 2.23. Scheme illustrating graphene synthesis from ethanol and sodium ¹⁶⁸.

Another method of bottom-up one-step solvothermal synthesis of carbon nanosheets from inexpensive chemical reagents by dehydrating glycerol with sulfuric acid in the presence of melamine, was recently reported ¹⁶⁹. Firstly, 0.5 g of melamine and 10 mL of glycerol were mixed, and the mixture was stirred until melamine was completely dissolved in glycerol. Sulfuric acid (98%, 10 mL) was then added into the mixture under vigorous stirring. Next, the mixture was heated in an autoclave reactor at 180 °C for 4 hours for carbonisation of the carbon precursor. The black residue obtained from the reactor was then washed and calcinated at 800 °C for 2 hours at 10 °C min⁻¹ under argon gas protection for further carbonisation. The final product was found to have thickness of 1 to 5 nm and possess excellent adsorption properties comparable to most carbon-based materials, with an adsorption capacity of 585 mg g⁻¹ for methylene blue.

In general, bottom-up solvothermal approaches produce graphene-like nanomaterials from inexpensive carbon precursors such as ethanol and glycerol. However, the information on these novel methods are limited, demanding more work to confirm their feasibility in commercialised applications.

2.3.2.1.4 Conversion from Carbon Gases

Graphene is also reported to be obtainable through conversion of carbon gases. A recent report described the reduction of carbon monoxide (CO) in a reaction with aluminium sulphide (Al₂S₃). Al₂S₃ powder was calcined at high temperatures (1200 °C – 1300 °C) under a mixed gas flow of argon and 10 vol% CO. The resulted products from the reaction were α-Al₂O₃ and graphene sheets ¹⁷⁰.

Burning magnesium in carbon dioxide (CO₂) environment was also reported to produce graphene. Dubbed “dry ice method” (Figure 2.24), 3 g of Mg ribbon was ignited in a dry ice bowl, covered by another slab of dry ice (solid CO₂). Once the combustion of Mg in CO₂ completed, the black residue produced was collected and stirred in 100 ml of 1 M HCl at room temperature overnight. As both excess Mg and the MgO formed react with HCl to form water-soluble MgCl₂, they can be removed easily by washing with deionized water to obtain the pure carbon material as the final product. After drying overnight under vacuum at 100 °C, the yield of graphene was found to be 680 mg (92%) ¹⁷¹.

These methods might be worth exploring as they have provided an innovative route to produce graphene from raw materials that are more commonly known as greenhouse gases.

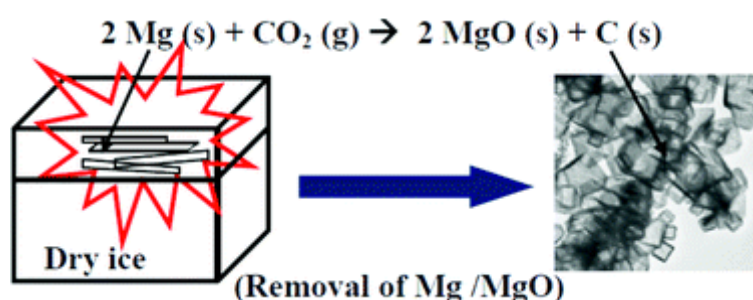


Figure 2.24. Schematic diagram illustrating "dry ice method" ⁷³.

2.3.2.2 Top-down Approach

Despite the breakthroughs in bottom-up approaches, the applications of the films produced are still limited and the process involved are often less feasible in terms of economic value and scalability. In order to improve the feasibility of graphene production, researchers have developed several methods, mainly chemical, to process graphene sheets. Top-down approaches generally have higher yields yet cost only a fraction of the previously discussed bottom-up approaches.

2.3.2.2.1 Chemical Reduction of Graphene Oxide (GO)

The four standard graphene synthesis via chemical reduction methods are those pioneered by Brodie, Staudenmeier, Hofmann, and the widely used Hummer's method (Figure 2.24). Although Staudenmeier's elaborated method produces the most oxidized graphite, Staudenmeier, Brodie and the Hofmann method results in ClO_2 gas which decomposes in air and causes explosions. Because of this, Hummer's method becomes the most popular technique to date, despite the fact that the exposure to permanganate contamination in this method leads to subsequent laborious washing of the samples with hydrogen peroxide^{172, 173}.

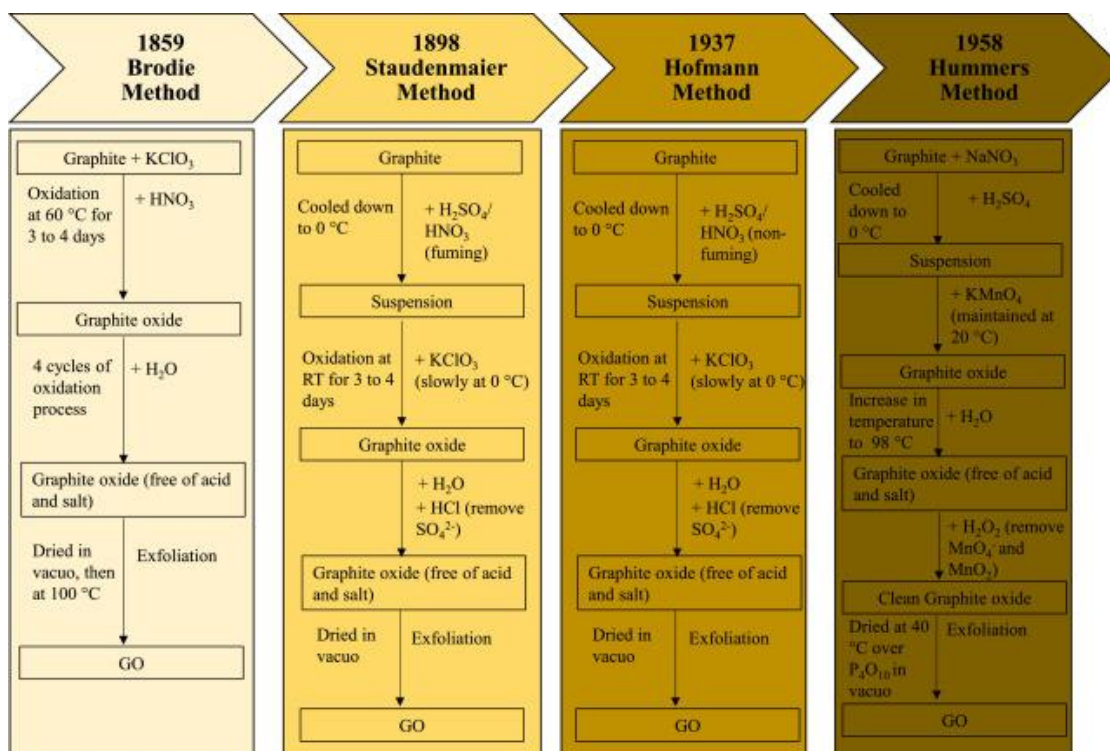


Figure 2.25. Evolution of graphite oxidation schemes ¹⁴⁹.

A typical Hummers method procedure is as follows: 3 grams of graphite added into 400ml of sulphuric acid, 18 grams of potassium permanganate was slowly added and left to oxidize for 3 days while stirred. The resulting solution will then be poured onto ice along with 27ml of 30% hydrogen peroxide to be cooled. It is then centrifuged and washed with hydrogen chloride and water forming a light brown solution. The graphite oxide sheets obtained from this method can then be reduced into graphene with the help of reducing agents such as hydrazine or sodium borohydrate.

In Hummer's method, the harsh chemical oxidation process creates oxygen-containing functional groups at the graphene surface. These functional groups such as hydroxyl, epoxide, carbonyl, and carboxyl provide polar surface properties to the (graphene

oxide) sheets, making GO highly hydrophilic. Due to this trait, the exfoliation of GO into GO sheets can be done easily in solvents.

One of the most common and most suitable reducing agents used for GO reduction would be hydrazine hydrate. In a typical synthesis, ~100 mg of GO is first added into a round bottomed flask containing 100mL of water. The mixture is sonicated until a homogeneous dispersion is obtained before 1mL of hydrazine is added into the solution. The solution is then heated at 100 °C in an oil bath for 24 hours. As the oxygenated groups in GO are reduced, GO loses its hydrophilicity and precipitates out of the solution. When this occurs, complete reduction is assumed to be achieved ¹⁷⁴.

However, reducing agents like hydrazine is known to be highly corrosive and flammable. GO subjected to these harsh chemicals would result in high level of defects in the graphene produced due to the extreme conditions during reduction, subsequently causing poor electronic properties which would not be ideal for use in electrochemical applications as the defects would hamper the performance of supercapacitors and reduce the effectiveness of chemical sensors.

2.3.2.2.2 CNT Slicing

As carbon nanotubes (CNT) are essentially graphene folded in tubes, they can be used as a precursor for graphene as well. By principle, cutting open CNTs could yield two-dimensional graphene sheets of good quality¹⁷⁵. Thus, researchers all over the globe have been developing innovative methods to perform the unzipping of CNT, such as the plasma etching of nanotubes¹⁷⁶. Borrowing the technique from the semiconductor industry, the CNTs were partly embedded on a polymer film and ionized argon gas was used to scrape away a strip of each tube. The graphene nanoribbons obtained via this method was found to be only 10-20 nanometers wide. Another group of researchers opted to tackle the problem by placing the CNTs in a solution where the combination of potassium permanganate and sulphuric acid tears the tubes open along a single axis¹⁷⁷. Although easier to make in large amounts, the ribbons produced are wider (100–500 nm) and not semiconducting. The formation of the graphene nanoribbons from CNT unzipping are shown in Figure 2.26, along with its proposed chemical mechanism.

A two-step mechanical exfoliation in organic solvent was also used to unzip the CNTs¹⁷⁸. The CNTs were first calcined and then dispersed in 1,2-dichloroethane organic solution of poly(m-phenylenevinylene-co-2,5-dioctoxy-p-phenylenevinylene) by sonication. Another method reported was the catalytic unzipping of CNTs. The microwave induced opening of CNTs was carried out in the presence of palladium nanoparticles and water. The palladium nanocatalysts function as a pair of scissors to 'cut' the CNTs lengthways¹⁷⁹. Graphene layers can also be synthesised from CNTs by friction¹⁸⁰. The CNTs were abraded between ground-glass surface while applying a

constant load of 0.06 N/cm^2 onto the materials. The abrasive force would then slice them into graphene sheets.

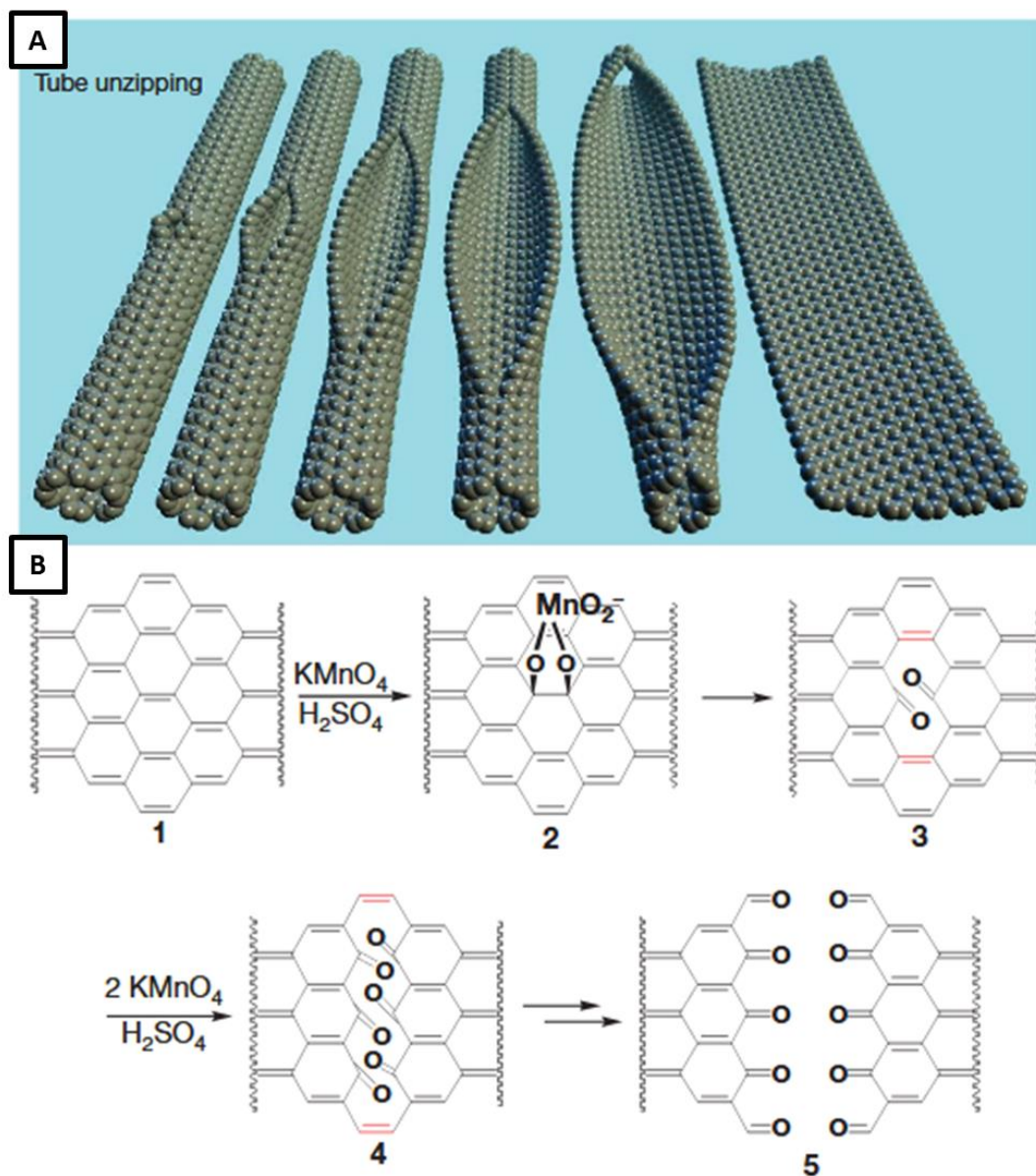


Figure 2.26. Illustration depicting A) gradual unzipping of CNT to form graphene nanoribbons, and B) proposed chemical mechanism for nanotube unzipping¹⁷⁷.

2.3.2.2.3 Electrolytic Exfoliation

Graphene synthesis is also achievable via electrochemical means. A one-pot solution was demonstrated by Lu *et al.* which involves the electrolytic exfoliation of graphite in ionic liquids. Different forms of nanocarbon, including graphene, were successfully synthesised using this method. In this setup, graphite rod and platinum wires acted as the anode and the cathode respectively. The electrolyte employed was 1-butyl-3-methylimidazolium tetrafluoroborate or 1-methyl-3-butylimidazolium chloride in water and the static potentials applied ranged from 1.5 V to 5 V. The products would then be washed with water and ethanol, and isolated by filtration and ultracentrifugation, yielding the final product of nanocarbons ¹⁸¹.

Another electrolytic method reported the usage of 0.1 M H₂SO₄ solution as the electrolyte. Graphite flakes served as the working electrode while platinum wires work as the counter-electrode in the experiment. By applying a positive charge of +10 V to the electrode, the graphite flakes dissociated into the solution. To complete the exfoliation process, the bias voltage was maintained for two minutes. The exfoliated product was then isolated by vacuum filtration and rinsed with water to remove acid residues. In the last step, exfoliated graphene sheets were obtained by dispersing the powder in N,N'-dimethylformamide (DMF). The visual representation of the electrolytic exfoliation process is shown in Figure 2.27 ¹⁸².

Recently, Hoffman *et al.* investigated on the electrochemical exfoliation process in graphene synthesis. They fabricated large scale electrodes by combining graphite flakes with polyvinylidene fluoride (PVDF), a binder, and solvent, 1-methyl-2-pyrrolidone (NMP). The mixture was applied onto tungsten foil which acted as a

conductive carrier. As oxidation occurred on the anodic end, graphene layers appeared in the form of black precipitates. The end-product could have varying size and thickness dependent upon different voltages, duration and electrolytes ¹⁸³.

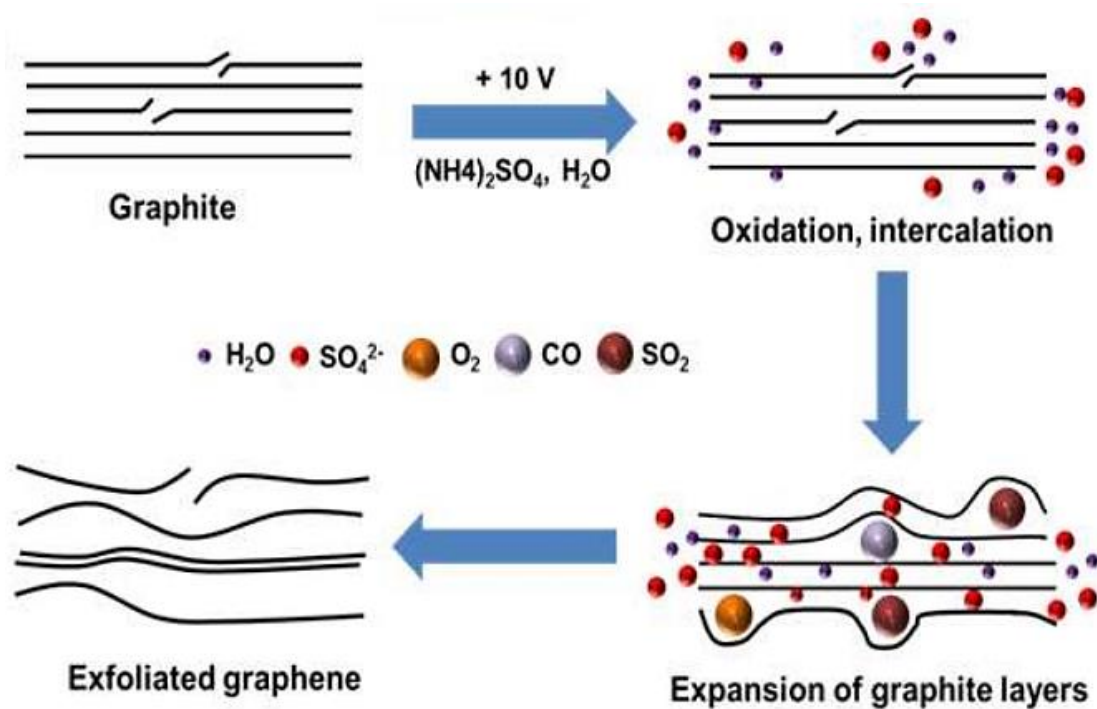


Figure 2.27. Schematic diagram illustrating the proposed mechanism of electrochemical exfoliation of graphite using 0.1 M H₂SO₄ as the electrolyte ¹⁸².

2.3.2.2.4 Sonochemical Exfoliation

In the course of searching for simpler and reliable means to isolate defect-free graphene, liquid-phase mechanical exfoliation was developed. Deemed as an epitome of top-down approach, the method requires the graphite or graphene precursors to be bombarded with ultrasonic energy which scatters them into un-oxidized graphite or ultrathin graphene flakes of high quality. The graphene precursor must be ultrasonicated in specific solvents so that the surface energy of both the solvent and graphene matches to enable the exfoliation process to occur where the balance between graphene and solvent surface energies was estimated using the Hildebrand-Scratchard expression^{184, 185}.

Hernandez *et al.* attempted to exfoliate graphite in NMP with the aid of mild bath sonication. Dispersed graphene in the form of dark homogeneous suspension was successfully obtained after removing the aggregates via centrifugation. The success was then repeated in other solvents such as γ -butyrolactone (GBL), N,N-Dimethylacetamide (DMA) and 1,3-dimethyl-2-imidazolidinone (DMEU)¹⁸⁶. However, there are some major drawbacks with this method. Other than being expensive, toxic and possessing high boiling points, the solvents leave residual amount that adsorbs onto the graphene surface even after the exfoliation process which requires an extra laborious step of rinsing with acetone or ethanol, causing losses in the final yield¹⁸⁷. Taking a step further, another group of scientists researched on the exfoliation of graphite in low boiling point solvents such as acetone, chloroform and isopropanol. Whilst homogeneous suspensions of few layered graphene are successfully achieved, the problem lies at the properties of the solvent itself limiting the solvent choices and the lengthy processing time of 48 hours in the actual synthesis¹⁸⁸. The extended

duration of sonication might be a concern as excessive sonication destroys the graphene structure^{189, 190}.

To provide a better solution, the researchers also explored the possibilities of utilizing surfactants instead of solvents in graphite exfoliation. In their research, sodium dodecylbenzene sulphonate and sodium cholate were found to be good alternatives with less hazardous properties^{185, 191}. Unfortunately, removing the surfactants from the graphene still proves to be a hindrance.

A breakthrough occurred when an interesting method to exfoliate inorganic graphene analogues (IGAs) was reported by Zhou *et al.* where the liquid phase involved is simply a mixture of ethanol and water. The dispersion of IGAs in the ethanol-water system was predicted using the theory of Hansen Solubility Parameters (HSP). The development of the method is very important as it opened up countless options by demonstrating the combination of two originally unsuitable solvents into a good solvent. Due to the generic nature of HSP and the versatility of the solvent choices, researchers can now design their own ideal solvent mixture based on their advantageous properties for each specific application in nanomaterial dispersions¹⁹².

By exploiting the HSP theory, a solution was proposed by Chia *et al.*, using a combination of ethanol and water to find the lowest HSP distance, R_a which when lowered, increases the ability to allow materials to be dissolved more uniformly into solution¹⁹³. HSP is as follows,

$$(R_a)^2 = 4(\delta_{d2} - \delta_{d1})^2 + (\delta_{p2} - \delta_{p1})^2 + (\delta_{h2} - \delta_{h1})^2 \quad (2.5)$$

Where δ_d , δ_p , δ_h are the energy from dispersion forces between molecule, intermolecular force, and hydrogen bonds between molecule respectively.

The lowest HSP distance R_a for graphite was found to be at 40% ethanol with 60% water in solution, and graphite can be easily dispersed and exfoliated through ultrasonication. The power of sonication generates cavitation bubbles, producing normal and shear forces on graphite to achieve exfoliation. The final yield shows good crystallinity and over 70% efficiency in converting graphite into single to few sheet graphene. The graphene synthesis process is represented in Figure 2.28¹⁹³.

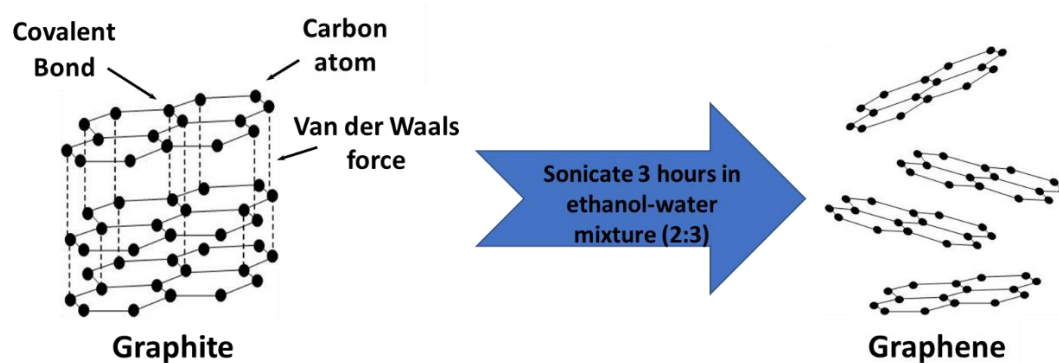


Figure 2.28. Schematic representation of the sonochemical liquid phase exfoliation process for graphene synthesis.

Due to selection of the solvent mixture, the advantages of this method are obvious. The production cost is inexpensive, the toxicity is low, and the low boiling points indicate easy removal of the solvents. This method is by far the simplest way to produce pristine quality graphene, as the starting material is only pure graphite without any oxidation or reduction occurring, is the safest and eco-friendly as no hazardous material was used, and biocompatible due as the whole process is additive free. Last but not least, it is also scalable for mass production if needed.

2.3.3 Graphene Biosensors

Today, graphene has provided a new angle to electrochemical biosensor research for its immense potential in electrochemical biosensing applications thanks to its unique physiochemical properties (high surface area, high thermal conductivity, excellent mechanical flexibility, fast electron transportation, and ease of functionalisation and mass production) ^{16, 19, 52, 194}.

The usage of graphene on electrochemical sensing platforms has been researched extensively ²³. Graphene's high specific area and ease of functionalisation enables the accommodation of highly active probes and targets of interest, encouraging various innovative bio-interface designs for biosensing applications ^{22, 195}.

The number of publications on graphene-based biosensors is massive, as represented by the 1110 publications linked to keywords "graphene biosensor" on the Web of Knowledge in 2018 alone. Graphene-based biosensors are expected to continue their progression and evolution in the coming years. Graphene-based electrochemical biosensors have found applications in medical, pharmaceutical, and environmental fields, by detecting and quantifying important compounds such as glucose ^{196, 197}, H₂O₂ ¹⁹⁸, ascorbic acid ¹⁹⁹, uric acid ²⁰⁰, NADH ²⁰¹, acetaminophen ²⁰², metal ions ²⁰³, and pesticides ²⁰⁴. The promising performance of graphene-based biosensors has led scientists to emphasise on researches regarding its potential applications in medical diagnostics ²⁰⁵.

Chia *et al.* reported on the fabrication of a glucose biosensor based on graphene obtained from liquid phase exfoliation ¹⁹⁶. Glucose oxidase (GO_x) was immobilised on the graphene-enhanced SPCE with the aid of a bi-functional linker:1-Pyrenebutyric

acid *N*-hydroxysuccinimide ester (PSE). The pyrenyl group of PSE binds non-covalently to graphene via π - π interaction while GO_x attaches to the succinimidyl fragment of PSE via nucleophilic substitution, as illustrated in Figure 2.29. The constructed biosensor was able to provide linear amperometric response on glucose concentrations from 0.1 mM to 1 mM under -0.4 V operating potential, with an LOD of 28.3 μ M. The author has also noted that the generic non-covalent enzyme immobilisation strategy of PSE could be potentially used in other electrochemical based enzymatic biosensors and immunosensors¹⁹⁶.

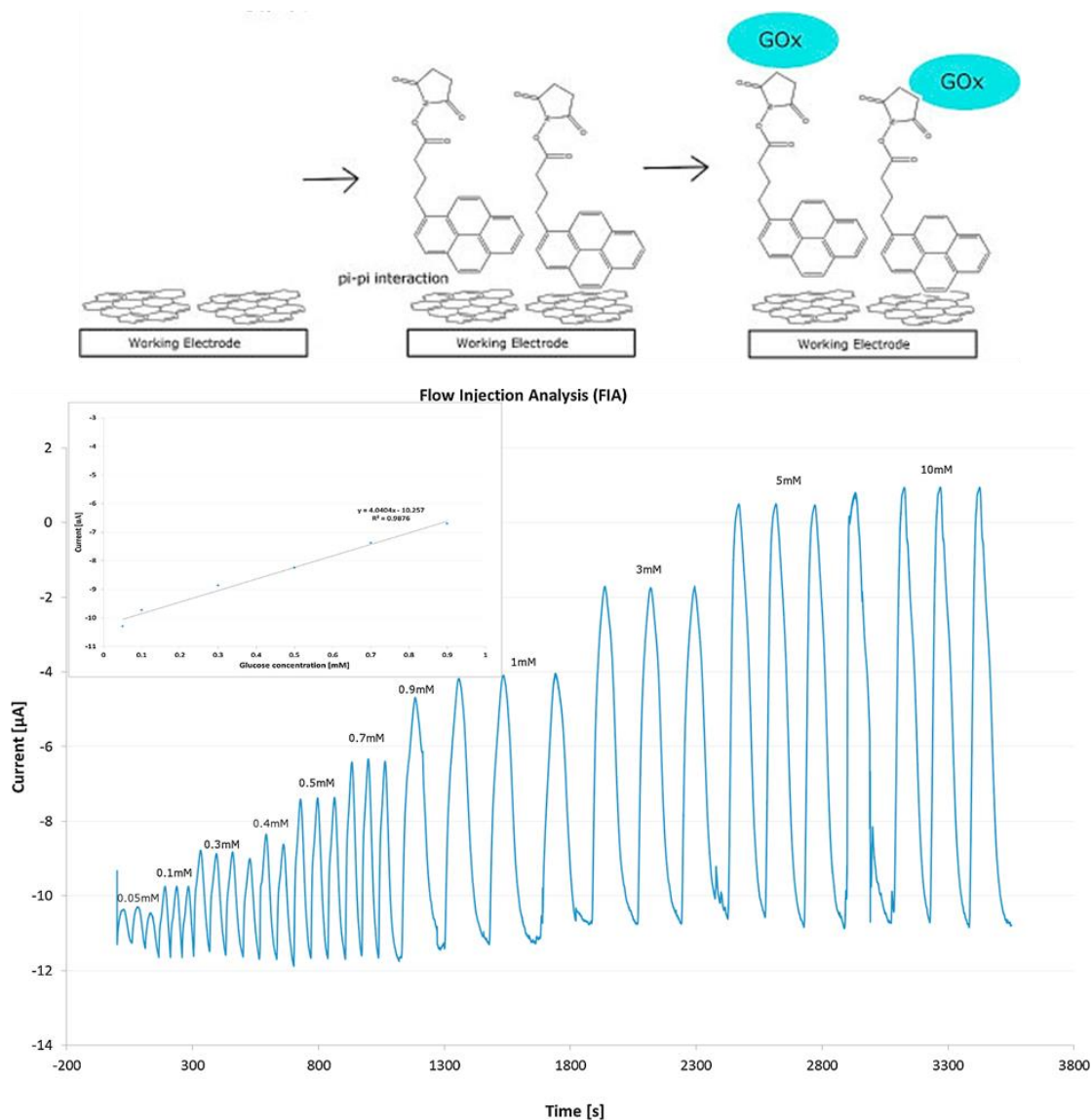


Figure 2.29. Visual representation of PSE functionalisation of graphene for glucose detection and the amperometric response of the graphene-based biosensor on successive additions of glucose with increasing concentrations. Inset shows calibration plot indicating the linear working range ¹⁹⁶.

A graphene-based electrochemical genosensor was developed for the amperometric detection of avian influenza (H5N1) ²⁰⁶. The H5 DNA sequences of H5N1 was first amplified by modified biotin- and fluorescein- labelled primer pairs via polymerase chain reaction (PCR) to form biotin and fluorescein labelled PCR amplicons. Streptavidin was applied onto graphene/PSE-modified SPCEs prior to the incubation of the PCR amplicons. Upon incubation with the H5 amplicons, the biotin label binds

covalently to the streptavidin on the electrode platform. Subsequently, horse radish peroxidase (HRP)-conjugated anti-fluorescein antibodies are incubated on the electrodes, attaching themselves to the fluorescein segment of the H5 amplicons. Using 3,3',5,5'-Tetramethylbenzidine (TMB) membrane peroxidase substrate as the hydrogen donor, the H_2O_2 reduction catalysed by HRP on the electrode was detected as a measurable current signal. The graphene-based platform was able to detect the H5N1-derived amplicons linearly in the range on 0.27-8.51 ng/ μ L. The stepwise assembly of the graphene-enhanced genosensor for H5N1 detection is shown in Figure 2.30²⁰⁶.

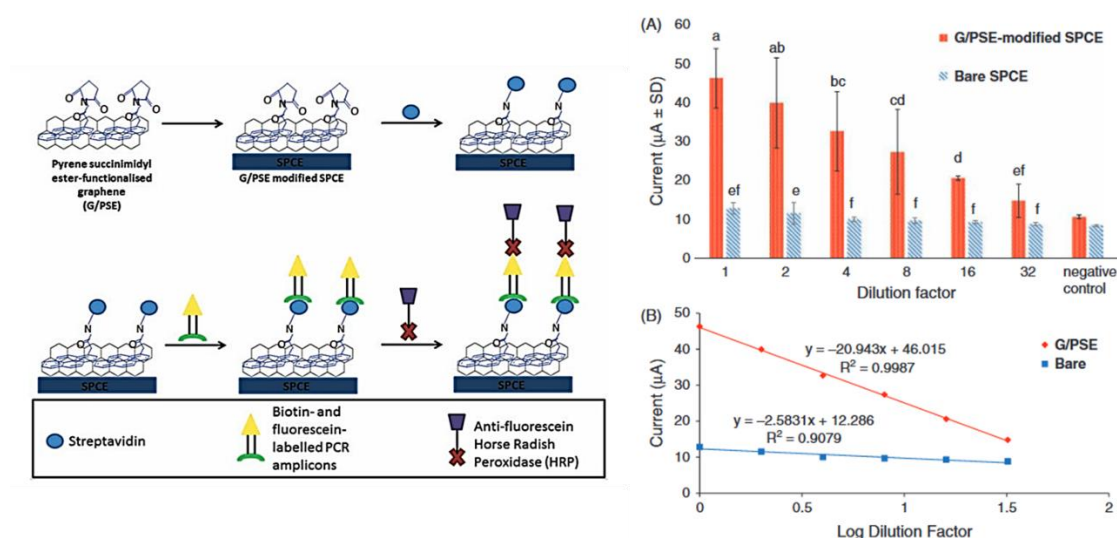


Figure 2.30. Schematic representation of the step-by-step assembly of the graphene-enhanced genosensor for H5N1 detection and the analytical results: (A) Amperometric response of bare and G/PSE-modified SPCE with different dilutions of PCR amplicon; (B) Calibration plot of current signals against different dilution factors of H5 PCR amplicon in logarithmic scale²⁰⁶.

Another DNA-based biosensor was reported for the sensitive detection of breast cancer-related BRCA1 gene via a similar indirect/"sandwich" detection strategy²⁰⁷. The genosensor involves the immobilisation of a capture probe (DNA-c) and receptor probe (DNA-r) DNAs on graphene modified glassy carbon electrode (GCE) in a

“sandwich” model to detect the target BRCA1 DNA (DNA-t). The DNA-r is conjugated with gold nanoparticles as the electrochemical label, producing detectable current upon hybridisation between DNA-c and DNA-t, which is then recorded in CV and chronoamperometry measurements. Operating at the oxidation potential of 1.1 V, the genosensor was found to be stable, reproducible, and sensitive, successfully detecting up to 1 fM of BRCA1 gene (5.896 fg/ml) with a linear range from 1 fM to 1 nM (Figure 2.31).

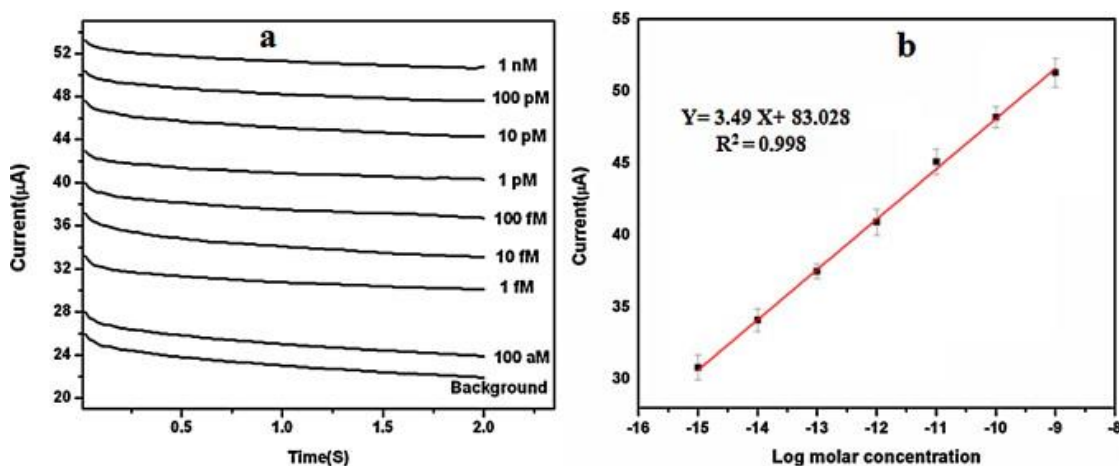


Figure 2.31. (a) Chronoamperometric response of the genosensor towards various DNA-t concentrations. (b) Redox current at the oxidation potential of 1.1 V vs logarithmic molar concentrations of DNA-t²⁰⁷.

Graphene-based materials are also popularly used for the development of various immunosensors. Singal *et al.* have reported on the fabrication of a graphene-multi-walled CNT-modified GCE (G-MWCNT/GCE) for the impedimetric detection of human cardiac troponin-1 (cTn1)²⁰⁸. PSE was used to anchor the bioreceptor, anti-cTn1 antibodies, onto the G-MWCNT/GCE platform. Based on the EIS measurements, the charge transfer resistance of the electrode before and after the incubation of the cTn1

target antigen are recorded and analysed to quantify cTnI detection. The LOD of the immunosensor was determined to be 0.94 pg mL^{-1} , with a linear range of 1 pg mL^{-1} to 10 ng mL^{-1} . The immunosensing platform was also found to be highly specific when challenged against non-specific IgG and another cardiac biomarker. C-reactive protein (CRP). Figure 2.32 illustrates the calibration curve of the immunosensor and its specific response towards cTnI ²⁰⁸.

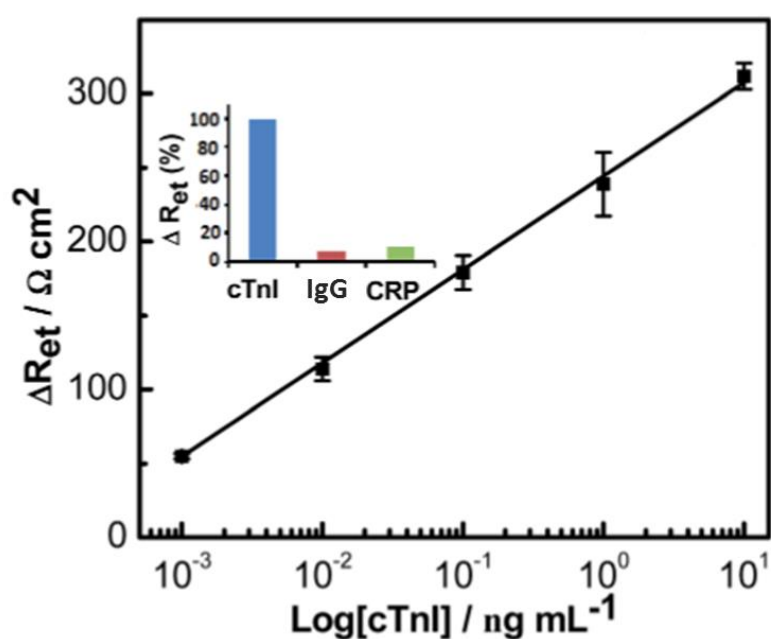


Figure 2.32. Calibration curve of the immunosensor showing linear response of cTnI concentration towards change in R_{ct} . Inset: normalised impedimetric response towards non-specific IgG and CRP with respect to cTnI ²⁰⁸.

2.4 Graphene/Metal Oxide Synthesis and Biosensor

Applications

The successful integration of graphene with other different nanomaterials such as metals, metal oxides, and quantum dots, have produced various novel biosensors with enhanced performance due to the synergistic effects involved^{209, 210}. Particularly, the incorporation of graphene and nanostructured metal oxides has aroused much interest as metal oxide nanoparticles offers significant advantages for electrochemical analysis such as having high proportion of atoms on the surface with free valences compared to the cluster of total atoms that leads to catalytic activity and promotes electron transfer, and providing electrochemical reversibility for redox reactions²¹¹⁻²¹³. In addition, metal oxide nanoparticles also promises biocompatibility, chemical stability, high surface area to volume ratios, surface reaction activity, and tuneable electron transport properties due to quantum confinement effect, all of which are important features in the development of sensitive and selective biosensing applications²¹³⁻²¹⁵.

The unique properties and large surface area of graphene makes it an ideal candidate as the matrix material for the synthesis of metal oxide-based biosensor. The resulting graphene/metal oxide biosensor can be functionalised to insert functional groups at active sites so that the biosensor can bind specifically to targeted biomolecules or cells via the active sites²¹⁶. The processes used to bind metal oxide nanoparticles onto graphene sheets include *in-situ* chemical synthesis²¹⁷, hydrothermal method²¹⁸, microwave²¹⁹ and electrodeposition²²⁰. The binding mechanism of metal oxide nanoparticles onto graphene sheets is the ionic bonding between the positively-

charged metal oxide ions and negatively-charged functional groups on graphene (such as -OH , C=O of carboxylic, O=C-O of carboxylate, C-O and O-C-O)²²¹. For instance, Zhao *et al.* (2011) have constructed graphene/tin oxide nanocomposites using a facile microwave method²²². Lim *et al.* (2012) have also used microwave treatment to synthesize graphene/tin oxide nanoparticles from a mixture of graphene oxide and Sn^{2+} ions in the presence of sodium hydroxide²²³.

2.4.1 Graphene/Copper Oxide Biosensor

Recent studies have unveiled the successful implementation of copper (II) oxide (CuO) nanoparticles in the biosensors to detect glucose oxidation²²⁴ and hydrogen peroxide²²⁵. CuO nanoparticles are promising in the development of biosensors due to their high specificity, good electrochemical activity and the capability of promoting electron transfer at a lower overpotential. These properties are attributed to the narrow band gap of 1.2 eV in CuO, a *p*-type semiconductor²²⁶. The integration of graphene with CuO nanoparticles generates a biosensor that has enhanced detection ability of analytes. In one study, a graphene/CuO glucose sensor was created by electrodeposition of CuO nanocubes onto graphene sheets. The optimized electrodeposition conditions were found to be 120 s in 0.1 M of NaOH solution and +0.55 V of applied potentials. A linear range of up to 4 mM and a sensitivity of 1360 $\mu\text{A mM}^{-1} \text{cm}^{-2}$ was observed at the positive potential (+0.55 V) for the sensor²²⁷.

One of the factors that influence the sensitivity of graphene/CuO sensor is the particle size of CuO nanoparticles. Hsu *et al.* have shown that the particle sizes of CuO were affected by pH values in the solution²²⁸. Seven pH values ranging from 11.50 to 13.59 were investigated. In the case of CuO, it was observed that its particle size decreased

with increasing pH. Interestingly under a potential of +0.60 V vs. Ag/AgCl, the highest sensitivity of $1065.21 \mu\text{A mmol}^{-1} \text{L cm}^{-2}$ was achieved at the mean diameter of 15.75 nm instead of the smallest particle size. The resulting graphene/CuO-modified GC electrode in this study has low loading with low glucose detection limit of $1 \mu\text{mol L}^{-1}$ and a wide linear range of $1\text{--}8 \mu\text{mol L}^{-1}$ ²²⁸. Figure 2.33 shows the key findings in this work.

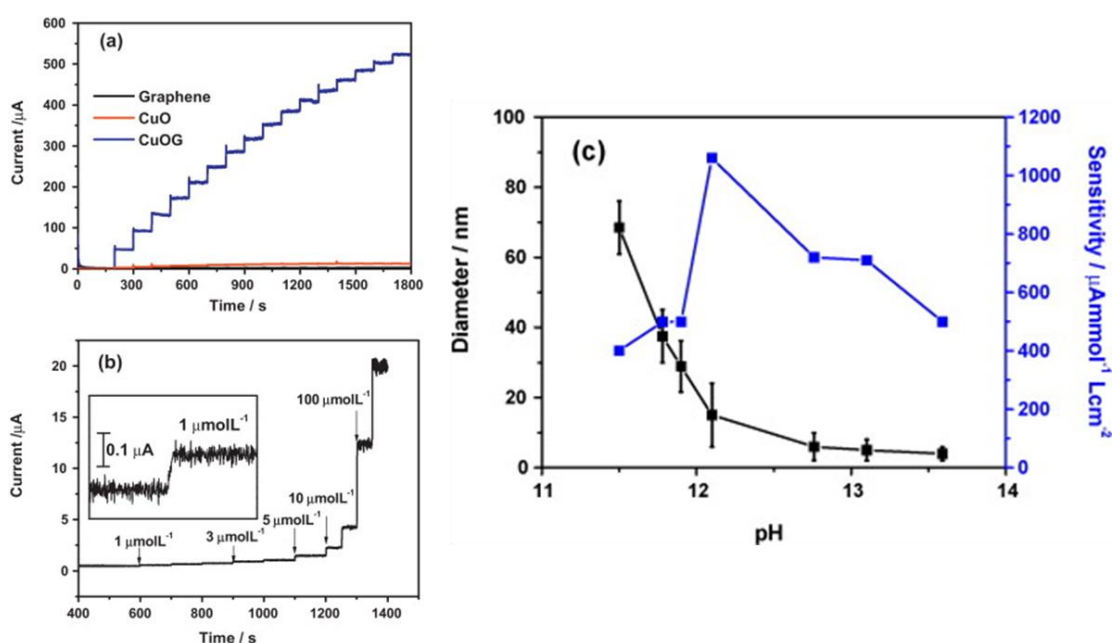


Figure 2.33. (a) Amperometric responses of GC electrodes modified with graphene-, CuO nanoparticle-, and CuO/graphene after successive additions of 0.5 mmol L^{-1} glucose in a 0.1 mol L^{-1} NaOH solution. (b) Amperometric response of CuO/graphene-modified GC electrode after subsequent glucose addition in 0.1 mol L^{-1} NaOH solution. Inset shows the corresponding calibration curve at $1 \mu\text{mol L}^{-1}$ glucose. (c) The summary of the pH-dependent diameters of CuO nanoparticles and their respective sensitivities in CuO/graphene-modified GC electrodes²²⁸.

The most common method to produce graphene/metal oxide nanocomposites uses hazardous chemicals, therefore in the past few years, researchers have been seeking a greener alternative chemical method to produce graphene/metal oxide. A study by

Qian *et al.* (2012) has revealed the successful decoration of copper (I) oxide (Cu_2O) nanoparticles onto graphene sheets at room temperature via ultrasonication at low power²²⁹. Sodium citrate was added to act as the reductant and stabilizer in alkaline medium. Cu_2O is one of the two stable oxides of copper, the other being CuO . The prepared chemically reduced graphene (CRG)/ Cu_2O modified electrode showed better non-enzymatic electrocatalytic response towards glucose compared to CRG or Cu_2O in alkaline media. The electrode has high selectivity towards glucose and a detection limit of $1.2 \mu\text{M}$ at a signal to noise ratio (S/N) of 3²²⁹. It has been hypothesized that the interactions of both Cu(II) and Cu(III) species in the oxidation of glucose in alkaline medium gave rise to the high electrocatalytic activity of Cu-based hybrids towards glucose^{230, 231}.

Apart from the common graphene/ CuO glucose sensor, Li *et al.* (2013) have synthesized an enzyme-free amperometric glucose sensor by immobilizing graphene/ CuO nanocomposites onto a glassy carbon electrode (GCE) with Nafion. The assembled sensor demonstrated a linear dependence on glucose oxidation from 2-60 μM with high sensitivity of $1480 \mu\text{A mM}^{-1} \text{cm}^{-2}$, fast response time of 3 s and low detection limit of $0.29 \mu\text{M}$ (S/N = 3). The sensor showed a larger peak current to glucose compared to GCE or CuO/Nafion/GCE . Not only did the sensor displayed long-term stability towards glucose, it was also highly resistant towards poisoning by chloride ions and interference from common interfering species such as ascorbic acid (AA), dopamine (DA) and uric acid (UA)²³².

Recently, an electrochemical immunosensor using cuprous oxide nanowires decorated graphene oxide nanosheets ($\text{Cu}_2\text{O@GO}$) as the electrode platform for the

detection of alpha fetoprotein (AFP) tumour biomarker was reported ²³³. The Cu₂O nanowires were synthesised by subjecting a mixture of copper (II) acetate and o-anisidine in autoclave reactor to 200°C for 10 hours while GO nanosheets were obtained from an improved Hummers method ¹⁷³. Both materials were mixed and dispersed in water, and then stirred for 12 hours under room temperature to produce Cu₂O@GO. Toluidine blue (TB), which acts as the electron transfer mediator, was adsorbed on Cu₂O@GO via electrostatic interactions by adding TB solution into the Cu₂O@GO precipitate and stirred for another 12 hours. The resulting TB@Cu₂O@GO nanocomposites were added to the surface of bare GCE to construct the electrode platform, and anti-AFP antibodies were then immobilised on the electrode platform. As immunoreaction between anti-AFP and AFP molecules occurred on the electrode surface, the current response was measured via square wave voltammetry (SWV). The stepwise fabrication of the immunosensor was verified via EIS technique, as displayed in the Nyquist plots shown in Figure 2.34A. Figure 2.34B and Figure 2.34C show the current responses from AFP concentrations of 0.001 pg/mL to 100 ng/mL and the corresponding calibration curve, respectively. The LOD of the immunosensor was found to be 0.1 fg/mL with a linear detection range of 0.001 pg/mL–100 ng/mL. The specificity of the immunosensor was also investigated by using CEA, PSA, IgG, and BSA as the interfering species. Each interference solution (100 ng/mL) were added into 1 ng/mL of AFP and detected by the proposed immunosensor. The electrochemical signal responses due to interferences varied less than 5% of that without the interference, indicating acceptable selectivity of the immunosensor towards AFP (Figure. 2.34D) ²³³.

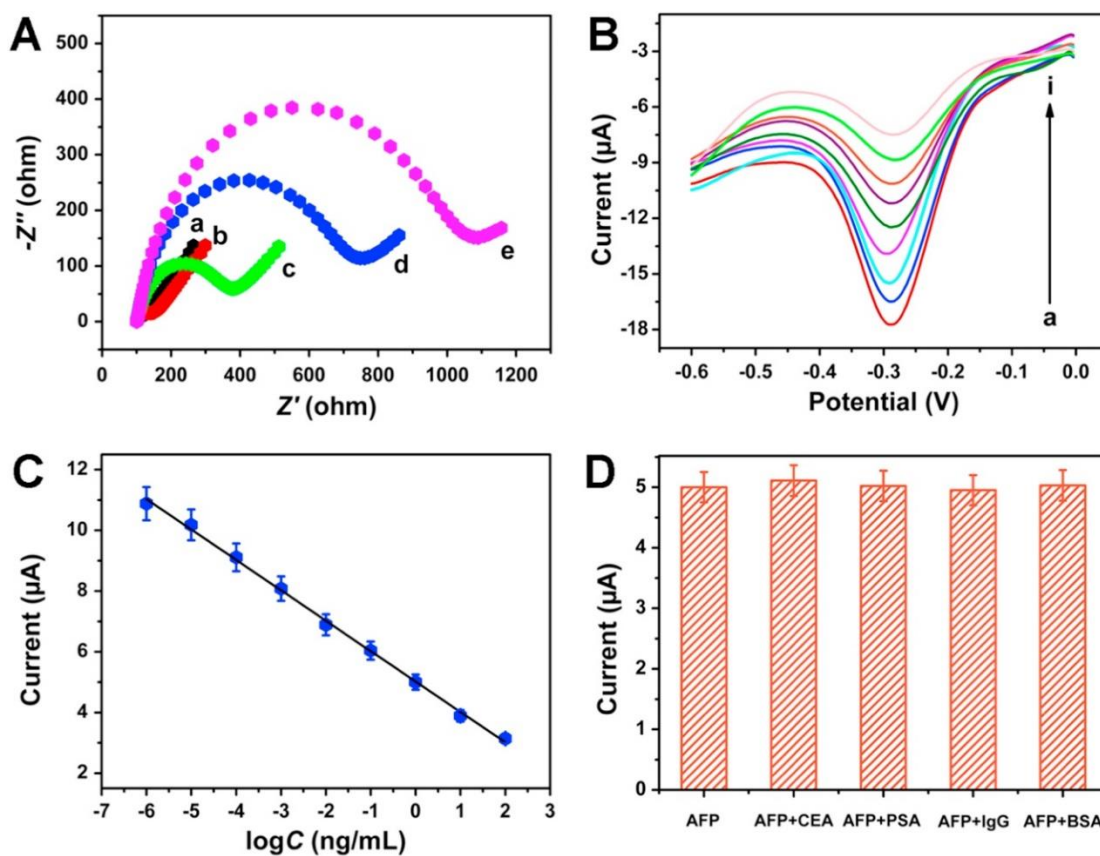


Figure 2.34. Electrochemical characterisations of the TB@Cu₂O@GO immunosensor for AFP detection. (A) Nyquist plots of EIS : GCE showing the stepwise fabrication of the immunosensor: (a) GCE, (b) TB@Cu₂O@GO/GCE, (c) anti-AFP/TB@Cu₂O@GO/GCE, (d) BSA/anti-AFP/TB@Cu₂O@GO /GCE, (e) AFP/BSA/anti-AFP/ TB@Cu₂O@GO/GCE; (B) Current signal responses of the immunosensor for the detection of different concentrations of AFP: (a) 0.001 pg/mL, (b) 0.01 pg/mL, (c) 0.1 pg/mL, (d) 1 pg/mL, (e) 0.01 ng/mL, (f) 0.1 ng/mL, (g) 1 ng/mL, (h) 10 ng/mL and (i) 100 ng/mL; (C) Calibration curve of the immunosensor for the detection of different concentrations of AFP; (D) Interference study on the immunosensor for AFP detection.²³³

2.4.2 Graphene/Zinc Oxide Biosensor

Zinc oxide (ZnO), a semiconductor with a wide band gap of 3.37 eV and high excitation energy of 60 meV at room temperature, is an important metal oxide with potential applications in electronic and optoelectronic devices such as sensors, displays, solar cells and field emission ²³⁴. ZnO is also capable of photocatalytic degradation of organic pollutants under UV or visible light irradiation ²³⁵. Besides, ZnO is one of the most common gas-sensing materials favoured for its excellent sensitivity towards a wide range of gases including NH₃ ²³⁶, ethanol ²³⁷, NO₂ ²³⁸, H₂S ²³⁹, O₃ ²⁴⁰ and H₂O ²⁴¹. In the field of biosensors, ZnO-based sensors were greatly researched because ZnO is highly specific, chemically stable and possess high electrical conductivity ²⁴². The high isoelectric point (pI) of 9.5 and positive charge of ZnO enables rapid immobilization of negatively charged biomolecules. This property was illustrated in a report where the negatively charged glucose oxidase (pI = 4.2) was immobilized on reduced graphene oxide (RGO)/ZnO nanocomposites at pH 7-7.4 ²⁴³.

Norouzi *et al.* (2011) introduced a novel glucose electrochemical biosensor constructed from the immobilization of glucose oxidase (GO_x) onto graphene/ZnO nanocomposites ²⁴⁴. A GCE coated with Nafion was employed as the transducer in the sensor and Fast Fourier transformation continuous cyclic voltammetry (FFTCCV) was used as the detection method of a flow injection system. Because Nafion possess unique physicochemical qualities such as easy fabrication, high chemical stability, good electrical conductivity and biocompatibility, it is widely employed as a protective coating material and a platform for enzyme immobilization. The fabricated sensor was a graphene/ZnO/GO_x/Nafion modified GCE. The biosensor has a linear response range

of 0.1-20 μM with a calculated detection limit of 0.02 μM ($S/N = 3$). In this study, it was confirmed that the sensor coupled with FFTCCV method displayed a remarkably reproducible sensitivity result. The sensor maintained 94.8% of its initial sensitivity up to 45 days, after which its sensitivity declined gradually. The loss in catalytic activity of the sensor might be the cause of decrease in sensitivity²⁴⁴. This test of sensor stability has proven the potential for the development of biosensors with long shelf lives and commercial viability.

A similar construction method was undertaken by Palanisamy *et al.* (2012) to prepare their own enzyme-based glucose biosensor, which was an RGO/ZnO/ GO_x modified GCE. The sensor was built via one step electrodeposition of ZnO microflowers onto RGO modified GCE, which presented a simple and cost-effective decoration method. The sensor demonstrated good electrocatalytic response towards the oxidation of glucose over a linear range of 0.02-6.24 mM. A sensitivity of 18.97 $\mu\text{A mM}^{-1}$ and detection limit of 0.02 mM was achieved²⁴⁵.

In a study by Kavitha *et al.* (2012), ZnO nanoparticles were bound onto graphene sheets using *in-situ* thermal decomposition at a relatively low temperature of 200 °C. Zinc benzoate dihydrazinate complex was used as the source precursor for ZnO. Three different physicochemical analyses (X-ray diffraction (XRD), transmission electron microscopy (TEM) and X-ray photoelectron spectroscopy (XPS)) illustrated the fine dispersion of ZnO nanoparticles on the surface of graphene. The graphene/ZnO dispersion was then drop-casted onto the surface of an indium tin oxide (ITO) electrode. GO_x was then immobilised onto working electrode, resulting in a ZnO/graphene/ GO_x enzymatic sensor. The ZnO/graphene/ GO_x -modified biosensor

performed better at glucose detection than bare graphene/ GO_x -modified electrode, as shown in the CVs recorded in Figure 2.35. The cathodic peak current at around -0.2V was found to decrease further as the H_2O_2 generated from the immobilised GO_x upon the addition of 10 mM glucose was reduced on $\text{ZnO}/\text{graphene}/\text{GO}_x$ electrode. It was observed that the H_2O_2 reduction current was much higher on $\text{ZnO}/\text{graphene}/\text{GO}_x$ electrode as compared to the reduction peak on $\text{graphene}/\text{GO}_x$ electrode. The sensor was also shown to display noteworthy antibacterial effect against *E. coli*, a gram-negative bacteria²³⁴.

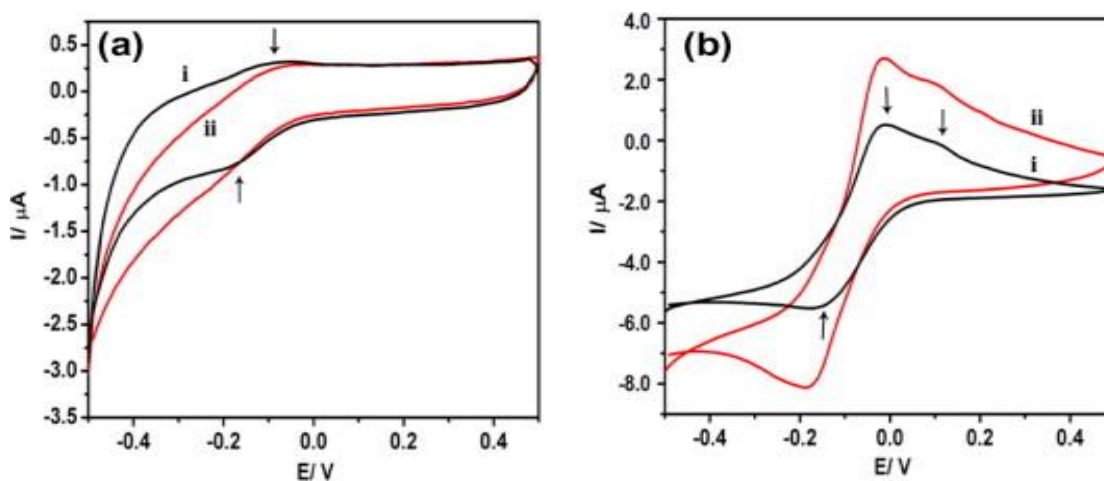


Figure 2.35. CVs of (a) $\text{graphene}/\text{GO}_x$ and (b) $\text{ZnO}/\text{graphene}/\text{GO}_x$ electrodes (i) before and (ii) after the addition of 10 mM glucose in 0.1 M PBS buffer ($\text{pH}=6$). The redox peaks are indicated on the graphs with arrows²³⁴.

An impedimetric genosensor was developed based on $\text{graphene}/\text{ZnO}$ nanocomposite for the detection Coconut Cadang-Cadang Viroid disease (CCCVd), a lethal disease to coconut palm (*Cocos nucifera* L.)²⁴⁶. Graphene was synthesised from graphite via liquid phase ultrasonic exfoliation and mixed with zinc acetate hexahydrate to obtain G/ZnO nanocomposite through a low temperature hydrothermal growth process where the mixture was heated at 90°C for 10 hours in an autoclave reactor. After

modifying SPCEs with the G/ZnO nanocomposite, amino-modified ssDNA probe complementary to CCCVd RNA sequence was immobilised onto the electrode surface by using PSE as the bi-linker. Upon hybridisation with ssRNA target (CCCVd genomic RNA sequence), the additional insulative layer on the electrode surface caused an increase in the charge transfer resistance. Figure 2.36 illustrates the development of the G/ZnO-modified impedance genosensor for ssRNA detection and its corresponding Nyquist diagram. The LOD of the genosensor was determined to be 4.3×10^{-12} M with a linear range from 1×10^{-11} to 1×10^{-6} M ²⁴⁶.

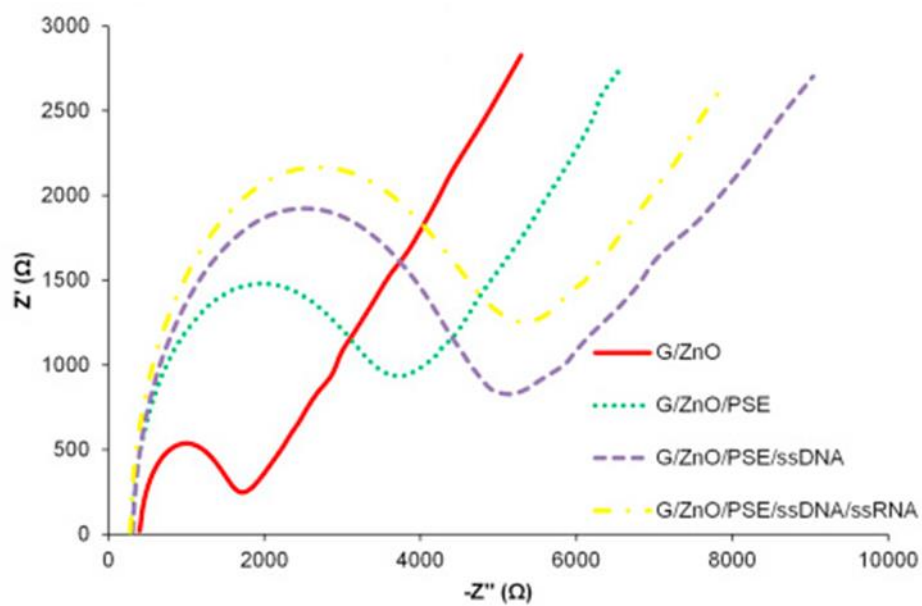
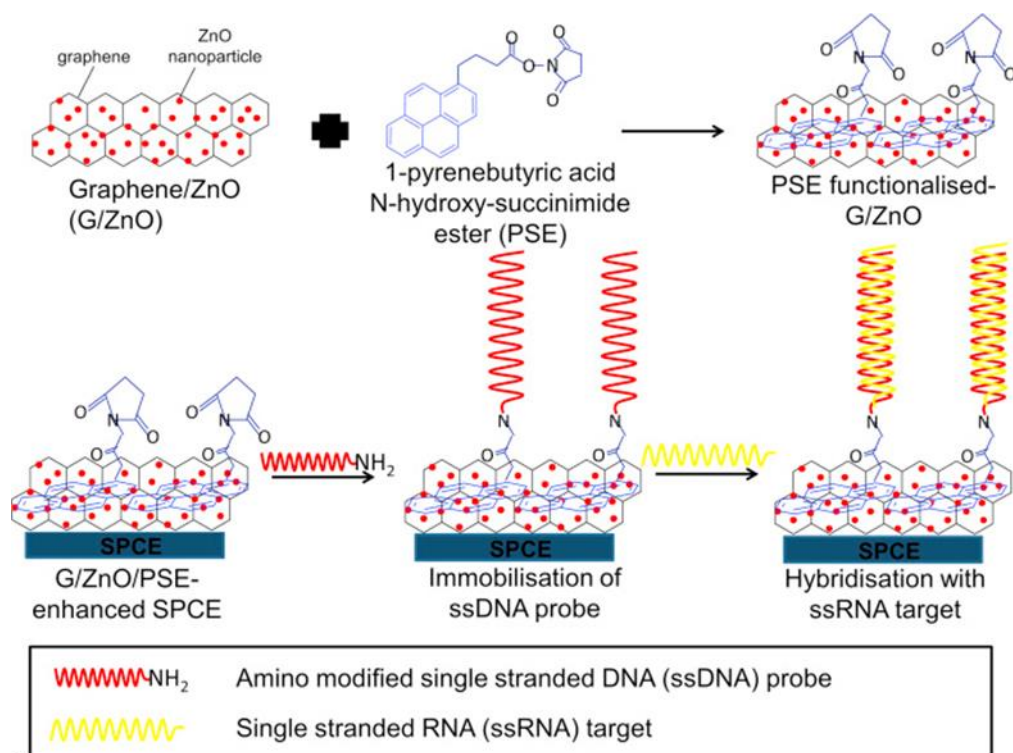


Figure 2.36. Scheme illustrating the development of G/ZnO genosensor for ssRNA detection and its corresponding Nyquist diagram ²⁴⁶.

2.4.3 Graphene/Nickel Oxide Biosensor

Due to the high cost of producing electrodes using expensive metal oxides, some researchers have focused their attention towards cheaper metal oxides such as nickel oxide (NiO) ²⁴⁷. Graphene/NiO is becoming more important in electrochemical sensors, due to its great electrocatalytic property, low cost and absence of interference by other electroactive compounds, such as AA, DA and UA ^{248, 249}. For in vitro sensing applications, graphene/NiO sensor presents a cheaper alternative compared to using other more expensive metal oxides.

Zhu *et al.* (2013) had designed a chemically stable and highly sensitive enzyme-free glucose biosensor by integrating reduced graphene (RG)/NiO nanocomposites onto GCE ²⁵⁰. Nickel was directly electrodeposited onto the GCE with graphene modifier using a multi-potential pulse process. Then, the GCE underwent potential cycling to oxidise the nickel nanoparticles to NiO. Compared to traditional NiO-modified GCE, the newly created RG/NiO-modified GCE recorded an approximate 1.5-fold greater current response towards the oxidation of glucose in alkaline media. The glucose biosensor responded linearly in the range of 20 μ M to 4.5 mM glucose with a short response time of less than 3 s and detection limit of 5 μ M (S/N = 3), as shown in Figure 2.37. The amperometric current responses of five different graphene/NiO GCEs were tested at +0.35 V, and their relative standard deviation (RSD) was 3.2%, indicating good reproducibility. In addition, the sensor was left exposed to air and its sensitivity tested every 2 days. It was found that after 25 days, the sensor still retained 92% of its original response, indicating that the sensor could remain chemically stable and active under exposed condition for a prolonged duration. Lastly, the sensor was

applied in real life to test the glucose concentration in commercial red wines. The sensor's results closely agreed with the results from high-performance liquid chromatography (HPLC), demonstrating the promising potential of graphene/metal oxide biosensors as a more simple and rapid alternative to conventional analysis techniques²⁵⁰.

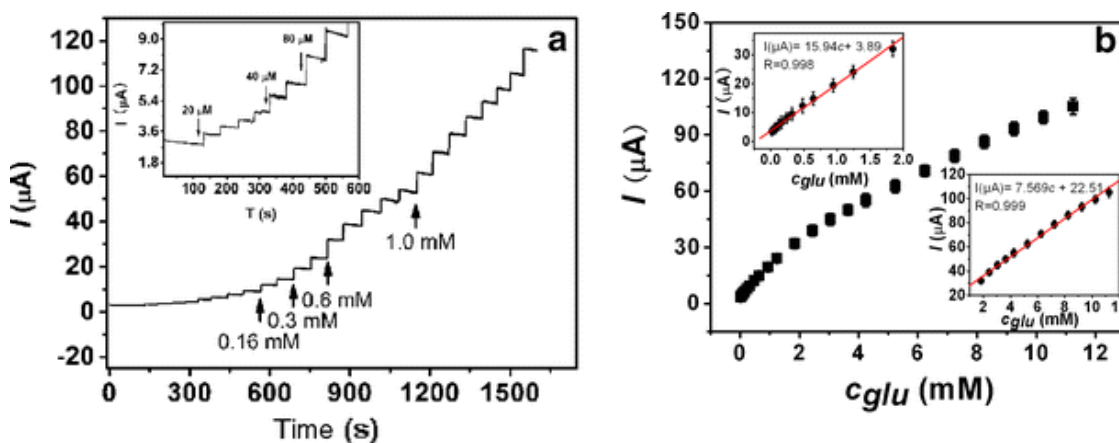


Figure 2.37. (a) Chronoamperometric response of NiO-GR/GCE in 0.2 mol L^{-1} NaOH solution towards increasing glucose concentrations at 0.35 V . Inset shows the current-time response at low concentrations; (b) Calibration curve of glucose obtained from the modified electrode²⁵⁰.

Another study by Kumary *et al.* (2013) revealed the preparation GO/Ni/NiO via solar exfoliation of GO/nickel acetate precursor. The GO/Ni/NiO was then immobilized onto a GCE, giving rise to the final sensor GO/Ni/NiO-modified GCE. The fabrication of the sensor included dispersing GO/Ni/NiO in methanol, dropping the GO/Ni/NiO-methanol suspension onto the surface of GCE and allowing the drop to dry in air. This method enables quick fabrication of the sensor. Cyclic voltammetry (CV) was used to test the current response of the sensor. The sensor displayed a linear range of $0.1\text{--}5 \mu\text{M}$. A sensitivity of $48,270 \mu\text{A mM}^{-1} \text{ cm}^{-2}$ and a detection limit of $0.28 \mu\text{M}$ were

obtained. The sensor also exhibited no interference response from AA and UA, indicating the high selectivity of the sensor towards glucose ²⁴⁸.

Graphene/metal oxide hybrids exhibit poor dispersion in water, and this causes difficulties for the fabrication of sensing electrodes. To remedy this situation, appropriate dispersants can be used, such as DNA, alcohol and sulfonated poly(ether-ether-ketone) ²⁵¹. Lv *et al.* (2012) developed a non-enzymatic glucose sensor using powdered graphene nanosheets (GNS) and NiO. Single strand DNA (ss-DNA) was selected as the dispersant, and the dispersed solution was dropped on polished GCE, resulting in GNS/NiO/DNA-GC electrode. Selecting amperometry as the mode of sensing, the operating potential was determined to be 0.6 V, as shown in Figure 2.38a, by the prominent current responses on successive glucose additions compared to other potentials (0.4 V and 0.5 V). The effect of NiO wt% in the composite material on glucose sensing was also investigated. As observed in Figure 2.38b, 0 wt% of NiO in the composite material produced minimal current responses while the increment of NiO wt% from 20 wt% to 45 wt% did not enhance the current responses significantly. Hence, using the optimised operating potential and NiO wt%, the electrocatalytic activity of graphene/NiO/DNA hybrid had a linear range of 1-200 μM and a detection limit of 2.5 μM at a potential of 0.6 V (Figure 2.38c) ²⁵².

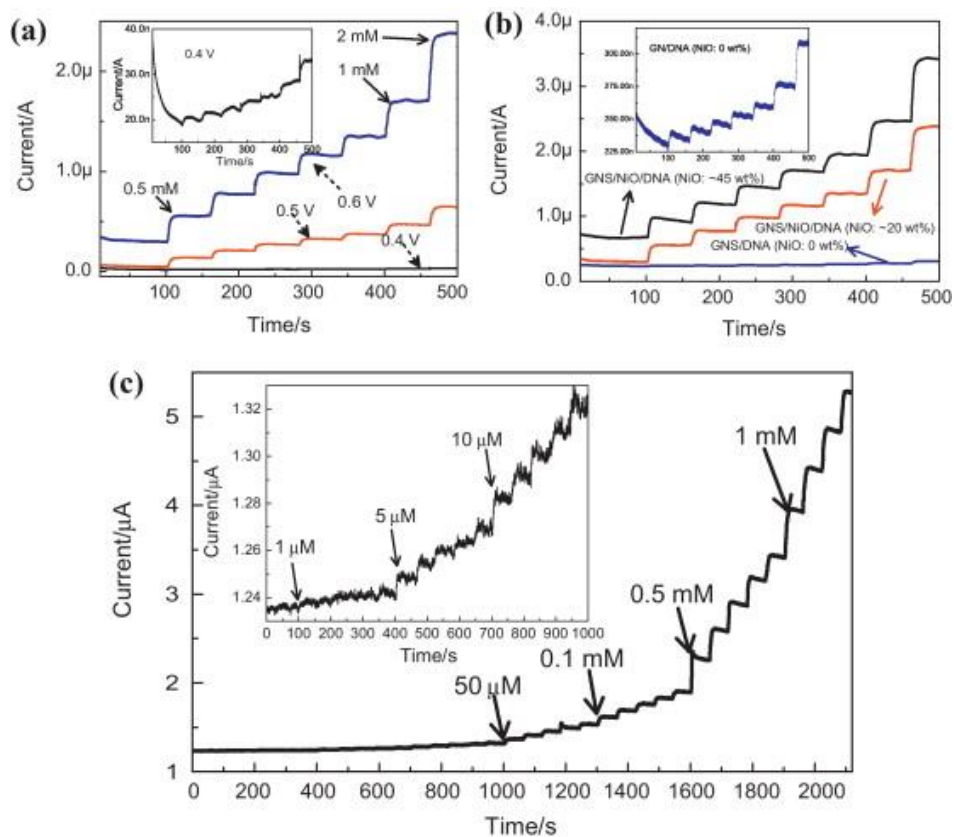


Figure 2.38. Amperometric glucose sensing performance of GNS/NiO/DNA-GC electrode towards successive additions of glucose in 0.1 M NaOH: (a) Effects of different potentials on the current responses; (b) Effects of different NiO wt% in the hybrid material on the current responses; (c) Detailed chronoamperometric response of the GNS/NiO/DNA-GC electrode (20 wt%) towards successive additions of glucose at 0.6 V ²⁵².

2.4.4 Graphene/Titanium Oxide Biosensor

Titanium dioxide (TiO₂) nanoparticles have attracted vast interests due to their superior properties such as large specific surface area, high uniformity, remarkable biocompatibility and environmentally friendly. TiO₂ has been widely applied in photocatalysis²⁵³, fuel cells²⁵⁴ and biosensors²⁵⁵. In the field of biosensors, different TiO₂ nanostructures can be decorated on electrodes to enhance the catalytic performance of the sensor towards enzymes. For instance, TiO₂ nanocrystals²⁵⁶, TiO₂ nanotubes²⁵⁷ and TiO₂ nanofibers²⁵⁸ had been studied as the receptor for glucose biosensors. The physicochemical qualities of TiO₂ nanostructures are greatly affected by their particle sizes, crystalline formation and aggregation states³³. A crucial factor influencing the performance of TiO₂ as an immobilisation platform for biomolecules is the particle size of TiO₂. Smaller TiO₂ nanoparticles are more favourable for the binding of enzyme on the sensor surface²⁵⁹. Due to this reason, many studies have been done to produce TiO₂ with controllable morphology and smaller particle size. For the past two decades, extensive knowledge from template-based nanoengineering techniques has been used to synthesise TiO₂ with different nanostructures. Various materials have been tested as templates for TiO₂ including porous alumina^{260, 261}, polymer gel²⁶², surfactant^{263, 264}, activated carbon²⁶⁵, carbon fibre²⁶⁶ and carbon nanotube²⁶⁷.

Fan *et al.* (2011) developed a facile hydrothermal method to prepare graphene/TiO₂ nanocomposites. Graphene oxide was generated using modified Hummers method^{35, 268}. The graphene oxide was then mixed in water with hydrazine hydrate and chemically reduced to form graphene. The graphene produced was mixed with

titanium isopropoxide and hydrothermally treated to form graphene/TiO₂. The final sensor was made by dropping graphene/TiO₂ onto the GCE and allowed to dry at room temperature, forming graphene/TiO₂ modified GCE biosensor. The sensor has higher peak current response and selectivity towards DA compared to bare GCE or graphene-GCE. In the presence of AA and UA, the sensor demonstrated a linear range of 5-200 μM DA with a detection limit of 2 μM (S/N = 3) ²⁶⁹. A follow-up study by Fan *et al.* (2011) proceeded to use the same biosensor for the detection of adenine and guanine, which are base units for DNA structure. The sensor exhibited high selectivity and improved response to adenine and guanine compared with bare GCE or graphene-GCE. A wide linear range of 0.5-200 μM with a detection limit of 0.10 and 0.15 μM were obtained for adenine and guanine respectively (Figure 2.39). The enhanced performance of the biosensor could be attributed to the high conductivity and adsorptivity of graphene/TiO₂ nanocomposites. This investigation had shown that TiO₂-based biosensors were efficient in the detection of purine bases ²⁷⁰.

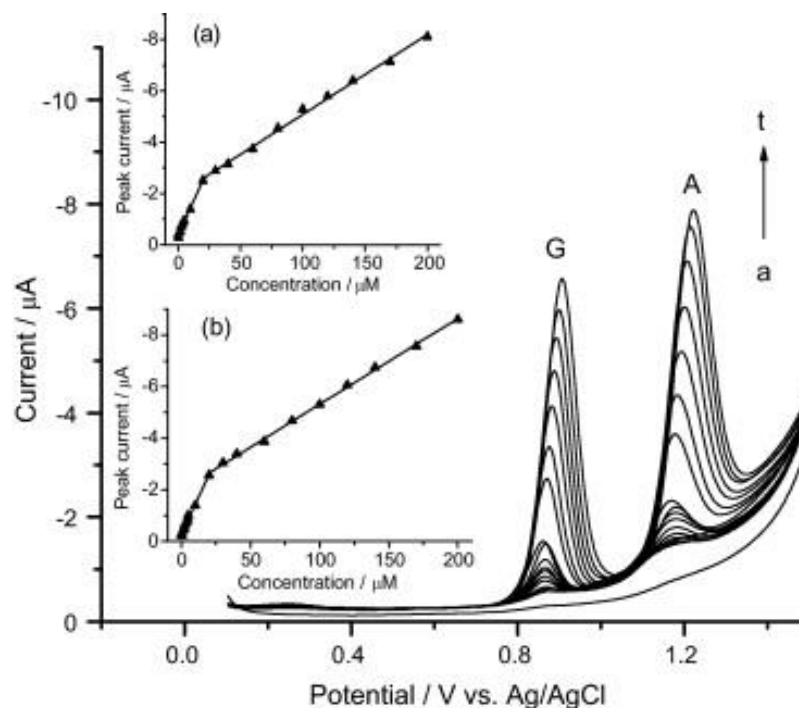


Figure 2.39. DPVs of increasing concentrations (0, 0.5, 1.0, 1.5, 2.0, 2.5, 3.5, 4.5, 5.5, 10, 20, 30, 40, 60, 80, 100, 120, 140, 170 and 200 μM) of adenine and guanine (a-t) in 0.1 M HAc-NaAc (pH 4.5) buffer solution. Insert shows (a) peak current against adenine concentration, and (b) peak current against guanine concentration ²⁷⁰.

Luo *et al.* (2013) had constructed an RGO/TiO₂/GOx modified GCE for glucose sensing. The TiO₂ nanoparticles and RGO were dispersed in a toluene-water system and subjected to microwave treatment. The sensor contained high loading and showed good detection for glucose in a linear range of 0.032-1.67 mM. A response time of 10 s, sensitivity of 35.81 $\mu\text{A mM}^{-1} \text{cm}^{-2}$ and detection limit of 4.8 μM were reported at a low potential of -0.7 V. Interference from AA and UA which normally coexist with glucose in human blood was found to be negligible ²⁷¹.

Chen *et al.* have reported on the development of a sandwich-type immunosensor for the determination of carcinoembryonic antigen (CEA) with the aid of Au nanoparticles-titanium dioxide-graphene (AuNPs-TiO₂-graphene) nanocomposites ²⁷². Firstly, dopamine-functionalised graphene was prepared via π -stacking in water under

sonication. TiO₂ dispersed in water was then added into the mixture and stirred vigorously to obtain TiO₂-dopamine-graphene nanocomposites. The enediol ligands of dopamine reacts strongly with the Ti atoms, effectively functionalising graphene for TiO₂ immobilisation. Due to excellent photoelectric conversion properties of TiO₂, AuNPs can be attached to TiO₂-graphene using photocatalytic method as TiO₂ becomes a good reducing agent under ultraviolet lamp irradiation. Horse radish peroxidase labelled secondary antibody (HRP-Ab₂) was then added to the AuNPs-TiO₂-graphene dispersion and incubated at 4°C for 24 hours to obtain HRP-Ab₂-AuNPs-TiO₂-graphene. Polished GCEs were electrodeposited with AuNPs before incubation with anti-CEA antibodies and blocked with bovine serum albumin (BSA) to obtain BSA/anti-CEA/AuNPs/GCE. The modified electrodes were then incubated with CEA for specific antigen-antibody recognition. Subsequently, the bioconjugate of HRP-Ab₂-AuNPs-TiO₂-graphene was incubated on the electrode to form a sandwich platform. The sandwich immunosensor was then immersed in an electrochemical cell containing H₂O₂ and hydroquinone (HQ), where CEA determination was achieved through measurements regarding the increment of peak current of HRP/H₂O₂ toward HQ reduction. The construction of the sandwich immunosensor for CEA detection is shown in Figure 2.40. Under optimum conditions, the immunosensor was able to detect CEA linearly within the wide concentration range from 0.005 to 200 ng mL⁻¹ ($R^2 = 0.994$) with an LOD of 3.33 pg mL⁻¹ ²⁷².

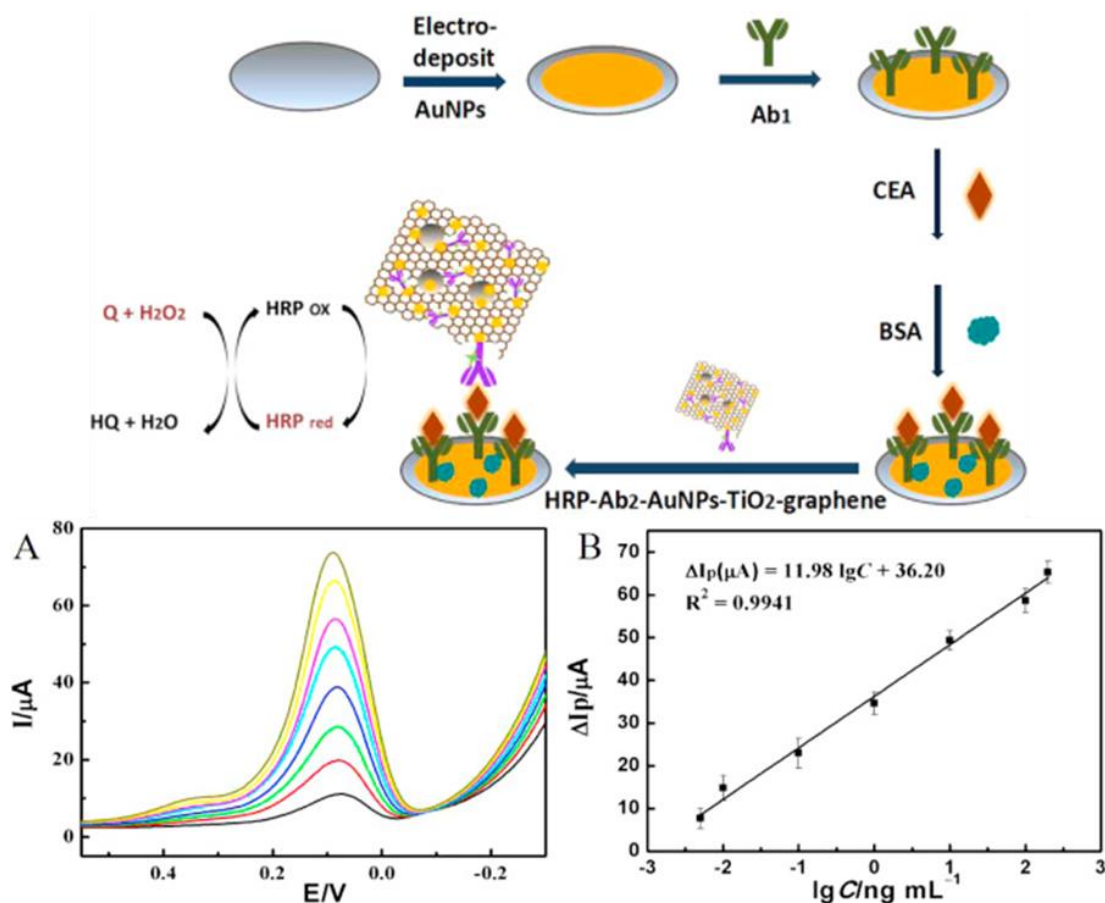


Figure 2.40. Schematic diagram illustrating the fabrication of the sandwich immunosensor for CEA detection and its electrochemical performance. (A) DPVs of the immunosensor towards different concentrations of CEA: 0.005, 0.01, 0.1, 1, 10, 100, and 200 ng mL^{-1} (from a to j); (B) the corresponding calibration curve of peak current vs. CEA concentrations in logarithmic scale showing linearity²⁷².

A label-free immunosensor was developed by Yan *et al.* for the detection of human epididymis specific protein 4 antigen (HE4 Ag)²⁷³. A multi-amplification signal system was employed where bimetallic Au@Pd holothurian-shaped nanoparticles (Au@Pd HSs) were loaded onto titanium oxide nanoclusters functionalised nitrogen-doped reduced graphene oxide ($\text{TiO}_2\text{-NGO}$), forming $\text{TiO}_2\text{-NGO}/\text{Au@Pd HSs}$. The $\text{TiO}_2\text{-NGO}$ was pre-modified with 3-aminopropyl triethoxysilane (APTES) for enhanced loading capacity and stability. GCEs are modified with $\text{TiO}_2\text{-NGO}/\text{Au@Pd HSs}$, and then incubated with anti-HE4 antibodies. The stepwise fabrication of the immunosensor

was monitored using EIS technique (Figure 2.41A). The reduction of H_2O_2 substrate occurred as HE4 Ag attached to the anti-HE4 on the TiO_2 -NGO/Au@Pd HSs, producing a measurable current response. The hydrothermally synthesised TiO_2 -NGO's high catalytic activity and large specific area combined with the good biocompatibility and electrocatalytic ability of Au@Pd HSs resulted in wide linear detection range of 40 fM to 60 nM, high sensitivity and low detection limit of 13.33 fM for HE4 Ag detection. The electrochemical performance of the HE4 immunosensor is shown in Figure 2.41

273.

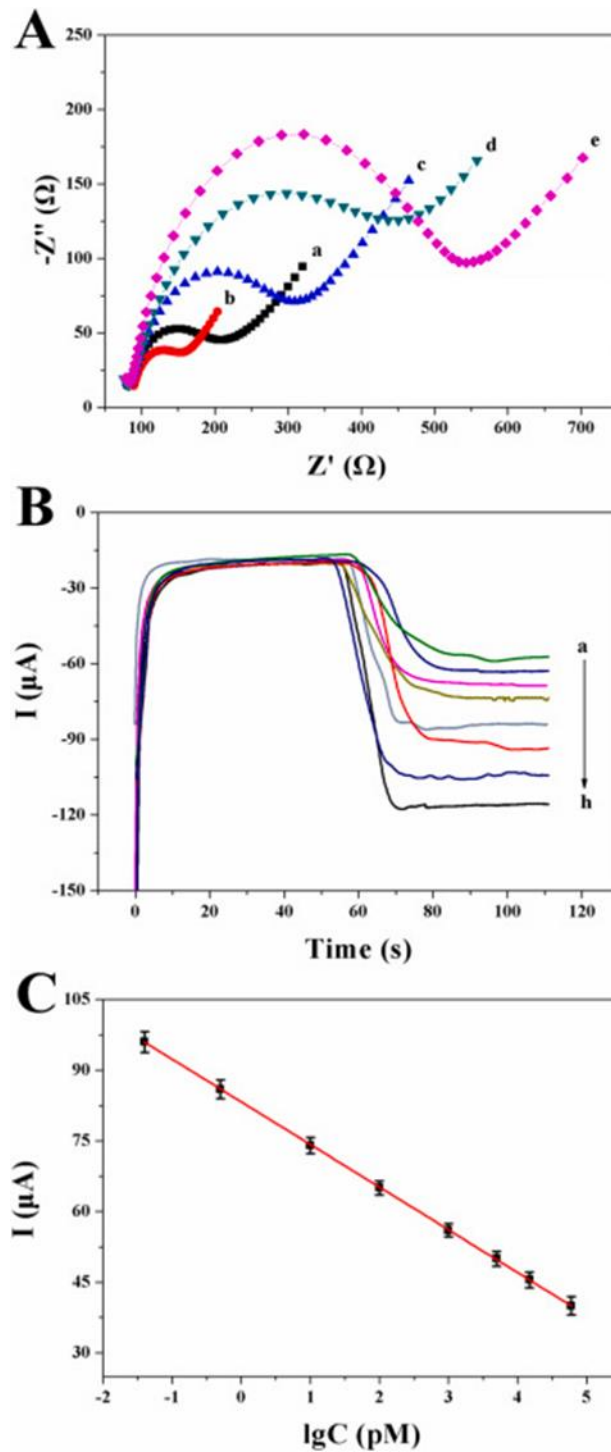


Figure 2.41. (A) Nyquist plots from the EIS technique: (a) GCE, (b) $\text{TiO}_2\text{-NGO/Au@Pd HSs/GCE}$, (c) anti-HE4/ $\text{TiO}_2\text{-NGO/Au@Pd HSs/GCE}$, (d) BSA/anti-HE4/ $\text{TiO}_2\text{-NGO/Au@Pd HSs/GCE}$, (e) HE4 Ag/BSA/anti-HE4/ $\text{TiO}_2\text{-NGO/Au@Pd HSs/GCE}$; (B) Amperometric responses of the immunosensor towards different concentrations of HE4 Ag: (a) 60 nM, (b) 5 nM, (c) 1 nM, (d) 100 pM, (e) 10 pM, (f) 5 pM, (g) 60 fM, (h) 40 fM; (C) Calibration curve of the immunosensor for HE4 Ag detection. Error bar = RSD ($n = 5$)²⁷³.

2.5 Dengue Diagnostics

Dengue, an infectious disease that causes acute febrile illness with centuries of history, has resurfaced in the past decades. Being the most prevalent arboviral disease at present times, dengue is caused by the mosquito-borne dengue viruses (DENV) of the *Flaviviridae* family. The primary and secondary vectors for dengue are the *Aedes aegypti* and *Aedes albopictus* mosquitoes, respectively, and the virus is transmitted to humans through the bites of infected female mosquitoes. Infected humans serve as virus multipliers, providing a source of DENV for uninfected mosquitoes. Dengue is currently endemic in over 100 countries worldwide, affecting 2.5 billion inhabitants in the subtropical and tropical regions and also their 120 million visitors every year ²⁷⁴. An estimate by World Health Organisation (WHO) in 2012 reports that there are up to 390 million dengue fever cases annually, with approximately 3.9 billion people are at risk of dengue infections worldwide. The global presence of dengue is illustrated in Figure 2.42, highlighting the countries with low, medium, and high presence of dengue ²⁷⁵.

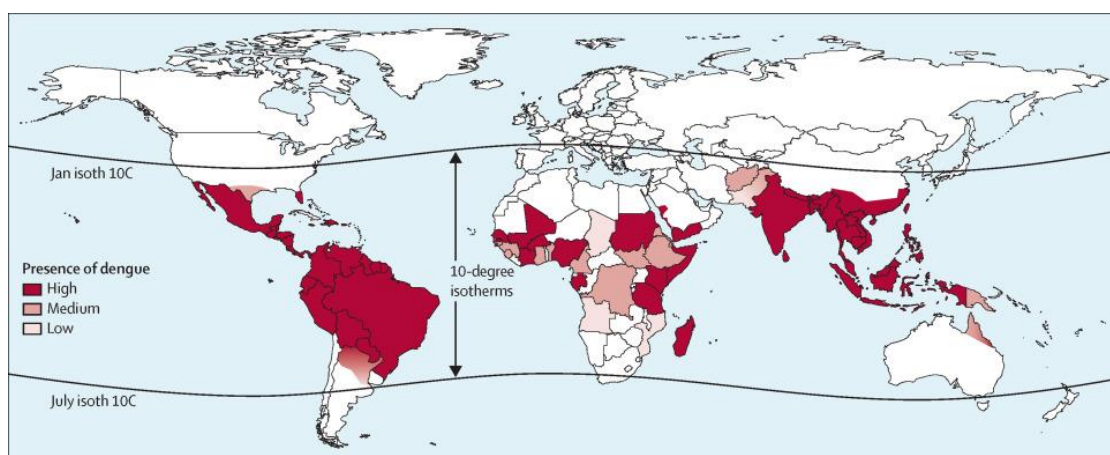


Figure 2.42. Global presence of dengue ²⁷⁵.

The dengue virus is a spherical, lipid-enveloped virus and its structure consists a positive strand RNA genome of approximately 10,200 nucleotides coding for three structural proteins of capsid, membrane, and envelope, and also seven non-structural proteins (NS1, NS2a, NS2b, NS3, NS4a, NS4b, NS5). The envelope protein (E) has several key functions in important processes such as receptor binding, blood cell, hemagglutination, membrane fusion, virion assembly, and the induction of protective immune response²⁷⁶⁻²⁷⁸. There are four antigenically related but genetically distinctive serotypes of DENV, viz. DENV-1, DENV-2, DENV-3, and DENV-4. The infection by one serotype provides long term immunity against reinfection of that specific serotype, but only transient and partial immunity to other serotypes²⁷⁹⁻²⁸¹. Upon infection, dengue manifests in very dissimilar clinical presentations, ranging from asymptomatic to potentially lethal severe illness. The symptomatic categorisation are as follows²⁸²⁻²⁸⁷:

- **Undifferentiated febrile illness (UF):** Impossible to diagnosed clinically. Maculopapular rash may or may not appear. Diagnosis is based on serology or virology.
- **Dengue fever (DF):** Classic dengue fever reaching 40 °C accompanied with a sudden onset of frontal headache, chills, retro-orbital pain, body aches, nausea, and visible exanthem (rash). Death is rarely reported but massive bleeding may occur.
- **Dengue haemorrhagic fever (DHF):** Complication from DF primarily found in children under 15 years of age (may also occur in adults). Other characterisations include coagulopathy, increased vascular fragility, and loss of fluid due to capillary permeability. Patients can also present with petechiae, rash, epistaxis, and gingival

and gastrointestinal bleeding. Plasma leakage into the pleural and peritoneal cavities resulting in pleural effusion and ascites are common.

- **Dengue shock syndrome (DSS):** Circulatory collapse or failure (shock) developed from DHF due to severe plasma leakage.

In mild cases of dengue, patients usually recover after fluid and electrolyte therapy. However, approximately 5-10% of DF patients progress to DHF/DSS, which could probably lead to deaths when not handled carefully. One of the most important risk factors for developing DHF or DSS is the secondary infection by a heterologous DENV serotype. The reason behind this phenomenon is due to the cross-reactive antibodies raised after a primary DENV infection, also known as antibody-dependent enhancement (ADE) effect^{288, 289}. While serotype-specific antibodies induce life-long immunity to that homologous serotype, the cross-protection against heterologous serotypes last for only 3-4 months. If the secondary infection occurs beyond this period of cross-protection, cross-reaction between the pre-existing antibodies of sub neutralising concentration and heterologous virus occur instead, which will then facilitate viral infection of FcγR-bearing cells. Hence, the ability of a diagnostic assay to identify different serotypes is extremely important to monitor and control the severity of dengue.

There is a need for effective and accurate diagnosis of dengue for better clinical management (early detection, differential diagnosis with other infectious diseases, and case confirmation), surveillance support, pathogenesis studies and vaccine research²⁹⁰⁻²⁹². A reliable diagnosis would also allow early intervention to treat patients and prevent or control the epidemicity of dengue. Currently, there are four main categories of laboratorial methods for dengue diagnosis: virus isolation, viral

nucleic acid detection, antigen detection, and serological tests. The merits and demerits of these diagnostic methods are outlined in Figure 2.43, showing the general inverse relationship between accessibility of a diagnostic method and the confidence level of the test results. While direct methods such as virus isolation and nucleic acid detection are slow, labour-intensive, expensive, and demand complicated techniques, they also offer higher sensitivity and specificity compared to antibody detection via serological methods.

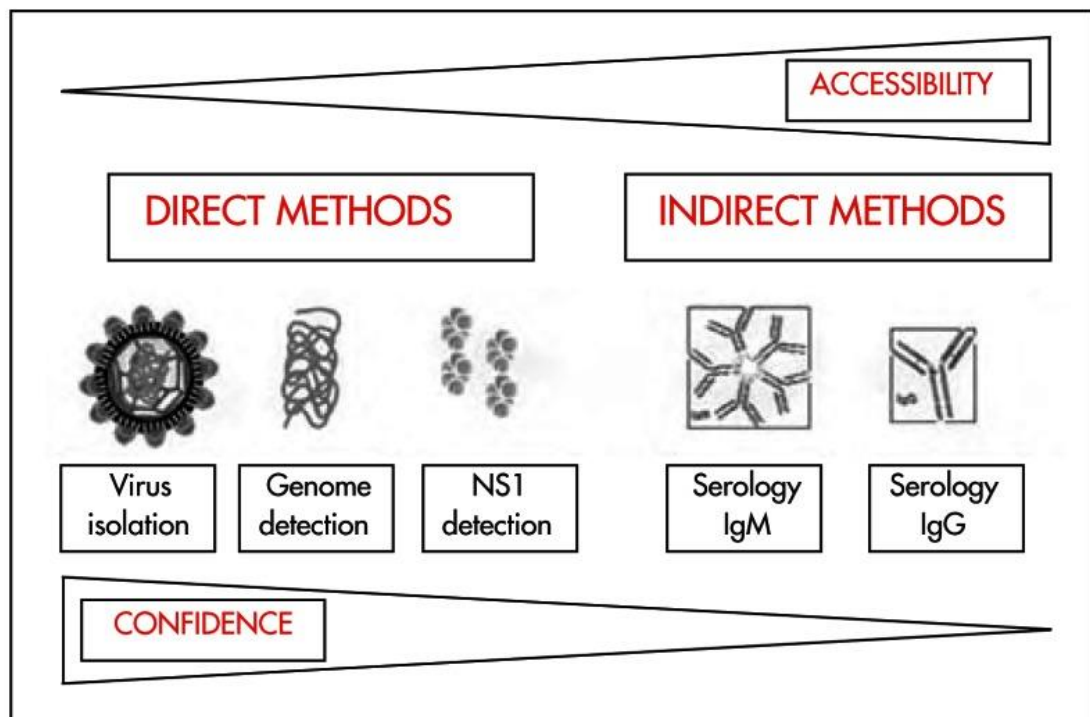


Figure 2.43. Dengue diagnostic tests and their comparative merits ²⁹³.

2.5.1 Virus Isolation

The dengue virus can be isolated by inoculating diagnostic samples into mosquitoes, cell culture (mosquito or mammalian cell lines), or intracerebral inoculation of suckling mice. During acute phase of the disease, blood, serum, or plasma samples are collected from the patients, or in fatal cases, tissue samples from liver, lungs, lymph nodes, thymus, or bone marrow are collected at autopsy. Specimens must be handled with extreme care under controlled low temperatures to avoid sample degradation due to the heat-lability of the dengue virus. Samples should always be kept in refrigerators or packed in wet ice, or frozen at -70°C for storage beyond 24 hours. Following successful inoculation, the virus is confirmed by an immunofluorescence assay. The confirmation requires 1-2 weeks in general and is only possible if the viability of the virus in the specimen is preserved from delicate handling. In addition, this method requires highly skilled laboratory personnel and delicate facilities for cell culture and fluorescent microscopy^{292, 294}.

2.5.2 Nucleic Acid Detection

Similarly heat-labile, samples for nucleic acid detection must also be handled with the delicate procedures described for virus isolation to preserve the viability of the RNA. Nucleic acid detection assays involve three steps consisting of extraction, amplification, and detection. Firstly, the viral RNA is extracted and purified from the blood, serum, or tissue samples obtained from patients in acute phase of the disease, either through traditional liquid phase separation methods or silica-based commercial kits. The nucleic acid is then amplified via reverse transcriptase polymerase chain

reaction (RT-PCR) ²⁹⁵ and the amplified products are finally identified by the size of their bands of different molecular weights in agarose gel. Compared to virus isolation, nucleic acid detection assays offer a much shorter turnaround time. However, it is possible to obtain false positive results due to the high chances of contamination. The technique is also expensive, and requires expertise and delicate laboratory equipment

²⁹².

2.5.3 Antigen Detection

Compared to viral isolation and nucleic acid detection, the detection of antigen molecules in the patient's bloodstream is a much-simplified method. Recent enzyme-linked immunosorbent assay (ELISA) and dot-blot assays are directed to the envelope (E) or membrane (M) antigen and the non-structural protein 1 (NS1) of DENV. Results from these tests showed that the detection of these antigens in the form of immunocomplexes is possible in patients with primary and secondary dengue infections up to 9 days after the onset of illness ²⁹². The NS1 glycoprotein is produced by all flaviviruses and secreted by infected mammalian cells. The high amount of NS1 in the bloodstream produces a very strong humoral response. A large number of studies has been dedicated to the exploitation of NS1 as a diagnostic marker for early dengue diagnosis ²⁹⁶.

2.5.4 Serological Tests

The infection of dengue virus stimulates the production of immunoglobulins (IgM, IgG, and IgA) as an acquired immune response. One of the most popular serological tests is the IgM antibody-capture enzyme-linked immunosorbent assay (MAC-ELISA). In MAC-ELISA, the IgM molecules in the patient's serum sample is detected by capturing them using anti-human IgM antibodies pre-coated onto a microplate. Dengue specific antigens will then bind to the anti-dengue IgM antibodies and are detected by enzyme-conjugated monoclonal or polyclonal dengue antibodies, turning a non-coloured substrate into a coloured product. Measurements of the optical density provide information on the amount of IgM available in the sample and is measured by

a spectrophotometer. MAC-ELISA possess good selectivity and sensitivity especially when used five or more days after fever onset ^{292, 297, 298}.

The dengue virus and its viral RNA and antigen are only detected in the patient's blood at the early stage of the infection, around four to five days after the onset of symptoms. In this period, virus isolation, viral RNA and antigen detection methods can be used to diagnose dengue. In later stages of dengue, the indirect method of antibody detection via serological methods are commonly used to diagnose dengue. Anti-dengue antibodies are detectable in most patients five days after the onset of symptoms, especially IgG, which persists in the patient's body for many months and even years after dengue infection (Figure 2.44). The immune response towards dengue differs according to the patient's immune conditions. In a primary dengue infection in which the patient has contracted dengue for the first time, high levels of IgM are produced. For a secondary infection, IgM levels are lower, but the IgG levels increase instead. The difference between IgM and IgG allows clinicians to determine whether a patient has a primary or secondary by measuring the IgM and IgG amount. This ability to identify secondary and primary infections is invaluable, especially since secondary infections are usually linked to the antibody-dependent enhancement (ADE) effect which is extremely lethal.

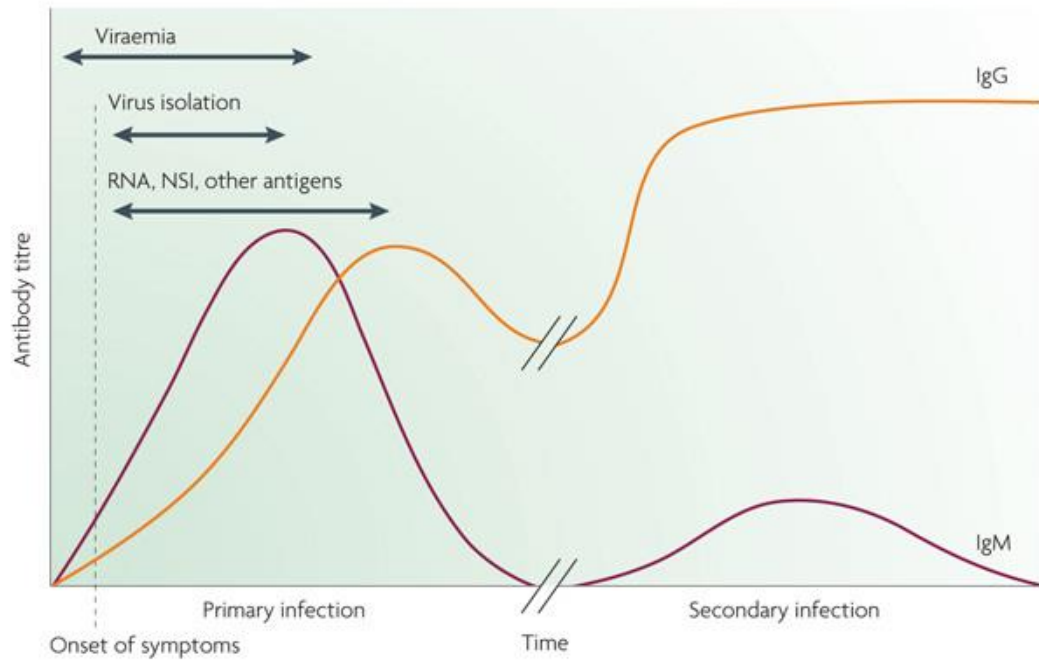


Figure 2.44. Major diagnostic markers for dengue diagnosis, and their respective detectable periods. IgG and IgM level differ depending on whether the infection is primary or secondary²⁹³.

2.5.5 Future Prospects of Dengue Diagnostics

The four major laboratorial dengue diagnostic techniques have been discussed in the previous sections. Their advantages and disadvantages are summarised in the table below:

Table 2.1. Strengths and weaknesses of current dengue diagnostic methods ^{293, 299}.

Diagnostic Methods	Advantages	Limitations
Virus isolation	<ul style="list-style-type: none"> • Specific • Identifies serotypes • Confirmed infection 	<ul style="list-style-type: none"> • Requires expertise and facility for cell culture and fluorescent microscopy • Takes more than a week • Does not differentiate between primary and secondary infection • Expensive
Nucleic acid detection	<ul style="list-style-type: none"> • Most sensitive and specific • Identifies serotype and genotype • Confirmed infection • Results in 24-48 hours 	<ul style="list-style-type: none"> • Potential false positive due to contamination • Expensive • Requires expertise and expensive laboratory equipment • Does not differentiate between primary and secondary infection
Antigen detection	<ul style="list-style-type: none"> • Easy to perform • Less expensive than virus isolation or RNA detection • Confirmed infection 	<ul style="list-style-type: none"> • Not as sensitive as virus isolation or RNA detection

Serological tests:	<ul style="list-style-type: none"> • Least expensive • Easy to perform • Differentiates primary and secondary infection • Confirmed infection 	<ul style="list-style-type: none"> • IgM level may be low or undetectable in secondary infections • Requires two or more serum samples
---------------------------	---	--

Based on all the drawbacks of these conventional assays, it is apparent that the development of an 'ideal' dengue test with minimal limitations is still in need. For the early diagnosis of dengue, an ideal dengue test should be able to distinguish dengue from other diseases with similar clinical presentations, highly sensitive, provides rapid results, inexpensive, easy to use, and highly stable; all of which could potentially be fulfilled with the successful development of rapid diagnostic tests ²⁹³. Generally, tests with high sensitivity and specificity are less accessible, time consuming, and difficult to perform. With rapid tests, sensitivity and specificity could be slightly compromised for better speed and accessibility, which is invaluable to improve dengue clinical management in resource-limited areas and point-of-care use. Currently, commercially available dengue rapid tests are dominated by lateral flow immunochromatographic assay kits such as the popular Panbio® Dengue Cassette (Abbott, USA) and Standard Diagnostics (SD) Bioline (SD, Korea) Dengue kits. In these tests, the analyte (NS1, IgG, or IgM) reacts with dye particles coated with the respective bioreceptors on the assay kit when the analyte-containing specimen is added to the kit. As the specimen/dye mixture travels along the length of the device, the analyte-dye complex is captured by the relevant test bands on the device window. The intensity of the band reflects the concentration of the analyte in the specimen. An example of a NS1 rapid diagnostic

kit is shown in Figure 2.45, along with its procedures and result interpretation guidelines ³⁰⁰.

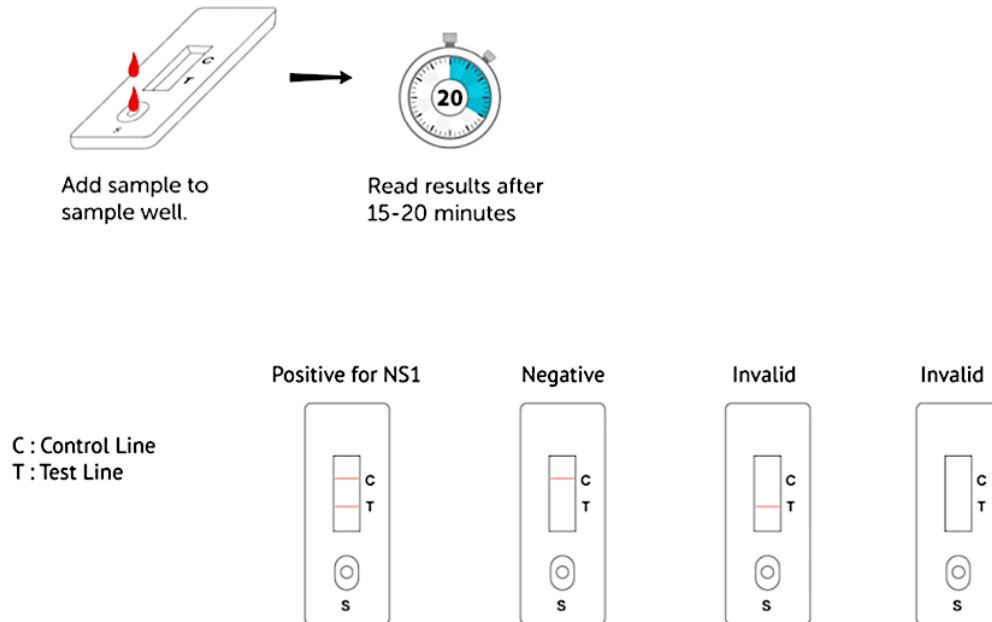


Figure 2.45. Schematic diagram of an NS1 rapid diagnostic kit illustrating its procedures and result interpretation ³⁰⁰.

While lateral flow immunochromatographic dengue diagnostic kits are widely adopted by healthcare providers now, their reliability in dengue diagnosis is still often questioned ³⁰¹⁻³⁰⁴. A recent comparative study conducted by Jang *et al.* has revealed that three commercially available rapid diagnostic tests for dengue diagnosis from CareUS, Humasis, and SD Bioline, could only detect NS1 antigens at sensitivities of 79.82, 63.30, and 48.62%, respectively ³⁰³. Meanwhile, the diagnostic performances for IgG and IgM are ranked from CareUs (89.91 and 82.57%, respectively) > SD Bioline (60.55 and 77.98%, respectively) > Humasis (51.38 and 72.48%, respectively). These results were found to not meet the claimed specifications provided by the

manufacturers of the rapid diagnostic kits. However, higher accuracies (80.73-96.73%) could be achieved by combining the detection of both NS1 and IgM. Therefore, dengue combo (NS1+IgM/IgG) rapid tests are recommended for more reliable dengue diagnosis, albeit at a much higher price compared to normal ones (RM80 versus RM30-40 in Malaysia) ³⁰⁵.

With the advancements in biosensor technologies, electrochemical biosensor platform holds a very high potential to be developed as the next generation of rapid diagnostic assays for dengue diagnosis. In the past few years, researches on electrochemical biosensors for dengue detection have been gaining vast popularity due to the merits they promise such as real time detection, ease of use and portability, amongst others, leading to the increasing amount of publications ³⁰⁶⁻³¹².

Jin *et al.* have developed an impedimetric biosensor for sensitive detection of dengue DNA and dengue RNA by employing primer hybridisation using different oligonucleotide sequences ³⁰⁸. Graphene oxide (GO) was synthesised via modified Hummer's method and functionalised with 3-Aminopropyltriethoxysilane (APTES), then wrapped on SiO₂ particles to form SiO₂@APTES-GO composite electrode material. The SiO₂@APTES-GO composite was deposited on platinum electrodes to construct the electrode platform. The modified electrodes were then immobilised with DNA and RNA oligonucleotide primers separately for hybridisation of complementary DENV-2 DNA and RNA, respectively. The biosensor showed good sensitivity and selectivity, successfully detecting 1 fM of DNA and RNA, with minimal response towards non-complementary West Nile virus DNA. as displayed in Figure 2.46 ³⁰⁸.

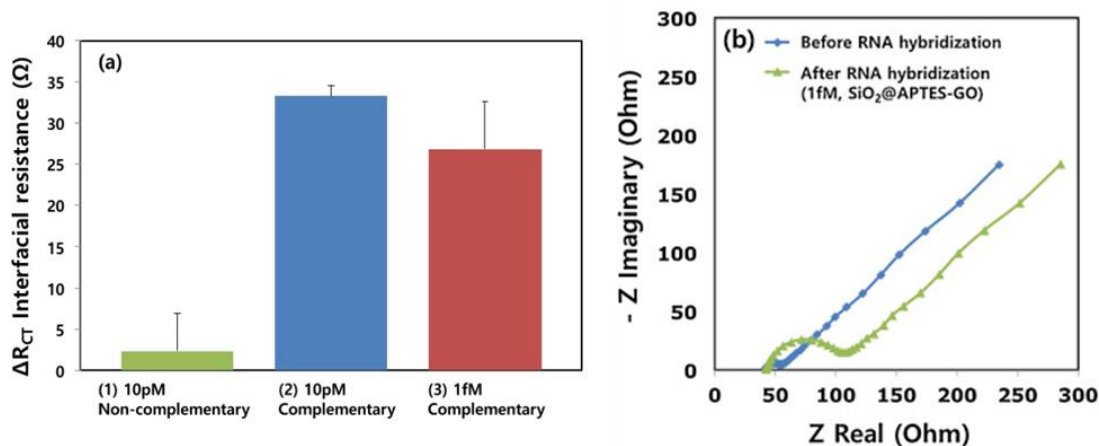


Figure 2.46. a) ΔR_{CT} of $SiO_2@APTES-GO$ composite-modified electrode versus (1) 10 pM non-complementary West Nile virus DNA, (2) 10 pM complementary DENV-2 DNA, and (3) 1 fM complementary DENV-2 DNA; b) Nyquist diagram before and after 1 fM complementary DENV-2 RNA hybridisation on $SiO_2@APTES-GO$ composite-modified electrode ³⁰⁸.

An electrochemical genosensor was developed by Singhal *et al.* for the detection of consensus DNA sequence of Dengue virus (DENV) where methylene blue (MB) was used as an intercalating agent ³¹⁰. The electrode platform was constructed by modifying fluorine doped tin oxide (FTO) glass plate with zinc oxide/platinum-palladium (ZnO/Pt-Pd) and immobilising it with single strand probe DNA (ssPDNA). The hybridisation between ssPDNA and single strand target DNA (ssTDNA) to form double strand DNA (dsDNA) produces a negative current response due to the anionic mediating interactions between MB with free guanine of ssDNA. Based on the CV and DPV results, the genosensor was found to operate linearly from 1×10^{-6} M to 100×10^{-6} M, with an LOD of 4.3×10^{-5} M and an LOQ of 9.5×10^{-5} M ³¹⁰.

The construction of an NS1-based immunosensor for early diagnosis of dengue was presented in a study by Nawaz *et al.* ³¹³. Bovine serum albumin (BSA) was first electro-grafted onto the working electrode of SPCE prior to the immobilisation of anti-NS1 monoclonal antibody. The detection of dengue NS1 was realised by measuring the

electron transfer resistance of the electrode before and after NS1 immobilisation. The quantitative and qualitative analysis of the sensing results was performed by plotting the ratio of the change in charge transfer resistance, impedimetric delta ratio (Δ_{ratio}) as a function of analyte (NS1) concentration, as shown in Figure 2.47. The impedimetric immunosensor was able to detect NS1 at a linear range of 1–200 ng/mL with an LOD of 0.3 ng/mL. The selectivity of the device was demonstrated by conducting experiment on human serum samples spiked with different concentrations of NS1. The recovery percentage was investigated and satisfactory recovery results of 96-103% were reported ³¹³.

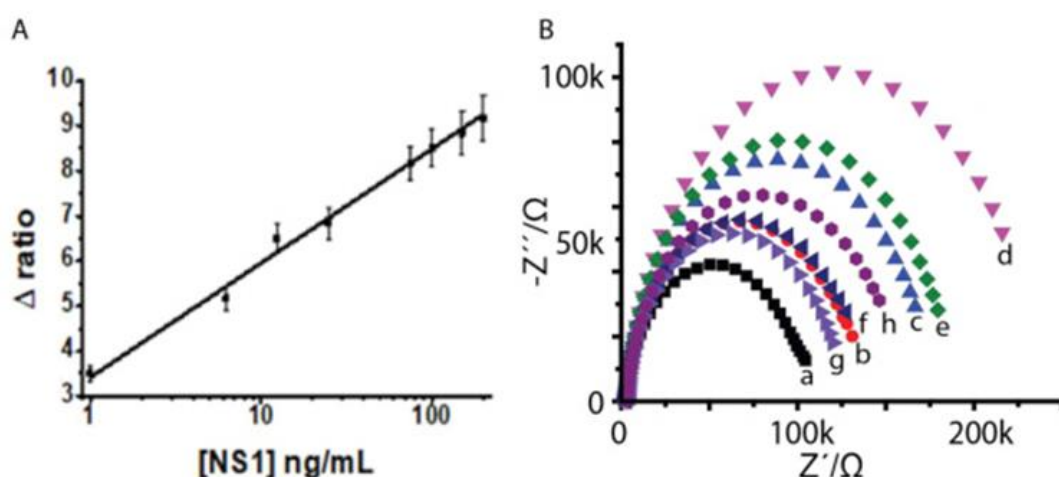


Figure 2.47. A) Calibration curve for NS1 detection and B) Nyquist plots of different concentrations of NS1 (a-h represent 1.0, 6.25, 12.5, 25.0, 75.0, 100.0, 150.0 and 200.0 ng/mL, respectively) in PBS containing 1 mM $[\text{Fe}(\text{CN})_6]^{4-/3-}$ ³¹³.

Recently, another impedimetric immunosensor for the detection of dengue virus antibody was reported ³¹⁴. Polished GCE was modified with multi walled CNT and functionalised via electro-polymerisation of pyrrole-NHS. DENV-2 NS1 was then covalently immobilised on the electrode set-up as the bioreceptor molecule via NHS activated amide coupling. Different concentrations of DENV-2 anti-NS1 antibodies

were prepared in PBS buffer solutions and incubated on the immunosensor setup to evaluate the sensor's performance using EIS measurements. The experiment was also repeated with anti-NS1 antibodies dissolved in bovine blood plasma for better representation of the biosensor's performance in realistic conditions. The performance of the biosensor in both media were then compared, yielding detection limits of 10^{-12} g mL⁻¹ in both systems, and linear working ranges of 10^{-12} - 10^{-5} g mL⁻¹ (PBS) and 10^{-11} - 10^{-5} g mL⁻¹ (plasma). Figure 2.48 shows the graphical representation of the immunosensor setup and its performance in both PBS buffer and bovine serum plasma ³⁰⁰.

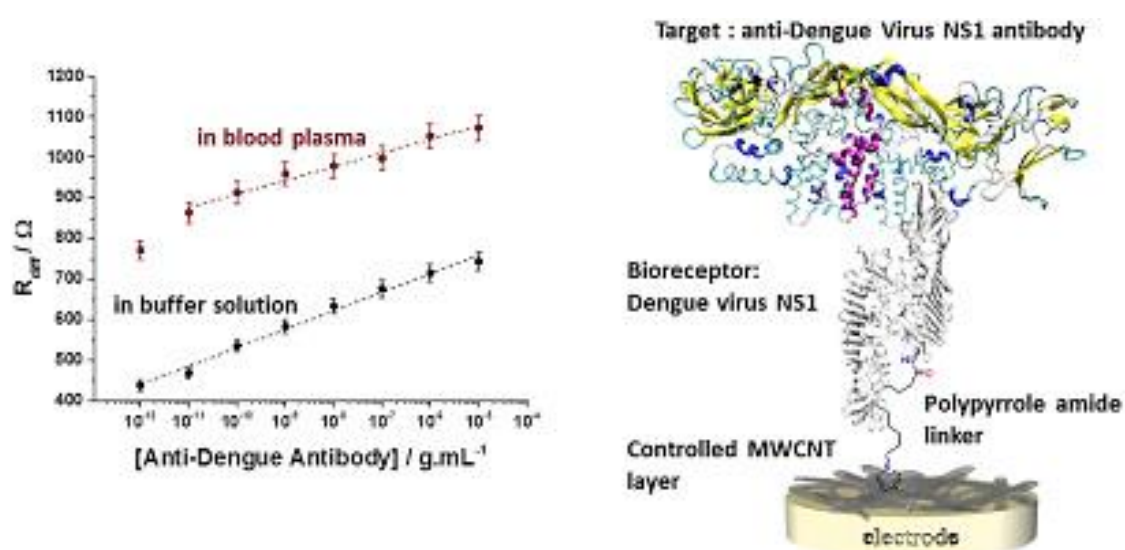


Figure 2.48. Graphical representation of the NS1-based impedimetric immunosensor setup and the biosensor's performance ³⁰⁰.

The publications of electrochemical dengue biosensor are largely comprised of sensing strategies involving DNA/RNA sensing or NS1 biomarkers, both with clear demerits. DNA/RNA-based biosensors could have low stabilities as DNA/RNA molecules are sensitive to heat. On the other hand, NS1 proteins of all flaviviruses

have been reported to exhibit high degree of homology ^{315, 316}, leading to massive concerns on cases of potential misdiagnosis. An alternative diagnostic biomarker for dengue sensing was suggested by Cardoso *et al.* to be the envelope glycoprotein domain III (EDIII) of DENV ³¹⁷. Being one of the three domains of the DENV envelope glycoprotein, EDII was found to highly antigenic ³¹⁸. EDIII is also responsible for receptor binding and contains multiple type and sub-type specific neutralising epitopes ^{319, 320}, contributing to its high potential as diagnostic marker. The successful development of EDIII-based ELISA tests for the detection of dengue antibodies has also verified the potential of EDIII as antigenic determinant for serological diagnostic purposes ^{317, 321-323}. The results showed high specificity, presenting no cross-reaction to antibodies from the similarly structured flavivirus, yellow fever (YF) ³²¹, compared to the cross reactivity found in the NS1-based Panbio ELISA assay towards antibodies of Japanese encephalitis (JE) and YF viruses ³²⁴. The EDIII-based approach was proposed to have a high specificity, as exhibited by the specific detection of West Nile virus infection ³²⁵ and tick-borne encephalitis virus infection ³²⁶, even when tested against other closely related flavivirus infections.

Another important factor that contributes to the accessibility of a rapid diagnostic test is its cost. Currently, antigens employed in dengue diagnosis are structural viral proteins that obtained through a gruelling and expensive method where the antigens are extracted from brains of artificially infected new-born mice, which has limited its large-scale production ³¹⁷. The costs for DNA/RNA synthesis/isolation are also high, in addition to the delicate processes involved. While Cardoso *et al.* have reported on the large-scale expression of DENV-1 EDIII protein in yeast (*Pichia pastoris*), a superior process was introduced by Pang *et al.* where a consensus sequence of EDIII (cEDIII)

reactive to all 4 serotypes of dengue was successfully expressed in *Nicotiana benthamiana* tobacco plant³²⁷. Coupled with the benefits of EDIII sensing strategy, this plant-based approach promises excellent scalability and safety advantages, potentially revolutionising the accessibility of dengue rapid diagnostic assays

Hence, by combining the exquisite advantages of high-performance electrochemical biosensors and innovative biosensing interface designs such as plant-based EDIII, future dengue diagnostics are anticipated to be deliverable at point-of-care stages with improved accessibility, which is extremely vital in combatting dengue outbreaks especially in rural areas where resources are scarce. Other than accurate diagnosis, high performance point-of-care dengue diagnostics are also instrumental in improving clinical management, patient surveillance, and outbreak investigations; ultimately improving the survival rate in the fight against dengue.

2.6 Chapter Summary

The groundwork behind the motivation of this project is laid out in this chapter, which is the fabrication and establishment of a graphene/metal oxide nanocomposite material with superior properties compared to conventional graphene and other graphene/metal oxide nanocomposites, and capable of disease detection via electrochemical biosensing. Having discussed past researches and principles on synthesis methods for graphene and graphene/metal oxide nanocomposites, it is apparent that there is a necessity to improve the synthesis process in order to achieve efficient production of graphene/metal oxide nanocomposite with superior quality. The proposed methodology for the synthesis of graphene/TiO₂ nanocomposite and the reason behind its selection will be discussed in detail in Chapter 3. The chapter

also discusses the variety of graphene/metal oxide-based biosensors and their applications. The basics of biosensors are also discussed for better comprehensibility of the project. As the model disease selected in the study, the elementary knowledge of dengue and its current available laboratorial diagnostic measures are also covered. The advantages and limitations of the conventional dengue diagnostic techniques are also outlined, with an indication on how a nanomaterial-enhanced electrochemical biosensing platform can potentially revolutionise the field of disease diagnostics.

Chapter 3 : One-step Green Hydrothermal Synthesis of Graphene/TiO₂ Nanocomposites for Non-enzymatic H₂O₂ Detection

3.1 Overview

Materials in the nanoscale have an excellent potential for designing powerful and remarkably sensitive bioanalytical protocols. Graphene has garnered much attention and scientific interests since its discovery¹⁸, and has provided a new angle to electrochemical biosensor research for its immense potential in electrochemical biosensing applications, owing to its unique physiochemical properties (high surface area, high thermal conductivity, excellent mechanical flexibility, fast electron transportation, and ease of functionalisation and mass production)^{16, 38, 194}. The excellent electronic conduction, particularly, is due to the unique sp² hybridisation of carbon bonds present in graphene, which facilitates the delocalisation of electrons¹⁸. Not only that, the electrochemical performance of graphene can be improved further by incorporating various inorganic nanoparticles, such as metal oxide nanoparticles, onto its surface³²⁸. Due to the catalytic and synergistic effects between graphene and metal oxide nanoparticles and their enhanced electrical and electronic properties, graphene/metal oxide nanocomposites offer tremendous potentials for a variety of applications including energy storage, energy conversion and electrochemical sensing devices²⁸.

One of the main reasons for the ever-growing interest on graphene-based composites is their unique trait of being able to combine desirable properties of different

materials for a given application, producing a tailor-made nanocomposite with properties that are not found in the individual components. To date, various metal oxide nanoparticles have been incorporated on graphene in the effort to further broaden their applications and enhance their performance. In the field of biosensing, anchoring metal oxide catalyst nanoparticles was found to be advantageous as it offers more versatile and selective approaches while also enhances the sensing performances³²⁹. Metal-oxide nanomaterials such as titanium dioxide (TiO₂) were reported to provide a novel mechanism to enhance the electron-transfer between the receptor and the sensing matrix, while offering other desirable properties such as excellent biocompatibility²⁶.

Various metal oxide nanoparticles such as CuO, SiO₂, CeO₂, MnO₂, ZnO, ZrO₂ have been used as sensor electrode platforms³³⁰⁻³³³. Among the many metal oxides, TiO₂ nanoparticles have attracted vast interests due to their superior properties such as large specific surface area, high uniformity, remarkable biocompatibility and environmentally-friendly^{31, 32}. TiO₂ can also act as a semiconductor and has been widely applied in photocatalysis²⁵³, fuel cells²⁵⁴ and biosensors²⁵⁵. Studies have proven that the addition of TiO₂ is an excellent modification for graphene in its application as sensors and biosensors^{33, 269}. However, the crystal structure, surface properties and texture properties are still important factors in determining the effectiveness of the sensor³³. In recent years, a handful of synthesis methods such as sol-gel, hydrothermal, and microwave-assisted reduction have been employed to incorporate TiO₂ onto graphene-based materials, producing nanocomposites with improved electronic or photocatalytic performance³⁴. These synthesis approaches however largely come with a common disadvantage, which is the usage of strong

reducing agents such as hydrazine hydrate in the formation of reduced graphene oxide (RGO) via the well-known Hummers method³⁵. Not only hazardous, hydrazine hydrate also creates dangerous by-products such as hydrogen fluoride³⁶. Furthermore, it may also destroy the 2D structure and reduce the electron properties of the carbon material, thus decreasing the overall performance of the biosensor^{37,38}.

Thus, in this work, a facile, pristine, green, simple, low-cost, and efficient approach to prepare graphene/titanium dioxide (G/TiO₂) nanocomposites was proposed. Pristine graphene flakes were firstly synthesised by subjecting raw highly pyrolytic graphite flakes to sonication¹⁹³, before the incorporation of TiO₂ metal oxides via low temperature hydrothermal processing step. Comparing to other works on G/TiO₂ synthesis, this method is both novel and environmentally friendly as no harsh chemicals were used, preserving the pristine nature of graphene. It is also economically efficient as the raw materials (ethanol and water) are inexpensive. The surface characteristics, structural and electrochemical properties of the G/TiO₂ nanocomposites were thoroughly investigated and its potential in biosensing application was explored in a series of electrochemical assessments against hydrogen peroxide (H₂O₂).

H₂O₂ is a very simple yet indispensable compound in biological studies. Besides serving as a signaling molecule in the regulation of diverse physiological processes from cellular growth to apoptosis³³⁴, it is also a common by-product generated by various biochemical reactions³³⁵. Therefore, the sensitive detection of H₂O₂ is fundamental in the development of biosensors, especially those involving oxidase enzymes.

3.2 Experimental Details

3.2.1 Materials

Raw highly pyrolytic graphite (HOPG) flakes (99% carbon purity) were purchased from Bay Carbon (Michigan, USA). Titanium (IV) isopropoxide (TTIP), $\text{Ti}(\text{O}i\text{Pr})_4$ (98%, reagent grade), potassium ferricyanide (III), $\text{K}_3\text{Fe}(\text{CN})_6$ (99%), and phosphate buffer saline (PBS) tablets were purchased from Sigma-Aldrich (USA). Reagent grade ethanol and hydrogen peroxide, H_2O_2 (30%) were obtained from R&M Chemicals (Malaysia). All the chemicals were used as received without further purification. Deionised (DI) water used throughout the experiment was filtered by the Milli-Q[®] System (Millipore, USA). Screen printed carbon electrodes (SPCE), C110 were purchased from Dropsens (Spain). Each of the electrodes had a 4mm diameter carbon working electrode, a counter electrode and a reference electrode made of silver, as shown in Figure 3.1.

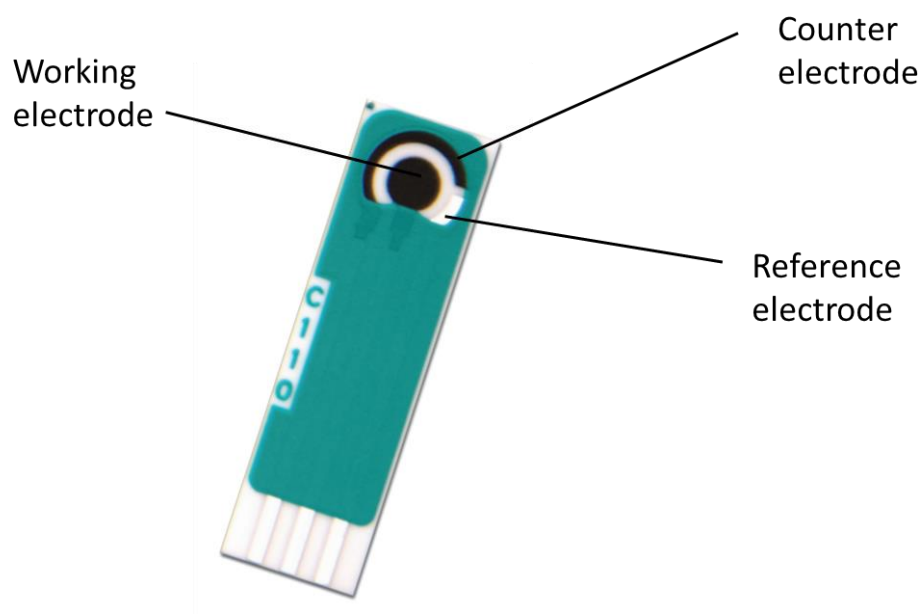


Figure 3.1. Screen-printed carbon electrode (SPCE) consisting working, counter, and reference electrodes.

3.2.2 Synthesis of Graphene

Graphene synthesis was conducted via a sonochemical-assisted solvent exfoliation method previously reported by Chia et al. ¹⁹³. In a typical synthesis, 50 mg of graphite was dispersed in a 100-ml mixture solution of denatured ethanol and DI water in 2:3 ratio. The materials were sonicated in an Elmasonic E30H ultrasonic water bath for 3 hours with the sonication frequency of 37 kHz at room temperature to produce a darkish black suspension. The solution was washed repeatedly via centrifugation with ethanol and deionised water. After removing the supernatant, the remaining black residue was dried overnight in an oven at 70 °C.

3.2.3 Hydrothermal Synthesis of G/TiO₂

G/TiO₂ nanocomposites were synthesised by employing a one-pot hydrothermal synthesis method. First, 20 mg of graphene obtained from Section 3.2.2 was dispersed into a mixture of 20 ml ethanol and 30 ml water by 1 hour of sonication. TTIP was added into the solution afterwards and sonicated for another hour. The addition of TTIP was carried out in a fume hood as TTIP fumes in air. After sonication, the solution was transferred to 50 ml Teflon-lined stainless-steel autoclave container and annealed in furnace at 130°C for 12 hours. When the heating process concluded, the solution containing G/TiO₂ in the container was then collected and transferred to centrifugal tubes and centrifuged for 15 minutes at 3500 rpm. The isolated solids were then washed twice with ethanol and twice with DI water. The precipitate was then dried in oven at 70°C overnight to obtain powder samples. The hydrothermal synthesis of G/TiO₂ is outlined in the schematic Figure 3.2.

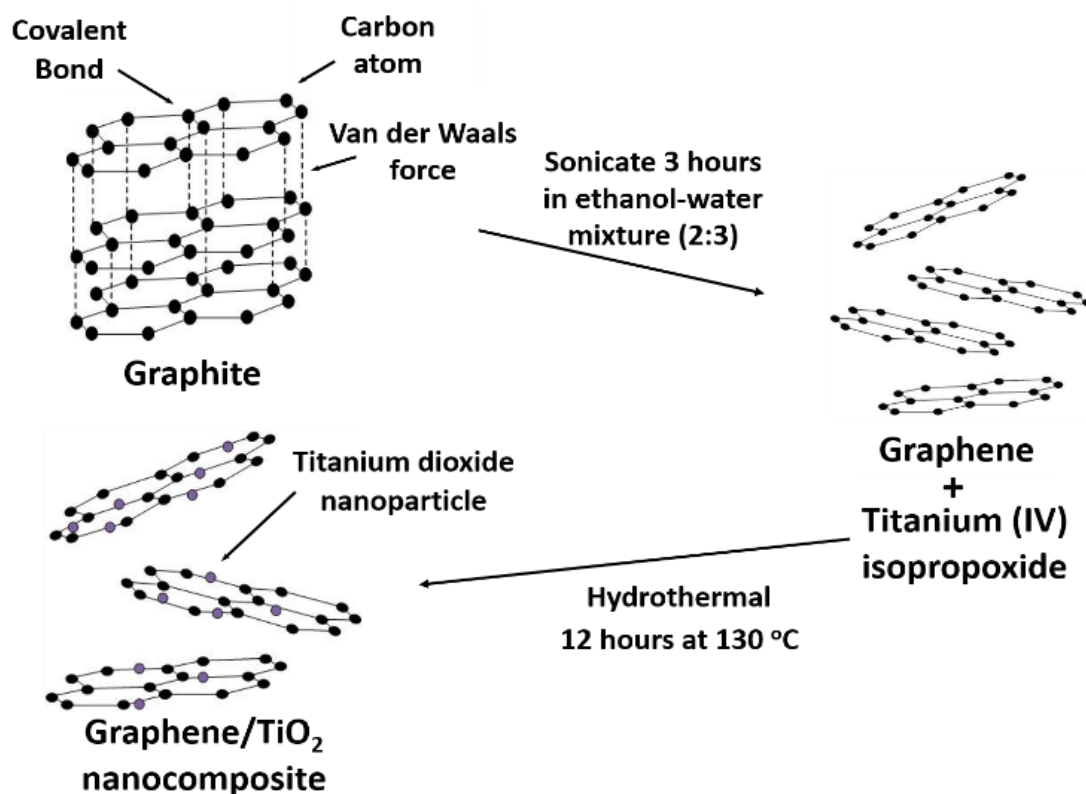


Figure 3.2. Schematic diagram illustrating the preparation of G/TiO₂ nanocomposites via a facile green hydrothermal synthesis.

When TTIP was added to the mixture, it reacted with water to form TiO₂ and propanol.

The reaction process can be expressed in the following equations:

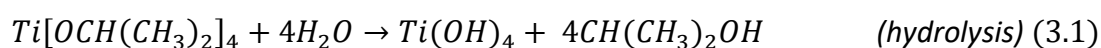


Table 3.1 shows detailed information of the different configurations of graphene to TTIP ratio which were used to synthesise the G/TiO₂ nanocomposites (1 μl of TTIP was

approximated to weigh 1 mg based on its density of 0.96 g/cm³). GTi1, GTi2, GTi3, GTi4, and GTi5 represent G/TiO₂ nanocomposite with ratios 1:1, 1:2, 1:4, 1:8, and 1:16 respectively.

Table 3.1. Different mass ratios of graphene to titanium dioxide precursor used to form G/TiO₂ nanocomposites.

Sample	Mass of graphene (mg)	Mass of TTIP (mg)	Mass ratio of graphene: titanium dioxide precursor
GTi1	20	20	1:1
GTi2	20	40	1:2
GTi3	20	80	1:4
GTi4	20	160	1:8
GTi5	20	320	1:16

3.2.4 Characterisation of the Materials

X-ray diffraction (XRD) was used to study the crystallographic structure of the materials. The X-ray diffractometer (X'pert Pro Powder, PANalytical) was used to conduct the analyses operated at a scanning rate of $0.02\theta \text{ s}^{-1}$ in a 2θ range of $10\text{-}80^\circ$ with Cu $K\alpha$ radiation ($\lambda = 1.54056 \text{ \AA}$).

A scanning electron microscope (SEM) (FEI Quanta-400 FESEM, 20 kV) was employed to observe the surface morphology and characteristics while an energy dispersive x-ray spectroscopy (EDX) (Oxford Instruments X-Max, 20 mm² detector) was conducted in conjunction with SEM to identify the chemical composition of the nanocomposites. The morphology of the nanomaterials was also studied using a transmission electron microscope (TEM, JEOL JEM-2100F) at an operating voltage of 200kV.

The electronic and structural properties of the graphene and G/TiO₂ nanocomposites were investigated using Raman spectroscopy. The Raman spectra of the powdered samples were recorded using a Renishaw (UK) inVia Raman microscope at room temperature ranging from 130 to 3000 cm⁻¹. The system was equipped with a charge coupled device (CCD) detector and holographic notch filter using a 514-nm diode laser excitation source with power below 0.5 mW.

3.3 Results and Discussion

3.3.1 Characterisation of the Materials

The X-ray diffractograms of the as-prepared G/TiO₂ nanocomposites, graphene, and TiO₂ are shown in Figure 3.3. As observed, the XRD patterns of the nanocomposites at different mass ratios are combinations of the patterns of both graphene and TiO₂, with different intensities. The XRD patterns attributed to TiO₂ in the nanocomposites are similar to that of pure TiO₂, indicating the absence of other impurity peaks. It can be indexed to the anatase phase of TiO₂ (ICSD No. 98-006-4230) with lattice constants $a = b = 3.7840 \text{ \AA}$, $c = 9.5000 \text{ \AA}$. The peaks at 2θ values, namely 25.3, 37.8, 48.0, 54.0, 55.1, 62.7, 68.8, 70.3, 75.1° can be identified as (1 0 1), (0 0 4), (2 0 0), (1 0 5), (2 1 1), (2 0 4), (1 1 6), (2 2 0), and (2 1 5) crystal planes, respectively. This suggests the complete formation of anatase nanoparticles from the precursor via the hydrothermal process. It was also observed that the increase in intensities of the corresponding diffraction peaks of the nanocomposites is a direct reflection of the mass loading increase of TiO₂. The diffraction peaks of graphite are identified as the (0 0 2) and (1 $\bar{2}$ 0) planes of graphite (ICSD No. 98-005-2916) at 2θ values 26.8 and 54.9°. The (1 $\bar{2}$ 0) peak of graphite is merged with the (2 1 1) peak of anatase in the nanocomposites due to their nearly identical 2θ values of 54.9° and 55.1°. The high intensity and narrow full width at half maximum (FWHM) of the graphite peak indicates that the crystallinity and the pristine nature of the graphene material were still intact. However, the anatase produced was of relatively lower crystallinity, as exhibited by the lower overall intensities and wider peaks. This might be desirable in the applications of biosensor in terms of production and safety, as high crystallinity of TiO₂ often involves complex

synthesis methods^{336, 337} and high temperature³³⁸, while having a higher cytotoxicity

339.

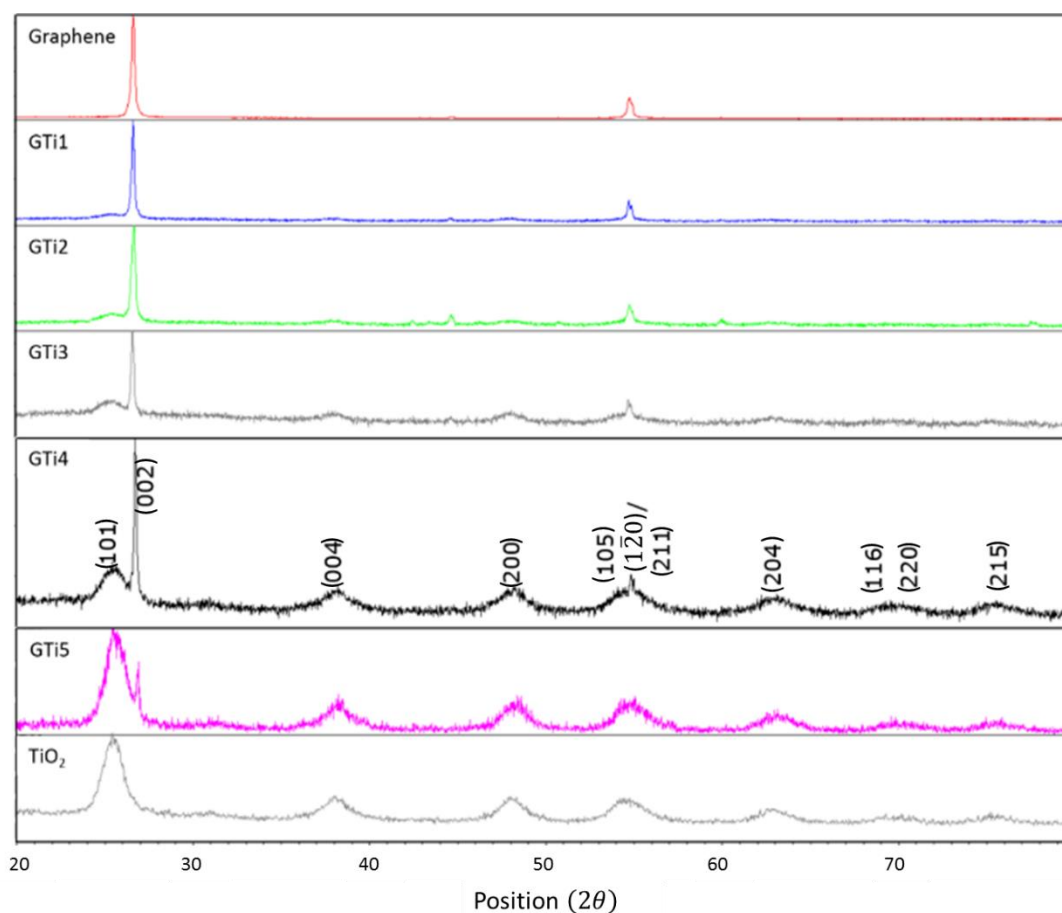


Figure 3.3. XRD patterns of graphite, TiO₂, and G/TiO₂ nanocomposites. Peaks indexed to both graphene and TiO₂ show a successful formation of G/TiO₂ nanocomposite.

SEM analysis on the as-synthesised nanomaterials showed the morphology of pristine graphene sheet (Figure 3.4a), and the increasing formation of TiO₂ nanoparticles on the surfaces and edges of graphene sheets with increasing mass loading of Ti precursor (Figure 3.4b-f). The TiO₂ nanoparticles were observed to be homogeneously covering the entirety of the graphene sheet for GTi4 (Figure 3.4e), before the formation of irregular heavy clusters (agglomeration) of the metal oxides at the highest mass loading of the precursor (Figure 3.4f). The absence of free TiO₂

nanoparticles outside of graphene sheets indicated the successful hybridisation of G/TiO₂ nanocomposite via the hydrothermal treatment.

The presence of C, Ti and O peaks on the EDX spectrum confirmed that the as-prepared samples were composed of carbon, titanium, and oxygen elements (Figure 3.4g). The presence of Si peak was attributed to the silicon substrate used for the characterisation. No other elements were observed from the spectrum, validating the purity of the as-synthesised nanocomposites.

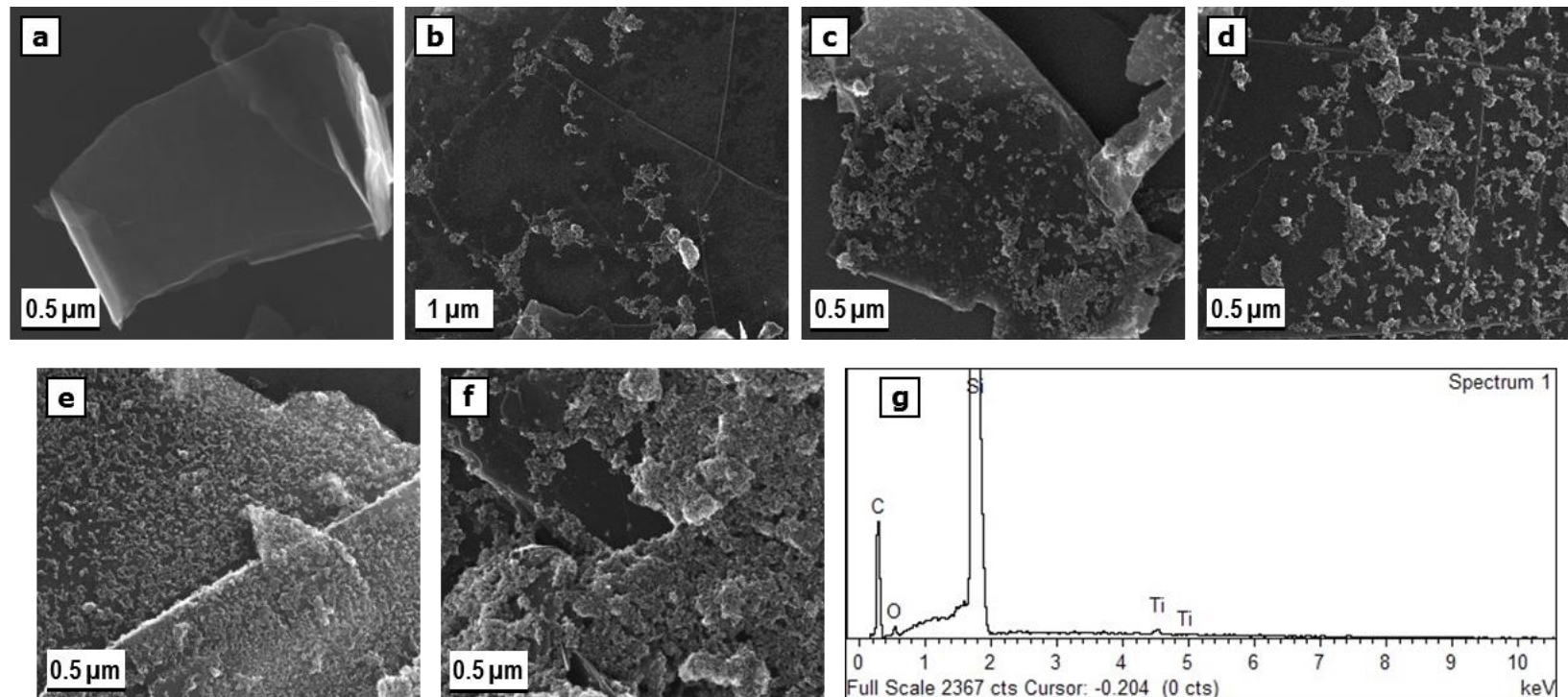


Figure 3.4. FESEM images of (a) Graphene, (b) GTi1, (c) GTi2, (d) GTi3, (e) GTi4, (f) GTi5, and (g) EDX spectrum of GTi4. No foreign elements indicated in the EDX spectrum except Si background, indicating the pristine quality of G/TiO₂ nanocomposites produced.

The surface morphology and crystal structure of the nanomaterials were further analysed using TEM. It can be seen that the graphene samples were film-like, demonstrating the successful facile exfoliation process (Figure 3.5a). Consistent with SEM results, TiO₂ nanoparticles were observed to be well-anchored onto the graphene surface and edges, with no free TiO₂ nanoparticles discerned outside of the graphene films (Figure 3.5c). The size of the nanoparticles is in the range of 6.8 to 13.1 nm and their distributions appear to be superimposed onto the transparent plate-like graphene surface, providing a good contact which likely leads to better conductivity. In the high resolution TEM image, lattice fringes with interplanar spacing of 0.35 nm and 0.34 nm, which corresponds to the (1 0 1) plane of anatase TiO₂, and the (0 0 2) plane of graphene from the XRD analysis respectively, are clearly observed (Figure 3.5d).

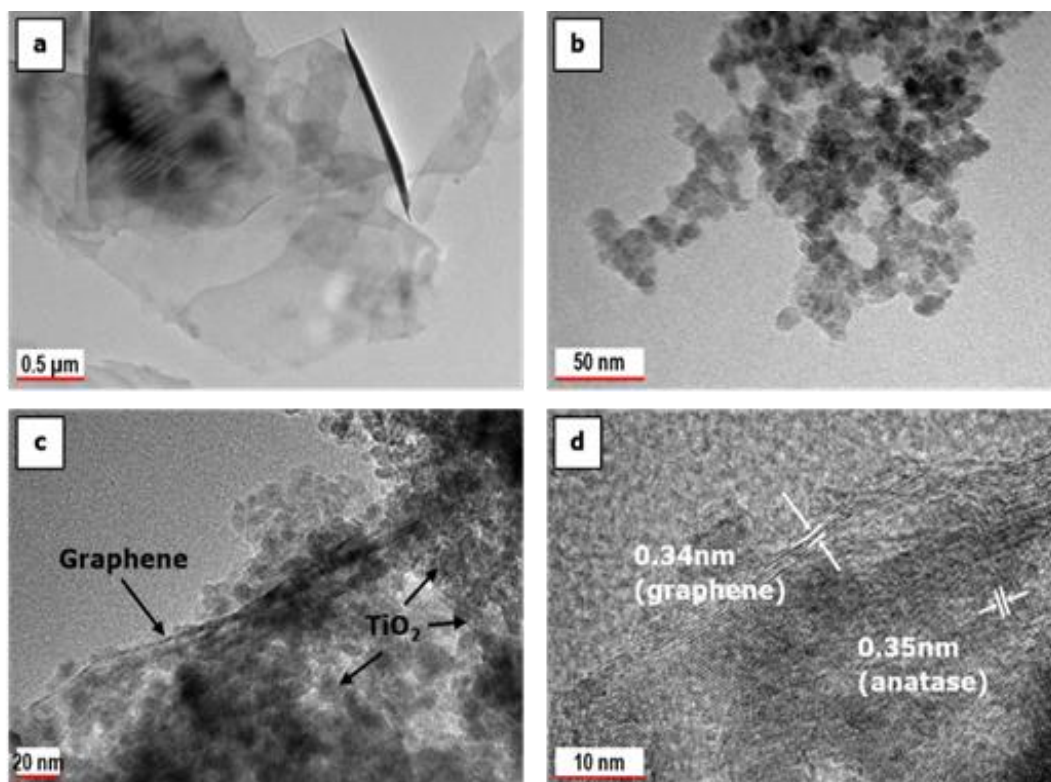


Figure 3.5. TEM images of (a) graphene, (b) TiO₂ nanoparticles, (c) G/TiO₂-nanocomposites (GTi4), and HRTEM image of (d) G/TiO₂ nanocomposite (GTi4).

Figure 3.6 shows the Raman spectra of graphene and G/TiO₂ nanocomposite materials. The Raman spectrum of graphene is characterised by its three distinctive vibrational bands, designated as the G band ('C-C bond stretching') at $\sim 1579 \text{ cm}^{-1}$, the D band ('disorder band') at $\sim 1350 \text{ cm}^{-1}$, and the 2D band ('multipeak feature') at $\sim 2715 \text{ cm}^{-1}$. These three vibrational bands are imperative, as detailed information on the as-produced graphene and its thickness can be acquired by studying the band's shape, peak position, and intensity^{340, 341}. The presence of the D band is caused by the defects formed during the exfoliation process of graphene from graphite^{193, 341, 342}. Upon incorporation with TiO₂, the Raman spectrum of the nanocomposite now exhibits additional peaks. The new Raman active modes are the two E_g modes at $\sim 150 \text{ cm}^{-1}$ and $\sim 645 \text{ cm}^{-1}$, B_{1g} modes at $\sim 413 \text{ cm}^{-1}$, and A_{1g}+B_{1g} modes at $\sim 520 \text{ cm}^{-1}$, respectively,

which are characteristics of anatase TiO_2 ^{34, 343}. The slight shifting of the G band and 2D band to $\sim 1587 \text{ cm}^{-1}$ and $\sim 2725 \text{ cm}^{-1}$ respectively was most likely caused by the doping effects of TiO_2 on the graphene sheets ³⁴⁴. The Raman spectrum further confirms the successful synthesis of G/ TiO_2 nanocomposites, and the structure of graphene flakes remained intact after hydrothermal treatment.

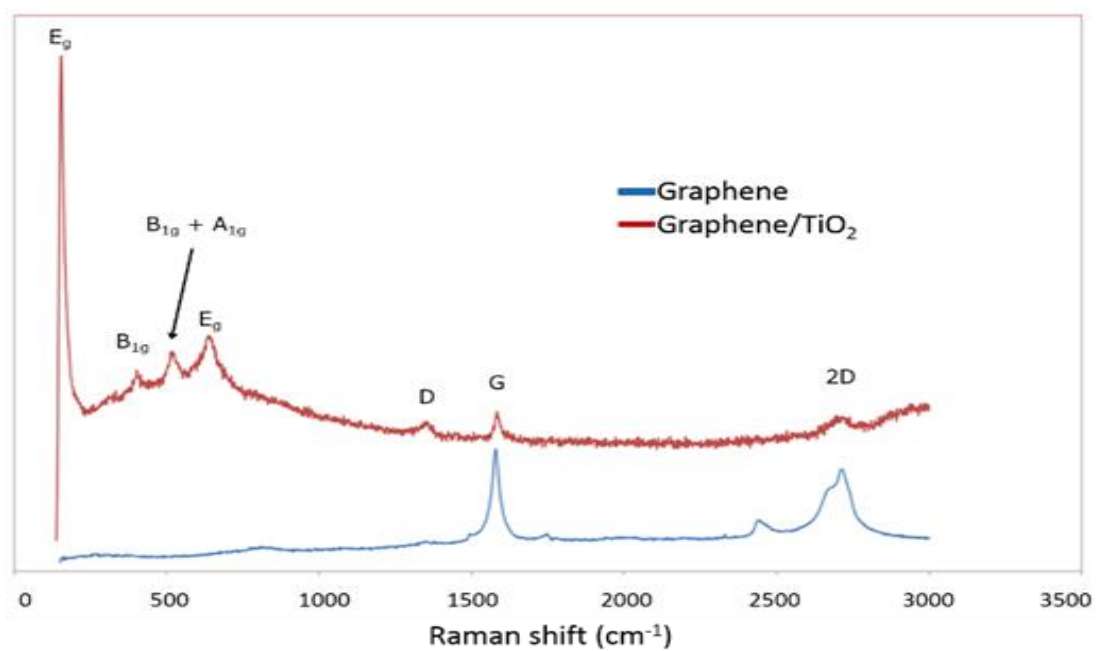


Figure 3.6. Raman spectra of graphene and G/ TiO_2 nanocomposite. Raman spectrum of G/ TiO_2 nanocomposite (GTi4) shows additional TiO_2 peaks along with the original graphene peaks.

3.3.2 Electrochemical Response of Modified Electrodes towards

Potassium Ferricyanide

To compare the electrochemical performance of the as-prepared nanomaterials, cyclic voltammetry (CV) analysis were conducted at a scan rate of 50 mV/s in 0.1 M PBS (pH 7.4) within the potential range of -0.4 to 0.8 V, using 0.5 mM potassium ferricyanide as the redox active probe (Figure 3.7). All CV responses showed peak currents in pairs of anodic peak potential (E_{pa}) at approximately 0.2 V and cathodic peak potential (E_{pc}) at approximately 0.0 V. The formal peak potential (E^0) was found to be at around 0.1 V. The electrochemical responses were quite consistent for all modifications, with only slight shifting in some electrodes. The CV was conducted in triplicates and the peak currents showed acceptable RSD values of 0.3 to 3.2% for every modification. In general, modified electrodes exhibited improvement in current response when compared to bare electrodes. As observed, GTi4 modified electrodes exhibited the best electrochemical response, attaining the highest anodic peak current (I_{pa}) and the lowest cathodic peak current (I_{pc}) of 6.92 μ A and -7.94 μ A, respectively. Lower current response was observed for GTi5, which is likely due to agglomeration of TiO₂ nanoparticles at higher mass loading, forming a less conductive layer onto the graphene surface, thus reducing the surface area accessible to the electrolyte ions. Accordingly, GTi4 was used in all subsequent analyses.

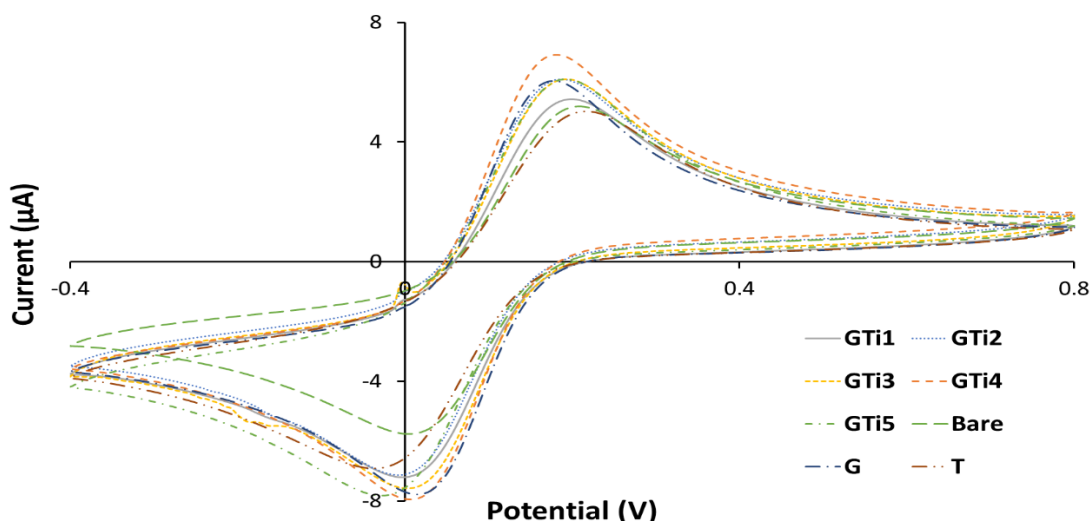


Figure 3.7. CVs of 0.5 mM potassium ferricyanide on bare SPCE (Bare), graphene-modified SPCE (G), TiO₂-modified SPCE (T), and G/TiO₂-modified SPCE (GTi1, GTi2, GTi3, GTi4, GTi5) in 0.1 M PBS (pH 7.4). Scan rate, 50 mV/s. GTi4 exhibits the best electrochemical response.

EIS is an important analytical tool that can be used to characterise the electrical properties of a substance by measuring the impeded flow of ions through solutions, interfaces and coatings, enabling researchers to assess the resistive characteristics of the electrode³⁴⁵. One of the most prominent ways to interpret the EIS data is by using a Nyquist plot where each data point is at a different frequency. In a typical Nyquist plot, the imaginary component of the impedance (Z'') is plotted against the real component of the impedance (Z'). These plots typically consist of a semi-circular portion at high frequencies representing the electron transfer occurring at the electrode/electrolyte interface, and a linear straight line portion at low frequencies representing the diffusion of ions in the electrode material³⁴⁶. From the analysis, the solution resistance R_{sol} can be obtained from the x-intercept at the start of the semicircle arc and the charge transfer resistance R_{ct} can be directly measured as the diameter of the semicircle arc on the x-axis³⁴⁷. EIS analysis were carried out on the modified electrodes in 0.1 M PBS buffer with 10 mM potassium ferricyanide as the

electrochemical probe. 100 mV amplitude of sine voltage signal was applied to the three-electrode-system under open circuit potential (OCP), and the frequency varied from 10 Hz to 1 MHz. The impedance test was conducted in triplicates for each electrode and the average values of R_{ct} obtained from the Nyquist plots (Figure 3.8) are tabulated in Table 3.2. The relative standard deviation (RSD) calculated from the experiments was found to be between 0.5% and 3.8%. As observed, G/TiO₂ nanocomposite-modified electrode exhibited the lowest R_{ct} values, demonstrating improved charge transfer characteristic compared to its individual counterparts. The results obtained from both CV and EIS evidently affirms the advantageous synergistic effect between graphene and TiO₂.

Table 3.2. Charge transfer resistance R_{ct} and solution resistance R_{sol} of the electrodes.

SPCE	R_{ct} (Ω)
Bare	2212.60
Graphene-modified	1886.70
TiO₂-modified	1911.20
G/TiO₂-modified (GTi4)	1525.90

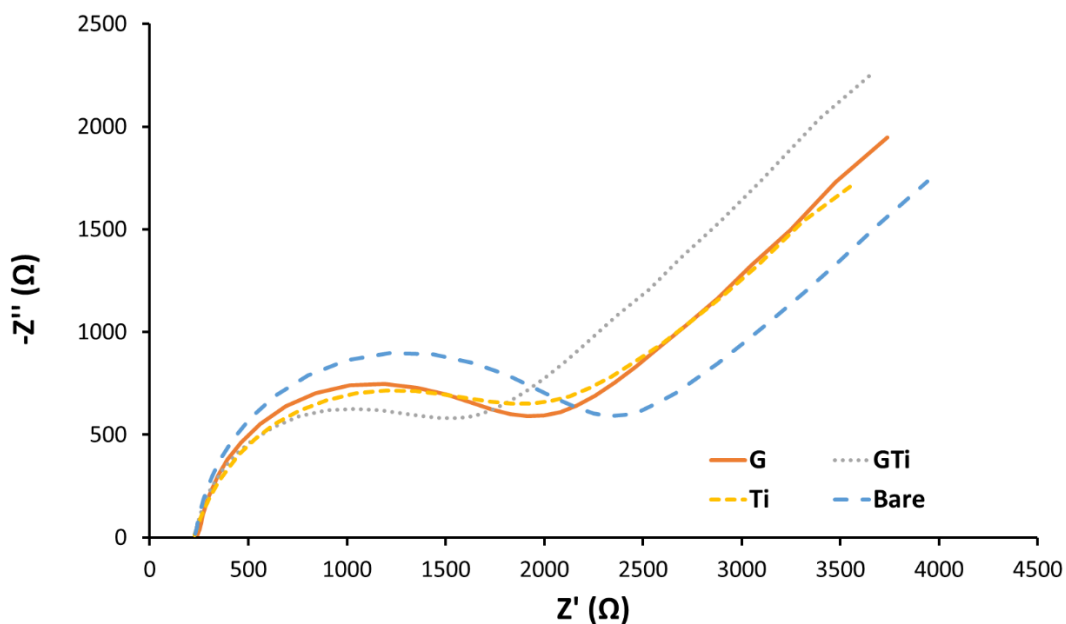


Figure 3.8. Nyquist plots for bare SPCE, graphene-modified SPCE, TiO₂-modified SPCE, and G/TiO₂-modified SPCE. G/TiO₂-modified SPCE shows the least resistance among all 4.

3.3.3 Electrochemical Response of Modified Electrodes towards H₂O₂

The CV responses of bare electrode, graphene-modified electrode, TiO₂-modified electrode, and G/TiO₂-modified electrode towards 0.5 mM of H₂O₂ in 0.1 M PBS are compared in Figure 3.9. It can be observed that G/TiO₂-modified SPCE had the best electrochemical response out of all four. The nanocomposite-modified SPCE showed significant increase in the anodic peak current (0.83 μA) compared to the response in bare SPCE (0.43 μA). The enhanced electrochemical properties of the nanocomposites could be attributed to the large surface area-to-volume ratio of the graphene, the porous nature of TiO₂ providing more active sites for analytes to diffuse, and the synergistic effect between graphene and TiO₂ facilitating electron transfer³⁴⁸. Another possible factor contributing to the fast electron transfer and electrocatalytic activity of the nanocomposites is the edge plane defects that open up during the

hydrothermal synthesis process of G/TiO₂, which further increases the surface area of the synthesised nanocomposite ²⁶⁹.

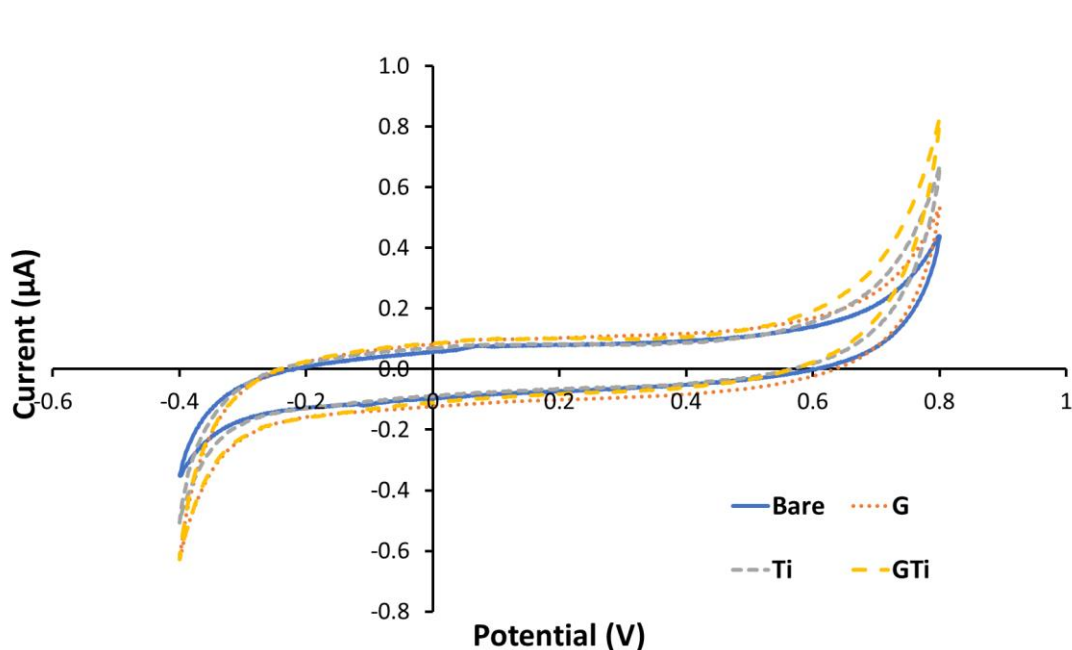


Figure 3.9. CVs of 0.5 mM H₂O₂ on bare SPCE, graphene-modified SPCE, TiO₂-modified SPCE, and G/TiO₂-modified SPCE in 0.1 M PBS (pH 7.4). Scan rate, 50 mV/s. G/TiO₂-modified electrode displays the best performance. GTi4 was used in this analysis.

Figure 3.10 shows the cyclic voltammograms recorded for G/TiO₂-modified SPCE by varying scan rates from 25 to 200 mV/s. The CV curves have the same form with peak currents occurring at the same voltage regardless of the applied voltage. Additionally, the overall current responses were observed to increase with increasing scan rate. This is due to dependency of the size of the diffusion layer above the electrode surface towards applied scan rate. Generally, the size of the diffusion layer will grow larger at lower scan rates, as compared to higher scan rates, resulting in smaller flux towards the electrode. Thus, as current is proportional to the flux towards the electrode, the overall current response will decrease at lower scan rate and vice versa.

As described by the Randles-Sevcik equation (Equation (3.3)), in any Nernstian system (reversible system), where it's chemically reversible and a controlled diffusion electrochemical process, the peak current (i_p) is always linearly proportional to the scan rate (v)³⁴⁹.

$$i_p = (2.69 \times 10^5) n^{1.5} A D^{0.5} C v^{0.5} \quad (3.3)$$

Where at 25 °C, i_p is the peak current (A), n is the electron stoichiometry, A is the electrode area (cm^2), D is the diffusion coefficient ($\text{cm}^2 \text{s}^{-1}$), C is the concentration (mol cm^{-3}), and v is the scan rate (V/s)

As observed, the linear proportionality is apparent for both anodic and cathodic peak currents, with correlation coefficients, R^2 of 0.9645 and 0.9891, respectively (inset, Figure 3.10). This suggests that the reaction is a diffusion controlled process, confirming that the measurements obtained correlate to surface confined reactions at the electrode³⁵⁰.

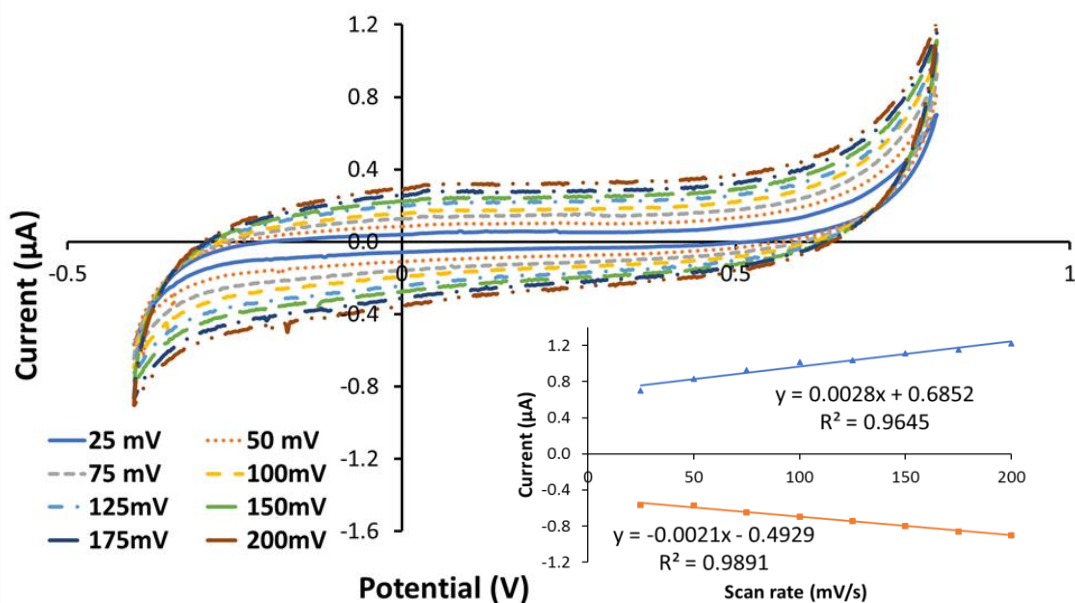


Figure 3.10. (i) CVs of 0.5 mM H_2O_2 on G/TiO_2 -modified SPCE in 0.1 M PBS (pH 7.4) at different scan rates. The scan rate from inner to outer are 25, 50, 75, 100, 125, 150, 175, 200 mV/s, respectively; (ii) peak currents versus scan rates (inset). Linear proportionality can be observed for both anodic and cathodic peak currents.

3.3.4 Amperometric Detection of H₂O₂

Amperometry is a common electrochemical technique used to characterise the performance of a biosensor. The sensor's electrocatalytic activity towards the analyte was evaluated by measuring the change in electric current at a fixed potential. In this study, the electrochemical performance of the as-synthesised G/TiO₂ was assessed by subjecting the nanocomposite-modified electrode to a real time amperometric analysis to verify the nanomaterial's potential in biosensing. The working potential was fixed at -0.4 V, while aliquots of 1 mM H₂O₂ were dispensed into the PBS buffer every 50 seconds successively. The stirring speed was kept low to prevent excessive baseline drift. Results showed that upon successive additions of H₂O₂, the proposed sensor platform exhibited a fast response time of <5 s and linear response range between 1-15 mM with correlation coefficient, R² = 0.985 (Figure 3.11 and inset). The sensitivity of the modified electrode was found to be 0.557 μA/mM and the limit of detection (LOD) was calculated as 56.89 nM, using the following equation where σ is the standard deviation of signal generated by the blank.

$$LOD = \frac{3\sigma}{Slope} \quad (2.1)$$

The performance of this H₂O₂ the proposed sensor is comparable to other similar work reported elsewhere (Table 3.3).

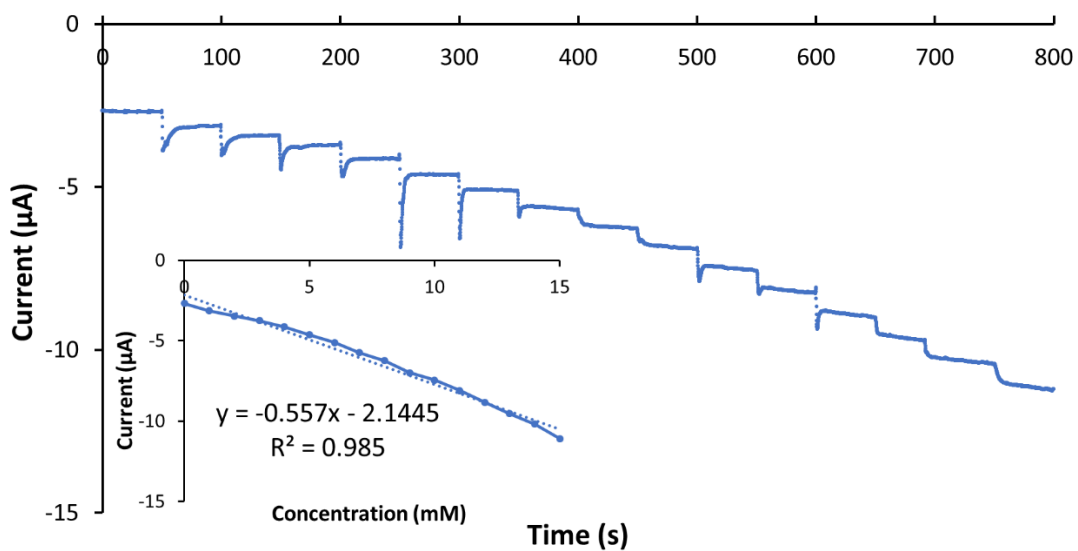


Figure 3.11. Real time amperometric response of G/TiO₂-modified electrode for successive additions of H₂O₂ ranging from 1 to 15 mM in 0.1 M PBS at a fixed potential of -0.4 V. The sensitivity of the modified electrode was found to be 0.557 µA/mM and the limit of detection (LOD) was calculated as 56.89 nM.

Table 3.3. Comparison between the performance of the proposed G/TiO₂-modified electrode on H₂O₂ detection against H₂O₂ biosensors fabricated from other materials.

Electrode modification	LOD	Sensitivity	Reference
Graphene and TiO ₂ on carbon electrode	56.89 nM	0.557 μA/mM	This work
Graphene on carbon electrode	-	0.022 μA/mM	¹⁹³
Multi-wall carbon nanotubes (MWCNT) modified gold electrode	-	0.059 μA/mM	³⁵¹
MWCNT/silver nanoparticle nanohybrids on gold electrode	5 × 10 ⁻⁷ M	1.42 μA/mM	³⁵¹
Copper nanoparticles (CuNPs)-reduced graphene oxide (rGO) nanocomposite on glassy carbon electrode	0.601 mM	-	³⁵²

The selectivity of the biosensor against possible interfering species commonly found in real samples was further investigated via real time amperometric test. As the H_2O_2 determination mechanism in the proposed sensor is non-enzymatic, the operating potential is vital in improving the biosensor's selectivity. The low working potential of -0.4 V was selected to minimise the otherwise significant interferences from well-known electroactive species with redox potentials close to H_2O_2 , such as ascorbic acid (AA) and uric acid (UA). After achieving a stable baseline, $1\text{ mM H}_2\text{O}_2$, 1 mM AA , 1 mM UA , 1 mM glucose , $1\text{ mM H}_2\text{O}_2$, were successively added into the system (0.1 M PBS , $\text{pH} = 7.4$), respectively. Negligible responses were observed for UA and glucose, while significantly lower response ($\sim 36\%$ of the response generated by the same amount of H_2O_2) was observed for AA interferent (Figure 3.12). AA is advised to be avoided in the operation of this biosensor at the selected working potential for accurate determination of H_2O_2 .

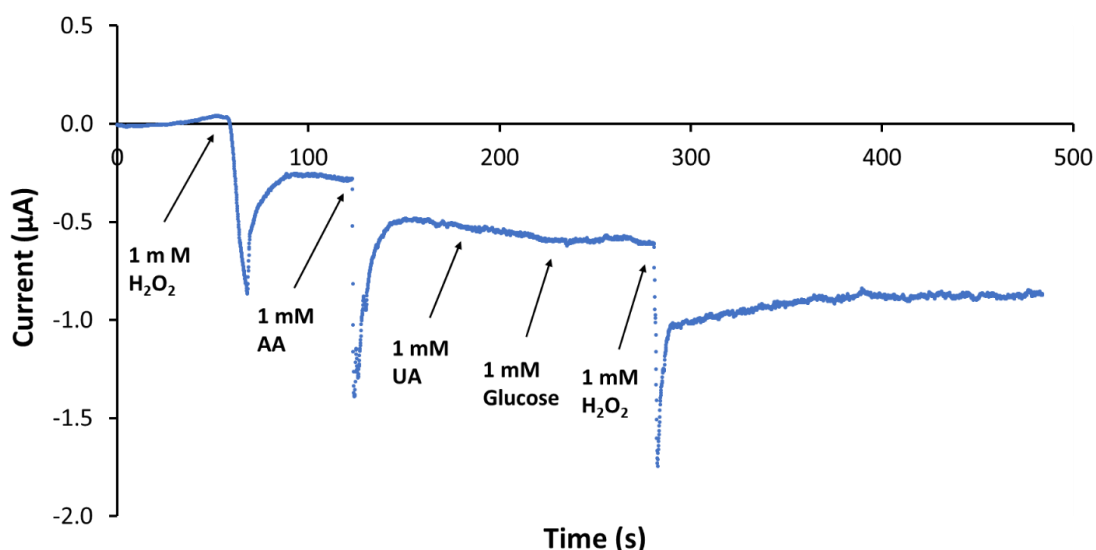


Figure 3.12. Real time amperometric response of G/TiO_2 -modified electrode for successive additions of $1\text{ mM H}_2\text{O}_2$, 1 mM AA , 1 mM UA , 1 mM glucose , $1\text{ mM H}_2\text{O}_2$ into 0.1 M PBS at fixed potential of -0.4 V .

3.4 Chapter Summary

In this chapter, G/TiO₂ nanocomposites were successfully synthesised from highly pyrolytic graphite and titanium (IV) isopropoxide via a green, facile, effective route which is also economic and scalable. The structural and electrochemical characterisations of the G/TiO₂ nanocomposites were studied comprehensively. Modifying the screen-printed carbon electrode with the nanocomposite had proven to enhance the electrochemical response, compared to both bare SPCE, TiO₂-modified SPCE and graphene-modified SPCE. The nanocomposite with the weight ratio of 1:8 (graphene: titanium precursor) showed the best responses. Real time amperometric response of the modified electrode demonstrated its ability to detect H₂O₂ reliably, upon addition of H₂O₂ at increasing concentration from 1 to 15 mM. The sensitivity of the sensor was 0.557 μA/mM with an LOD of 56.89 μM. The biosensor showed good response towards H₂O₂ with minimal to no response against other interferences, indicating great potential of the graphene/TiO₂ nanocomposite to be utilised as the core electrode material for the future development of high-performance biosensor.

Chapter 4: Simple One Step Exfoliated Graphene Flakes as Potential Electrochemical Immunosensing Platform for Dengue Diagnosis

4.1 Overview

Dengue, an arthropod-borne viral disease affecting human which is transmitted by *Aedes* mosquitoes, mainly *Stegomyia aegypti* (previously *Aedes aegypti*) mosquitoes²⁸⁵, is currently endemic in over 100 countries worldwide²⁷⁴, with more prevalent cases found in the subtropical and tropical zones. An estimate by World Health Organisation (WHO) in 2012 reports that there are up to 390 million dengue fever cases annually, with approximately 3.9 billion people are at risk of dengue infections worldwide. The disease is caused by the dengue virus (DENV), which is a member of the *Flavivirus* genus within the *Flaviviridae* family. DENV is classified into four antigenically related but genetically distinctive serotypes, namely DENV-1, DENV-2, DENV-3 and DENV-4. The infection by any serotype will provide long term immunity against the specific serotype, but only temporary and limited immunity to other serotypes²⁷⁹. It is challenging to apply differential diagnosis based on symptoms after infection as dengue presents wide-ranging symptoms, from asymptomatic to severe illness that may lead to death if not managed properly. The manifestation of the disease is according to three distinct clinical symptoms: Dengue fever (DF), which is a febrile illness reaching 40 °C accompanied with other symptoms such as headache, nausea, vomiting, pain behind the eyes, muscle and joint pains, swollen glands or a characteristic rash; dengue haemorrhagic fever (DHF) or severe dengue, a potentially

deadly complication from DF due to plasma leaking, fluid accumulation, respiratory distress, severe bleeding, or organ impairment; and dengue shock syndrome (DSS), where DHF leads to extremely low blood pressure and circulatory collapse (shock). Epidemiological studies have reported that the risk of DHF and DSS is increased with incidence of secondary infection with different serotypes³⁵³. Till date, there is yet an effective and reliable cure or vaccine for dengue. Although the world's first dengue vaccine, Dengvaxia® was launched in December 2015, the adoption rate was low due to unconvincing safety and efficacy profiles³⁵⁴. Early and effective detection of dengue disease is thus critical for better disease management and outbreak control, which essentially reduce the morbidity and mortality rates.

Current laboratorial diagnostic methods for dengue include virus isolation, viral nucleic acid detection, antigen detection, and serological tests, all of which possess clear drawbacks²⁸². Virus isolation and nucleic acid detection via reverse transcriptase polymerase chain reaction (RT-PCR) require sophisticated laboratory facilities and highly trained professionals, where complicated and time-consuming procedures are involved, effectively limiting their usage as routine diagnostic procedures. On the other hand, conventional assays for antigen detection and serological tests such as the popular IgM antibody-capture enzyme-linked immunosorbent assay (MAC-ELISA), are plagued by subpar sensitivities and antigenic cross reactivity with other infections, thus limiting their clinical applications. Hence, there is a clear and urgent need for alternative methods to provide rapid infectious disease diagnosis, facilitating effective disease treatment and management.

Electrochemical biosensors are promising alternatives compared to conventional molecular detection approaches, due to their advantages such as simplicity, low power, low cost, rapid response and ease of miniaturisation. The fabrication process of the electrode platform containing three electrode system is simple and low cost, while the transducer, the key component that translates electrochemical data to meaningful results for analysis, is also straightforward and inexpensive, involving only electronics components, compared to other biosensors such as surface plasmon resonance (SPR)-based biosensors which require fibre optics to function. Among the many measurement methods applicable on electrochemical biosensors, electrochemical impedance spectroscopy (EIS) holds great promise to be exploited as a tool for studying biorecognition events at the electrode surface by measuring the impeded flow of ions through solutions and interfaces, providing insight on the interfacial changes ³⁵⁵. In the recent years, several electrochemical biosensor platforms had been developed for dengue detection, albeit with different strategies. Researchers have successfully developed biosensors with the ability to detect DENV particles ^{306, 309}, DENV RNA ³⁵⁶, and DNA sequences ^{307, 357, 358}. Some researchers investigated on the detection of dengue non-structural protein 1 (NS1), a glycoprotein secreted by infected cells which has been shown to be a useful biomarker for the detection of dengue infection ^{359, 360}. These platforms usually immobilise anti-NS1 antibodies on the electrode surface to detect the NS1 protein molecules in samples ^{311, 361, 362}. There are also researchers who opted for the serological approach, where NS1 was immobilised as the probe and IgM or IgG antibodies became the target analyte ^{311, 314}. While the results reported were favourable, some potential issues persist for these NS1-based immunosensors as NS1 proteins of all flaviviruses have

been reported to exhibit high degree of homology^{315, 316}, causing concerns in probable misdiagnosis. An alternative option for antigenic probe in serological detection was found to be the envelope glycoprotein domain III (EDIII) of the dengue virus (DENV)³¹⁸. The envelope (E) glycoprotein of the DENV is composed of three domains (I, II, and III) where domain III was found to be highly antigenic³⁶³. The potential of EDIII as antigenic determinant for serological diagnostic purposes has been verified through the successful development of EDIII-based enzyme-linked immunosorbent assay (ELISA) assays for the detection of dengue antibodies^{317, 321-323}. The results showed high specificity, presenting no cross-reaction to antibodies from the similarly structured flavivirus, yellow fever (YF)³²¹, compared to the cross reactivity found in the NS1-based Panbio ELISA assay towards antibodies of Japanese encephalitis (JE) and YF viruses³²⁴. The EDIII-based approach was proposed to have a high specificity, as exhibited by the specific detection of West Nile virus infection³²⁵ and tick-borne encephalitis virus infection³²⁶, even when tested against other closely related flavivirus infections.

While already known for their good sensitivities, the performance of electrochemical biosensors could be further improved with the incorporation of nanomaterials on the biosensor¹¹. Notably, graphene offers a unique two dimensional (2D) environment for fast electron transport and high surface to volume ratio that are known to enhance the electrochemical catalytic activity of biosensors, which leads to enhanced sensitivity and signal amplification¹⁹⁻²¹. Graphene also holds a very high prospective in the application of sensitive bioanalytical protocols because of its ability to allow easy and reliable immobilisation of biomolecules²³. This unique tuneable property of

graphene makes it a suitable nanomaterial to be employed in the development of the dengue immunosensor.

In this work, a highly sensitive graphene based electrochemical biosensor for the detection of anti-DENV antibodies is proposed, where a consensus envelope glycoprotein domain III (cEDIII) that reacts to all 4 serotypes of DENV, is selected as the antigenic probe to be immobilised on the sensing platform. Pristine graphene was synthesised from a novel sono-assisted liquid phase exfoliation method¹⁹³ while the cEDIII was obtained via plant-based molecular pharming via *Nicotiana benthamiana* tobacco plant³⁶⁴ which offers excellent scalability and safety advantages. It is important to note that the conventional methods for the acquisition of antigens are usually arduous, expensive, and unfit for mass production as they either involve antigen extraction from the brains of artificially infected new born mice or the expression cloning of the antigens via microorganisms³¹⁷. The synthesis pathways of the key components (graphene and cEDIII) are simple, economic, efficient, and easily scalable; ensuring that the eventual production costs of the immunosensor to be relatively low when compared to other immunoassay solutions. The immunosensing platform was optimised on various parameters, which include graphene mass loading, probe concentration and immobilisation time, and target hybridisation time. Using the optimised biosensing approach, the as-developed immunosensor was subjected to a series of tests to determine its sensitivity and detection limits for the detection of DENV IgG. The selectivity of immunosensor was evaluated against antibodies from different viral species including the Zika flavivirus IgG which is known for its high homogeneity with DENV IgG. The sensor platform was also tested for its feasibility to detect the presence of DENV IgG in immunised mouse serum.

4.2 Experimental Details

4.2.1 Materials

Graphite flakes (99% carbon purity) were purchased from Bay Carbon (Michigan, USA), ethanol was obtained from Merck (New Jersey, USA). Phosphate buffered saline (PBS) tablet, potassium ferricyanide, 1-pyrenebutyric acid N-hydroxysuccinimide ester (PSE), and skim milk powder were purchased from Sigma Aldrich (St. Louis, USA). Avian influenza H5N1 neuraminidase polyclonal antibody and dengue virus type 1-4 (DENV 1-4) monoclonal antibody (anti-dengue primary antibody) were purchased from Thermo Fisher Scientific (Massachusetts, USA). Infectious bursal disease virus (IBDV) polyclonal antibody, horseradish peroxidase (HRP)-conjugated anti-mouse secondary antibody, and 3, 3', 5, 5'-tetramethylbenzidine (TMB) ELISA substrate were obtained from Abcam (Cambridge, United Kingdom). Chicken anaemia viral protein 3 (VP3) monoclonal antibody was purchased from TropBio (Sydney, Australia). Zika virus (ZIKV) envelope protein antibody was purchased from Genetex (California, USA). The screen-printed carbon electrodes (SPCE) were purchased from DropSens (Spain), consisting a three-electrode configuration which comprise of carbon working electrode (4 mm diameter), carbon reference electrode and silver reference electrode.

Both cEDIII protein and mouse sera were provided by Professor Sandy Loh (The University of Nottingham Malaysia, Selangor, Malaysia) in kind. The production of cEDIII protein and mouse sera is briefed as following: The cEDIII protein in fusion to cholera toxin B subunit (CTB) was expressed in plant-based system (*Nicotiana benthamiana*) and purified by immobilised metal affinity chromatography (IMAC)²⁹⁴,

^{327, 364}. CTB fusion makes the plant-made cEDIII protein highly stable and long-lasting³⁶. On the other hand, a group of healthy female BALB/c mice was bled to collect serum samples prior to any immunisation procedure and named as blank serum (G1). The purified cEDIII protein at 20 µg dosage and 1 mg of Alum adjuvant (Sigma, Germany) were injected into another group of female BALB/c mice via the intraperitoneal route on day 0 and day 14. The mouse sera were then collected from these BALB/c mice 28 days after the prime immunisation and thereafter referred as immunised serum (G2).

4.2.2 Fabrication of Graphene-modified Electrodes

The graphene nanomaterial was synthesised as reported in Chapter 3, Section 3.2.2. For fabrication of the graphene-modified electrode, the as produced, graphene powder was re-dispersed in 2:3 ethanol-water mixture to form a 1 mg/mL suspension. After rinsing the SPCE with DI water, graphene suspension was drop-casted onto the working electrode surface of SPCE and air-dried. The electrodes were washed with deionised water prior to electrochemical measurements to remove impurities.

4.2.3 Fabrication of Immunosensing Platform

The as-synthesised graphene was homogeneously dispersed via sonication in ethanol-water (2:3) mixture to form a 1 mg/mL suspension. 1-pyrenebutyric acid N - hydroxysuccinimide ester (PSE) was added into the suspension in the ratio of 1:4 graphene to PSE ratio, and further sonicated for 30 minutes, allowing the π - π stacking of PSE onto the surface of graphene sheet to occur¹⁹⁶. The G/PSE suspension was then washed with DI water and subjected to centrifugation at 3000 rpm for 30 minutes to remove unbound PSE molecules. After removing the supernatant, the remaining

G/PSE composite was re-dispersed in a mixture of ethanol-water (2:3 ratio). The G/PSE suspension was then drop-casted on the working electrode of SPCE and left to dry.

G/PSE-modified SPCE was first rinsed with DI water and soaked in PBS for 15 minutes for conditioning purposes. For the immobilisation of cEDIII antigenic probe onto the SPCE, 5 μ L of diluted cEDIII solution was deposited on the G/PSE-modified SPCE and left for incubation under room conditions. The incubation was then terminated, and the electrode was rinsed with DI water, before introducing 50 μ L of blocking buffer (0.1% skim milk in PBS) onto the SPCE and left for 10 minutes. The modified SPCE was washed in PBS prior to electrochemical measurements.

As the probe immobilisation and blocking steps were completed, the hybridisation of the target (DENV 1-4 IgG antibodies) was performed by incubating 5 μ L diluted target stock solution onto the working electrode. The incubation was terminated by washing the SPCE with DI water and PBS, before subjecting to electrochemical measurements.

Figure 4.1 illustrates the assembly steps involved in the fabrication of the as-proposed DENV immunosensor.

The immunosensing platform was finally tested against mouse sera to verify its reliability on non-commercial samples.

4.2.4 Enzyme-linked Immunosorbent Assay (ELISA)

In-house ELISA was used to validate the detection of DENV IgG using EDIII probe antigen. Commercial primary anti-dengue antibodies (DENV 1-4 IgG) were diluted to different dilutions (1:1000, 1:2000, 1:4000, 1:8000, 1:16,000, 1:32,000, 1:64,000) and tested to obtain a standard curve for calibration purpose. The optical density (OD)

values, a reflection of DENV IgG concentration, for mouse sera were obtained from blank (G1) and immunised (G2) groups as described in 4.2.1.

Stock cEDIII antigen (1.5 mg/mL) was produced from plant-based expression approach³⁶⁴, and was diluted to 2 µg/µL with 1X PBS buffer (NaCl, Na₂HPO₄, KH₂PO₄, KCl, pH 7.0). Briefly, immunoplate was coated with 100 µL of diluted cEDIII along with coating buffer (NaHCO₃, Na₂CO₃, pH 9.5) overnight at 4°C. The solutions were discarded, and wells were washed thrice with 200 µL of washing buffer (1X PBS buffer + 0.05% Tween 20) after each incubation step. The protein binding sites were saturated with 200 µL of blocking buffer (5% skim milk in PBS) at room temperature for 1 hour. After washing, 100 µL of primary antibodies (mouse sera) at respective dilutions were added into the wells and incubated at 37°C for 1 hour. Mouse sera were obtained from two groups of mice: G1 serving as a negative control and G2 as a positive sample. Both groups of mouse sera were diluted with blocking buffer in the following concentrations: G1 in 1:25 and G2 in 1:50,000. The secondary anti-mouse antibodies (100 µL) were added into the immunoplate and incubated for 1 hour at room temperature. The immunoplate was then washed 5 times with washing buffer. TMB substrate (100 µL) was added into wells and enzymatic activity was allowed for 20 minutes. One hundred microliter of stop solution (1M phosphoric acid) was added and the optical density (OD) was determined at the wavelength of 450 nm. This absorbance was measured by Epoch Microplate Spectrophotometer (Biotek, USA).

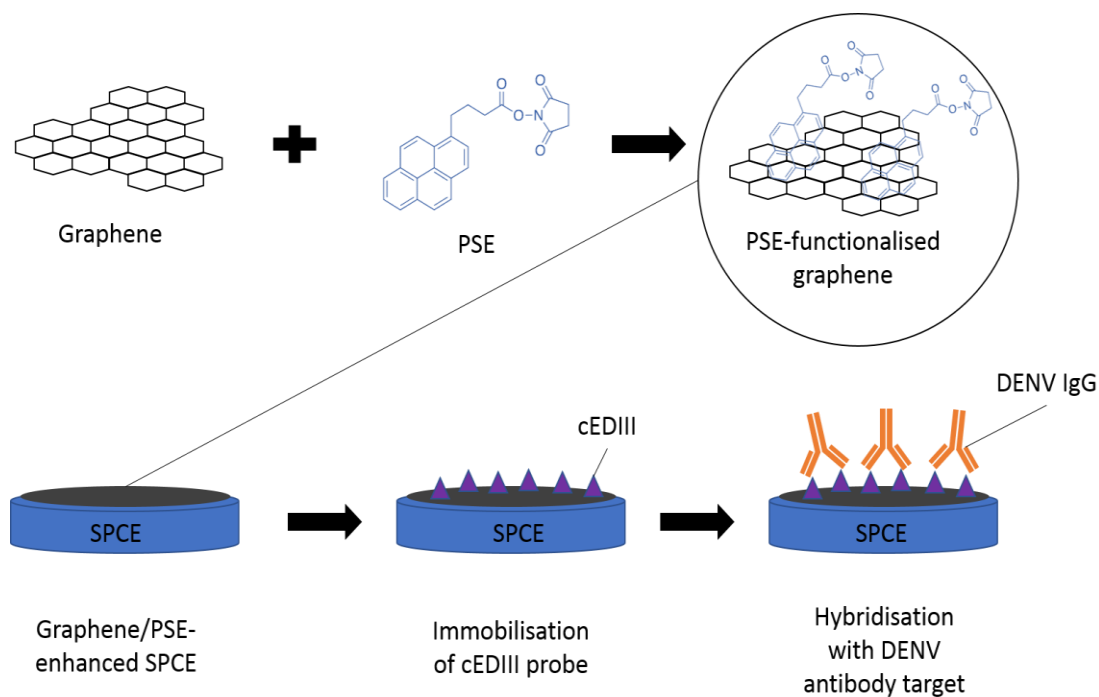


Figure 4.1. Schematic diagram for the development of graphene/PSE-modified electrochemical immunosensor for dengue detection.

4.2.5 Electrochemical Characterisation of Immunosensor Platform

The electrochemical analyses were performed using Autolab PGSTAT III potentiostat (Metrohm, Netherlands) interfaced with controlling software NOVA 1.10. All the electrochemical measurements were performed at room temperature ($27 \pm 1^\circ\text{C}$). Cyclic voltammetry (CV) measurements were performed on the as-prepared biosensor in 20 mL of 10 mM PBS buffer with 10 mM $\text{K}_3[\text{Fe}(\text{CN})_6]$ as the electrochemical probe covering the three electrodes' area, from potential ranging from -0.4 V to 0.6 V at a scan rate of 50 mV/s for 10 cycles. Impedance spectra were recorded from EIS analysis with a voltage amplitude of 100 mV in a frequency range from 0.1 Hz to 10 kHz under open circuit potential (OCP). All electrochemical analyses were conducted in triplicates.

4.3 Results and Discussion

4.3.1 Optimisation of Graphene Mass Loading on Sensor Platform

To establish a biosensing platform with low baseline for improved sensitivity, the optimum graphene deposition amount on the SPCE was determined. Different volumes of as-synthesised graphene suspension (1 mg/mL) were drop-casted onto the SPCE, denoted as G01, G02, G03, G04, and G05 (1 μL , 2 μL , 3 μL , 4 μL and 5 μL). The equivalent mass loadings of graphene were calculated using Equation 4.1 below:

$$\text{Mass loading} = \frac{\text{Volume} \times \text{Concentration}}{\text{Surface area}} \quad (4.1)$$

where the surface area of the working electrode is 0.1257 cm^2 . Accordingly, the graphene mass loadings of the modified electrodes (G01, G02, G03, G04, and G05) are estimated as 7.96 $\mu\text{g}/\text{cm}^2$, 15.91 $\mu\text{g}/\text{cm}^2$, 23.87 $\mu\text{g}/\text{cm}^2$, 31.83 $\mu\text{g}/\text{cm}^2$, and 39.78 $\mu\text{g}/\text{cm}^2$, respectively. The electrochemical responses of the modified electrodes were compared via CV analysis (Figure 4.2a). The anodic peak potential (E_{pa}) and cathodic peak potential (E_{pc}) of bare electrodes were found to be 0.23 V and -0.05 V, respectively, with a peak separation (ΔE_{p}) of 0.28 V. With the addition of graphene, the E_{pa} shifted to the left while the E_{pc} shifted to the right, causing a decrease in the interpeak distance. The ΔE_{p} decreased gradually with increasing graphene mass loading, with lowest peak separation of 0.22 V for G04. The low ΔE_{p} indicates high redox reversibility and Nernst equilibrium can be achieved more easily with faster electron transfer rate, suggesting the excellent electrochemical performance of G04.

The current responses recorded from the electrodes showed good consistency, with low RSD values of 0.5 to 4.2%. In general, graphene-modified electrodes exhibited

improvement in current response when compared to bare electrodes. The current response increased with increasing mass loading of graphene with G04 exhibiting the best electrochemical response, attaining the highest anodic peak current (I_{pa}) and the lowest cathodic peak current (I_{pc}) of 98.81 μA and -120.86 μA , respectively. However, further increased in graphene mass loading (G05), resulted in lower current response. This is likely due to the agglomeration of graphene and reverting to graphite, resulting in lower surface area and slower electron transfer kinetics.

The electrochemical properties of the modified electrodes were further investigated with EIS measurements. Nyquist plots obtained from EIS measurements (Figure 4.2b) were used to analyse the response of the electrodes in the frequency domain, where the diameter of the semicircle on the real axis indicates the charge transfer resistance (R_{ct}) between the electrode and electrolyte interfaces. As measured R_{ct} represent the insulating characteristic of the electrode/electrolyte interface, it is directly affected by the modification of the electrode surface. Average values of R_{ct} were collected over triplicates of data, with RSD between 0.6 to 6.7%. Generally, the addition of graphene had improved the conductivity of the electrode, as discerned from lower R_{ct} values as compared to bare electrode. The R_{ct} values of the electrodes were observed to decrease with increasing mass loading of graphene, with G04 having the lowest R_{ct} of 1012.48 Ω . However, further increased in mass loading result in higher R_{ct} as observed for G05 (1449.33 Ω).

Herein, the findings from CV and EIS experiments affirmed that G04 exhibited the best electrochemical performance with fastest electron transfer and thus, was used for subsequent analyses.

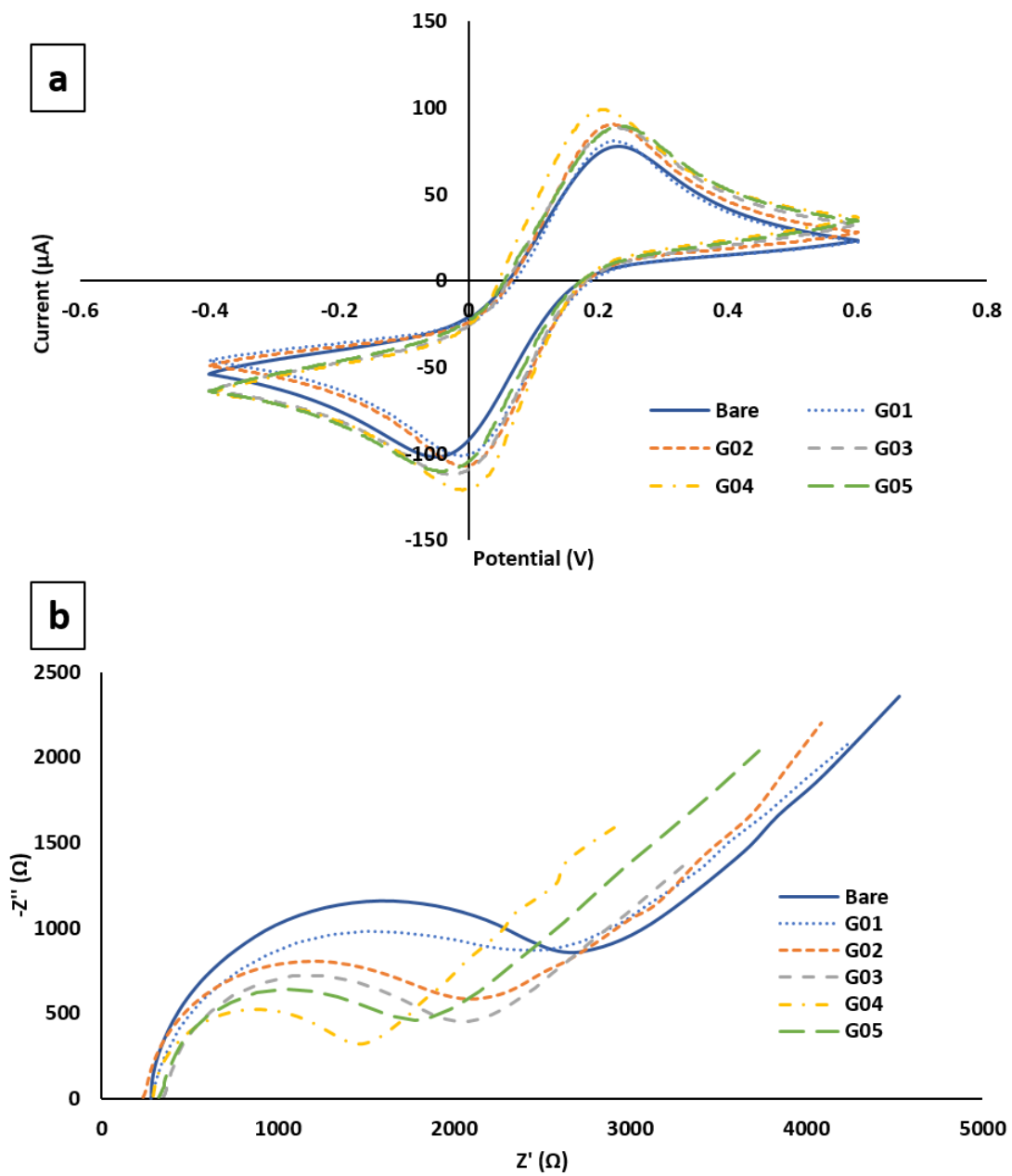


Figure 4.2. CVs (a) and Nyquist plots (b) obtained from electrodes with increasing mass loading of graphene. G04 exhibits the best electrochemical response.

4.3.2 Electrochemical Characterisation of Biosensor Platform

The stepwise fabrication of the proposed biosensor was characterised using CV and EIS with $[\text{Fe}(\text{CN})_6]^{3-/4-}$ as the active redox probe. In this work, PSE was used as a bi-linker to anchor the probe protein (cEDIII) molecules onto the graphene nanomaterials loaded on the working electrode of the SPCE. The highly aromatic pyrenyl group of PSE interacts strongly with graphene via π - π interaction while the succinimidyl fragment is reactive to nucleophilic substitution by primary and secondary amines that are found on the surface of most biological molecules including cEDIII^{365, 366}. The immobilised cEDIII protein would in turn enable hybridisation between cEDIII and DENV IgG antibodies due to antigen-antibody reaction.

From the CV analysis (Figure 4.3a), two distinct redox peaks were observed for graphene-modified electrode at E_{pa} of 0.22 V and E_{pc} of 0.00 V, with a ΔE_p of 0.22 V. Upon functionalisation with PSE bio-linkers, significant decrease in the peak currents was observed. In addition, the oxidation and reduction peaks respectively shifted more positively and negatively, increasing ΔE_p to 0.27 V. These observations indicate slower electron transfer rate, likely due to the hydrophobic nature of PSE, forming a physical barrier that increased the overpotential of the redox process and impeded the flow of electrons on the electrode surface²⁰⁸. Successive modifications with cEDIII probe and skim milk solution as blocking agent, also resulted in further decrease in redox peak currents and slight shift in ΔE_p , ascribed to the electron transfer hindering effects of both insulative protein layers. Upon introduction of target DENV 1-4 IgG onto the immunosensor platform, notable decrease in redox peak currents was also observed, resulted from the formation of insulative cEDIII-IgG immunocomplexes

layers on the electrode surface. From the EIS analysis, the increase in R_{ct} value for each subsequent modification step, in the order of G/G/PSE/G/PSE/cEDIII/G/PSE/cEDIII/milk/G/PSE/cEDIII/milk/IgG was observable (Figure 4.3b). The increase in R_{ct} indicates interfacial changes on the sensor platform with formation of more insulative layers upon each successful modification step. This amplifies the electrical resistivity of the electrode surface against the diffusion of redox probes, which also corresponds to the continual decrease in redox peak currents as discerned from the CV analysis. As such, the results obtained from both CV and EIS analyses evidently affirmed the successful development of the immunosensing platform for the detection of DENV1-4 IgG.

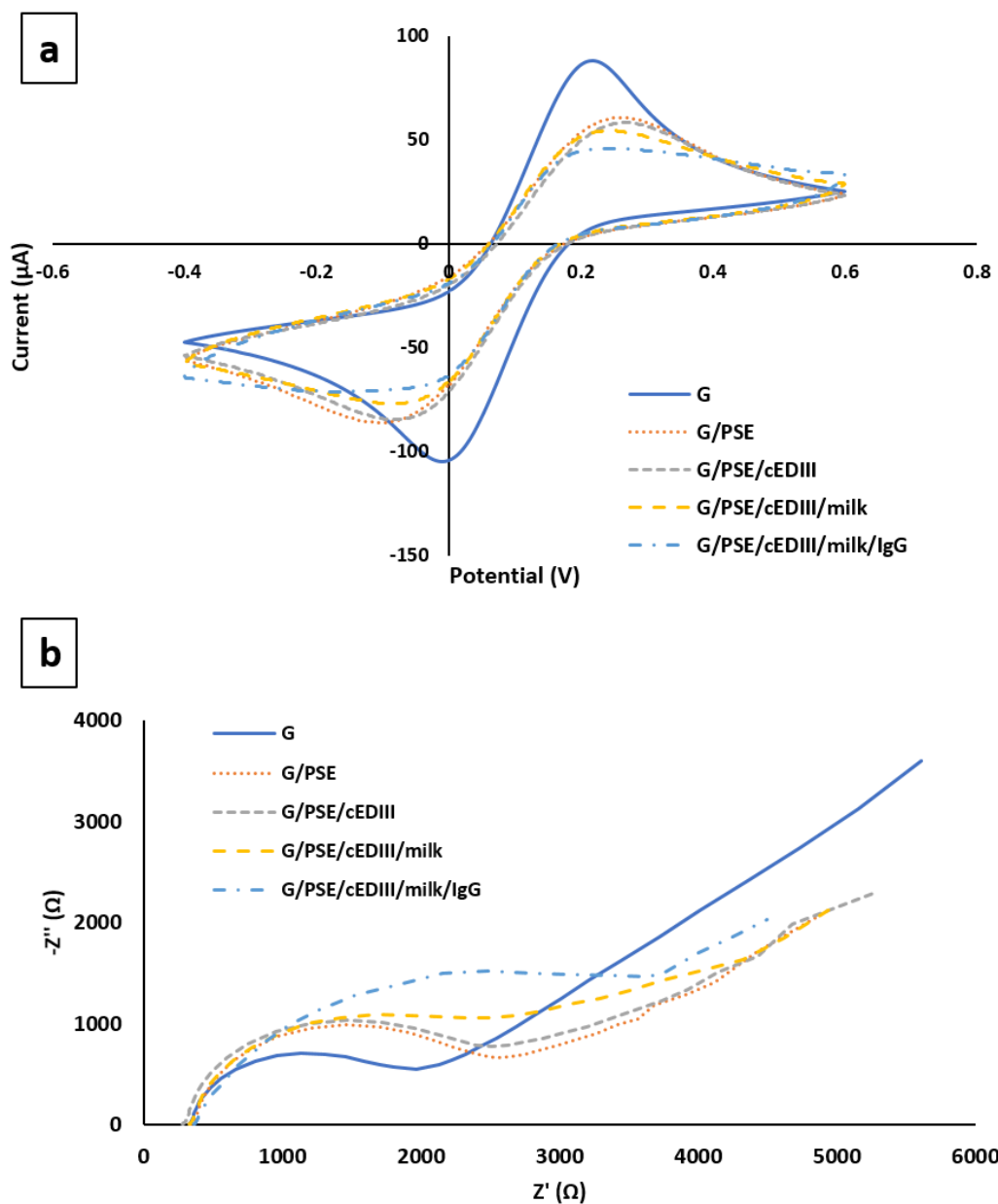


Figure 4.3. a) CV measurements of G, G/PSE, G/PSE/cEDIII, G/PSE/cEDIII/milk, G/PSE/cEDIII/milk/IgG. Conductivity reduces as elements on SPCE increases. b) Nyquist plot of G-modified SPCE, G/PSE, G/PSE/cEDIII, G/PSE/cEDIII/milk, G/PSE/cEDIII/milk/IgG. Impedance value increases as elements on SPCE increases.

4.3.3 Optimisation of Biosensor Platform

In biosensor development, it is important to ensure that the amount of probes immobilised on the electrode platform is not too densely packed or vice versa, to ensure effective detection of targets. Generally, the amount of immobilised probe will be influenced by the probe concentration used and the immobilisation time allowed. In addition, probe-target hybridisation time will also affect the sensing performance of the platform due to the time needed for the probe and target molecules to achieve binding equilibrium. As such, for optimal sensing performance, the influence of parameters was evaluated by monitoring the change in charge transfer resistance (R_{ct}) before and after target hybridisation. Different concentrations of cEDIII (1 $\mu\text{g/mL}$, 5 $\mu\text{g/mL}$, 10 $\mu\text{g/mL}$, 25 $\mu\text{g/mL}$ and 50 $\mu\text{g/mL}$) were immobilised onto the SPCE, and their effects on DENV 1-4 IgG detection were evaluated. In order to correct for electrode-to-electrode or film-to-film variation, the normalized value of R_{ct} (relative R_{ct}) was applied instead of absolute R_{ct} to evaluate the signal response. Relative R_{ct} or $\Delta R(\%)$ is calculated in percentage using the following equation:

$$\Delta R(\%) = \frac{\Omega_{antibody} - \Omega_{blank}}{\Omega_{blank}} \times 100 \quad (4.2)$$

where $\Omega_{antibody}$ is the impedance value of electrode after the formation of cEDIII-IgG immunocomplex (G/PSE/cEDIII/milk/IgG) and Ω_{blank} represents the impedance value of electrode before any addition of the antibodies (G/PSE/cEDIII/milk). A higher $\Delta R(\%)$ value indicates a larger number of immunocomplexes formed, suggesting the platform's ability to capture more antibody, hence, better performance.

In this optimisation step, both incubation periods of cEDIII and DENV 1-4 IgG antibody were fixed at 30 minutes. As observed in Figure 4.4a, the $\Delta R(\%)$ increased from 47.9%

to 56.2% when cEDIII concentration was increased from 1 $\mu\text{g}/\text{mL}$ to 5 $\mu\text{g}/\text{mL}$. However, insignificant changes in ΔR (%) was observed for concentration above 5 $\mu\text{g}/\text{mL}$, suggesting that sufficient amount of cEDIII had been immobilised to provide optimal signal response upon detection of DENV IgG. As such, 5 $\mu\text{g}/\text{mL}$ of cEDIII was used for subsequent analyses work.

To determine the optimum incubation time for the immobilisation of cEDIII, the immobilisation step was carried out at different durations (15, 30, 45, 60, 90 minutes). As incubation time increased from 15 to 30 minutes, ΔR (%) increased from 36.7% to 56.3% upon target hybridisation. Further prolongation in duration did not result in improved signal response, with ΔR (%) values ranging between 54.6% to 56.4% (Figure 4.4b). As such, 30 minutes is chosen as the optimal immobilisation period for subsequent analyses. The short immobilisation period compared to overnight incubation in ELISA assays could be largely contributed by the PSE covalent immobilisation instead of passive adsorption in ELISA.

Similarly, optimisation on target hybridisation time was conducted by incubating the target antibody with varying periods from 15 to 90 minutes at optimised probe concentration and immobilisation time. As shown (Figure 4.4c), ΔR (%) continually increased from 50.1% to 67.1% at prolonged probe-target hybridisation time and achieved saturation at 60 minutes with insignificant improvement at 90 minutes (67.7%). The saturated signal suggests complete hybridisation of target antibody with available cEDIII probe anchored on the sensing platform. Thus, considering assay time and sensitivity, 60 minutes was chosen as the optimum hybridisation time.

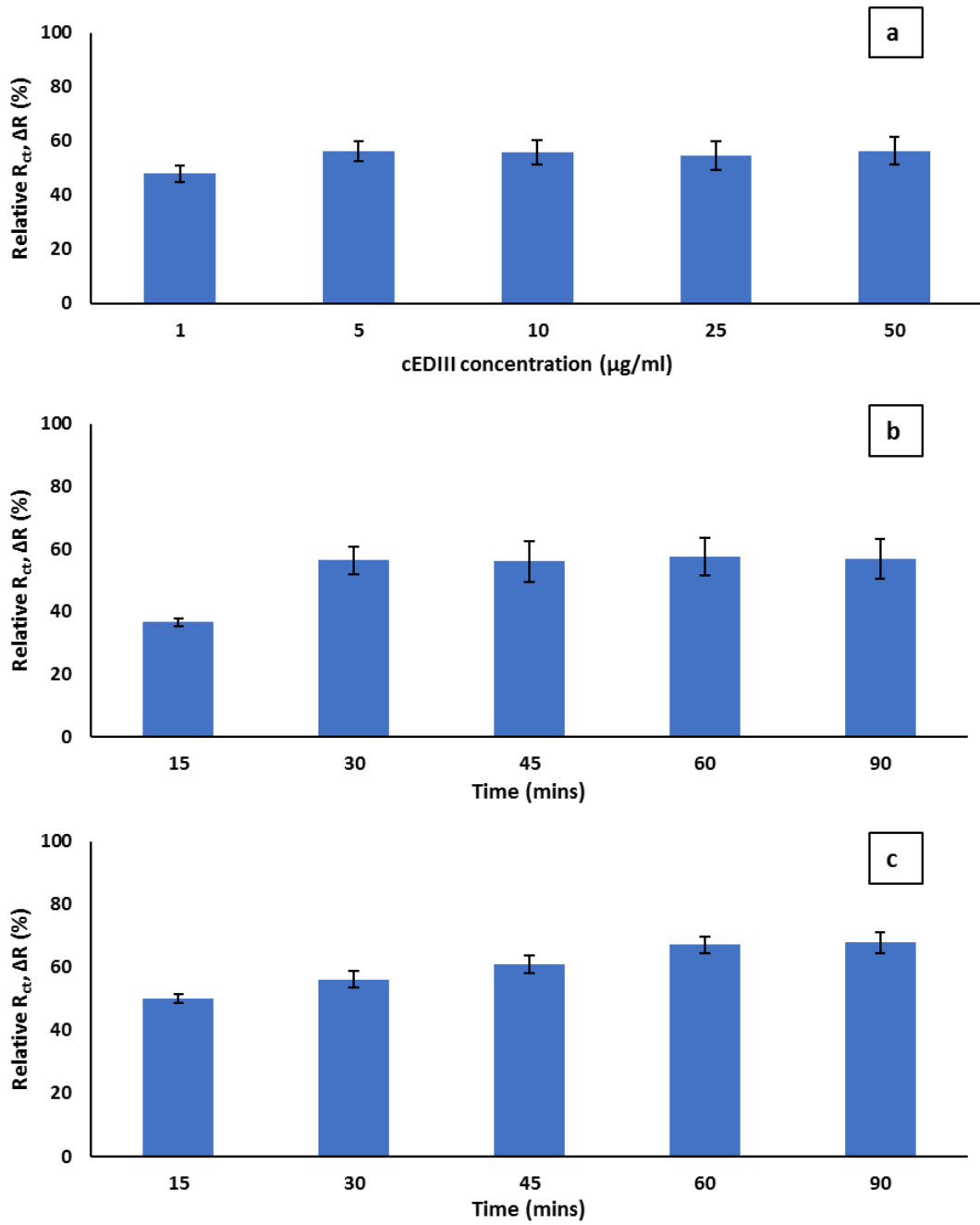


Figure 4.4. Effects of a) cEDIII probe concentration, b) cEDIII probe immobilisation time, and c) target antibody hybridisation time on relative R_{ct} , ΔR (%). The optimum cEDIII probe concentration and immobilisation time were found to be 5 $\mu\text{g/ml}$ and 30 minutes, respectively. The optimised target hybridisation time was 60 minutes.

4.3.4 Analytical Performance of the Biosensor Platform

Under optimised conditions, the performance of the immunosensor was evaluated by incubating the immunosensing platform with DENV IgG at different dilutions ranging from 1:500 to 1:32000 (4 ng/mL to 62.5 pg/mL). The results are shown in Figure 4.5, and a calibration curve was obtained by plotting $\Delta R(\%)$ against the logarithmic value of DENV IgG concentrations (Figure 4.5 inset). The $\Delta R(\%)$ values were found to be escalating with increasing concentrations of DENV IgG. This could be due to the abundance of DENV IgG molecules at higher DENV IgG concentrations promoting the binding of DENV IgG molecules onto the immobilised cEDIII molecules on the immunosensing platform. The increase in formations of cEDIII-IgG immunocomplexes resulted in more resistive deposited layers, causing hindrance in the interfacial charge transfer. From the calibration graph, the linear working range of the immunosensor was found to be from IgG concentration of 62.5 pg/mL to 1 ng/mL, and the limit of detection (LOD) for DENV IgG of the immunosensor was determined to be 5.58 pg/mL. The linearity can be represented by the equation below with an R^2 -value of 0.9952:

$$\Delta R (\%) = 5.8622 + 14.444 * \log [\text{DENV IgG}] (\text{pg/mL}) \quad (4.3)$$

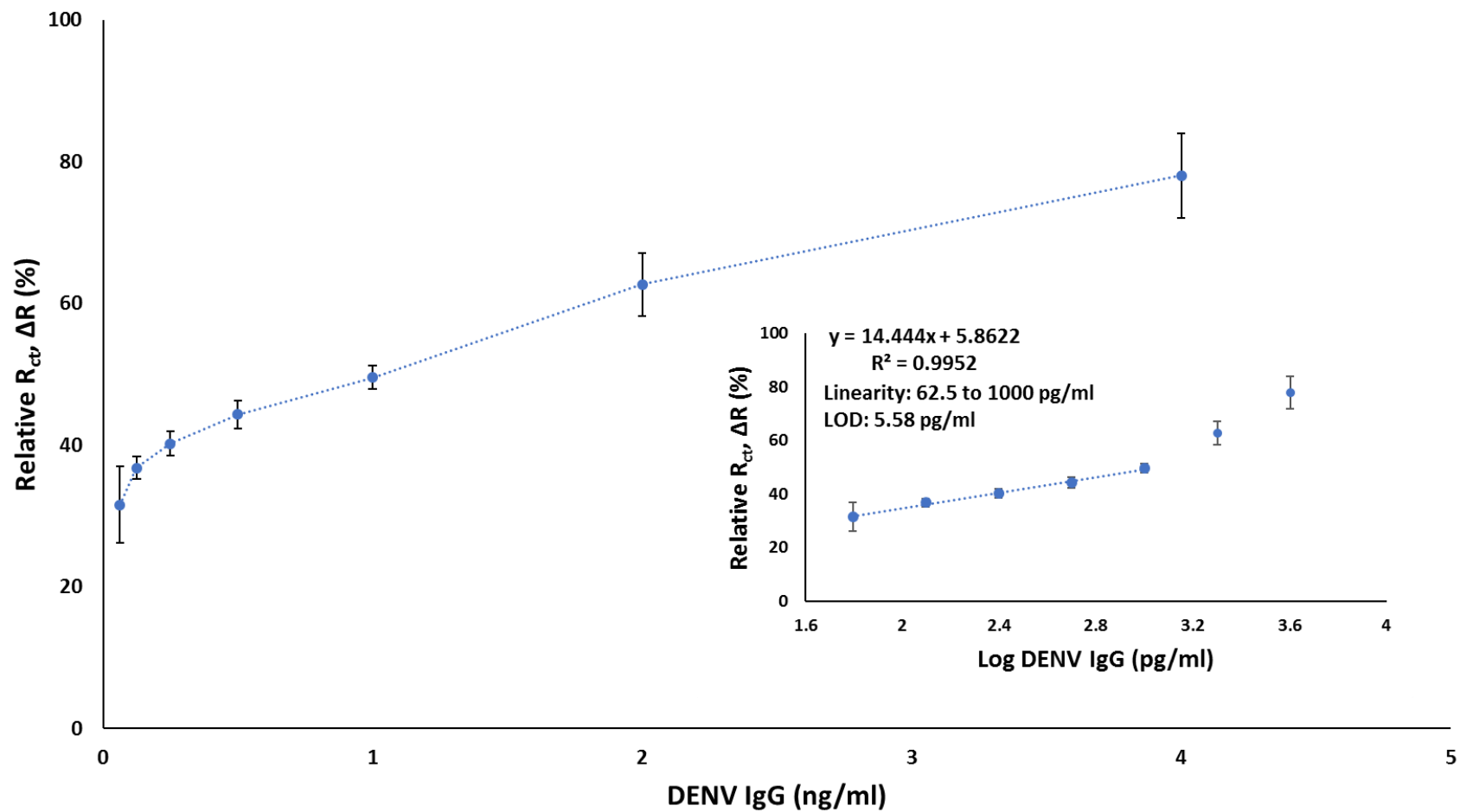


Figure 4.5. Analytical measurement curve obtained for DENV IgG detection of the proposed sensor, using relative R_{ct} , ΔR (%) as function of DENV IgG concentration. Inset shows the corresponding calibration plot of the immunosensor.

4.3.5 Specificity Study of the Biosensor Platform

The specificity of the proposed sensor was evaluated against antibodies of avian influenza A virus (H5N1), infectious bursal disease virus (IBDV), chicken anaemia virus (CAV), and Zika virus (ZIKV). Among these infectious diseases, there is great interest to differentiate DENV and ZIKV due to their high resemblances in many ways. ZIKV is a flavivirus transmitted by *Aedes* mosquitoes, has the similar structure and epidemiology, and brings similar symptoms of fever, skin rashes, conjunctivitis, muscle and joint pain, malaise, and headache ³⁶⁷. Hence differentiating DENV and ZIKV infections is often difficult. The immunological cross-reactivity caused by the high degree of sequence and structural homology also proved to be a challenge for the researchers to tackle in the development of new diagnostic measures ³⁶⁸. The specificity tests were carried out by replacing DENV IgG antibody with the antibodies above in the target hybridisation step. As illustrated in Figure 4.6, the immunosensor exhibited good selectivity, reflected by significantly lower R_{ct} responses (<34%) against other viral antibodies. These findings indicate the potential of the proposed immunosensor platform to discriminate DENV from other viruses, including ZIKV. The ability to differentiate DENV from ZIKV in particular, is highly valuable as currently available NS1-based dengue diagnostic kits were reported to have cross-reactivity issues towards closely related flaviviruses such as ZIKV ^{369, 370}. The study conducted by Felix *et. al.* has proved that currently available popular commercial anti-dengue immunoassays exhibits cross-reactivity with anti-Zika antibodies at certain degrees, some even reaching positivity as high as 68.8% ³⁷⁰.

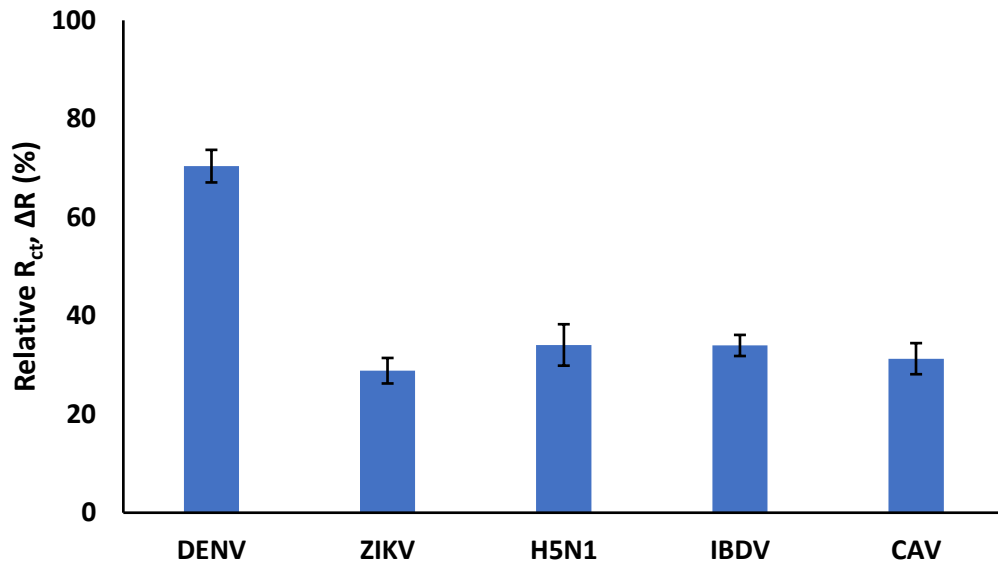


Figure 4.6. Response of immunosensor to antibodies raised against DENV and other viral diseases including ZIKV, H5N1, IBDV, and CAV. Results show that the immunosensor is specific in detecting DENV.

4.3.6 Preliminary Testing on Mouse Sera Samples

The performance of the constructed immunosensor against real serum samples was examined to provide an insight on the feasibility of the immunosensor. An antibody titre of >1280 in an acute-phase serum sample is considered presumptive evidence of a current dengue infection²⁸⁵. In other words, DENV IgG could be detected in serum samples diluted up to 1280 times during a current dengue infection. Therefore, with the application of optimised parameters, diluted (1:1000) mouse serum samples were incubated as the target instead of commercial DENV 1-4 IgG solution. Mouse sera used were derived from G1, the blank or negative control and G2, the immunised groups. As shown in Figure 4.7, the proposed sensor platform exhibited different $\Delta R(\%)$ responses, with 72.8% response for G1 control sample and 133.3% response for G2 positive sample. This significant difference in $\Delta R(\%)$ responses demonstrated the capability of as developed immunosensor in differentiating immunised samples (G2) from control (G1). The $\Delta R(\%)$ response exhibited from G1 sample was high likely due to the presence of common serum components such as electrolytes, antibodies, antigens, hormones etc., resulted in non-specific binding onto the sensor electrode. These components are also present in the positive/immunised G2 serum sample. As such, the $\Delta R(\%)$ response from G1 blank sample also ascertain the threshold or baseline level, in which any $\Delta R(\%)$ reading exceeding this level will indicate the presence of DENV IgG, confirming positive diagnosis of dengue infection. Based on these results, despite the complicated matrix of serum samples, it is plausible to utilise the developed immunosensor for qualitative

determination of dengue disease in serum samples of those are infected with DENV.

The performance of the dengue immunosensor was also compared to the results obtained from in-house indirect ELISA, using cEDIII as the antigen immobilised on the immunoplates. As shown in Table 4.1, the optical density (OD) value for G1 was found to be close to blank value (≈ 0) while G2 sample exhibited positive 0.431 OD reading. The comparable results indicate the capability of the immunosensor to provide binary response (negative/positive) on serum samples.

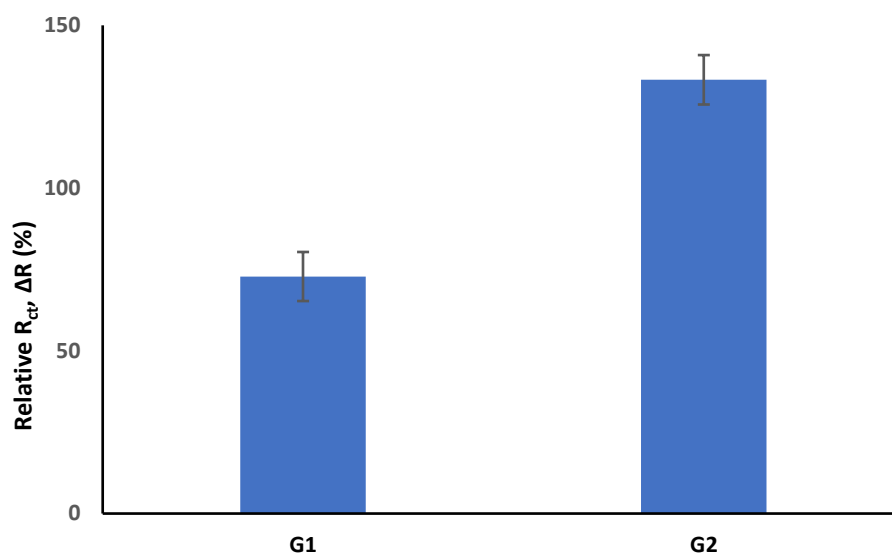


Figure 4.7. Response of immunosensor against mouse serum samples. G1 represents blank mouse serum while G2 represents serum extracted from immunised mice. Results show that immunosensor can detect the presence of DENV IgG in serum samples.

Table 4.1. OD values resulted from ELISA and relative R_{ct} , ΔR (%) from immunosensor on mouse serum samples.

	G1	G2
OD (Optical Density)	0.022	0.431

Relative R_{ct}, ΔR (%)	72.8	133.3
Results	Negative	Positive

4.4 Chapter Summary

In this study, an impedimetric electrochemical immunosensor has been developed for dengue detection. The immunosensor was constructed on graphene-modified SPCE by employing plant-based cEDIII protein as the probe. This sensor can detect DENV 1-4 IgG antibodies at low concentrations (LOD = 5.58 pg/mL), with a linear working range of 62.5 pg/mL to 1 ng/mL. In addition, the immunosensor has a high specificity towards DENV IgG, even when tested against related species such as Zika, which was known to cause false-positive cases for conventional NS1-based immunoassays. The ability of the immunosensor to detect dengue antibodies in serum samples was also verified with preliminary tests on mouse serum samples. The as-constructed immunosensor was able to generate binary (positive/negative) response for the serum samples comparable to results obtained from ELISA tests, correctly differentiating positive samples from control. Compared to conventional ELISA, the immunosensor approach eliminates the use of secondary antibodies as labels which leads to lower costs and less non-specific binding, while also offering rapid turnaround time due to the rapid response of the electrochemical approach and the short incubation times provided by the effective functionalisation of PSE. In addition, the requirement of delicate equipment and incubation chambers are also abolished. The synthesis pathway proposed for graphene is simple, efficient, and easily scalable. Similarly, the plant-based approach allows safe and inexpensive large-scale production of the cEDIII antigen. The electrochemical-based biosensor platform, on the other hand, promises rapid response, low fabrication, and operating costs. These advantages coupled with the sensor's

sensitivity and specificity provide an excellent opportunity for the proposed immunosensor to be further developed into point-of-care diagnostic assay for clinical use, especially in endemic regions where resources and facilities are scarce.

Chapter 5 : Highly Sensitive and Selective Graphene/TiO₂ Impedimetric Immunosensor based on Plant-derived Tetravalent Envelope Glycoprotein Domain III (EDIII) Probe Antigen for Dengue Diagnosis

5.1 Overview

As demonstrated in Chapter 3, the incorporation of TiO₂ onto graphene had improved the electrocatalytic properties of the nanomaterial. Furthermore, by ensuring optimal graphene-to-precursor ratio, TiO₂ nanoparticles were hybridised on graphene sheets homogeneously with no agglomeration, allowing maximum surface area accessible for electron transfer.

As such, in order to improve the analytical performance of the DENV IgG impedimetric biosensor, as reported in Chapter 4, this chapter reports on the use of G/TiO₂ nanocomposite, replacing graphene, as the sensor electrode platform. The optimal graphene-to-precursor ratio of 1:8 (GTi4), with the highest anodic peak current (I_{pa}) and the lowest cathodic peak current (I_{pc}) of 6.92 μ A and -7.94 μ A, respectively; and, the lowest charge transfer resistance (R_{ct}) of 1525.9 Ω , was used. Common optimisation and performance evaluation studies were carried out. In addition, the stability of the immunosensor across 15 days was also evaluated. For improved feasibility of the immunosensor in realistic applications, the blocking

protocols for detection in serum samples were optimised. The analytical performance of the immunosensor towards serum samples was further evaluated by subjecting the as-developed biosensor platform to negative and positive serum samples of different dilutions (1:500 to 1:32000) to determine its working dilution range. Finally, the immunosensor was challenged against 5 random serum samples and the results were compared to the those obtained via ELISA to demonstrate its reliability in serum sample detection, providing insight on its potential in replacing conventional immunoassays.

5.2 Experimental Details

5.2.1 Materials

Materials used are as described in Section 4.2.1, with the inclusion of G/TiO₂ nanocomposites. The G/TiO₂ nanocomposites were prepared as described in Section 3.2.3 in 1:8 of graphene-to-precursor ratio (GTi4). Additionally, 5 mouse serum specimens were provided by Prof. Sandy Loh in kind (S2, S3, S4, S5, S6), along with a negative control serum sample (S1).

5.2.2 Fabrication of G/TiO₂-modified Electrodes

G/TiO₂-modified Electrodes were fabricated as described in Chapter 3.

5.2.3 Fabrication of Immunosensing Platform

The immunosensing platform was fabricated following the procedures detailed in Section 4.2.4, with graphene being replaced by G/TiO₂ as nanomaterial for electrode modifications (Figure 5.1). Figure 5.1 illustrates the assembly steps involved in the fabrication of the as-proposed DENV immunosensor.

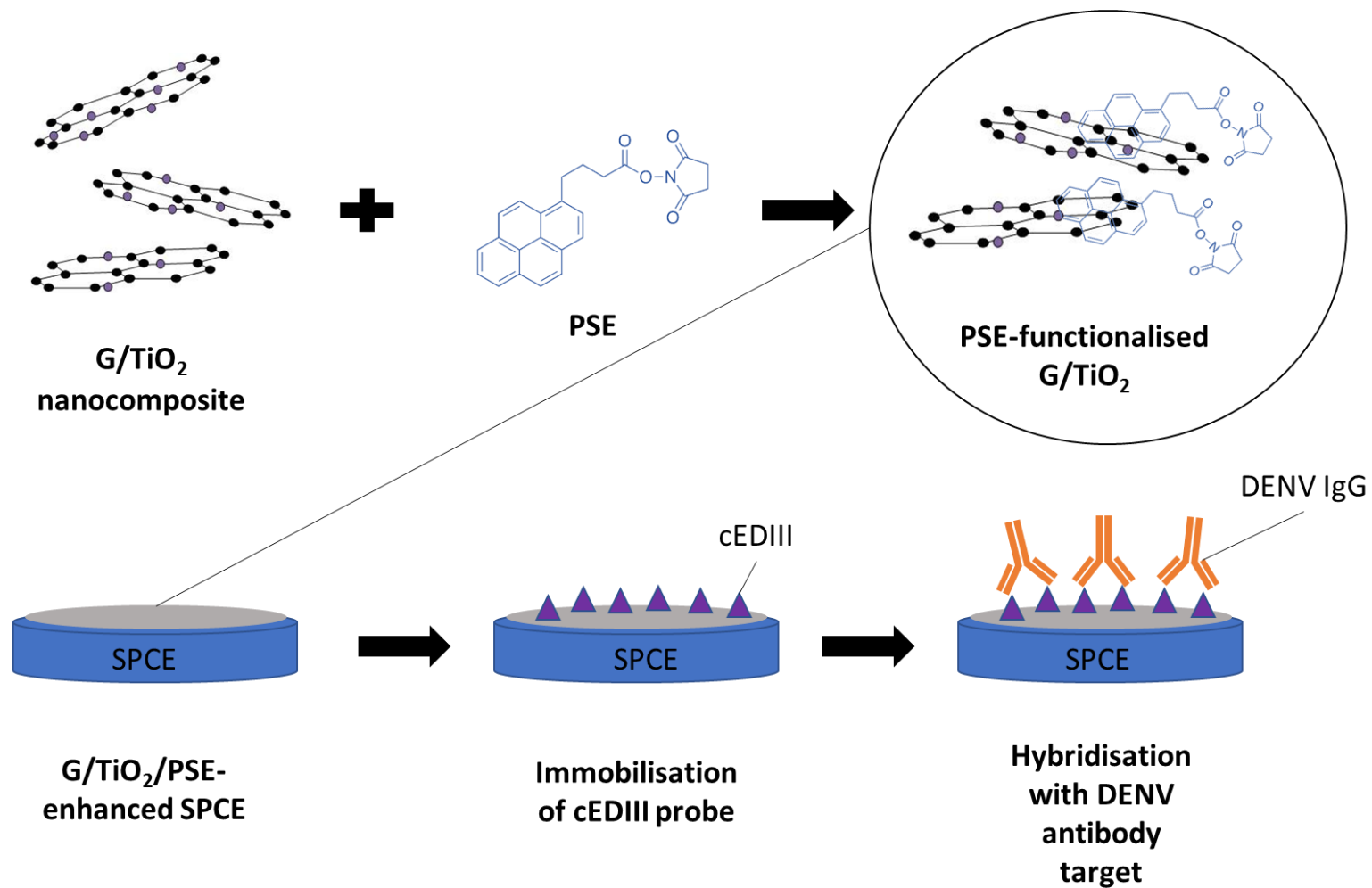


Figure 5.1. Schematic diagram for the development of G/TiO₂/PSE-modified electrochemical immunosensor for dengue detection.

5.2.4 Enzyme-Linked Immunosorbent Assay (ELISA)

In-house ELISA was carried out as detailed in Section 4.2.5 on serum samples (S1, S2, S3, S4, S5 and S6) in 1:1000 dilutions.

5.2.5 Electrochemical Characterisation of Immunosensor Platform

The electrochemical analyses were performed using Autolab PGSTAT III potentiostat (Metrohm, Netherlands) interfaced with controlling software NOVA 1.10. All the electrochemical measurements settings used were similar to Section 4.2.5.

5.3 Results and Discussion

5.3.1 Optimisation of G/TiO₂ Mass Loading on Biosensor Platform

The optimum deposition amount of G/TiO₂ nanocomposites on the SPCE was first determined to establish a sensing platform with improved sensitivity and minimal baseline. G/TiO₂ nanocomposites were loaded onto the SPCE by dispensing G/TiO₂ suspension (1 mg/mL) in different volumes, denoted as GT01, GT02, GT03, GT04, and GT05 (1 μ L, 2 μ L, 3 μ L, 4 μ L and 5 μ L). Their equivalent mass loadings of G/TiO₂ were calculated using Equation 4.1 and shown in the Table 5.1 below:

Table 5.1. SPCEs modified with different volumes of G/TiO₂ suspension and their equivalent mass loadings.

Electrode	Volume of G/TiO ₂ suspension (μ L)	Equivalent mass loading (μ g/cm ²)
GT01	1	7.96
GT02	2	15.91
GT03	3	23.87
GT04	4	31.83
GT05	5	39.78

The CV analysis of the bare and modified electrodes are shown in Figure 5.2a. As shown, a pair of well-defined redox peaks, which correspond to the oxidation and reduction process of $\text{Fe}(\text{CN})_6^{-4}/\text{Fe}(\text{CN})_6^{-3}$, can be observed for all the electrodes. The bare electrode exhibited anodic, E_{pa} and cathodic, E_{pc} peaks potential, at 0.24 V and -0.05 V respectively. With increasing G/TiO₂ mass loadings, reduction in the interpeak distance and increased in current responses can be observed. GT05 modified electrode attained the highest peak current responses of 117.05 μA (anodic) and -134.06 μA (cathodic) (~2.2% RSD) with lowest interpeak distance (ΔE_p) of 0.17 V. The minimal ΔE_p suggests the enhanced electrochemical performance of GT05 due to high redox reversibility and ease of reaching Nernst equilibrium from high electron transfer rate.

EIS analysis was also carried out to detect changes of the interfacial properties due to deposition of G/TiO₂. It can be observed that increasing amount of G/TiO₂ mass loading resulted in the decrease of interfacial charge transfer resistance, R_{ct} , in the order of Bare>GT01>GT02>GT03>GT04>GT05. The incorporation of G/TiO₂ onto the electrode resulted in better electrons transfer between the electrode/electrolyte interfaces due to the excellent electroconductivity of the nanocomposite material. These results are consistent with the findings from CV analysis, in which GT05 modified electrode attained the lowest R_{ct} of 1036.17 Ω (3.2% RSD), with the highest current response for CV analysis. As such, GT05 modified electrode, determined to have the optimum deposition amount, will be used in the subsequent analysis and development of immunosensor.

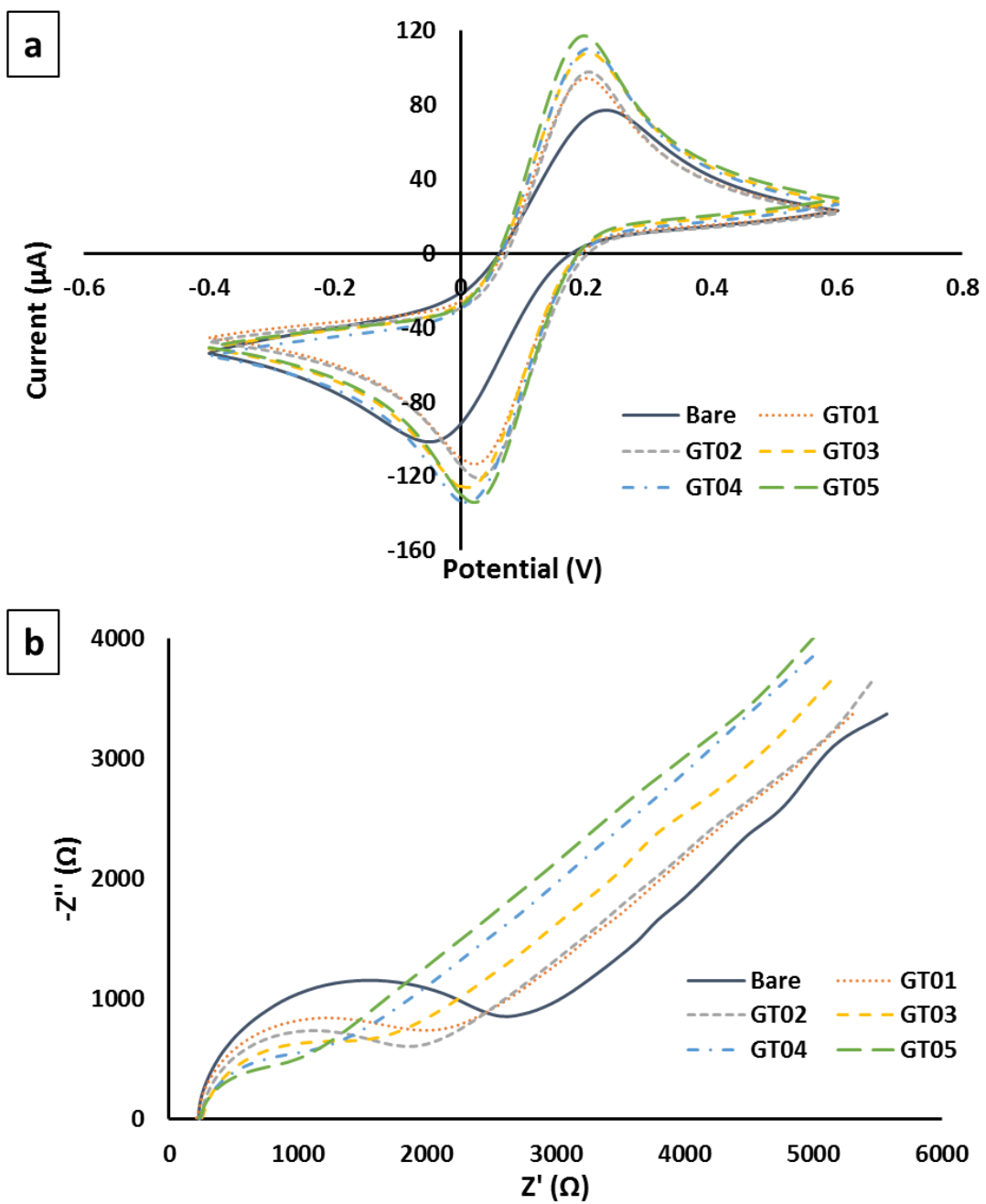


Figure 5.2. CVs (a) and Nyquist plots (b) obtained from electrodes with increasing mass loading of G/TiO₂ nanocomposites. GT05 exhibits the best electrochemical response.

5.3.2 Electrochemical Characterisation of Biosensor Platform

Similar to the work reported in Chapter 4, PSE was used as a bio-linker to anchor cEDIII molecules onto the G/TiO₂ nanocomposites on the sensing platform. The step-by-step assembly of the dengue immunosensors was examined via CV and EIS analyses (Figure 5.3). As shown in the Figure 5.3a, two distinct redox peaks were originally found in the CV measurement from G/TiO₂-modified electrodes. Upon incorporation with PSE, the redox peaks showed reduced current response compared to that of G/TiO₂-modified electrodes, signifying successful functionalisation of G/TiO₂. The decrease in current response could be attributed to the PSE's hydrophobicity and the formation of a physical barrier hindering electron transfer to the electrode surface²⁰⁸. Further decrease in the peak currents was observed in G/TiO₂/PSE/cEDIII-modified electrodes, indicating the successful immobilisation of cEDIII. Skim milk solution that was used to prevent nonspecific binding on the active sites of cEDIII also contributed to a drop in current response, as shown in G/TiO₂/PSE/cEDIII/milk-modified electrodes. With the hybridisation of DENV IgG antibodies on the modified electrodes, the current peaks were reduced to a barely noticeable state. Additionally, the anodic peaks shifted more positive while the cathodic peak shifted more negative with each subsequent modification, effectively widening the interpeak distance. This suggests that the redox reversibility of [Fe(CN)₆]^{3-/4-} worsens upon the formation of accumulative insulative physical barriers from the sequential modification steps, making it more difficult to achieve Nernst equilibrium.

The EIS analysis showed that the charge resistance, R_{ct} , of the electrodes increased for each successive modification step in the order of G/TiO₂ < G/TiO₂/PSE

$\langle G/TiO_2/PSE/cEDIII \rangle < G/TiO_2/PSE/cEDIII/milk < G/TiO_2/PSE/cEDIII/milk/IgG$ (Figure 5.3b). The functionalisation of G/TiO_2 with PSE was found to induce a notable increment in R_{ct} , largely due to the hydrophobic nature of PSE as mentioned earlier. Comparatively, the increment that came with the successful immobilisation of cEDIII was on a smaller magnitude, probably to the small size of cEDIII (≈ 28 kDa)³⁶⁴. The insignificant increase in the blocking step ($G/TiO_2/PSE/cEDIII/milk$) confirmed that there was no immunoreaction between cEDIII and milk proteins. Upon successful hybridisation of DENV IgG antibodies on the immunosensing platform, large inert cEDIII-IgG immunocomplexes were formed on the electrode surface, which impeded the electron transfer process and caused a large increment in R_{ct} . In summary, successive addition of modified layers inhibited the diffusion of the redox probe, causing electron transfer resistance to increase further. The results correspond with the findings from CV analysis, evidently demonstrating the successful development of the G/TiO_2 immunosensor from each modification steps, capable of DENV IgG detection.

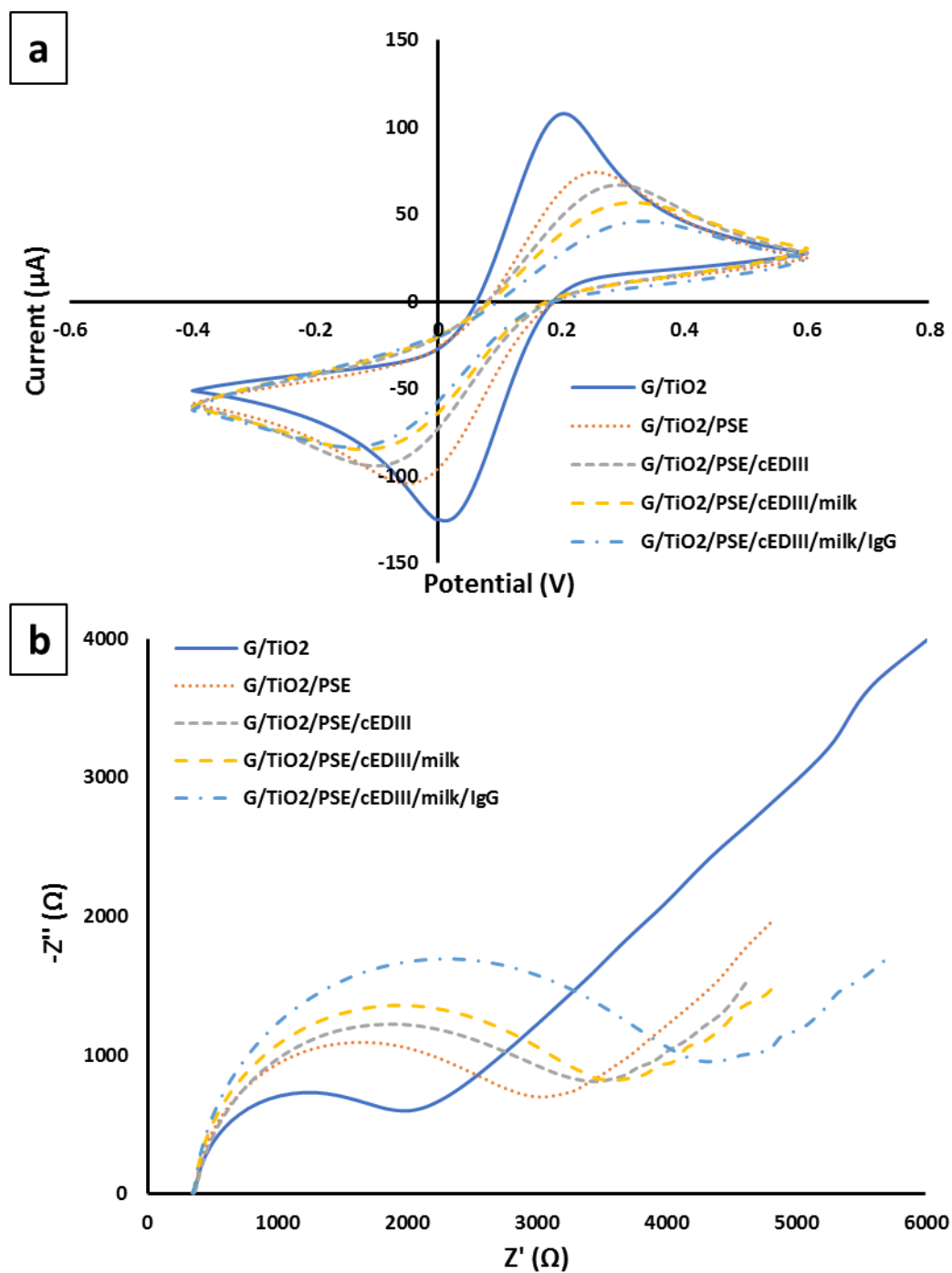


Figure 5.3. a) CV measurements of G/TiO₂, G/TiO₂/PSE, G/TiO₂/PSE/cEDIII, G/TiO₂/PSE/cEDIII/milk, G/TiO₂/PSE/cEDIII/milk/IgG. Conductivity reduces as elements on SPCE increases. b) Nyquist plot of G/TiO₂-modified SPCE, G/TiO₂/PSE, G/TiO₂/PSE/cEDIII, G/TiO₂/PSE/cEDIII/milk, G/TiO₂/PSE/cEDIII/milk/IgG. Impedance value increases as elements on SPCE increases.

5.3.3 Optimisation of Biosensor Platform

For improved sensing performance, the probe concentration, probe immobilisation time and target hybridisation time were optimised. Normalised R_{ct} or relative R_{ct} , $\Delta R(\%)$, was used to minimise the errors in electrode-to-electrode or film-to-film variation as discussed in Section 4.3.3. Recalling Equation 4.2:

$$\Delta R(\%) = \frac{\Omega_{antibody} - \Omega_{blank}}{\Omega_{blank}} \times 100 \quad (4.2)$$

where $\Omega_{antibody}$ is the impedance value of electrode after target hybridisation (G/TiO₂/PSE/cEDIII/milk/IgG) and Ω_{blank} represents the impedance value of electrode prior to target hybridisation (G/TiO₂/PSE/cEDIII/milk).

To determine the optimum cEDIII concentration for DENV IgG capture, different concentrations of cEDIII probe (1 µg/mL, 5 µg/mL, 10 µg/mL, 25 µg/mL and 50 µg/mL) were immobilised on the working electrode for 30 minutes, followed 30 minutes of incubation with DENV IgG (1000X dilution). As shown in Figure 5.4a, the use of different concentrations of cEDIII probe did not result in any significant differences in the detection signals. The finding suggested that 1 µg/mL was sufficient to ensure that the electrode platform was densely immobilised with cEDIII probe for effective target detection. Also, the saturated signals observed for higher concentrations may suggest excess probes introduced were washed away during the washing step, resulting in wastage. Therefore, 1 µg/mL cEDIII probe were used in subsequent analyses.

Following this, the influence of cEDIII incubation time was investigated for optimum probe density. Similarly, cEDIII probe were incubated over varying durations from 15 to 120 minutes, followed by incubation of DENV IgG (1000X dilution) for 30 minutes.

As shown, the $\Delta R(\%)$ increased gradually with increasing incubation time, reaching saturation at 60 minutes (Figure 5.4b). While prolonged probe incubation time provided ample time for cEDIII molecules to be immobilised properly on the electrode surface, the binding is still limited by the surface area and available active sites of the PSE-functionalised G/TiO₂ nanocomposites on the working electrode. The amount of cEDIII molecules bound on the electrode surface would in turn limit the amount of cEDIII-DENV IgG immunocomplexes that could be formed, hence the plateaued signal. Consequently, the optimum probe immobilisation time selected was 60 minutes, and used in all subsequent tests.

The effect of target hybridisation time was studied by incubating G/TiO₂/PSE/cEDIII/milk-modified electrodes with different incubation times ranging from 15 to 120 minutes (Figure 5.4c). Results showed that as target hybridisation time increased from 15 to 60 minutes, $\Delta R(\%)$ also experienced a steady increase, depicting a higher amount DENV IgG bound to the immobilised cEDIII thus improving the signal response. Extending the hybridisation time beyond 60 minutes, however, resulted in negligible difference in signal response, signifying binding equilibrium between cEDIII and DENV IgG could be reached by 60 minutes. As such, considering sensitivity and assay time, 60 minutes was chosen as the optimum target hybridisation time.

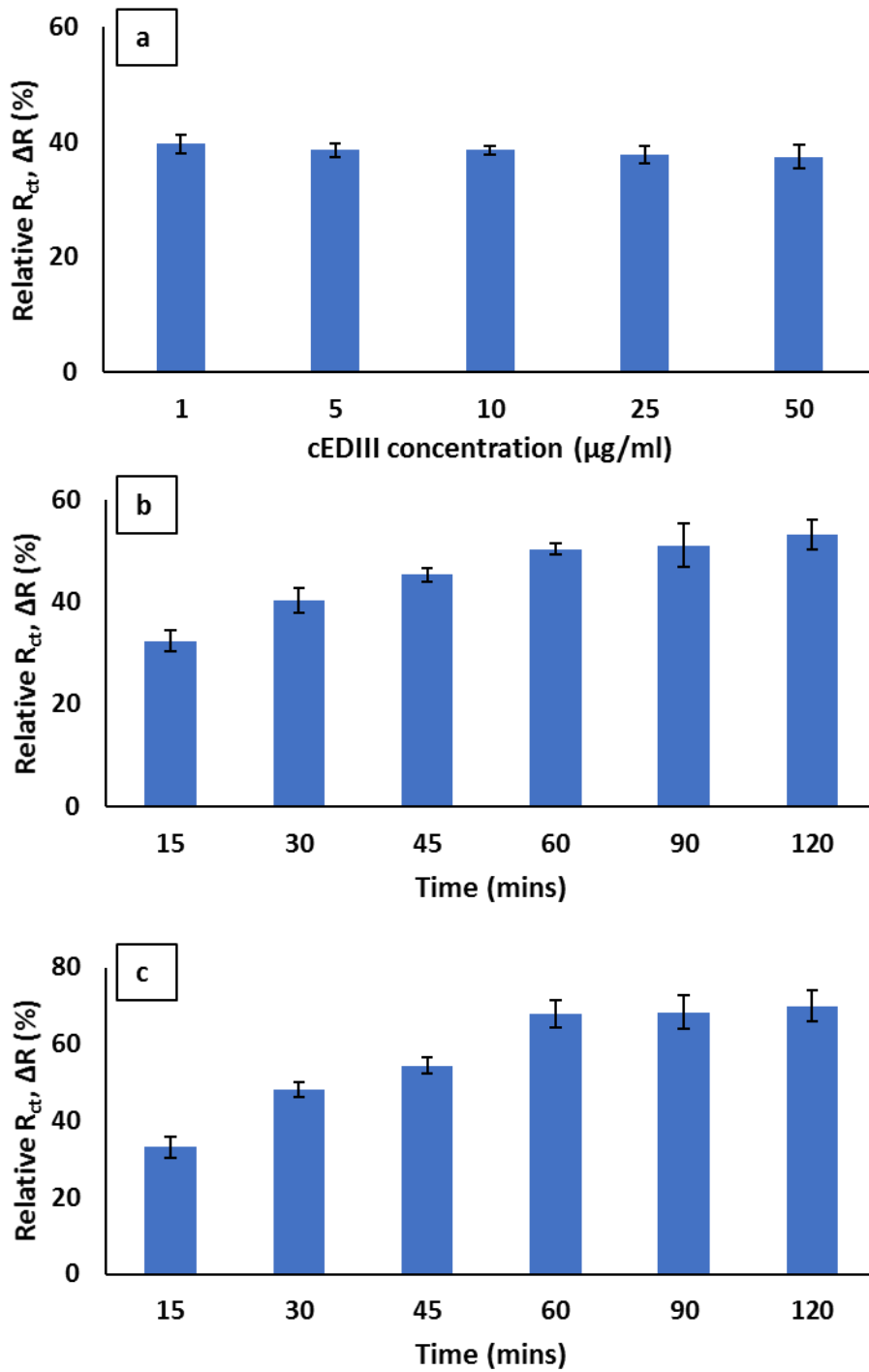


Figure 5.4. Effects of a) cEDIII probe concentration, b) cEDIII probe immobilisation time, and c) target antibody hybridisation time on relative R_{ct} , ΔR (%). The optimum cEDIII probe concentration and immobilisation time was found to be 1 $\mu\text{g/ml}$ and 60 mins, respectively. The optimised target hybridisation time was 60 mins.

5.3.4 Analytical Performance of the Biosensor Platform

Under optimised sensing conditions, the performance of the biosensor platform was evaluated against different concentrations of DENV IgG, ranging from 62.5 pg/mL to 4 ng/mL (Figure 5.5). As shown, increasing concentration of DENV IgG resulted in increasing signal responses due to formation of more insulative cEDIII-IgG immunocomplexes on the surface, which impede the transfer of electrons/charge between the electrolyte/electrode interfaces. The calibration curve was obtained by plotting $\Delta R(\%)$ values against the logarithmic values of DENV IgG concentrations (inset, Figure 5.5) and is represented by the regression equation below. The linear working range for the proposed immunosensor was found to be between 62.5 pg/mL to 2 ng/mL with good correlation coefficient of $R^2 = 0.995$.

$$\Delta R (\%) = 23.265 * \log [\text{DENV IgG}] (\text{pg/mL}) - 7.1945 \quad (5.1)$$

The limit of detection (LOD) of the as-prepared immunosensor was estimated to be 2.81 pg/mL. Comparing the performance of the immunosensor to the graphene-based platform (Chapter 4), the G/TiO₂ based platform exhibited wider linear working range with lower limit of detection. These results affirmed the excellent synergistic effect of graphene and TiO₂, in which the formation of Ti-O-C chemical bond narrowed the energy gap facilitating electron transfer while the large specific area and porous nature of the TiO₂ nanoparticles provided more active sites for the formation of cEDIII-IgG immunocomplexes and the diffusion of analytes, thus resulting in better performing sensor electrode platform³⁴⁸. Additionally, the performance of the two proposed immunosensor platform are comparable to other similar report work, as tabulated in Table 5.2.

Electrode material	Target	Method	Linear range	LOD	Ref.
Gold electrode	NS1	ECS	5-1000 ng/mL	0.2 ng/mL	371
	NS1	EIS	10-2000 ng/mL	3.0 ng/mL	371
ZnO/Pt-Pd nanocomposites on fluorine doped tin oxide glass electrode	DENV cDNA	CV, DPV	1-100 × 10 ⁻⁶ M	4.3 × 10 ⁻⁵ M	357
Pencil graphite electrode	DENV-3 sequence	DPV	1-100 nM	3.09 nM	307
GO-polymer matrix composite on gold electrode	DENV	EIS	1-2 × 10 ³ pfu/mL	0.12 pfu/mL	309
Bifunctional SAM on gold electrode	NS1	ECS	1-5000 ng/mL	220 pg/mL	311
	IgG	ECS	1-1000 ng/mL	231 pg/mL	311
Graphene-modified SPCE	IgG	EIS	62.5-1000 pg/mL	5.58 pg/mL	Chapter 4
G/TiO₂-modified SPCE	IgG	EIS	62.5-2000 pg/mL	2.81 pg/mL	This work

Table 5.2. Analytical performances of the proposed immunosensor compared against other dengue biosensor works.

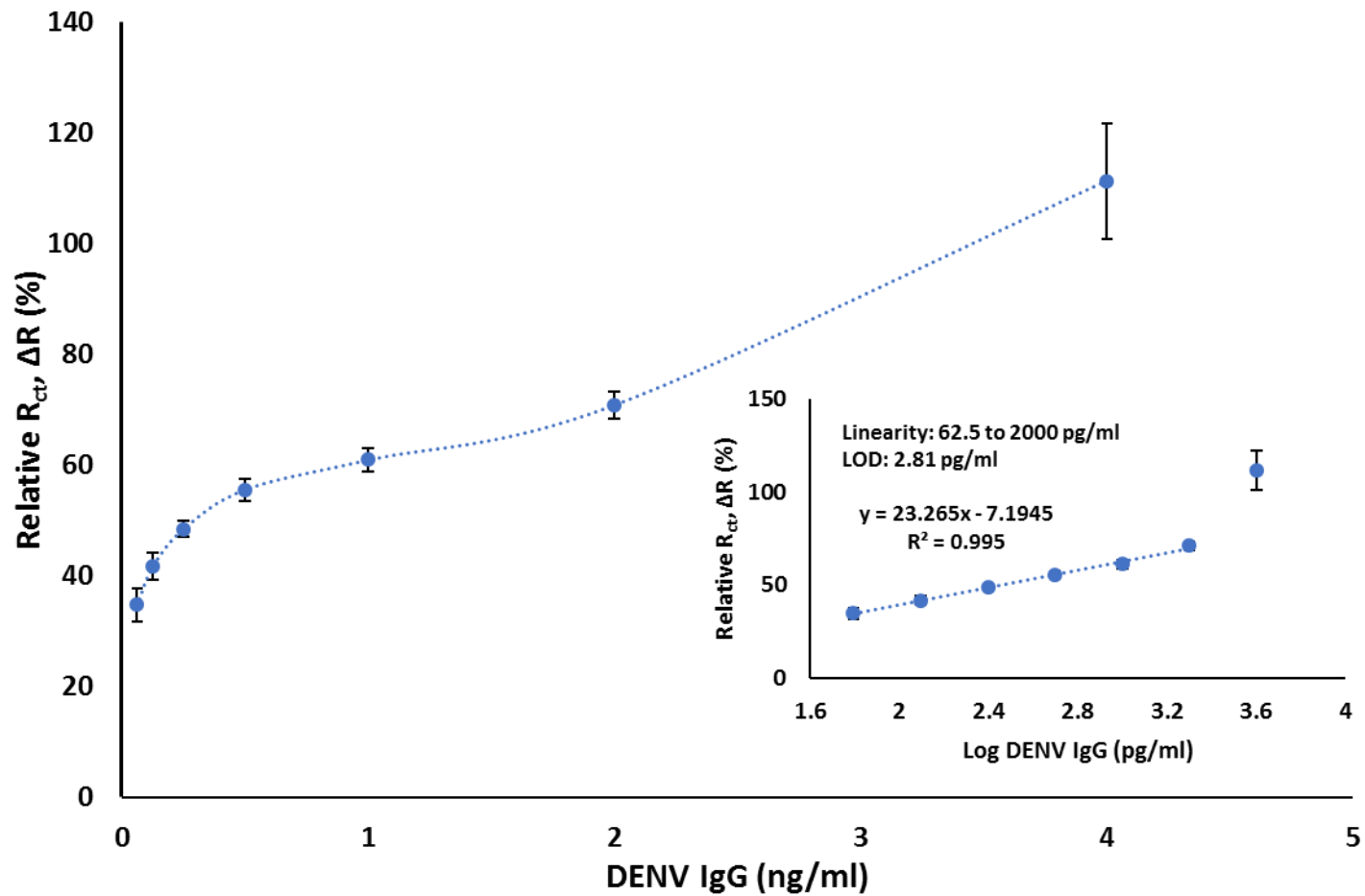


Figure 5.5. Analytical measurement curve obtained for DENV IgG detection of the proposed sensor, using relative R_{ct} , ΔR (%) as function of DENV IgG concentration. Inset shows the corresponding calibration plot of the immunosensor.

Selectivity is one of the most important aspect of a biosensor, in which it is the ability to differentiate the intended target analyte from others. Similar to Section 4.35, the selectivity of the proposed G/TiO₂ sensor platform was evaluated against different infectious diseases namely avian influenza A virus (H5N1), infectious bursal disease virus (IBDV), chicken anaemia virus (CAV), and Zika virus (ZIKV). As shown, the immunosensor exhibited excellent selectivity, reflected by significantly lower relative R_{ct} response (<32.7%) against other viral antibodies. Moreover, the immunosensor response against ZIKV antibodies had the lowest signal response (23.7%) relative to the others. These findings highlighted the potential of the proposed immunosensor platform to distinguish DENV from other viral diseases, and most importantly, ZIKV.

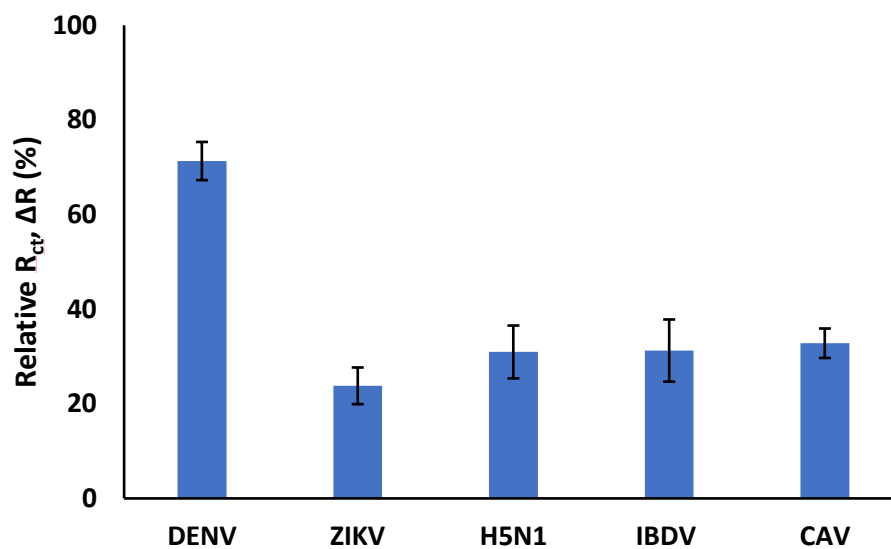


Figure 5.6. Response of immunosensor to antibodies raised against DENV and other viral diseases including H5N1, IBD, VP3 and ZIKV. Results show that the immunosensor is specific in detecting DENV.

To provide an insight on the stability of the developed immunosensor, multiple G/TiO₂/PSE/cEDIII-modified electrodes were prepared and stored under 4 °C. The performance of the modified electrodes on DENV IgG detection were inspected over a period of 15 days and presented in Figure 5.7. While the signal response of the as-developed immunosensor was found to be decreasing over time, it exhibited acceptable stability, recording only a 10.4% decrement in the signal response.

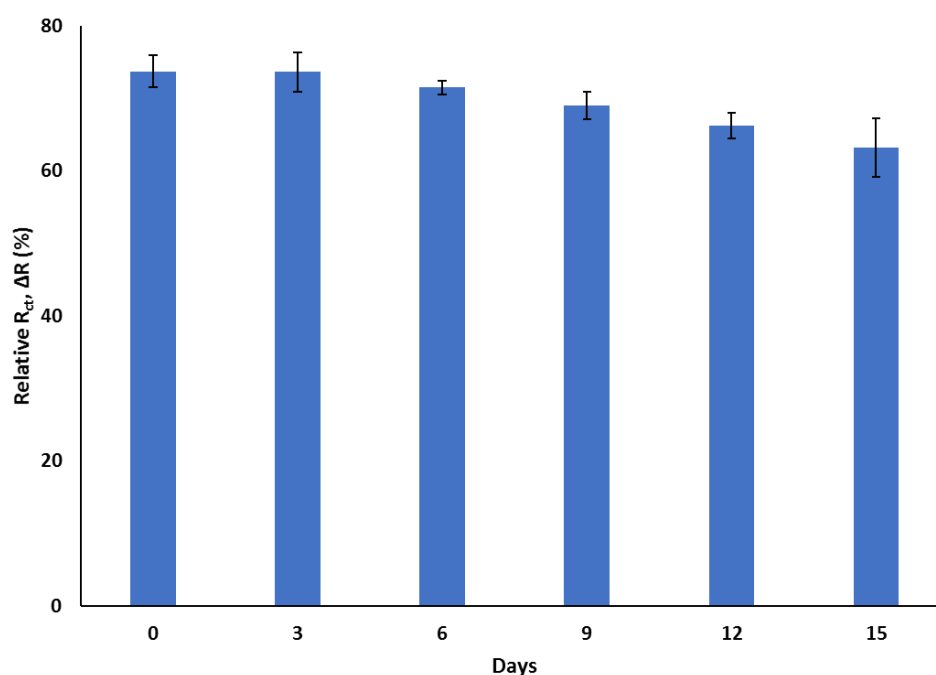


Figure 5.7. Signal response of the immunosensor towards DENV IgG over a period of 15 days. Signal response decreased slowly over time, indicating an acceptable shelf-life of at least 15 days.

5.3.5 Analytical Performance of the Biosensor Platform on Mouse Sera Samples

The compatibility of an immunoassay in complex biological matrices is extremely crucial in validating and determining the feasibility of the immunoassay. While Chapter 4 reported the successful development of a dengue immunosensing platform capable of delivering binary response for dengue detection on serum samples, the results left room for improvements particularly in the reduction of background noise. Serum samples are known to be complex biological matrices comprising various ions, organic molecules, proteins, and lipids³⁷². These components could potentially bind non-specifically to the probe molecules, leading to high background noise even in negative samples. An optimised blocking protocol is needed to not only suppress the non-specific bindings on the probe (cEDIII), while providing a distinguishable reading on positive samples. To achieve this goal, the blocking step was optimised by varying the blocking buffer (skim milk solution) in different concentrations (0.1% to 5%) in the fabrication of G/TiO₂/PSE/cEDIII/milk-modified electrodes and their respective readings on mouse serum samples from both the negative control group G1 and the experimental group G2 (DENV IgG-positive). As shown in Figure 5.8, electrodes blocked with 1% skim milk solution showed the highest difference between positive and negative samples (signal-to-noise ratio: 7.9). This is a major improvement compared to immunosensor blocked by 0.1% of skim milk solution where the binding difference is less significant. While using 5% skim milk solution as the blocking buffer gave the lowest reading for negative samples, the signal response obtained from positive samples was indistinguishable as well. It is suggested that the dramatic drop

in signal response is due to the abundant amount of milk proteins at high concentrations, which not only blocked the non-specific bindings but also covered the active sites of the cEDIII and DENV IgG molecules, essentially obstructing and limiting the specific bindings. Based on the results from this optimisation study, 1% skim milk solution was selected as the optimal blocking buffer concentration.

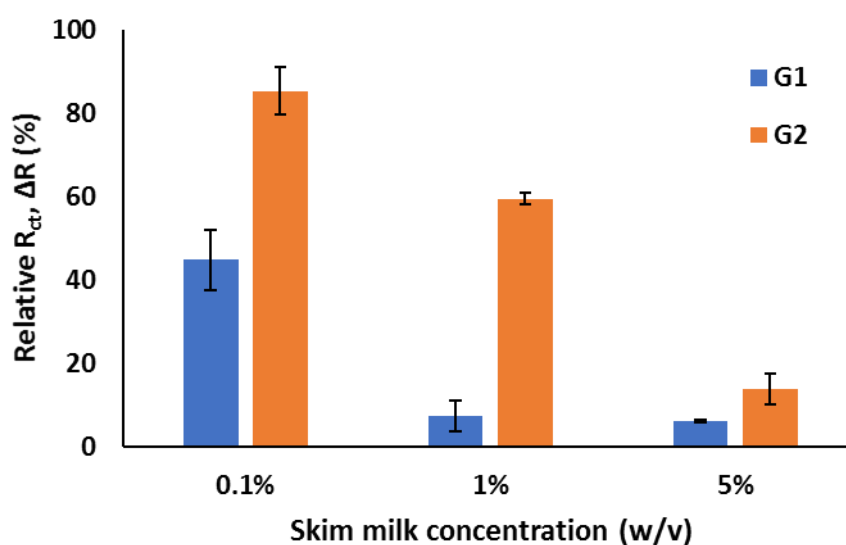


Figure 5.8. Effects of different concentrations of blocking buffer on the signal response of immunosensor. Immunosensor blocked by 1% of skim milk solution provided the highest difference between positive and negative samples.

The analytical performance of the immunosensor towards mouse serum samples was further evaluated by subjecting the as-developed biosensor platform to negative (G1) and positive (G2) mouse serum samples of different dilutions (1:500 to 1:32000). As presented in Figure 5.9, while the signal response decreased steadily as the dilution factor increased, significant difference was still observed between negative and positive serum samples at all dilutions. The gradual decline in signal response on positive samples reflected the decrease of DENV IgG in the increasingly diluted serum samples. The findings indicated that the immunosensor is capable of detecting the presence of DENV IgG in serum samples diluted up to a dilution factor of 32000 times, providing distinguishable readings to identify positive samples in a wide working range of 500X to 32000X dilution.

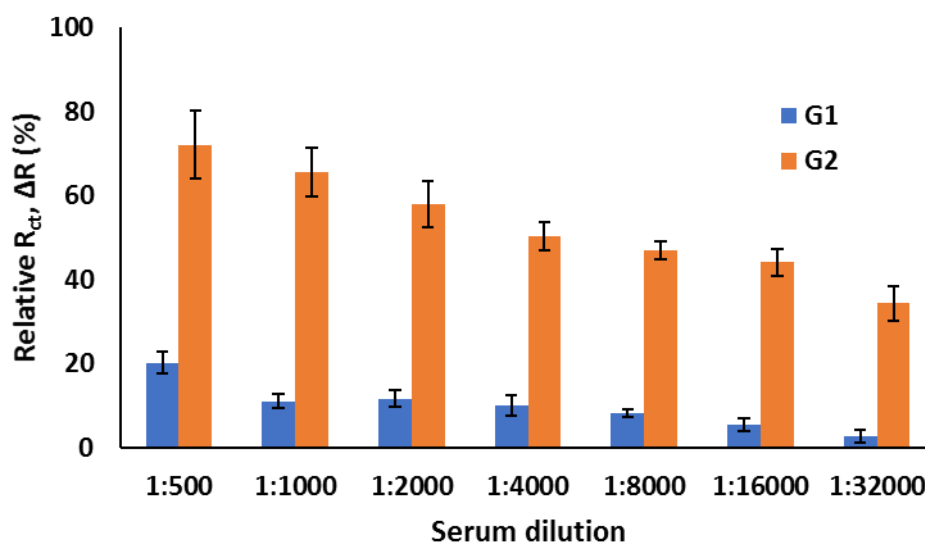


Figure 5.9. Signal response of immunosensor on positive (G1) and negative (G2) serum samples across different dilutions.

In order to evaluate the reliability of the immunosensor in DENV detection, the as-constructed impedimetric biosensor was challenged against a negative control sample (S1) and 5 random mouse serum specimens (S2, S3, S4, S5, and S6) at 1000X dilution. The recorded signal responses were then validated against the readings obtained from an indirect ELISA test on the same samples with cEDIII as the antigen immobilised on immunoplates (Table 5.3). The results showed that the proposed immunosensor platform was comparable and acceptable for the detection of DENV IgG, in which the readings from the electrochemical sensor correlate well to the readings from the ELISA analysis, providing potential quantitative estimation of DENV IgG present in the serum samples.

Table 5.3. Signal response from immunosensor and O.D. value resulted from ELISA on mouse serum samples.

Sample	Signal response, ΔR (%)	Absorbance, O.D.	Results
S1	9.982	0.072	Negative
S2	13.186	0.095	Negative
S3	21.409	0.762	Positive
S4	52.438	3.368	Positive
S5	47.561	3.29	Positive
S6	60.340	3.408	Positive

5.4 Chapter Summary

This chapter reports on the development of an impedimetric immunosensor based on G/TiO₂ nanocomposite modified electrode platform for the detection of DENV IgG. Plant-based cEDIII peptide was used as a probe and various sensing parameters were optimised for improved sensitivity and selectivity. The proposed immunosensor demonstrated high sensitivity (slope=23.265) towards DENV 1-4 IgG detection, with 2.81 pg/mL limit of detection within a linear working range of 62.5 pg/mL to 2 ng/mL. Moreover, the immunosensor exhibited high specificity for discriminating DENV IgG against antibodies of other infectious disease, including ZIKV. In general, the performance G/TiO₂ based platform was better in terms of wider linear working range, lower limit of detection and better sensitivity, compared to the graphene-based platform reported in Chapter 4. The immunosensor was also stable and had an acceptable shelf-life, with only minute signal decrease over the course of 15 days. The analytical performance of the immunosensor to detect dengue antibodies in serum samples was also investigated with the aid of optimised blocking protocol. The immunosensor was capable of producing distinctive readings to identify DENV IgG-positive samples in a wide working range from a dilution factor of 1:500 up until 1:32,000. The results were also comparable to readings from conventional ELISA assay. The key elements of the immunosensor offer attractive merits on their own: the large specific area and excellent catalytic properties of G/TiO₂ nanocomposites, the scalability and low cross-reactivity of plant-based cEDIII, and the rapid response, miniature size and low costs of electrochemical biosensors. Combining all these qualities, a promising analytical tool with good sensitivity and specificity could be

developed for DENV detection; which holds a great potential to be further developed into point-of-care diagnostic assay for clinical use.

Chapter 6 : Cytotoxicity Study of Graphene and G/TiO₂ Nanomaterials

6.1 Overview

Owing to their versatility and the excellent properties, there has been a surge in research regarding the biomedical applications of graphene and graphene-based nanomaterials in the recent years. Other than biosensing ²¹, the diverse applications include bioimaging ³⁷³, drug delivery ³⁷⁴, antiviral ³⁷⁵, antibacterial ³⁷⁶, and anticancer ³⁷⁷. Recent works also studied the prospect of graphene in enhancing the performance of biomedical engineering and tissue engineering applications ^{378, 379}. With such promising prospects of graphene and graphene-based nanomaterials, their safety and biocompatibility have become prioritised concern for many researchers.

Various works reported that the biocompatibility of graphene is largely determined by their intrinsic physico-chemical properties, which is highly dependent on the raw materials and synthesis method used ^{29, 30}. While many of the nanomaterials' performance in various applications are attributed to their small size and novel properties that they exhibit at nanoscale, there are also growing evidence to suggest that the minute particle sizes, large surface area, and shapes can also trigger undesired side-effects such as toxicity ³⁸⁰⁻³⁸². A possible solution or improvement to the cytotoxicity of graphene-based materials is the addition of metal oxides. Overlaying the edges and surfaces of the graphene sheets with metal oxides potentially reduces the harmful effects of graphene against cells. As mentioned, a possible factor that contributes to the cytotoxicity of graphene-based materials is its shape, where certain

synthesis processes that involves harsh conditions resulted in graphene with sharp edges which would then damage the membrane of cells^{29,30}. Therefore, a cushioning layer of metal oxide nanoparticles would mitigate the damage and protect the cells from graphene. Other factors determining the safety of graphene include its hydrophobicity and aggregation^{53, 383}, which might also be improved by the incorporation of metal oxides nanoparticles. Furthermore, metal oxide nanoparticles are generally found to be less hazardous when compared to carbon-based materials³⁸⁴. Therefore, the successful hybridisation between graphene and metal oxide nanoparticles could potentially create novel material that combines both the advantages of both graphene and metal oxides, while having synergistic enhancement on their performance.

When it comes to the cytotoxicity evaluation of graphene and graphene-based nanomaterials, it is difficult to draw a concrete conclusion due to the inconsistencies and lack of standardised data from previous studies. Thus, it is evident that the biocompatibilities of graphene and graphene-based nanomaterials should be evaluated on a case-by-case basis. In previous chapters, graphene and G/TiO₂ nanocomposites have demonstrated great potential as electrode platform for high performance biosensing applications. Hence, it is imperative to evaluate their biocompatibility/ cytotoxicity against human keratinocytes (HaCat) and lung fibroblasts cells (MRC5), since inhalation and skin contact are the major routes of exposures for nanomaterials.

6.2 Experimental Details

6.2.1 Materials

Raw highly pyrolytic graphite (HOPG) flakes (99% carbon purity) were purchased from Bay Carbon (Michigan, USA). Titanium (IV) isopropoxide (TTIP), $\text{Ti}(\text{O}^i\text{Pr})_4$, fetal bovine serum (FBS) were purchased from Sigma-Aldrich (USA). Reagent grade ethanol were obtained from R&M Chemicals (Malaysia). DMEM media, RPMI-1640 media, penicillin-streptomycin solution, trypsin were acquired from Nacalai (Japan). T-75 flasks were purchased from SPL Life Sciences (Korea). Deionized (DI) water was used throughout the experiment (Millipore, USA). All the chemicals were used as received without further purification.

6.2.2 Synthesis of Graphene and G/TiO₂

Graphene was synthesised as described in Section 3.2.2. Subsequently, G/TiO₂ was synthesised as discussed in Section 3.2.3 in the optimised graphene-to-precursor ratio of 1:8.

6.2.3 Cell Culture

Two mammalian cell lines, namely MRC5 (human lung fibroblast) and HaCat (human immortalised keratinocyte) were cultured in RPMI-1640 and DMEM media respectively, supplemented with 10% fetal bovine serum (FBS) and 100 U/ml of penicillin-streptomycin solution. The cells were incubated in a 37°C-humidified CO₂ incubator (ESCO, USA). Routinely, cells were trypsinised at approximately 70-80% confluency. The media were aspirated, and 3 ml of 0.25% trypsin were added into the respective T-75 flask and returned to the incubator for 5 min to allow cell detachment.

Following that, cell suspensions were collected by centrifugation at 1,500 rpm for 5 min. Cell pellet were dissolved in 4 ml of complete media. One millilitre of cell suspension was added to a T-75 flask for maintaining the cells.

6.2.4 Cell Proliferation Study

The 3-(4,5-dimethylthiazol-2-yl)-2,5-diphenyltetrazolium bromide) tetrazolium (MTT) reduction assay ³⁸⁵ was used to study the cytotoxicity of the as-synthesised nanomaterials, by measuring the metabolic activity of the cells. The MTT solution was prepared by dissolving MTT in Dulbecco's phosphate buffered saline, pH=7.4 (DPBS) to 5 mg/ml. The MTT solution was then filter-sterilised through a 0.2 µM filter into a sterile, light protected container, and stored at 4°C.

The cultured cells were seeded in 96-well plates containing a final volume of 100 µl/well, and incubated with various concentrations (0, 2, 5, 25, 50, 250, 500 µg/ml) of G/TiO₂ for the desired period of exposure (24, 48, 72 hours). At the end of the incubation period, the 96-well plate was removed from the incubator and placed under an inverted microscope (Nikon Eclipse TS100) to capture high resolution images (100X magnification) for the morphological characterisation of the cells. Next, 10 µl MTT solution was then added per well to achieve a final concentration of 0.5 mg/ml, and incubated for another 4 hours at 37°C. Finally, 100 µl dimethyl sulfoxide (DMSO) solution was added to each well and the absorbance was recorded at 570 nm.

6.3 Results and Discussions

6.3.1 Microscopic Visualisation of Nanomaterials Interactions with MRC5 and HaCaT Cells

The cytotoxicity effects of as-synthesised graphene and G/TiO₂ nanocomposites were evaluated by incubation with two different cell lines: MRC5 fetal lung cells and HaCaT immortal keratinocytes (skin epidermal cells). Interactions of nanomaterials with the cultured cells were observed at different period of exposures (24, 48, 72 hours) after treating the cells with 50 µg/ml of graphene and G/TiO₂. The morphologies of MRC5 cells upon nanomaterial treatment are shown in Figure 6.1. Untreated MRC5 cells exhibited elongated and spindle-shaped with fibroblastic features as seen in the negative controls (Figure 6.1a-c). The images of MRC5 cells in absence of nanomaterials showed continuous proliferation and increase in cell density throughout 72 hours. As an adherent cell line, MRC5 cells grow anchored on substrate, and would detach themselves from substrate upon cell death, forming free-floating spherical bodies visible under microscope. Once treated with 50 µg/ml of graphene, MRC5 cells showed signs of deterioration such as irregularly shaped membrane and cytoplasmic shrinkage (Figure 6.1d-f). Cell deterioration continued further through 72 hours of exposure with graphene, as suggested by the cytoplasmic vacuolation and membrane blebbing found in the images. Graphene nanoparticles were also found to be surrounding MRC5 cells, forming aggregates adsorbed on the cell membranes. Comparatively, cells that were exposed to G/TiO₂ appeared healthy and retained their elongated spindle shape morphology throughout 72 hours of incubation period (Figure 6.1g-i). There were no signs of deterioration across time, while cell density was

found to increase without changes in cell appearances and membrane integrity, indicating that the presence of G/TiO₂ nanocomposites did not threaten the viability of MRC5 cells.

On the other hand, the morphologies of HaCaT cells under exposure of graphene and G/TiO₂ are illustrated in Figure 6.2. The HaCaT cell line comprises of human keratinocytes with rounded cobblestone appearance. Like MRC5 cells, HaCaT cells are anchorage-dependent and will detach from substrate upon death. HaCaT cell lines in the absence of nanocomposites served as negative controls, in which continuous proliferation and increased in cell density throughout 72 hours were observed (Figure 6.2a-c). From the optical micrographs, both graphene (Figure 6.2d-f) and G/TiO₂ (Figure 6.2g-i) demonstrated low cytotoxicity on both cell lines, inducing only minimal changes in the cell appearances. Among these 2 nanomaterials, graphene showed a slightly higher cytotoxicity with prolonged exposure, as indicated by the minimal blebbing and decrease in cell density from 48 hrs onwards. In comparison, HaCaT cells treated with G/TiO₂ nanocomposites showed no signs of cell deterioration and lowering of cell density throughout 72 hours of incubation, indicating the absence of inhibitory effects towards the proliferation of the cells.

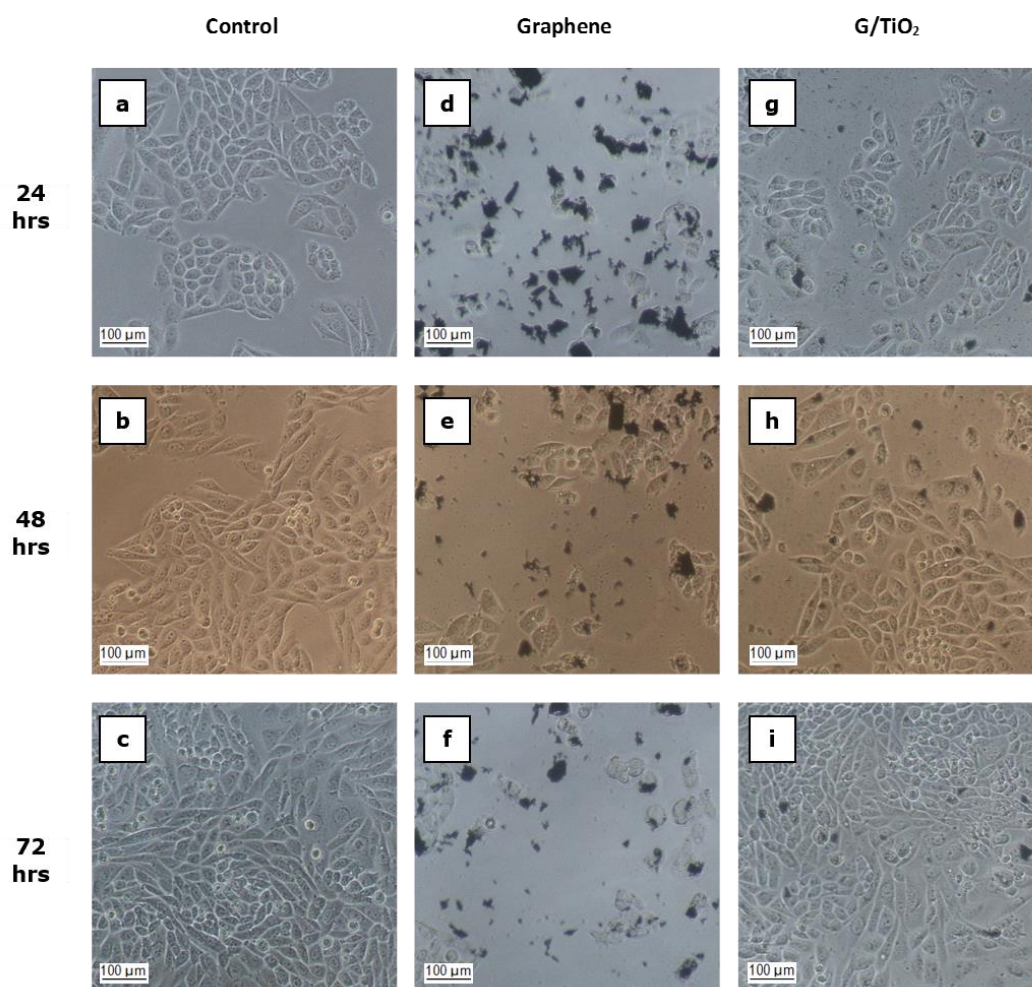


Figure 6.1. Optical microscopic morphological characterisation of untreated MRC5 cells at (a) 24 h, (b) 48 h, (c) 72 h; and MRC5 cells treated with 50 $\mu\text{g/ml}$ of graphene nanoparticles at (d) 24 h, (e) 48 h, (f) 72 h.; 50 $\mu\text{g/ml}$ of G/TiO₂ nanocomposites at (g) 24 h, (h) 48 h, (i) 72 h.

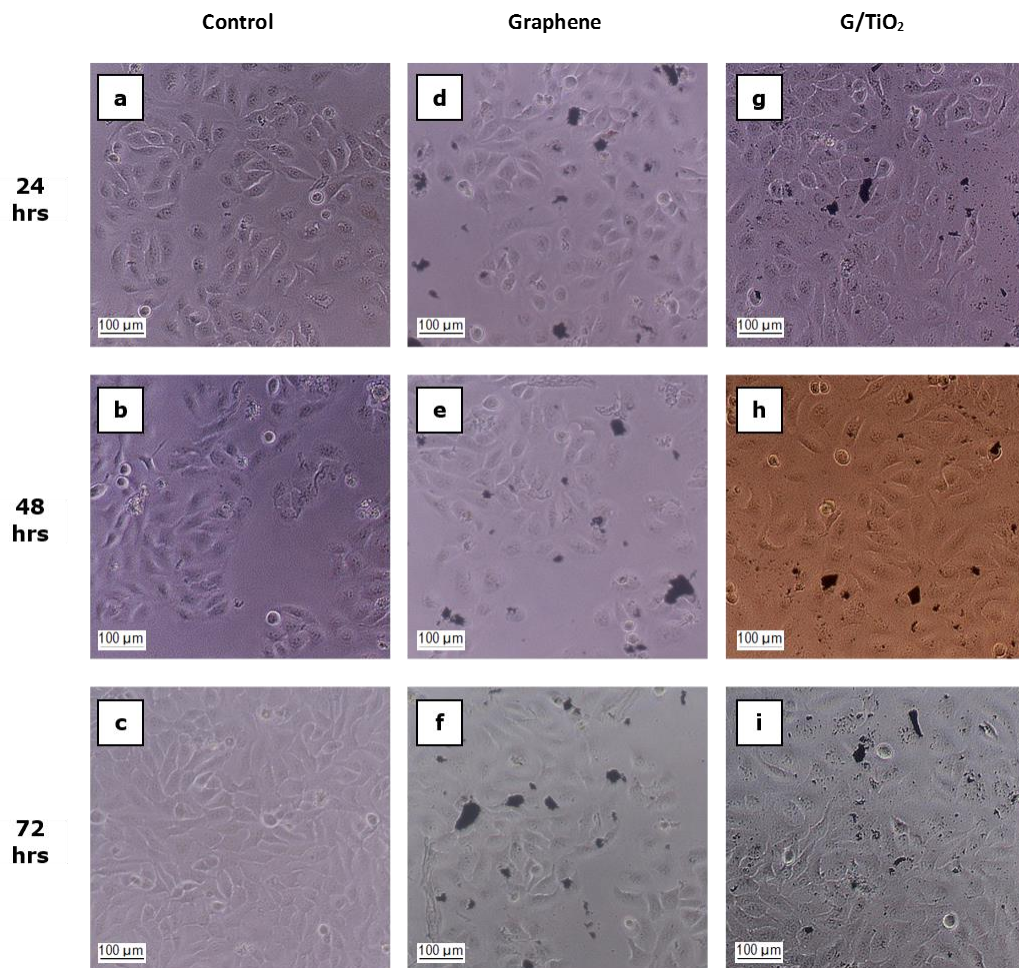


Figure 6.2. Optical microscopic morphological characterisation of untreated HaCaT cells at (a) 24 h, (b) 48 h, (c) 72 h; and HaCaT cells treated with 50 $\mu\text{g/ml}$ of graphene nanoparticles at (d) 24 h, (e) 48 h, (f) 72 h.; 50 $\mu\text{g/ml}$ of G/TiO₂ nanocomposites at (g) 24 h, (h) 48 h, (i) 72 h.

6.3.2 Cell Viability Assessment of Nanomaterials

In parallel to microscopic analysis of material-cell interaction, cell viability was evaluated via conventional MTT reduction assays. The MTT assay quantified the mitochondrial metabolic activity of the viable cells and henceforth served as indication of the intracellular redox state³⁸⁶. HaCaT cells and MRC5 cells were plated in 96-wells plate and incubated with different concentrations of graphene and G/TiO₂ nanocomposite (0.5, 2.5, 5, 25, 50, 250 and 500 µg/ml). Cell viability, calculated via Equation 6.1, was determined at several time points (24, 48, and 72 hours).

$$\text{Cell viability, \%} = \frac{\text{Absorbance}_{\text{treated sample}} - \text{Absorbance}_{\text{control}}}{\text{Absorbance}_{\text{untreated sample}}} \times 100 \quad (6.1)$$

In general, assessment of cytotoxicity of the nanomaterials through MTT assay exhibited time-dependant and dose-dependent toxic effects on cell viability, where cell viability declined greater with prolonged exposure to nanomaterials; and higher concentration of nanomaterials induced further loss of viability given the same incubation time. The cell viability profiles of MRC5 cells treated with graphene and G/TiO₂ nanocomposites of different concentrations across 72 hours, are shown in Figure 6.3. After exposure to graphene nanoparticles, both MRC5 and HaCaT cells experienced greater loss of viability with increasing incubation time. The magnitude of cell deterioration increased further at higher concentrations, with a cell viability of only 8.8% after treating MRC5 cells with 500 µg/ml of graphene nanoparticles for 72 hours. The results complied with the images seen under microscope where increasing apoptotic symptoms seen in the cell culture across time (Figure 6.1d-f). G/TiO₂ nanocomposites, however, displayed a very low cytotoxicity on MRC5 cells. Cell viability decreased with a much lower magnitude with increasing G/TiO₂

concentrations and its losses were negligible with increasing incubation time, conforming the observations made on the microscopic images previously (Figure 6.1g-i).

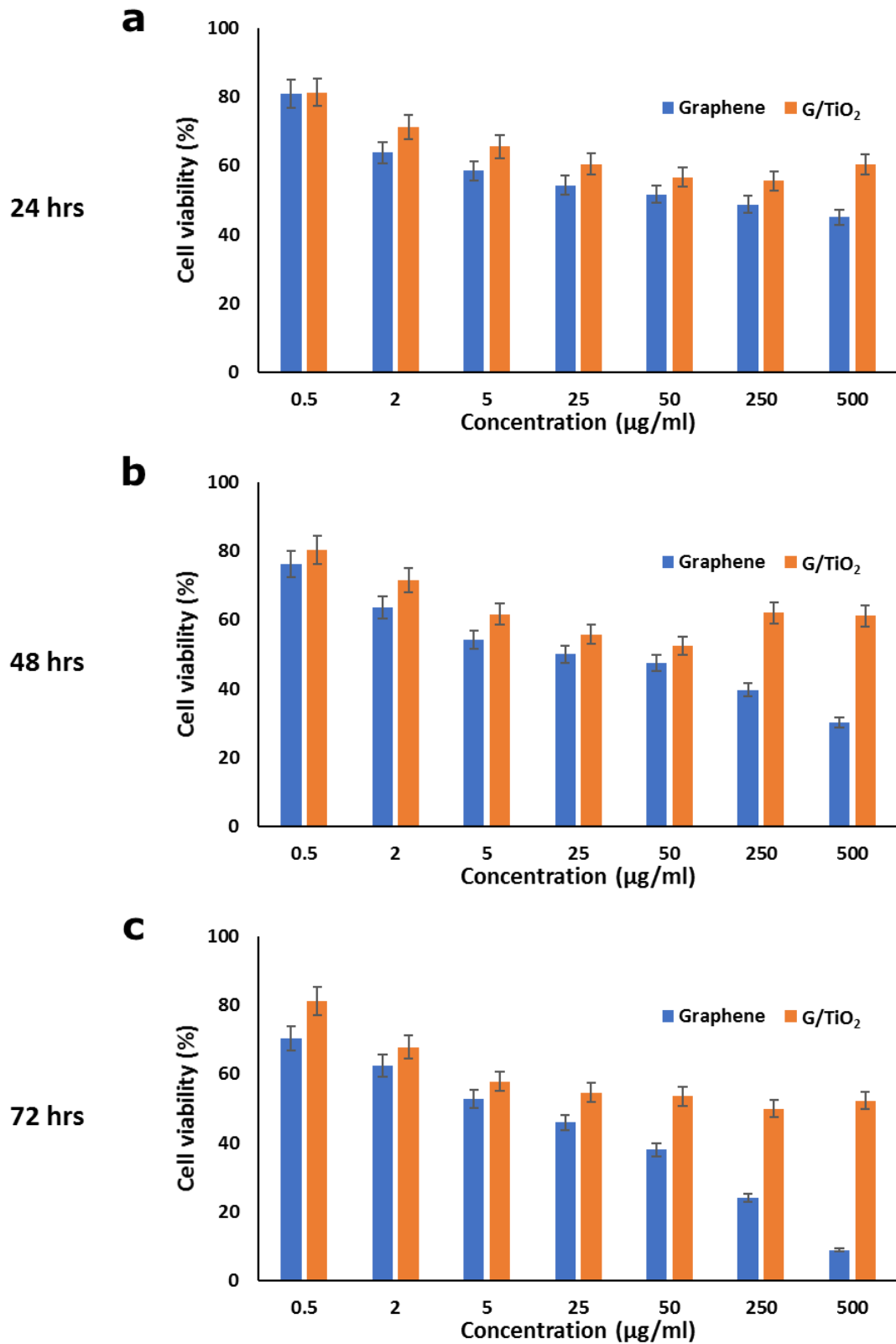


Figure 6.3. Cell viability profile of MRC5 cell line treated with graphene and G/TiO₂ nanocomposite of different concentrations at (a) 24 h, (b) 48 h, (c) 72 h. G/TiO₂ nanocomposite was found to be less cytotoxic compared to graphene.

The effects of graphene and G/TiO₂ nanocomposite towards the viability of HaCaT cells are shown in Figure 6.4. Upon incubation with graphene, the viability of HaCaT cells decreased gradually with increasing dosage and time. Treating HaCaT cells with 500 µg/ml of graphene nanoparticles for 72 hours reduced the cell viability drastically to a value of 23.4%. Similarly, upon exposure to G/TiO₂ nanoparticles, HaCaT cells experienced loss of viability with increasing incubation time and concentration, albeit at a smaller degree compared to graphene. The cell viability was at its lowest (36.7%) after treating HaCaT cells with 500 µg/ml of graphene/TiO₂ nanoparticles for 72 hours.

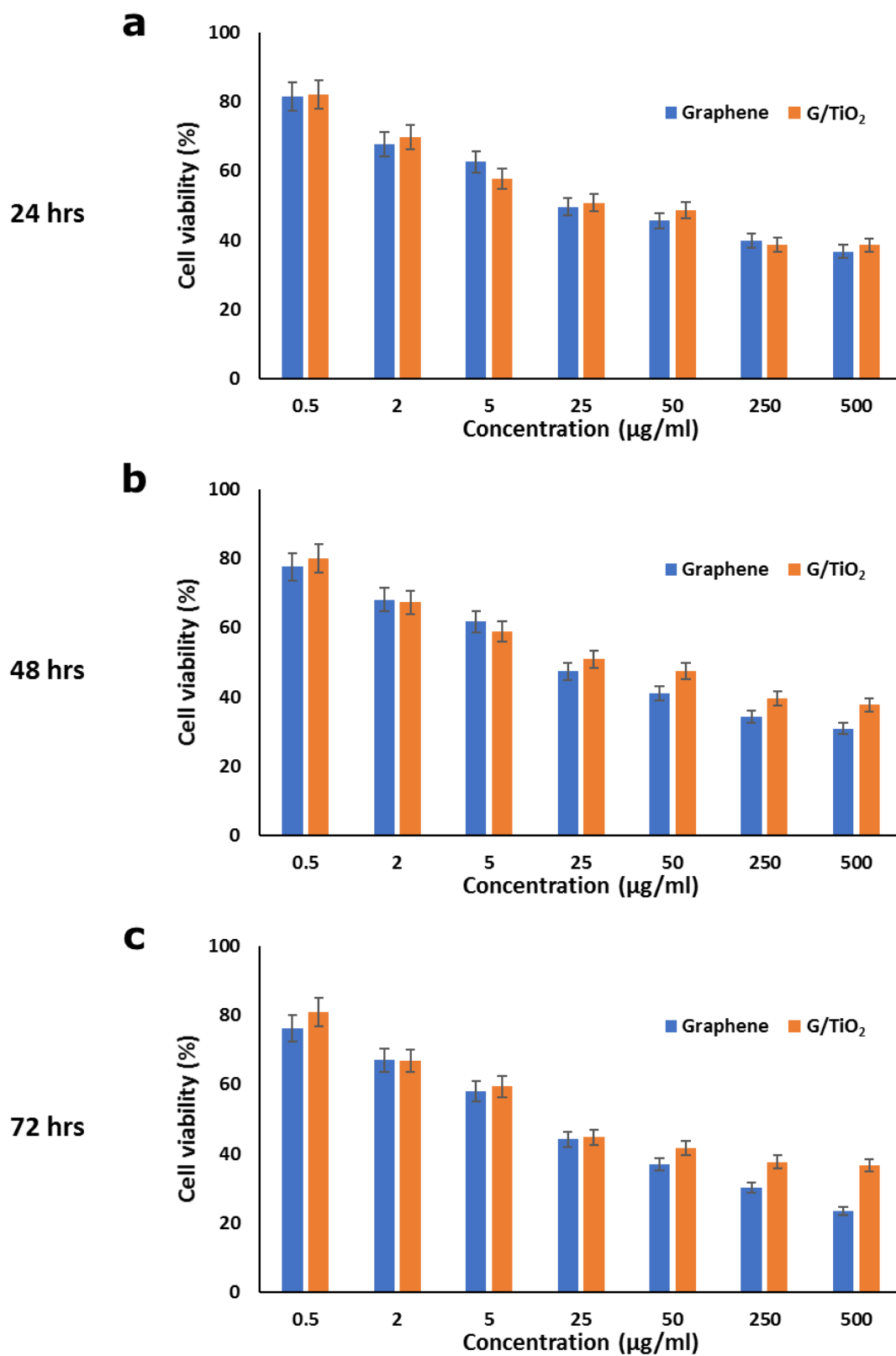


Figure 6.4. Cell viability profile of HaCaT cell line treated with graphene and G/TiO₂ nanocomposite of different concentrations at (a) 24 h, (b) 48 h, (c) 72 h. G/TiO₂ nanocomposite was found to be less cytotoxic compared to graphene.

6.3.3 Discussions

As with most nanomaterials, the cytotoxicity of graphene-based nanomaterials is heavily affected by the dosage and exposure duration, and may vary according to the cell types used³⁸⁷⁻³⁹⁰. Based on the cell viability profiles, it is apparent that G/TiO₂ displayed lower cytotoxicity across both MRC5 and HaCaT cell lines compared to graphene. While G/TiO₂ showed remarkable biocompatibility with MRC5 cells, it was observed that HaCaT cells are less resilient towards the nanocomposite, especially at higher concentrations. The cytotoxic effects of graphene were implied by the microscopic images where graphene was observed to be surrounding the MRC5 cells. Study has shown that aggregations of hydrophobic graphene-based nanomaterials could result in cell deaths or apoptosis, possibly through cell wrapping mechanism^{29, 391, 392}. When cell wrapping occurs, the agglomerated nanoparticles trap and isolate the cells, effectively disconnecting them biologically from their environment thus inhibiting glucose uptake.

The half-maximal inhibitory concentration, IC₅₀, is used to determine the lethal dosage of a substance in inhibiting biological functions, defined simply as the inhibitor concentration (in this case the concentration of nanocomposites) that decreases the cell viability by 50%³⁹³. Table 6.1 summarises the IC₅₀ for the nanomaterials in this work, compared to the IC₅₀ of other commonly used nanomaterials in biosensors fabrication. While the graphene nanomaterial investigated in this work was found to be inferior in terms of biocompatibility compared to the as-synthesised G/TiO₂ nanocomposites, it still possesses a higher IC₅₀ value compared to the values for other reported graphenic materials³⁹⁴. This improvement may be due to the exclusion of

harsh chemicals in the proposed ultrasonic-assisted liquid phase exfoliation method, as compared to other methods, such as Hummer's. The absence of harsh chemicals also avoided the formation of potentially harmful sharp edges on the graphene sheets. All in all, the in-vitro cytotoxicity study coupled with the supporting microscopic images showed that the as-synthesised G/TiO₂ is relatively biocompatible within the appropriate dosage and contact time. These promising results proved that the synthesised nanocomposite possesses a great potential as a viable candidate for the future development of biocompatible biosensors for *in-vivo* biosensing.

Table 6.1. Comparison of IC₅₀ for nanomaterials commonly used in biosensors fabrication.

NANOPARTICLES	CELL LINE	ENDPOINT	TOXICITY VALUE	REF
GRAPHENE	MRC5	MTT assay (24 h) MTT assay (48 h) MTT assay (72 h)	IC ₅₀ between 50 to 250 µg/ml IC ₅₀ ca 25 µg/ml IC ₅₀ between 5 to 25 µg/ml	This work
	HaCaT	MTT assay (24 h) MTT assay (48 h) MTT assay (72 h)	IC ₅₀ ca 25 µg/ml IC ₅₀ between 5 to 25 µg/ml IC ₅₀ between 5 to 25 µg/ml	This work
G/TIO ₂	MRC5	MTT assay (24 h) MTT assay (48 h) MTT assay (72 h)	IC ₅₀ > 500 µg/ml IC ₅₀ > 500 µg/ml IC ₅₀ > 500 µg/ml	This work
	HaCaT	MTT assay (24 h) MTT assay (48 h) MTT assay (72 h)	IC ₅₀ ca 25 µg/ml IC ₅₀ ca 25 µg/ml IC ₅₀ between 5 to 25 µg/ml	This work
ZINC OXIDE	Human fetal lung fibroblasts HFL1	ATP assay (24 h)	IC ₅₀ ca 5 µg/ml	395
	Human epithelial colorectal adenocarcinoma cells Caco2	NRU assay (24 h)	IC ₅₀ ~30.2 µg/ml	382
	Human lung adenocarcinoma cells A549	NRU assay (24 h)	IC ₅₀ ~24.9 µg/ml	382
TIO ₂	HFL1	ATP assay (48 h)	IC ₅₀ > 1000 µg/ml	395
	Caco2	NRU assay (24 h)	IC ₅₀ >100 µg/ml	382
	A549	NRU assay (24 h)	IC ₅₀ >100 µg/ml	382
SWCNT	A549	MTT assay (72 h)	IC ₅₀ between 250 to 500 µg/ml	396
GO NANOSHEETS	A549	MTT assay (24 h)	IC ₅₀ ca 100 µg/ml	397
NANO GRAPHEN OXIDE	Lymphocyte cells	Trypan Blue Exclusion assay (24 h)	IC ₅₀ = 50.07±7.2 µg/mL	398
GRAPHENE NANOPLATELETS	Mouse embryo fibroblasts	MTT assay (48 h)	IC ₅₀ ca 10 µg/ml	394

6.4 Chapter Summary

In this chapter, the biocompatibility of graphene and G/TiO₂ nanocomposites were evaluated by investigating their cytotoxic effects towards two mammalian cell lines: MRC5 and HaCaT. The cytotoxicity of the nanomaterials was found to be exposure time and dose-dependent, in which higher concentrations and prolonged incubation periods lead to higher magnitude of losses in cell viability. The correlation between the physiochemical properties (size and surface charge) of the nanomaterials and their cytotoxicity was also established. Overall, G/TiO₂ exhibited lesser cytotoxicity effects on both cell lines compared to graphene. The cytotoxicity of the nanomaterials on MRC5 cells at 24-hour time-point was determined to be IC₅₀ between 50 to 250 for graphene, and IC₅₀ > 500 µg/ml for G/TiO₂ nanocomposites. On the other hand, for HaCaT cells, the IC₅₀ was found to be around 25 µg/ml for both graphene and G/TiO₂ nanocomposite. The biocompatibility evaluation of G/TiO₂ was found to be satisfactory according to results obtained from MTT assay. In conclusion, the addition of inert TiO₂ onto graphene sheets successfully enhanced their biocompatibility, as hypothesised in the beginning of the research work. The results reported in this work affirmed that G/TiO₂ nanocomposite is a promising biocompatible nanomaterial candidate for the ever-growing field of biomedical applications such as biosensing.

Chapter 7: Conclusions and Future Direction

7.1 Conclusions

Medical diagnostics are invaluable in promoting general public health and improving mortality. In cases of fatal diseases, the ability to provide fast and accurate diagnosis of diseases at their initial and treatable pre-symptomatic stages is extremely crucial in determining effective treatment and management plan for the best clinical outcomes. However, conventional medical diagnostics often require complex equipment, centralised laboratories, complicated procedures, and slow response time, implying the void that needs to be filled in the form of a better diagnostic tool. An ideal diagnostic tool must fulfil the criteria of accessibility, simplicity, rapid, high sensitivity and specificity, and ease-of-use. The selection of electrochemical biosensor platform allows the development of rapid and easy to-use diagnostic assay. There are two key components in a biosensor that contribute to its sensitivity and selectivity: a high surface area-to-volume electrode platform for electron transfer and the use of suitable probes for specific recognition of target of interest. The choice of these components must also be low cost and easily mass producible to ensure the biosensor's accessibility. Considering safety in handling and the potential in long-term healthcare development, the material chosen should be biocompatible as well. Thus, the research had three main focuses:

1. To synthesise and characterise suitable nanomaterial as electrode platform for electrochemical sensing application. The material should have high surface to volume ratio for excellent electron transfer, easily mass producible and low toxicity

2. To develop a sensitive and selective impedimetric biosensor platform based on the nanomaterial of choice for detection of infectious or chronic disease.
3. To evaluate the cytotoxic effects of the nanomaterials of choice against human skin and lung cells since inhalation and skin contact are the major routes of exposures for nanomaterials.

The G/TiO₂ nanocomposite material take into account the high surface area to volume ratio and excellent conductivity of graphene, and the high specific surface area, porosity, and electrocatalytic effect of TiO₂ nanoparticles. In this work, G/TiO₂ nanocomposites were synthesised by utilising sonochemical exfoliation and low temperature hydrothermal approaches, which are safe, efficient, and easily scalable. Different ratios of TiO₂ precursor (TTIP) was used in the preparation of G/TiO₂ nanocomposite to determine the optimal configuration for producing G/TiO₂ with the best electrochemical performance. The different ratios were found to affect the material morphology and electrochemical performance, where the graphene-to-TTIP ratio of 1:8 emerged as the optimum ratio. With increasing ratio of TTIP, more TiO₂ nanoparticles were formed on the surfaces and edges of graphene sheets, ultimately reaching a uniform layer homogeneously covering the entire graphene sheet at 1:8 ratio. From the electrochemical analysis, the incorporation of more TiO₂ nanoparticles exhibited better electrochemical performance, likely due to improved surface area and availability of more active sites for the diffusion of analytes. However, further mass loading (1:16) resulted in agglomeration of TiO₂ nanoparticles which likely inhibit electron transfer, as observed from its deteriorating electrochemical performance. The electrochemical characterisations such CV and EIS also confirmed the superior electrochemical performance of G/TiO₂-modified electrodes compared to bare and

graphene-modified electrodes. The electrochemical sensing capabilities of G/TiO₂ nanocomposites were further evaluated through the development of a sensing platform for the detection of H₂O₂, a fundamental analyte for electrochemical biosensor development. The modified electrode demonstrated its ability to detect H₂O₂ reliably, with a sensitivity of 0.557 μA/mM and limit of detection (LOD) of 56.89 μM. The as-constructed sensor showed good selectivity towards H₂O₂ even in presence of interfering species, indicating the great potential of the nanocomposite to be utilised as the core electrode material for high-performance biosensors.

To further explore the potential of G/TiO₂ for biosensing application, immunosensor based on G/TiO₂ was developed. Dengue was chosen as the model disease since it is known to be rampant in Malaysia, and thus calling the need for an effective and cheap diagnostic tool for better disease control. To ensure high specificity, dengue envelope glycoprotein domain III (EDIII) peptide probe was used as the bio-recognition element in the dengue immunosensor due to its promising potential in specific detection of dengue. The homogeneity between dengue virus (ZIKV) and closely related flaviviruses such as Zika virus (ZIKV) was found to be a challenge for specific detection of dengue in conventional NS1-based diagnostic kits. While recent research works that incorporated EDIII into conventional ELISA approach for dengue detection has shown promising results with low cross-reactivity between closely related flaviviruses, the pioneering unison of EDIII and electrochemical-based biosensor platform reported in this work is the first of its kind. Additionally, the EDIII peptide used in this work, a consensus protein that bind specifically to all 4 serotypes of dengue (cEDIII), was obtained from a novel plant-based molecular pharming system, which can be easily mass produced at low costs. Impedimetric sensing was used in the proposed platform

as this mode of sensing allows the developed device to be label-free, leading towards a simple detection mechanism and relatively inexpensive fabrication process. Upon detection of the target analyte (dengue antibodies), the formation of cEDIII-IgG immunocomplexes creates an insulative layer on the electrode platform, whereby EIS is known to be a sensitive technique capable of detecting small changes occurring at the solution-electrode interface, which in this case, the change of charge transfer resistance resulting from the formation of insulative immunocomplexes. The cEDIII was immobilised onto the nanomaterials loaded on the working electrodes of the SPCE by functionalising the nanomaterials with a bi-functional linker, 1-pyrenebutyric acid N-hydroxysuccinimide ester (PSE), which can also be used to anchor any biomolecule with amine group present in its structure. Employing the innovative biosensing strategy, both graphene and G/TiO₂-based platforms were investigated to compare their performances. In order to optimise the sensing conditions for minimum wastage and efficient detection, the effects of different parameters such as probe concentration and incubation time were investigated for both platforms. The optimal cEDIII concentration and incubation time for the graphene-based platform were found to be 5 µg/mL and 30 minutes, respectively; and the optimal target (DENV IgG) incubation time was determined as 60 minutes. Meanwhile, for the G/TiO₂-based platform, the optimal cEDIII concentration and incubation time were 1 µg/mL and 60 minutes, respectively; and the optimal target incubation time, 60 minutes. The reduced amount of cEDIII needed for optimal response in G/TiO₂-based immunosensor is probably due to the increased specific surface area and bioaffinity provided by the TiO₂ nanoparticles adsorbed on graphene. However, a longer duration is also needed for the cEDIII molecules in the less concentrated cEDIII solution to be

properly adsorbed onto the active sites of the PSE-functionalised G/TiO₂ nanocomposites. Increasing the concentration and incubation times beyond the optimised configuration did not result in any significant differences in the detection signals. This suggests that the binding of cEDIII is still limited by the surface area and available active sites on the working electrode, and the amount of cEDIII molecules bound on the electrode surface would in turn limit the amount of cEDIII-DENV IgG immunocomplexes that could be formed, hence the saturated signal. Under optimised conditions, the as-developed graphene-based immunosensor was found to be able to detect dengue virus (DENV) 1-4 IgG antibodies as low as 5.58 pg/mL with a linearity of 62.5 pg/mL to 1 ng/mL (slope=14.444), while the G/TiO₂-based platform demonstrated higher sensitivity (slope=23.265) and lower limit of detection (2.81 pg/mL) within a linear working range of 62.5 pg/mL to 2 ng/mL. Both immunosensor exhibited high specificity towards DENV IgG, even when tested against antibodies of other infectious diseases including the closely related ZIKV. The homogeneity between dengue virus (DENV) and closely related flaviviruses such as Zika virus (ZIKV) was found to be a challenge for specific detection of dengue in conventional NS1-based diagnostic kits. As such, the ability of the proposed biosensing platforms to differentiate DENV IgG from ZIKV IgG is highly noteworthy. Comparing to the graphene-based platform, the overall performance G/TiO₂ based platform was clearly better in terms of wider linear working range, lower limit of detection and better sensitivity. The performance of the proposed biosensor platform was also evaluated against real mouse serum samples. Accordingly, the as-developed immunosensor was able to identify positive samples in a wide working range from a dilution factor of 1:500 up until 1:32,000, with results comparable to classical ELISA assay. Comparing

to conventional diagnostic methods, the proposed immunosensor exhibited rapid response time, is miniature in size and low costs, making it suitable for point-of-care diagnosis, enabling timely treatment and effective disease surveillance especially in endemic regions where resources and facilities are scarce.

While the as-synthesised nanomaterials demonstrated great potential for biosensing application, it is important to know whether they exhibit any adverse biological effects towards human. As such, preliminary study on the cytotoxicity effects of the as synthesised graphene and G/TiO₂ on two mammalian cell lines: MRC5 (lung fibroblasts) and HaCaT (keratinocytes) were evaluated. The cytotoxicity of the nanomaterials was found to be exposure time and dose-dependent, where higher concentrations and prolonged exposure lead to decrease in cell viability. Generally, G/TiO₂ exhibited lesser cytotoxic effects on both cell lines compared to graphene. The half maximal inhibitory concentrations (IC₅₀) of both nanomaterials were estimated accordingly. The cytotoxicity of the graphene on MRC5 cells at 24-hour time-point was determined to be between 50 to 250, while G/TiO₂ nanocomposites yielded the value of IC₅₀ > 500 µg/ml. In contrast, the IC₅₀ was found to be around 25 µg/ml for both graphene and G/TiO₂ nanocomposite in the case of HaCaT cells. In summary, the incorporation of inert TiO₂ onto graphene flakes demonstrated enhanced biocompatibility, as compared to graphene alone. The satisfactory biocompatibility results of G/TiO₂ nanocomposite indicated that it is a promising biocompatible nanomaterial candidate for various biomedical applications such as *in vitro* biosensing, and potentially, *in vivo* biosensing.

In short, the research work reported the great potential of G/TiO₂ nanocomposite as an electrode platform for the development of high-performance electrochemical sensor. The versatility of the sensor platform allows the immobilisation of other biomolecular probes (antibody, DNA, RNA, short peptide) for the detection of other diseases. Furthermore, the relatively lower cytotoxicity effects on human lung and skin cells suggested the potential of the proposed G/TiO₂ nanocomposite to be employed in other medical and industrial applications.

7.2 Future Directions

The work accomplished here will serve as a foundation for future works to be based upon. Despite the success of this project, efforts could be made to further the study and expand the work, as discussed below.

All of the biosensing work carried out in this research was based on commercially available screen-printed carbon electrodes (SPCE). The sensing platform was fabricated by drop-casting G/TiO₂ dispersion onto the SPCE working electrode for modification purpose. The modification step left a room for errors and inconsistencies due to the uncontrollable distribution of nanoparticles on the carbon layer. The future work could address this issue by eliminating the modification step through direct electrode fabrication or printing from G/TiO₂ nanocomposite-based ink.

The promising biosensing potential of the as-synthesised G/TiO₂ nanocomposite has been demonstrated in this research. The effective immunosensing platform developed for dengue detection represents the limitless possibilities of the G/TiO₂ nanocomposite in other biosensing and immunosensing applications. By changing the probe molecule immobilised on the G/TiO₂ platform, the biosensing platform can be tailored for the detection of other diseases.

This study has developed an immunosensor capable of detecting the IgG molecules from a mixture of DENV 1, 2, 3, and 4 serotypes. Though efficient in general dengue detection, the immunosensor could not provide serotype-specific differentiation of DENV. Future work could investigate on the serotype-specific detection of dengue using the immunosensor platform, which is extremely valuable to prevent antibody-dependent enhancement (ADE) cases in dengue that often lead to the fatal dengue

haemorrhagic fever (DHF) or dengue shock syndrome (DSS). Moreover, the immunosensing platform has only been tested on immunised mouse serum samples. To expand the research work further with the ultimate goal of commercialisation, experiment involving human serum samples must be conducted to fully represent clinical use.

The biocompatibility of the as-synthesised G/TiO₂ has been verified via the cytotoxicity assessments. Exploiting this intriguing property and the excellent electrochemical analytical performance, future works can study on revolutionary biosensor designs based on G/TiO₂ nanocomposites to develop the next generation of medical biosensors in forms of implantable devices.

References

1. T. R. Kozel and A. R. Burnham-Marusich, *Journal of clinical microbiology*, 2017, **55**, 2313-2320.
2. A. Turner, I. Karube and G. S. Wilson, *Biosensors: fundamentals and applications*, Oxford university press, 1987.
3. R. F. Taylor and J. S. Schultz, *Handbook of chemical and biological sensors*, CRC Press, 1996.
4. D. R. Thevenot, K. Toth, R. A. Durst and G. S. Wilson, *Pure and applied chemistry*, 1999, **71**, 2333-2348.
5. L. C. Clark Jr and C. Lyons, *Annals of the New York Academy of sciences*, 1962, **102**, 29-45.
6. M. Gerard, A. Chaubey and B. Malhotra, *Biosensors and bioelectronics*, 2002, **17**, 345-359.
7. H. A. Alhadrami, *Biotechnology and applied biochemistry*, 2018, **65**, 497-508.
8. A. Chaubey and B. Malhotra, *Biosensors and bioelectronics*, 2002, **17**, 441-456.
9. S. Song, Y. Qin, Y. He, Q. Huang, C. Fan and H.-Y. Chen, *Chemical Society Reviews*, 2010, **39**, 4234-4243.
10. W. Putzbach and N. Ronkainen, *Sensors*, 2013, **13**, 4811-4840.
11. M. Holzinger, A. Le Goff and S. Cosnier, *Frontiers in Chemistry*, 2014, **2**.
12. X. Zhu, J. Li, H. He, M. Huang, X. Zhang and S. Wang, *Biosensors and Bioelectronics*, 2015, **74**, 113-133.
13. A. Chen and S. Chatterjee, *Chemical Society Reviews*, 2013, **42**, 5425-5438.
14. A. Bonanni, A. H. Loo and M. Pumera, *TrAC Trends in Analytical Chemistry*, 2012, **37**, 12-21.
15. P. Mukhopadhyay and R. K. Gupta, *Graphite, Graphene, and their polymer nanocomposites*, CRC press, 2012.
16. M. Pumera, *Chemical Society Reviews*, 2010, **39**, 4146-4157.
17. S. Cinti and F. Arduini, *Biosensors and Bioelectronics*, 2017, **89**, 107-122.
18. K. S. Novoselov, A. K. Geim, S. Morozov, D. Jiang, Y. Zhang, S. a. Dubonos, I. Grigorieva and A. Firsov, *science*, 2004, **306**, 666-669.
19. D. A. Brownson and C. E. Banks, *Analyst*, 2010, **135**, 2768-2778.
20. A. K. Geim, *science*, 2009, **324**, 1530-1534.
21. Y. Shao, J. Wang, H. Wu, J. Liu, I. A. Aksay and Y. Lin, *Electroanalysis: An International Journal Devoted to Fundamental and Practical Aspects of Electroanalysis*, 2010, **22**, 1027-1036.
22. Y. Song, Y. Luo, C. Zhu, H. Li, D. Du and Y. Lin, *Biosensors and Bioelectronics*, 2016, **76**, 195-212.
23. A. T. Lawal, *Biosensors and Bioelectronics*, 2018, **106**, 149-178.
24. S. Stankovich, D. A. Dikin, G. H. Dommett, K. M. Kohlhaas, E. J. Zimney, E. A. Stach, R. D. Piner, S. T. Nguyen and R. S. Ruoff, *nature*, 2006, **442**, 282-286.
25. H. Bai, C. Li and G. Shi, *Advanced Materials*, 2011, **23**, 1089-1115.
26. P. R. Solanki, A. Kaushik, V. V. Agrawal and B. D. Malhotra, *NPG Asia Materials*, 2011, **3**, 17-24.
27. S. Bai and X. Shen, *Rsc Advances*, 2012, **2**, 64-98.
28. X. Huang, X. Qi, F. Boey and H. Zhang, *Chemical Society Reviews*, 2012, **41**, 666-686.
29. A. M. Pinto, I. C. Gonçalves and F. D. Magalhães, *Colloids and Surfaces B: Biointerfaces*, 2013, **111**, 188-202.
30. S. Syama and P. Mohanan, *International journal of biological macromolecules*, 2016, **86**, 546-555.

31. E. Topoglidis, C. J. Campbell, A. E. Cass and J. R. Durrant, *Langmuir*, 2001, **17**, 7899-7906.
32. A. Liu, M. D. Wei, I. Honma and H. Zhou, *Advanced Functional Materials*, 2006, **16**, 371-376.
33. S. J. Bao, C. M. Li, J. F. Zang, X. Q. Cui, Y. Qiao and J. Guo, *Advanced Functional Materials*, 2008, **18**, 591-599.
34. G. Anjusree, A. S. Nair, S. V. Nair and S. Vadukumpully, *RSC Advances*, 2013, **3**, 12933-12938.
35. W. S. Hummers Jr and R. E. Offeman, *Journal of the American Chemical Society*, 1958, **80**, 1339-1339.
36. B. Y. S. Chang, N. M. Huang, M. N. An'amt, A. R. Marlinda, Y. Norazriena, M. R. Muhamad, I. Harrison, H. N. Lim and C. H. Chia, *International journal of nanomedicine*, 2012, **7**, 3379.
37. T. Skaltsas, N. Karousis, H.-J. Yan, C.-R. Wang, S. Pispas and N. Tagmatarchis, *Journal of Materials Chemistry*, 2012, **22**, 21507-21512.
38. S. Park and R. S. Ruoff, *Nature nanotechnology*, 2009, **4**, 217-224.
39. A. R. Dochez and O. T. Avery, *Journal of Experimental Medicine*, 1917, **26**, 477-493.
40. R. S. Yalow and S. A. Berson, *The Journal of clinical investigation*, 1960, **39**, 1157-1175.
41. E. Engvall and P. Perlmann, *Immunochemistry*, 1971, **8**, 871-874.
42. B. Van Weemen and A. Schuurs, *FEBS letters*, 1971, **15**, 232-236.
43. R. L. Campbell, D. B. Wagner and J. P. O'connell, *Journal*, 1987.
44. K. May, M. E. Prior and I. Richards, *Journal*, 1997.
45. W. R. Heineman and W. B. Jensen, *Biosensors and Bioelectronics*, 2006, **8**, 1403-1404.
46. L. C. Clark, Jr. and C. Lyons, *Annals of the New York Academy of Sciences*, 1962, **102**, 29-45.
47. N. L. Rosi and C. A. Mirkin, *Chemical reviews*, 2005, **105**, 1547-1562.
48. S. E. McNeil, *Journal of leukocyte biology*, 2005, **78**, 585-594.
49. W.-T. Liu, *Journal of bioscience and bioengineering*, 2006, **102**, 1-7.
50. K. K. Jain, *Clinica chimica acta*, 2005, **358**, 37-54.
51. H. M. Azzazy, M. M. Mansour and S. C. Kazmierczak, *Clinical chemistry*, 2006, **52**, 1238-1246.
52. M. Pumera, *The Chemical Record*, 2009, **9**, 211-223.
53. N. Chatterjee, H.-J. Eom and J. Choi, *Biomaterials*, 2014, **35**, 1109-1127.
54. B. Nagel, H. Dellweg and L. Gierasch, *Pure and Applied Chemistry*, 1992, **64**, 143-168.
55. C. R. Lowe, *Trends in biotechnology*, 1984, **2**, 59-65.
56. F.-G. Banica, *Chemical Sensors and Biosensors: Fundamentals and Applications*, John Wiley & Sons, Chichester, UK, 2012.
57. N. Bhalla, P. Jolly, N. Formisano and P. Estrela, *Essays Biochem*, 2016, **60**, 1-8.
58. A. Koyun, E. Ahlatcolu, Y. Koca and S. Kara, *A Roadmap of Biomedical Engineers and Milestones*, 2012, 117-142.
59. J. Wang, *Chemical reviews*, 2008, **108**, 814-825.
60. U. Yogeswaran and S.-M. Chen, *Sensors*, 2008, **8**, 290-313.
61. P. Jolly, N. Formisano and P. Estrela, *Chemical Papers*, 2015, **69**, 77-89.
62. N. Bhalla, N. Formisano, A. Miodek, A. Jain, M. Di Lorenzo, G. Pula and P. Estrela, *Biosensors and Bioelectronics*, 2015, **71**, 121-128.
63. A. C. R. Grayson, R. S. Shawgo, A. M. Johnson, N. T. Flynn, Y. Li, M. J. Cima and R. Langer, *Proceedings of the IEEE*, 2004, **92**, 6-21.
64. T. K. Sharma, R. Ramanathan, R. Rakwal, G. K. Agrawal and V. Bansal, *Proteomics*, 2015, **15**, 1680-1692.
65. M. Gavrilescu, K. Demnerová, J. Aamand, S. Agathos and F. Fava, *New biotechnology*, 2015, **32**, 147-156.

66. B. M. Paddle, *Biosensors and Bioelectronics*, 1996, **11**, 1079-1113.
67. L. A. Currie, *Pure and applied chemistry*, 1995, **67**, 1699-1723.
68. R. Ekins and P. Edwards, *Clinical chemistry*, 1997, **43**, 1824-1831.
69. G. M. Lawson, *Clinical chemistry*, 1994, **40**, 1218-1219.
70. D. A. Armbruster and T. Pry, *The clinical biochemist reviews*, 2008, **29**, S49.
71. V. L. D. S. N. Button, in *Principles of Measurement and Transduction of Biomedical Variables*, ed. V. L. D. S. N. Button, Academic Press, Oxford, 2015, DOI: <https://doi.org/10.1016/B978-0-12-800774-7.00001-5>, pp. 1-24.
72. I. BiPM, I. IFcc, I. IUPAC and O. ISO, *JcGM*, 2012, **200**, 2012.
73. P. Damborský, J. Švitel and J. Katrlík, *Essays Biochem*, 2016, **60**, 91-100.
74. M. A. Cooper, *Nature reviews Drug discovery*, 2002, **1**, 515.
75. L. Nicu, M. Guirardel, F. Chambosse, P. Rougerie, S. Hinh, E. Trevisiol, J.-M. Francois, J.-P. Majoral, A.-M. Caminade and E. Cattan, *Sensors and Actuators B: chemical*, 2005, **110**, 125-136.
76. C. Karunakaran, R. Rajkumar and K. Bhargava, in *Biosensors and bioelectronics*, Elsevier, 2015, pp. 1-68.
77. A. Kumar, *JOM-e*, 2000, **52**, 1-6.
78. B. Xie, K. Ramanathan and B. Danielsson, in *Thermal Biosensors, Bioactivity, Bioaffinity*, Springer, 1999, pp. 1-33.
79. T. Maskow, K. Wolf, W. Kunze, S. Enders and H. Harms, *Thermochimica acta*, 2012, **543**, 273-280.
80. P. Kirchner, J. Oberländer, P. Friedrich, J. Berger, G. Rysstad, M. Keusgen and M. J. Schöning, *Sensors and Actuators B: Chemical*, 2012, **170**, 60-66.
81. D. K. Soni, R. Ahmad and S. K. Dubey, *Critical reviews in microbiology*, 2018, **44**, 590-608.
82. K. K. Mistry, K. Layek, A. Mahapatra, C. RoyChaudhuri and H. Saha, *Analyst*, 2014, **139**, 2289-2311.
83. Ü. Anik, in *Medical Biosensors for Point of Care (POC) Applications*, Elsevier, 2017, pp. 275-292.
84. E. B. Bahadır and M. K. Sezgentürk, *Biosensors and Bioelectronics*, 2015, **68**, 62-71.
85. N. F. Silva, J. M. Magalhães, C. Freire and C. Delerue-Matos, *Biosensors and Bioelectronics*, 2018, **99**, 667-682.
86. S. J. Sadeghi, *Encyclopedia of Biophysics*, 2013, 61-67.
87. J. Wang, M. Musameh and Y. Lin, *Journal of the American Chemical Society*, 2003, **125**, 2408-2409.
88. S. Updike and G. Hicks, *Nature*, 1967, **214**, 986.
89. M. Belluzo, M. Ribone and C. Lagier, *Sensors*, 2008, **8**, 1366-1399.
90. T. Tsuchida and K. Yoda, *Clinical Chemistry*, 1983, **29**, 51-55.
91. M. Senda and Y. Yamamoto, *Electroanalysis*, 1993, **5**, 775-779.
92. G. J. Kost, T. H. Nguyen and Z. Tang, *Archives of pathology & laboratory medicine*, 2000, **124**, 1128-1134.
93. M. Gilis, H. Durliat and M. Comtat, *Analytica chimica acta*, 1997, **355**, 235-240.
94. J. Okuno, K. Maehashi, K. Kerman, Y. Takamura, K. Matsumoto and E. Tamiya, *Biosensors and Bioelectronics*, 2007, **22**, 2377-2381.
95. F. Li, Y. Li, J. Feng, Y. Dong, P. Wang, L. Chen, Z. Chen, H. Liu and Q. Wei, *Biosensors and Bioelectronics*, 2017, **87**, 630-637.
96. H. Tang, J. Chen, L. Nie, Y. Kuang and S. Yao, *Biosensors and Bioelectronics*, 2007, **22**, 1061-1067.
97. X. Gao, Y. Zhang, H. Chen, Z. Chen and X. Lin, *Analytical biochemistry*, 2011, **414**, 70-76.

98. M. Aizawa, A. Morioka, S. Suzuki and Y. Nagamura, *Analytical biochemistry*, 1979, **94**, 22-28.
99. R. Pemberton, J. Hart and T. Mottram, *Biosensors and Bioelectronics*, 2001, **16**, 715-723.
100. A. A. P. Ferreira, W. Colli, P. I. da Costa and H. Yamanaka, *Biosensors and Bioelectronics*, 2005, **21**, 175-181.
101. M. E. Ribone, M. S. Belluzo, D. Pagani, I. S. Macipar and C. M. Lagier, *Analytical biochemistry*, 2006, **350**, 61-70.
102. Y.-M. Zhou, Z.-Y. Wu, G.-L. Shen and R.-Q. Yu, *Sensors and Actuators B: Chemical*, 2003, **89**, 292-298.
103. B. Kazmierczak, D. Pijanowska, A. Baraniecka, M. Dawgul, J. Kruk and W. Torbicz, *Biocybernetics and Biomedical Engineering*, 2016, **36**, 29-41.
104. Q. Yan, L. Cao, H. Dong, Z. Tan, Q. Liu, W. Zhang, P. Zhao, Y. Li, Y. Liu and Y. Dong, *Analytica chimica acta*, 2019, **1069**, 117-125.
105. P. Protti, *AMEL srl*, 2001, p10.
106. A. J. Bard and L. R. Faulkner, *Electrochemical Methods*, 2001, **2**, 482.
107. H. S. Ali, A. A. Abdullah, P. T. Pinar, Y. Yardim and Z. Şentürk, *Talanta*, 2017, **170**, 384-391.
108. J. F. Rusling and S. L. Suib, *Advanced Materials*, 1994, **6**, 922-930.
109. P. Joshi and D. S. Sutrave, *International Journal of ChemTech Research*, 2018, **11**, 77-88.
110. F. Zhao, R. C. Slade and J. R. Varcoe, *Chemical Society Reviews*, 2009, **38**, 1926-1939.
111. A. Stobiecka, H. Radecka and J. Radecki, *Biosensors and bioelectronics*, 2007, **22**, 2165-2170.
112. O. D. Leite, K. O. Lupetti, O. Fatibello-Filho, I. C. Vieira and A. de M Barbosa, *Talanta*, 2003, **59**, 889-896.
113. K. M. Millan, A. Saraullo and S. R. Mikkelsen, *Analytical chemistry*, 1994, **66**, 2943-2948.
114. R. N. Goyal, V. K. Gupta and S. Chatterjee, *Sensors and Actuators B: Chemical*, 2010, **149**, 252-258.
115. M. M. Neves, M. B. González-García, A. Santos-Silva and A. Costa-García, *Sensors and Actuators B: Chemical*, 2012, **163**, 253-259.
116. V. Singh and S. Krishnan, *Analytical chemistry*, 2015, **87**, 2648-2654.
117. C. Thunkhamrak, P. Chuntib, K. Ounnunkad, P. Banet, P.-H. Aubert, G. Saianand, A.-I. Gopalan and J. Jakmunee, *Talanta*, 2020, **208**, 120389.
118. A. J. Bard, L. R. Faulkner, J. Leddy and C. G. Zoski, *Electrochemical methods: fundamentals and applications*, Wiley New York, 1980.
119. E. Bakker, in *Environmental Analysis by Electrochemical Sensors and Biosensors*, Springer, 2014, pp. 193-238.
120. N. R. Stradiotto, H. Yamanaka and M. V. B. Zanoni, *Journal of the Brazilian Chemical Society*, 2003, **14**, 159-173.
121. K. M. May, A. Vogt, L. G. Bachas and K. W. Anderson, *Analytical and bioanalytical chemistry*, 2005, **382**, 1010-1016.
122. C.-I. Feng, Y.-h. Xu and L.-m. Song, *Sensors and Actuators B: Chemical*, 2000, **66**, 190-192.
123. Y. Wang, Z. Zhang, V. Jain, J. Yi, S. Mueller, J. Sokolov, Z. Liu, K. Levon, B. Rigas and M. H. Rafailovich, *Sensors and Actuators B: Chemical*, 2010, **146**, 381-387.
124. N. F. Silva, C. M. Almeida, J. M. Magalhães, M. P. Gonçalves, C. Freire and C. Delerue-Matos, *Biosensors and Bioelectronics*, 2019, 111317.
125. E. P. Randviir and C. E. Banks, *Analytical Methods*, 2013, **5**, 1098-1115.

126. O. Heaviside, *The London, Edinburgh, and Dublin Philosophical Magazine and Journal of Science*, 1887, **24**, 479-502.
127. D. D. Macdonald, *Electrochimica Acta*, 2006, **51**, 1376-1388.
128. E. Barsoukov and J. R. Macdonald, *Impedance spectroscopy: theory, experiment, and applications*, John Wiley & Sons, 2018.
129. E. Katz and I. Willner, *Electroanalysis: An International Journal Devoted to Fundamental and Practical Aspects of Electroanalysis*, 2003, **15**, 913-947.
130. A. Lasia, in *Modern aspects of electrochemistry*, Springer, 2002, pp. 143-248.
131. C. Yuh and J. Selman, *AIChE journal*, 1988, **34**, 1949-1958.
132. E. Karden, S. Buller and R. W. De Doncker, *Journal of Power sources*, 2000, **85**, 72-78.
133. R. Wiart, *Electrochimica Acta*, 1990, **35**, 1587-1593.
134. I. I. Suni, *TrAC Trends in Analytical Chemistry*, 2008, **27**, 604-611.
135. L. Yang and R. Bashir, *Biotechnology advances*, 2008, **26**, 135-150.
136. M. Jie, C. Y. Ming, D. Jing, L. S. Cheng, F. Jun and C. Y. Xiang, *Electrochemistry communications*, 1999, **1**, 425-428.
137. S. Sharma, J. Zapatero-Rodríguez, R. Saxena, R. O'Kennedy and S. Srivastava, *Biosensors and Bioelectronics*, 2018, **106**, 78-85.
138. A. D. Chowdhury, A. De, C. R. Chaudhuri, K. Bandyopadhyay and P. Sen, *Sensors and Actuators B: Chemical*, 2012, **171**, 916-923.
139. P. N. Asrami, S. A. Mozaffari, M. S. Tehrani and P. A. Azar, *International journal of biological macromolecules*, 2018, **118**, 649-660.
140. M. Steinmetz, D. Lima, A. G. Viana, S. T. Fujiwara, C. A. Pessôa, R. M. Etto and K. Wohnrath, *Biosensors and Bioelectronics*, 2019, **141**, 111351.
141. A. K. Geim and K. S. Novoselov, in *Nanoscience and Technology: A Collection of Reviews from Nature Journals*, World Scientific, 2010, pp. 11-19.
142. M. S. A. Bhuyan, M. N. Uddin, M. M. Islam, F. A. Bipasha and S. S. Hossain, *International Nano Letters*, 2016, **6**, 65-83.
143. A. Shekhawat and R. O. Ritchie, *Nature communications*, 2016, **7**, 10546.
144. M. Chakraborty and M. S. J. Hashmi, *Advances in Materials and Processing Technologies*, 2018, **4**, 573-602.
145. K. I. Bolotin, K. J. Sikes, Z. Jiang, M. Klima, G. Fudenberg, J. Hone, P. Kim and H. Stormer, *Solid State Communications*, 2008, **146**, 351-355.
146. S. Morozov, K. Novoselov, M. Katsnelson, F. Schedin, D. Elias, J. A. Jaszczak and A. Geim, *Physical review letters*, 2008, **100**, 016602.
147. C. Lee, X. Wei, J. W. Kysar and J. Hone, *science*, 2008, **321**, 385-388.
148. A. A. Balandin, S. Ghosh, W. Bao, I. Calizo, D. Teweldebrhan, F. Miao and C. N. Lau, *Nano letters*, 2008, **8**, 902-907.
149. X. J. Lee, B. Y. Z. Hiew, K. C. Lai, L. Y. Lee, S. Gan, S. Thangalazhy-Gopakumar and S. Rigby, *Journal of the Taiwan Institute of Chemical Engineers*, 2019, **98**, 163-180.
150. J. Moser, A. Barreiro and A. Bachtold, *Applied Physics Letters*, 2007, **91**, 163513.
151. T. Kuila, S. Bose, A. K. Mishra, P. Khanra, N. H. Kim and J. H. Lee, *Progress in Materials Science*, 2012, **57**, 1061-1105.
152. Y. Chen, C. Tan, H. Zhang and L. Wang, *Chemical Society Reviews*, 2015, **44**, 2681-2701.
153. B. Y. Z. Hiew, L. Y. Lee, X. J. Lee, S. Thangalazhy-Gopakumar, S. Gan, S. S. Lim, G.-T. Pan, T. C.-K. Yang, W. S. Chiu and P. S. Khiew, *Process Safety and Environmental Protection*, 2018, **116**, 262-286.
154. A. Van Bommel, J. Crombeen and A. Van Tooren, *Surface Science*, 1975, **48**, 463-472.
155. C. Berger, Z. Song, T. Li, X. Li, A. Y. Ogbazghi, R. Feng, Z. Dai, A. N. Marchenkov, E. H. Conrad and P. N. First, *The Journal of Physical Chemistry B*, 2004, **108**, 19912-19916.
156. W. A. De Heer, C. Berger, X. Wu, P. N. First, E. H. Conrad, X. Li, T. Li, M. Sprinkle, J. Hass and M. L. Sadowski, *Solid State Communications*, 2007, **143**, 92-100.

157. P. Kumar and M. Wani, *Jurnal Tribologi*, 2017, **13**, 36-71.
158. K. V. Emtsev, A. Bostwick, K. Horn, J. Jobst, G. L. Kellogg, L. Ley, J. L. McChesney, T. Ohta, S. A. Reshanov and J. Röhrl, *Nature materials*, 2009, **8**, 203-207.
159. B. Gupta, M. Notarianni, N. Mishra, M. Shafiei, F. Iacopi and N. Motta, *Carbon*, 2014, **68**, 563-572.
160. V. Singh, D. Joung, L. Zhai, S. Das, S. I. Khondaker and S. Seal, *Progress in materials science*, 2011, **56**, 1178-1271.
161. W. Norimatsu and M. Kusunoki, *Physical Chemistry Chemical Physics*, 2014, **16**, 3501-3511.
162. J. Campos-Delgado, A. R. Botello-Méndez, G. Algara-Siller, B. Hackens, T. Pardoën, U. Kaiser, M. S. Dresselhaus, J.-C. Charlier and J.-P. Raskin, *Chemical Physics Letters*, 2013, **584**, 142-146.
163. B. H. Min, D. W. Kim, K. H. Kim, H. O. Choi, S. W. Jang and H.-T. Jung, *Carbon*, 2014, **80**, 446-452.
164. D. A. Brownson and C. E. Banks, *Physical Chemistry Chemical Physics*, 2012, **14**, 8264-8281.
165. K. S. Kim, Y. Zhao, H. Jang, S. Y. Lee, J. M. Kim, K. S. Kim, J.-H. Ahn, P. Kim, J.-Y. Choi and B. H. Hong, *Nature*, 2009, **457**, 706-710.
166. Q. Yu, J. Lian, S. Siriponglert, H. Li, Y. P. Chen and S.-S. Pei, *Applied Physics Letters*, 2008, **93**, 113103.
167. M. Choucair, P. Thordarson and J. A. Stride, *Nature Nanotechnology*, 2009, **4**, 30-33.
168. L. Speyer, S. Fontana, S. Cahen, J. Ghanbaja, G. Medjahdi and C. Hérol, *Solid State Sciences*, 2015, **50**, 42-51.
169. W. Wang, S. Chakrabarti, Z. Chen, Z. Yan, M. O. Tade, J. Zou and Q. Li, *Journal of Materials Chemistry A*, 2014, **2**, 2390-2396.
170. C.-D. Kim, B.-K. Min and W.-S. Jung, *Carbon*, 2009, **47**, 1610-1612.
171. A. Chakrabarti, J. Lu, J. C. Skrabutenas, T. Xu, Z. Xiao, J. A. Maguire and N. S. Hosmane, *Journal of Materials Chemistry*, 2011, **21**, 9491-9493.
172. D. R. Dreyer, S. Park, C. W. Bielawski and R. S. Ruoff, *Chemical Society Reviews*, 2010, **39**, 228-240.
173. D. C. Marcano, D. V. Kosynkin, J. M. Berlin, A. Sinitskii, Z. Sun, A. Slesarev, L. B. Alemany, W. Lu and J. M. Tour, *ACS nano*, 2010, **4**, 4806-4814.
174. S. Stankovich, D. A. Dikin, R. D. Piner, K. A. Kohlhaas, A. Kleinhammes, Y. Jia, Y. Wu, S. T. Nguyen and R. S. Ruoff, *Carbon*, 2007, **45**, 1558-1565.
175. G. Brumfiel, *Nature*, 2009.
176. L. Jiao, L. Zhang, X. Wang, G. Diankov and H. Dai, *Nature*, 2009, **458**, 877-880.
177. D. V. Kosynkin, A. L. Higginbotham, A. Sinitskii, J. R. Lomeda, A. Dimiev, B. K. Price and J. M. Tour, *Nature*, 2009, **458**, 872-876.
178. L. Jiao, X. Wang, G. Diankov, H. Wang and H. Dai, *Nature nanotechnology*, 2010, **5**, 321-325.
179. I. Janowska, O. Ersen, T. Jacob, P. Vennégues, D. Bégin, M.-J. Ledoux and C. Pham-Huu, *Applied Catalysis A: General*, 2009, **371**, 22-30.
180. J. Chen, L. Chen, Z. Zhang, J. Li, L. Wang and W. Jiang, *Carbon*, 2012, **50**, 1934-1941.
181. J. Lu, J.-x. Yang, J. Wang, A. Lim, S. Wang and K. P. Loh, *ACS nano*, 2009, **3**, 2367-2375.
182. K. Parvez, R. Li, S. R. Puniredd, Y. Hernandez, F. Hinkel, S. Wang, X. Feng and K. Müllen, *ACS nano*, 2013, **7**, 3598-3606.
183. M. Hofmann, W.-Y. Chiang, T. D. Nguyễn and Y.-P. Hsieh, *Nanotechnology*, 2015, **26**, 335607.
184. J. H. Hildebrand, J. M. Prausnitz and R. L. Scott, *Regular and related solutions: the solubility of gases, liquids, and solids*, Van Nostrand Reinhold New York, 1970.
185. J. N. Coleman, *Accounts of chemical research*, 2012, **46**, 14-22.

186. Y. Hernandez, V. Nicolosi, M. Lotya, F. M. Blighe, Z. Sun, S. De, I. McGovern, B. Holland, M. Byrne and Y. K. Gun'Ko, *Nature nanotechnology*, 2008, **3**, 563-568.
187. J. Paredes, S. Villar-Rodil, A. Martinez-Alonso and J. Tascon, *Langmuir*, 2008, **24**, 10560-10564.
188. A. O'Neill, U. Khan, P. N. Nirmalraj, J. Boland and J. N. Coleman, *The Journal of Physical Chemistry C*, 2011, **115**, 5422-5428.
189. X. Li, X. Wang, L. Zhang, S. Lee and H. Dai, *Science*, 2008, **319**, 1229-1232.
190. C. Ling, G. Setzler, M.-W. Lin, K. S. Dhindsa, J. Jin, H. J. Yoon, S. S. Kim, M. M.-C. Cheng, N. Widjaja and Z. Zhou, *Nanotechnology*, 2011, **22**, 325201.
191. M. Lotya, Y. Hernandez, P. J. King, R. J. Smith, V. Nicolosi, L. S. Karlsson, F. M. Blighe, S. De, Z. Wang and I. McGovern, *Journal of the American Chemical Society*, 2009, **131**, 3611-3620.
192. K. G. Zhou, N. N. Mao, H. X. Wang, Y. Peng and H. L. Zhang, *Angewandte Chemie International Edition*, 2011, **50**, 10839-10842.
193. J. S. Y. Chia, M. T. Tan, P. S. Khiew, J. K. Chin, H. Lee, D. Bien and W. S. Chiu, *Chemical Engineering Journal*, 2014, **249**, 270-278.
194. M. J. Allen, V. C. Tung and R. B. Kaner, *Chemical reviews*, 2009, **110**, 132-145.
195. S. K. Vashist and J. H. Luong, *Carbon*, 2015, **84**, 519-550.
196. J. S. Y. Chia, M. T. Tan, P. S. Khiew, J. K. Chin and C. W. Siong, *Sensors and Actuators B: Chemical*, 2015, **210**, 558-565.
197. M. Amatongchai, W. Sroysee, S. Chairam and D. Nacapricha, *Talanta*, 2017, **166**, 420-427.
198. B. Thirumalraj, C. Rajkumar, S.-M. Chen and P. Barathi, *Journal of Materials Chemistry B*, 2016, **4**, 6335-6343.
199. A. K. Deb, S. C. Das, A. Saha, M. B. Wayu, M. H. Marksberry, R. J. Baltz and C. C. Chusuei, *Journal of Applied Electrochemistry*, 2016, **46**, 289-298.
200. S.-M. Li, Y.-S. Wang, S.-T. Hsiao, W.-H. Liao, C.-W. Lin, S.-Y. Yang, H.-W. Tien, C.-C. M. Ma and C.-C. Hu, *Journal of Materials Chemistry C*, 2015, **3**, 9444-9453.
201. D. Sangamithirai, V. Narayanan, B. Muthuraaman and A. Stephen, *Materials Science and Engineering: C*, 2015, **55**, 579-591.
202. A. Cernat, M. Tertiş, R. Săndulescu, F. Bedioui, A. Cristea and C. Cristea, *Analytica chimica acta*, 2015, **886**, 16-28.
203. F. Arduini, L. Micheli, D. Moscone, G. Palleschi, S. Piermarini, F. Ricci and G. Volpe, *TrAC Trends in Analytical Chemistry*, 2016, **79**, 114-126.
204. Y. Zheng, Z. Liu, Y. Jing, J. Li and H. Zhan, *Sensors and Actuators B: Chemical*, 2015, **210**, 389-397.
205. N. Chauhan, T. Maekawa and D. N. S. Kumar, *Journal of Materials Research*, 2017, **32**, 2860-2882.
206. S. S. Low, J. S. Y. Chia, M. T. Tan, H.-S. Loh, P. S. Khiew, A. Singh and W. S. Chiu, *Journal of nanoscience and nanotechnology*, 2016, **16**, 2438-2446.
207. P. A. Rasheed and N. Sandhyarani, *Sensors and Actuators B: Chemical*, 2014, **204**, 777-782.
208. S. Singal, A. K. Srivastava, S. Dhakate and A. M. Biradar, *Rsc Advances*, 2015, **5**, 74994-75003.
209. H. Y. Mao, S. Laurent, W. Chen, O. Akhavan, M. Imani, A. A. Ashkarran and M. Mahmoudi, *Chemical reviews*, 2013, **113**, 3407-3424.
210. A. Ambrosi, C. K. Chua, A. Bonanni and M. Pumera, *Chemical reviews*, 2014, **114**, 7150-7188.
211. S. Hrapovic, E. Majid, Y. Liu, K. Male and J. H. Luong, *Analytical chemistry*, 2006, **78**, 5504-5512.

212. S. N. A. Mohd Yazid, I. Md Isa, S. Abu Bakar, N. Hashim and S. Ab Ghani, *Analytical Letters*, 2014, **47**, 1821-1834.
213. W. Q. Lim and Z. Gao, *Electroanalysis*, 2015, **27**, 2074-2090.
214. S. Immanuel, T. K. Aparna and R. Sivasubramanian, in *Graphene-Based Electrochemical Sensors for Biomolecules*, eds. A. Pandikumar and P. Rameshkumar, Elsevier, 2019, DOI: <https://doi.org/10.1016/B978-0-12-815394-9.00005-4>, pp. 113-138.
215. S. Kumar, S. D. Bukkitgar, S. Singh, V. Singh, K. R. Reddy, N. P. Shetti, C. Venkata Reddy, V. Sadhu and S. Naveen, *ChemistrySelect*, 2019, **4**, 5322-5337.
216. Z. Zhu, L. Garcia-Gancedo, A. J. Flewitt, H. Xie, F. Moussy and W. I. Milne, *Sensors*, 2012, **12**, 5996-6022.
217. L. Zhu, S. Zhang, Y. Cui, H. Song and X. Chen, *Electrochimica Acta*, 2013, **89**, 18-23.
218. A. M. Golsheikh, N. M. Huang, H. N. Lim, C. H. Chia, I. Harrison and M. Muhamad, *Chemical Engineering Journal*, 2013, **218**, 276-284.
219. S. Wang, S. P. Jiang and X. Wang, *Electrochimica Acta*, 2011, **56**, 3338-3344.
220. J. Luo, S. Jiang, H. Zhang, J. Jiang and X. Liu, *Analytica Chimica Acta*, 2012, **709**, 47-53.
221. S. Sheshmani and R. Amini, *Carbohydrate Polymers*, 2013, **95**, 348-359.
222. Y. Zhao, J. Li, C. Wu and L. Guan, *Nanoscale Research Letters*, 2011, **6**, 71.
223. H. N. Lim, R. Nurzulaikha, I. Harrison, S. Lim, W. Tan, M. Yeo, M. A. Yarmo and N. Huang, *Ceramics International*, 2012, **38**, 4209-4216.
224. X. Wang, C. Hu, H. Liu, G. Du, X. He and Y. Xi, *Sensors and Actuators B: Chemical*, 2010, **144**, 220-225.
225. C. Batchelor-McAuley, Y. Du, G. G. Wildgoose and R. G. Compton, *Sensors and Actuators B: Chemical*, 2008, **135**, 230-235.
226. E. Reitz, W. Jia, M. Gentile, Y. Wang and Y. Lei, *Electroanalysis*, 2008, **20**, 2482-2486.
227. L. Luo, L. Zhu and Z. Wang, *Bioelectrochemistry*, 2012, **88**, 156-163.
228. Y.-W. Hsu, T.-K. Hsu, C.-L. Sun, Y.-T. Nien, N.-W. Pu and M.-D. Ger, *Electrochimica Acta*, 2012, **82**, 152-157.
229. Y. Qian, F. Ye, J. Xu and Z.-G. Le, *International Journal of Electrochemical Science*, 2012, **7**, 10063-10073.
230. H.-X. Wu, W.-M. Cao, Y. Li, G. Liu, Y. Wen, H.-F. Yang and S.-P. Yang, *Electrochimica Acta*, 2010, **55**, 3734-3740.
231. L. Nagy and G. Nagy, *Microchemical Journal*, 2006, **84**, 70-74.
232. Y. Li, F. Huang, J. Chen, T. Mo, S. Li, F. Wang, S. Feng and Y. Li, *International Journal of Electrochemical Science*, 2013, **8**, 6332-6342.
233. H. Wang, Y. Zhang, Y. Wang, H. Ma, B. Du and Q. Wei, *Biosensors and Bioelectronics*, 2017, **87**, 745-751.
234. T. Kavitha, A. I. Gopalan, K.-P. Lee and S.-Y. Park, *Carbon*, 2012, **50**, 2994-3000.
235. K. Lee, S. Park and J. Lee, *Journal of Materials Science Letters*, 2003, **22**, 65-67.
236. G. T. Rao and D. T. Rao, *Sensors and Actuators B: Chemical*, 1999, **55**, 166-169.
237. T. Gao and T. Wang, *Applied Physics A*, 2005, **80**, 1451-1454.
238. N. Koshizaki and T. Oyama, *Sensors and Actuators B: Chemical*, 2000, **66**, 119-121.
239. C. Wang, X. Chu and M. Wu, *Sensors and Actuators B: Chemical*, 2006, **113**, 320-323.
240. B. Kang, Y. Heo, L. Tien, D. Norton, F. Ren, B. Gila and S. Pearton, *Applied Physics A*, 2005, **80**, 1029-1032.
241. Y. Zhang, K. Yu, D. Jiang, Z. Zhu, H. Geng and L. Luo, *Applied Surface Science*, 2005, **242**, 212-217.
242. J. Lu, K. M. Ng and S. Yang, *Industrial & Engineering Chemistry Research*, 2008, **47**, 1095-1101.
243. J. Zang, C. M. Li, X. Cui, J. Wang, X. Sun, H. Dong and C. Q. Sun, *Electroanalysis*, 2007, **19**, 1008-1014.

244. P. Norouzi, H. Ganjali, B. Larijani, M. R. Ganjali, F. Faridbod and H. A. Zamani, *International Journal of Electrochemical Science*, 2011, **6**, 5189-5195.
245. S. Palanisamy, A. E. Vilian and S.-M. Chen, *International Journal of Electrochemical Science*, 2012, **7**, 2153-2163.
246. S. S. Low, H.-S. Loh, J. S. Boey, P. S. Khiew, W. S. Chiu and M. T. Tan, *Biosensors and Bioelectronics*, 2017, **94**, 365-373.
247. F. Cao, S. Guo, H. Ma, D. Shan, S. Yang and J. Gong, *Biosensors and Bioelectronics*, 2011, **26**, 2756-2760.
248. V. A. Kumary, T. M. Nancy, J. Divya and K. Sreevalsan, *International Journal of Electrochemical Science*, 2013, **8**, 2220-2228.
249. B. Yuan, C. Xu, D. Deng, Y. Xing, L. Liu, H. Pang and D. Zhang, *Electrochimica Acta*, 2013, **88**, 708-712.
250. X. Zhu, Q. Jiao, C. Zhang, X. Zuo, X. Xiao, Y. Liang and J. Nan, *Microchimica Acta*, 2013, **180**, 477-483.
251. W. Lv, M. Guo, M.-H. Liang, F.-M. Jin, L. Cui, L. Zhi and Q.-H. Yang, *Journal of Materials Chemistry*, 2010, **20**, 6668-6673.
252. W. Lv, F.-M. Jin, Q. Guo, Q.-H. Yang and F. Kang, *Electrochimica Acta*, 2012, **73**, 129-135.
253. G. Palmisano, E. García-López, G. Marcì, V. Loddo, S. Yurdakal, V. Augugliaro and L. Palmisano, *Chemical Communications*, 2010, **46**, 7074-7089.
254. S. Von Kraemer, K. Wikander, G. Lindbergh, A. Lundblad and A. E. Palmqvist, *Journal of Power Sources*, 2008, **180**, 185-190.
255. Y. Luo, H. Liu, Q. Rui and Y. Tian, *Analytical Chemistry*, 2009, **81**, 3035-3041.
256. H. Cao, Y. Zhu, L. Tang, X. Yang and C. Li, *Electroanalysis*, 2008, **20**, 2223-2228.
257. X. Pang, D. He, S. Luo and Q. Cai, *Sensors and Actuators B: Chemical*, 2009, **137**, 134-138.
258. H. Tang, F. Yan, Q. Tai and H. L. Chan, *Biosensors and Bioelectronics*, 2010, **25**, 1646-1651.
259. Q. Li, G. Luo, J. Feng, Q. Zhou, L. Zhang and Y. Zhu, *Electroanalysis*, 2001, **13**, 413-416.
260. H. Imai, Y. Takei, K. Shimizu, M. Matsuda and H. Hirashima, *Journal of Materials Chemistry*, 1999, **9**, 2971-2972.
261. L. K. Tan, M. A. Chong and H. Gao, *The Journal of Physical Chemistry C*, 2008, **112**, 69-73.
262. J. H. Schattka, D. G. Shchukin, J. Jia, M. Antonietti and R. A. Caruso, *Chemistry of Materials*, 2002, **14**, 5103-5108.
263. H. Choi, Y. J. Kim, R. S. Varma and D. D. Dionysiou, *Chemistry of Materials*, 2006, **18**, 5377-5384.
264. L. Kavan, J. Rathouský, M. Grätzel, V. Shklover and A. Zukal, *The Journal of Physical Chemistry B*, 2000, **104**, 12012-12020.
265. X. Zhang, M. Zhou and L. Lei, *Carbon*, 2005, **43**, 1700-1708.
266. Y. Zhang, S. Deng, B. Sun, H. Xiao, L. Li, G. Yang, Q. Hui, J. Wu and J. Zheng, *Journal of Colloid and Interface Science*, 2010, **347**, 260-266.
267. S. Orlanducci, V. Sessa, M. L. Terranova, G. A. Battiston, S. Battiston and R. Gerbasi, *Carbon*, 2006, **44**, 2839-2843.
268. N. I. Kovtyukhova, P. J. Ollivier, B. R. Martin, T. E. Mallouk, S. A. Chizhik, E. V. Buzaneva and A. D. Gorchinskiy, *Chemistry of Materials*, 1999, **11**, 771-778.
269. Y. Fan, H.-T. Lu, J.-H. Liu, C.-P. Yang, Q.-S. Jing, Y.-X. Zhang, X.-K. Yang and K.-J. Huang, *Colloids and Surfaces B: Biointerfaces*, 2011, **83**, 78-82.
270. Y. Fan, K.-J. Huang, D.-J. Niu, C.-P. Yang and Q.-S. Jing, *Electrochimica Acta*, 2011, **56**, 4685-4690.

271. Z. Luo, X. Ma, D. Yang, L. Yuwen, X. Zhu, L. Weng and L. Wang, *Carbon*, 2013, **57**, 470-476.
272. Y. Chen, Y. Li, D. Deng, H. He, X. Yan, Z. Wang, C. Fan and L. Luo, *Biosensors and Bioelectronics*, 2018, **102**, 301-306.
273. Q. Yan, L. Cao, H. Dong, Z. Tan, Y. Hu, Q. Liu, H. Liu, P. Zhao, L. Chen, Y. Liu, Y. Li and Y. Dong, *Biosensors and Bioelectronics*, 2019, **127**, 174-180.
274. M. G. Guzmán and G. Kouri, *The Lancet infectious diseases*, 2002, **2**, 33-42.
275. M. G. Guzman and E. Harris, *The Lancet*, 2015, **385**, 453-465.
276. C. M. Rice, E. M. Lenches, S. Shin, R. Sheets and J. Strauss, *Science*, 1985, **229**, 726-733.
277. T. J. Chambers, C. S. Hahn, R. Galler and C. M. Rice, *Annual review of microbiology*, 1990, **44**, 649-688.
278. M. G. Guzmán and G. Kouri, *International journal of infectious diseases*, 2004, **8**, 69-80.
279. S. B. Halstead, *Journal of Infectious Diseases*, 1979, **140**, 527-533.
280. S. B. Halstead, *Science*, 1988, **239**, 476-481.
281. I. Kurane, *Comparative immunology, microbiology and infectious diseases*, 2007, **30**, 329-340.
282. W. H. Organization, S. P. f. Research, T. i. T. Diseases, W. H. O. D. o. C. o. N. T. Diseases, W. H. O. Epidemic and P. Alert, *Dengue: guidelines for diagnosis, treatment, prevention and control*, World Health Organization, 2009.
283. E. B. Hayes and D. J. Gubler, *The Pediatric infectious disease journal*, 1992, **11**, 311-317.
284. A. B. Sabin, *American journal of tropical medicine and hygiene*, 1952, **1**, 30-50.
285. D. J. Gubler, *Clinical microbiology reviews*, 1998, **11**, 480-496.
286. V. Dietz, D. Gubler, S. Ortiz, G. Kuno, A. Casta-Velez, G. Sather, I. Gomez and E. Vergne, *Puerto Rico health sciences journal*, 1996, **15**, 201-210.
287. S. Kalayanarooj, *Tropical medicine and health*, 2011, 1112080193-1112080193.
288. D. S. Burke, A. Nisalak, D. E. Johnson and R. M. Scott, *The American journal of tropical medicine and hygiene*, 1988, **38**, 172-180.
289. K. A. Hanley and S. C. Weaver, *Frontiers in dengue virus research*, Horizon Scientific Press, 2010.
290. M. G. Guzmán and G. Kouri, *Clinical and diagnostic laboratory immunology*, 1996, **3**, 621.
291. V. Vorndam and G. Kuno, *Dengue and dengue hemorrhagic fever. CAB International, New York, NY*, 1997, 313-333.
292. P. Buchy and R. Peeling, *Dengue: Guidelines for Diagnosis, Treatment, Prevention and Control: New Edition. France: World Health Organization Press, Geneva, Swisterland*, 2009, 91-109.
293. R. W. Peeling, H. Artsob, J. L. Pelegrino, P. Buchy, M. J. Cardoso, S. Devi, D. A. Enria, J. Farrar, D. J. Gubler and M. G. Guzman, *Nature Reviews Microbiology*, 2010, **8**, S30.
294. K.-I. Yamada, T. Takasaki, M. Nawa and I. Kurane, *Journal of Clinical Virology*, 2002, **24**, 203-209.
295. R. S. Lanciotti, C. H. Calisher, D. J. Gubler, G.-J. Chang and A. V. Vorndam, *Journal of clinical microbiology*, 1992, **30**, 545-551.
296. P. R. Young, P. A. Hilditch, C. Bletchly and W. Halloran, *Journal of clinical microbiology*, 2000, **38**, 1053-1057.
297. B. Innis, A. Nisalak, S. Nimmannitya, S. Kusalerdchariya, V. Chongswasdi, S. Suntayakorn, P. Puttisri and C. Hoke, *The American journal of tropical medicine and hygiene*, 1989, **40**, 418-427.

298. M. Nawa, T. Takasaki, K.-I. Yamada, T. Akatsuka and I. Kurane, *Journal of virological methods*, 2001, **92**, 65-70.
299. J. Pelegrino, *World Health Organization, Special Programme for Research and Training in Tropical Diseases*, 2006.
300. pop-bio, Dengue Rapid Combo Test (IgG/IgM and NS1 tests), <https://pop-bio.com/product/dengue-rapid-combo-test-iggigm-and-ns1-tests/?v=75dfaed2dded>, (accessed 10 Oct, 2019).
301. I. E. Vickers, K. M. Harvey, M. G. Brown, K. Nelson, M. B. DuCasse and J. F. Lindo, *Journal of biomedical science*, 2015, **22**, 55.
302. S. Mitra, R. Choudhari, H. Nori, K. P. P. Abhilash, V. Jayaseelan, A. Abraham, A. O. Cherian, J. Prakash and J. Muliylil, *Journal of vector borne diseases*, 2016, **53**, 30.
303. W. S. Jang, S. Y. Kwak, W. L. May, D. J. Yang, J. Nam and C. S. Lim, *PloS one*, 2019, **14**, e0213451.
304. A. Garg, J. Garg, D. V. Singh and T. Dhole, *Journal of laboratory physicians*, 2019, **11**, 63.
305. F. F. Loh, Dengue cases at an all-time high, <https://www.thestar.com.my/news/nation/2019/08/10/dengue-cases-at-an-all-time-high>, (accessed 10 Oct, 2019).
306. Y.-T. Tung, M.-F. Wu, G.-J. Wang and S.-L. Hsieh, *Nanomedicine: Nanotechnology, Biology and Medicine*, 2014, **10**, 1335-1341.
307. N. Oliveira, E. Souza, D. Ferreira, D. Zanforlin, W. Bezerra, M. Borba, M. Arruda, K. Lopes, G. Nascimento and D. Martins, *Sensors*, 2015, **15**, 15562-15577.
308. S.-A. Jin, S. Poudyal, E. E. Marinero, R. J. Kuhn and L. A. Stanciu, *Electrochimica Acta*, 2016, **194**, 422-430.
309. K. Navakul, C. Warakulwit, P.-t. Yenchtsomanus, A. Panya, P. A. Lieberzeit and C. Sangma, *Nanomedicine: Nanotechnology, Biology and Medicine*, 2017, **13**, 549-557.
310. C. Singhal, C. S. Pundir and J. Narang, *Biosensors and Bioelectronics*, 2017, **97**, 75-82.
311. A. Santos, P. R. Bueno and J. J. Davis, *Biosensors and Bioelectronics*, 2018, **100**, 519-525.
312. J. Anusha, B. C. Kim, K.-H. Yu and C. J. Raj, *Biosensors and Bioelectronics*, 2019, **142**, 111511.
313. M. H. Nawaz, A. Hayat, G. Catanante, U. Latif and J. L. Marty, *Analytica Chimica Acta*, 2018, **1026**, 1-7.
314. Q. Palomar, C. Gondran, R. Marks, S. Cosnier and M. Holzinger, *Electrochimica Acta*, 2018, **274**, 84-90.
315. V. Deubel, R. M. Kinney and D. W. Trent, *Virology*, 1988, **165**, 234-244.
316. C. W. Mandl, F. X. Heinz, E. Stöckl and C. Kunz, *Virology*, 1989, **173**, 291-301.
317. S. A. Cardoso, V. F. Paixão, M. D. Oliveira, E. R. Honda, L. L. Oliveira, C. C. da Silva and S. O. De Paula, *Protein Expression and Purification*, 2013, **92**, 9-13.
318. Y. Makino, M. Tadano, S. Arakaki and T. Fukunaga, *The American Journal of Tropical Medicine and Hygiene*, 1991, **45**, 636-643.
319. S. Sukupolvi-Petty, S. K. Austin, W. E. Purtha, T. Oliphant, G. E. Nybakken, J. J. Schlesinger, J. T. Roehrig, G. D. Gromowski, A. D. Barrett and D. H. Fremont, *Journal of virology*, 2007, **81**, 12816-12826.
320. G. D. Gromowski, N. D. Barrett and A. D. Barrett, *Journal of virology*, 2008, **82**, 8828-8837.
321. E. S. d. O. Rocha, J. G. de Oliveira, J. R. dos Santos, G. O. L. Rodrigues, L. B. Figueiredo, J. E. M. Pessanha, F. A. Proietti, F. G. da Fonseca, C. A. Bonjardim, P. C. P. Ferreira and E. G. Kroon, *Journal of Virological Methods*, 2013, **187**, 114-120.
322. D. H. Libraty, L. Zhang, A. Obcena, J. D. Brion and R. Z. Capeding, *Acta Tropica*, 2015, **142**, 103-107.

323. A. Rockstroh, B. Moges, L. Barzon, A. Sinigaglia, G. Palù, W. Kumbukgolla, J. Schmidt-Chanasit, M. Sarno, C. Brites and A. Moreira-Soto, *Emerging microbes & infections*, 2017, **6**, 1-9.
324. Y. W. Yew, T. Ye, L. W. Ang, L. C. Ng, G. Yap, L. James, S. K. Chew and K. T. Goh, *Ann Acad Med Singapore*, 2009, **38**, 667-675.
325. D. W. C. Beasley, M. R. Holbrook, A. P. A. Travassos da Rosa, L. Coffey, A.-S. Carrara, K. Phillippi-Falkenstein, R. P. Bohm, M. S. Ratterree, K. M. Lillibridge, G. V. Ludwig, J. Estrada-Franco, S. C. Weaver, R. B. Tesh, R. E. Shope and A. D. T. Barrett, *Journal of Clinical Microbiology*, 2004, **42**, 2759-2765.
326. M. R. Holbrook, R. E. Shope and A. D. T. Barrett, *Journal of Clinical Microbiology*, 2004, **42**, 4101-4110.
327. E. L. Pang, H. Peyret, A. Ramirez, H.-S. Loh, L. KokSong, C. M. Fang, W. M. Rosenberg and G. P. Lomonossoff, *Frontiers in plant science*, 2019, **10**, 455.
328. M. Khan, M. N. Tahir, S. F. Adil, H. U. Khan, M. R. H. Siddiqui, A. A. Al-warthan and W. Tremel, *Journal of Materials Chemistry A*, 2015, **3**, 18753-18808.
329. F. Xiao, Y. Li, X. Zan, K. Liao, R. Xu and H. Duan, *Advanced Functional Materials*, 2012, **22**, 2487-2494.
330. M. M. Rahman, A. Ahammad, J.-H. Jin, S. J. Ahn and J.-J. Lee, *Sensors*, 2010, **10**, 4855-4886.
331. J. Ding, W. Sun, G. Wei and Z. Su, *RSC Advances*, 2015, **5**, 35338-35345.
332. J. Ding, S. Zhu, T. Zhu, W. Sun, Q. Li, G. Wei and Z. Su, *RSC Advances*, 2015, **5**, 22935-22942.
333. Y. Li, P. Zhang, Z. Ouyang, M. Zhang, Z. Lin, J. Li, Z. Su and G. Wei, *Advanced Functional Materials*, 2016, **26**, 2122-2134.
334. M. Giorgio, M. Trinei, E. Migliaccio and P. G. Pelicci, *Nature reviews Molecular cell biology*, 2007, **8**, 722-728.
335. W. Chen, S. Cai, Q.-Q. Ren, W. Wen and Y.-D. Zhao, *Analyst*, 2012, **137**, 49-58.
336. W. Zhou, F. Sun, K. Pan, G. Tian, B. Jiang, Z. Ren, C. Tian and H. Fu, *Advanced Functional Materials*, 2011, **21**, 1922-1930.
337. H. Shen, H. Hu, D. Liang, H. Meng, P. Li, W. Tang and C. Cui, *Journal of Alloys and Compounds*, 2012, **542**, 32-36.
338. J. Yu, G. Wang, B. Cheng and M. Zhou, *Applied Catalysis B: Environmental*, 2007, **69**, 171-180.
339. C. Uboldi, P. Urbán, D. Gilliland, E. Bajak, E. Valsami-Jones, J. Ponti and F. Rossi, *Toxicology in Vitro*, 2016, **31**, 137-145.
340. I. Calizo, D. Teweldebrhan, W. Bao, F. Miao, C. Lau and A. Balandin, 2008.
341. J. Park, A. Reina, R. Saito, J. Kong, G. Dresselhaus and M. Dresselhaus, *Carbon*, 2009, **47**, 1303-1310.
342. A. C. Ferrari and D. M. Basko, *Nature nanotechnology*, 2013, **8**, 235-246.
343. P. Falaras, A. Hugot-Le Goff, M. Bernard and A. Xagas, *Solar energy materials and solar cells*, 2000, **64**, 167-184.
344. X. Dong, D. Fu, W. Fang, Y. Shi, P. Chen and L. J. Li, *Small*, 2009, **5**, 1422-1426.
345. M. E. Orazem and B. Tribollet, *Electrochemical impedance spectroscopy*, John Wiley & Sons, 2011.
346. L. Aravinda, K. Nagaraja, H. Nagaraja, K. U. Bhat and B. R. Bhat, *Electrochimica Acta*, 2013, **95**, 119-124.
347. J. V. Rushworth, A. Ahmed, H. H. Griffiths, N. M. Pollock, N. M. Hooper and P. A. Millner, *Biosensors and Bioelectronics*, 2014, **56**, 83-90.
348. S. G. Leonardi, D. Aloisio, N. Donato, P. A. Russo, M. C. Ferro, N. Pinna and G. Neri, *ChemElectroChem*, 2014, **1**, 617-624.

349. A. J. Bard and L. R. Faulkner, *Electrochemical Methods: Fundamental and Applications*. 2nd ed. New York: Wiley, 2001, **231**.
350. H. Matsuda and Y. Ayabe, *Zeitschrift fuer Elektrochemie and Angewandte Physikalische Chemie*, 1955, **59**, 494-503.
351. W. Zhao, H. Wang, X. Qin, X. Wang, Z. Zhao, Z. Miao, L. Chen, M. Shan, Y. Fang and Q. Chen, *Talanta*, 2009, **80**, 1029-1033.
352. P. M. Nia, P. M. Woi and Y. Alias, *Applied Surface Science*, 2017, **413**, 56-65.
353. D. J. Gubler and G. G. Clark, *Emerging infectious diseases*, 1995, **1**, 55.
354. S. S. Whitehead and K. Subbarao, *Cold Spring Harbor perspectives in biology*, 2018, **10**, a028811.
355. V. M. Huang, S.-L. Wu, M. E. Orazem, N. Pébère, B. Tribollet and V. Vivier, *Electrochimica Acta*, 2011, **56**, 8048-8057.
356. S. Kwakye, V. N. Goral and A. J. Baeumner, *Biosensors and Bioelectronics*, 2006, **21**, 2217-2223.
357. C. Singhal, C. Pundir and J. Narang, *Biosensors and Bioelectronics*, 2017, **97**, 75-82.
358. S. Tripathy, S. R. K. Vanjari, V. Singh, S. Swaminathan and S. G. Singh, *Biosensors and Bioelectronics*, 2017, **90**, 378-387.
359. H. Xu, B. Di, Y.-x. Pan, L.-w. Qiu, Y.-d. Wang, W. Hao, L.-j. He, K.-y. Yuen and X.-y. Che, *Journal of Clinical Microbiology*, 2006, **44**, 2872-2878.
360. M. d. R. Q. Lima, R. M. R. Nogueira, H. G. Schatzmayr and F. B. d. Santos, *PLOS Neglected Tropical Diseases*, 2010, **4**, e738.
361. J. Cecchetto, F. C. Carvalho, A. Santos, F. C. Fernandes and P. R. Bueno, *Sensors and Actuators B: Chemical*, 2015, **213**, 150-154.
362. N. T. Darwish, A. H. Alrawi, S. D. Sekaran, Y. Alias and S. M. Khor, *Journal of The Electrochemical Society*, 2016, **163**, B19-B25.
363. J. H. Chávez, J. R. Silva, A. A. Amarilla and L. T. Moraes Figueiredo, *Biologicals*, 2010, **38**, 613-618.
364. E. L. Pang, University of Nottingham, 2018.
365. R. J. Chen, Y. Zhang, D. Wang and H. Dai, *Journal of the American Chemical Society*, 2001, **123**, 3838-3839.
366. V. A. Karachevtsev, S. G. Stepanian, A. Y. Glamazda, M. V. Karachevtsev, V. V. Eremenko, O. S. Lytvyn and L. Adamowicz, *The Journal of Physical Chemistry C*, 2011, **115**, 21072-21082.
367. A. Chua, I. Prat, C. M. Nuebling, D. Wood and F. Moussy, *PLoS neglected tropical diseases*, 2017, **11**, e0005269.
368. L. Priyamvada, K. M. Quicke, W. H. Hudson, N. Onlamoon, J. Sewatanon, S. Edupuganti, K. Pattanapanyasat, K. Chokephaibulkit, M. J. Mulligan and P. C. Wilson, *Proceedings of the National Academy of Sciences*, 2016, **113**, 7852-7857.
369. S. Matheus, R. Boukhari, B. Labeau, V. Ernault, L. Bremand, M. Kazanji and D. Rousset, *Emerging infectious diseases*, 2016, **22**, 1691.
370. A. C. Felix, N. C. S. Souza, W. M. Figueiredo, A. A. Costa, M. Inenami, R. M. da Silva, J. E. Levi, C. S. Pannuti and C. M. Romano, *Journal of medical virology*, 2017, **89**, 1477-1479.
371. J. Cecchetto, F. C. Fernandes, R. Lopes and P. R. Bueno, *Biosensors and Bioelectronics*, 2017, **87**, 949-956.
372. P. Panuwet, R. E. Hunter Jr, P. E. D'Souza, X. Chen, S. A. Radford, J. R. Cohen, M. E. Marder, K. Kartavenka, P. B. Ryan and D. B. Barr, *Critical reviews in analytical chemistry*, 2016, **46**, 93-105.
373. J. Lin, X. Chen and P. Huang, *Advanced drug delivery reviews*, 2016, **105**, 242-254.
374. L. Zhang, J. Xia, Q. Zhao, L. Liu and Z. Zhang, *Small*, 2010, **6**, 537-544.

375. O. Akhavan, M. Choobtashani and E. Ghaderi, *The Journal of Physical Chemistry C*, 2012, **116**, 9653-9659.
376. O. Akhavan and E. Ghaderi, *ACS nano*, 2010, **4**, 5731-5736.
377. K. Yang, J. Wan, S. Zhang, B. Tian, Y. Zhang and Z. Liu, *Biomaterials*, 2012, **33**, 2206-2214.
378. S. S. Maktedar, S. S. Mehetre, G. Avashthi and M. Singh, *Ultrasonics Sonochemistry*, 2017, **34**, 67-77.
379. H. Zhou, M. Jiang, Y. Xin, G. Sun, S. Long, S. Bao, X. Cao, S. Ji and P. Jin, *Materials Letters*, 2017, **192**, 123-127.
380. A. Nel, T. Xia, L. Mädler and N. Li, *science*, 2006, **311**, 622-627.
381. J. Jiang, G. Oberdörster and P. Biswas, *Journal of Nanoparticle Research*, 2009, **11**, 77-89.
382. A. Ivask, T. Titma, M. Visnapuu, H. Vija, A. Kakinen, M. Sihtmae, S. Pokhrel, L. Madler, M. Heinlaan and V. Kisand, *Current topics in medicinal chemistry*, 2015, **15**, 1914-1929.
383. L. Ou, B. Song, H. Liang, J. Liu, X. Feng, B. Deng, T. Sun and L. Shao, *Particle and fibre toxicology*, 2016, **13**, 57.
384. R. Landsiedel, L. Ma-Hock, A. Kroll, D. Hahn, J. Schnekenburger, K. Wiench and W. Wohlleben, *Advanced Materials*, 2010, **22**, 2601-2627.
385. T. Mosmann, *Journal of Immunological Methods*, 1983, **65**, 55-63.
386. W. Khaodee, B. Jongsomjit, P. Praserttham, S. Goto and S. Assabumrungrat, *Journal of Molecular Catalysis A: Chemical*, 2008, **280**, 35-42.
387. S. K. Sohaebuddin, P. T. Thevenot, D. Baker, J. W. Eaton and L. Tang, *Particle and fibre toxicology*, 2010, **7**, 22.
388. F. M. Tonelli, V. A. Goulart, K. N. Gomes, M. S. Ladeira, A. K. Santos, E. Lorençon, L. O. Ladeira and R. R. Resende, *Nanomedicine*, 2015, **10**, 2423-2450.
389. D. Bitounis, H. Ali-Boucetta, B. H. Hong, D. H. Min and K. Kostarelos, *Advanced Materials*, 2013, **25**, 2258-2268.
390. G. Lalwani, M. D'Agati, A. M. Khan and B. Sitharaman, *Advanced drug delivery reviews*, 2016, **105**, 109-144.
391. O. Akhavan, E. Ghaderi and A. Esfandiari, *The Journal of Physical Chemistry B*, 2011, **115**, 6279-6288.
392. X. Zhou, M. Dorn, J. Vogt, D. Spemann, W. Yu, Z. Mao, I. Estrela-Lopis, E. Donath and C. Gao, *Nanoscale*, 2014, **6**, 8535-8542.
393. K. Bachmann, in *Pharmacology*, Elsevier, 2009, pp. 303-325.
394. A. M. Pinto, S. Moreira, I. C. Gonçalves, F. M. Gama, A. M. Mendes and F. D. Magalhães, *Colloids and Surfaces B: Biointerfaces*, 2013, **104**, 229-238.
395. H. Zhang, Z. Ji, T. Xia, H. Meng, C. Low-Kam, R. Liu, S. Pokhrel, S. Lin, X. Wang and Y.-P. Liao, *ACS nano*, 2012, **6**, 4349-4368.
396. S.-J. Choi, J.-M. Oh and J.-H. Choy, *Journal of Inorganic Biochemistry*, 2009, **103**, 463-471.
397. W. Hu, C. Peng, M. Lv, X. Li, Y. Zhang, N. Chen, C. Fan and Q. Huang, *ACS nano*, 2011, **5**, 3693-3700.
398. M. M. N. Babadaei, M. F. Moghaddam, S. Solhvand, E. Alizadehmollayaghoob, F. Attar, E. Rajabbeigi, K. Akhtari, S. Sari and M. Falahati, *International journal of nanomedicine*, 2018, **13**, 6871.